UNIVERSITY OF SOUTHAMPTON

Faculty of Engineering and Physical Sciences
Aeronautics and Astronautics

Development of scalable and flexible non-thermal Dielectric Barrier Discharge systems for novel low-temperature plasma applications

by

Henrike Jakob

ORCiD: 0000-0002-6035-2150

March, 2022

A thesis for the degree of
Doctor of Philosophy

UNIVERSITY OF SOUTHAMPTON

ABSTRACT

Faculty of Engineering and Physical Sciences

Aeronautics and Astronautics

A thesis for the degree of Doctor of Philosophy

Development of scalable and flexible non-thermal Dielectric Barrier Discharge systems for novel low-temperature plasma applications

by Henrike Jakob

Atmospheric non-thermal plasma has gained increasing interest for various applications due to its unique physical and chemical properties. For example, reactive species produced by atmospheric non-thermal plasma can decontaminate spacecrafts featuring thermally sensitive materials. Although Dielectric Barrier Discharge (DBD) systems have been demonstrated as one of the many promising methods to generate non-thermal plasma, the generation of non-thermal plasma over large and complex geometries, such as spacecraft or the human body, remains challenging to date. This thesis, therefore, aims to investigate and develop a scalable and flexible non-thermal plasma generation system, thus promoting further implementation of non-thermal plasma technology.

Firstly, a new method using printed electronics techniques on thin materials is employed for the fabrication of electrodes of DBD systems to enhance their scalability and flexibility. An experimental study is carried out, where the DBD systems are assessed for varying system sizes to assess the capability of large scale plasma geometries. Moreover, the flexibility of the systems is quantified for varying curvatures to allow the generation of non-thermal plasma over complex geometries.

A fully scalable and flexible plasma source can require a complex electrode geometry to be successfully used in an application. Therefore, in conjunction with the experimental study, a new electrical model is developed for complex electrode designs. This electrical model can play an important role in the characterization, design, and definition of optimal operating conditions for non-thermal plasma sources in a wide field of applications. The presented model focuses on the partitioning of the electrode surface into a plasma discharging and non-discharging area. Thus the electrical model accounts for the dynamic behaviour of the plasma generation over complex electrode geometries during operation.

Lastly, the developed DBD systems are employed for three feasibility studies, where they successfully demonstrate their ability for applications within the aerospace sector and the biomedical field. In the aerospace sector, the DBD systems and their ability to produce a high electron density are used for a new "Cold Radio Blackout Testing" solution. This approach aims to model the spatial gradient of the electron density within a re-entry plasma sheath around space vehicles, causing a communication interruption, the Radio Blackout. Further, the DBD systems are used as a decontamination system for medical equipment, such as Personal Protective Equipment (PPE) during the COVID-19 pandemic. The last feasibility study presents a new thin and narrow plasma source, the plasma yarn, which is successfully used for the sterilisation of biofilms in narrow spaces, such as endoscopes.

Contents

List of Figures

List of Tables

Nomenclature

α	Discharge fraction
A	Transition probability
A_A	Area of dielectric capacitive region
A_B	Area of discharge region
A_C	Area of non-discharge region
A_{PIV}	Area of of PIV region
A_{print}	Area of printed electrode
$A_{theo.}$	Theoretical are of electrode design
Amp_{Sample}	Amplitude of RF signal of sample
$Amp_{Reference}$	Amplitude of RF signal of reference
B_k	Intensity of blue image component
C	Capacitance
$C_{d,A}$	Dielectric capacitance in dielectric capacitive region
$C_{d,B}$	Dielectric capacitance in discharge region
$C_{d,C}$	Dielectric capacitance in non-discharge region
$C_{g,B}$	Dielectric capacitance in discharge region
$C_{g,C}$	Dielectric capacitance in non-discharge region
$C_{refl.}$	Reflective coefficient
C_p	Probe Capacitor
C_S	Parasitic Capacitance
D	plasma dose
d	Distance
e	Electron charge
ε_0	Permittivity of vacuum
ε_r	relative permittivity
E	Energy
f	AC frequency
f_{plasma}	Plasma frequency
f_{pp}	Print precision factor
f_{radio}	Radio frequency
G_k	Intensity of green image component
I	Current

I_A	Current in dielectric capacitive region
I_B	Current in discharge region
I_C	Current in non-discharge region
I_{CCS}	Current of controlled current source
I_{spec}	Spectral intensity
I_{img}	Image Intensity
κ	Attenuation per unit length
k	Excitation rate of excited species
λ	Wave length
L	Length
$L_{ant.}$	Characteristic length scale of antenna
n	Transformer turn ratio
m_e	Electron mass
n_e	Electron density
N	Number Density of excited species
N_{PIV}	Number of PIV particles
N_p	Windings of primary transformer side
N_s	Windings of secondary transformer side
φ	Phase shift
p_d	discharge propagation length
$P_{inst.}$	Instantaneous Power
P_{ave}	average discharge power
P_A	average discharge power per unit area
P_L	average discharge power per unit length
P_T	Discharge power over one period
Q	Weight of excited species
Q_{DBD}	Charge over DBD system plasma source
R_k	Intensity of red image component
R_{pl}	Resistance of microdischarges
σ	Excitation cross section
σ_{img}	Image uniformity
t	Thickness
t_{LS}	thickness of laser sheet
t_{int}	Integration time
t_{treat}	Treatment time
T_{PIV}	PIV Transmission
T_e	Electron temperature
T_g	Gas temperature
Θ_P	Scaling factor
ρ	Density
ρ_{dow}	relative particle density downstream

ρ_{up}	relative particle density upstream
V	Voltage
V_{bd}	Breakdown voltage
$V_{bd,pos.}$	Breakdown voltage in positive half period
$V_{bd,neg}$	Breakdown voltage in negative half period
V_{CP}	Voltage across probe capacitor
V_{pp}	Peak-to-peak voltage
V_p	Voltage on primary transformer side
V_s	Voltage on secondary transformer side
V_{rms}	Root mean square voltage
V_{plasma}	Plasma Volume
w	Velocity component in z-direction

APPJ	Atmospheric Pressure Plasma Jet
CD	Corona Discharge
CCS	Controlled current source
DBD	Dielectric Barrier Discharge
EM	Electromagnetic
FOV	Field of View
GND	Ground
HV	High Voltage
MHCD	Micro Hollow Cathode Discharge
PPE	Personal Protective Equipment
StA	Scans to average
RF	Radio frequency

Declaration of Authorship

I declare that this thesis and the work presented in it is my own and has been generated by me as the result of my own original research.

I confirm that:

1. This work was done wholly or mainly while in candidature for a research degree at this University;
2. Where any part of this thesis has previously been submitted for a degree or any other qualification at this University or any other institution, this has been clearly stated;
3. Where I have consulted the published work of others, this is always clearly attributed;
4. Where I have quoted from the work of others, the source is always given. With the exception of such quotations, this thesis is entirely my own work;
5. I have acknowledged all main sources of help;
6. Where the thesis is based on work done by myself jointly with others, I have made clear exactly what was done by others and what I have contributed myself;
7. Parts of this work have been published as:
    - Jakob, H., Kim, M.K. "Generation of non-thermal plasmas over large and complex surfaces." Plasma Research Express, vol. 2, no. 3, 2020
    - Jakob, H., Kim, M.K. "Electrical model for complex surface DBD plasma sources. IEEE Transaction on plasma science, vol. 49, no 10, 2021
    - Kim, M.K., Lawson, J., Hervé, R., Jakob, H., Ganapathisubramani, B., Keevil, C.W. "Development of a rapid plasma decontamination system for decontamination and reuse of filtering facepiece respirators." AIP Advances, vol. 11, no 10, 2021
    - "Generation of non-thermal plasmas over large and complex surfaces", presented by H. Jakob, H. at 46th Plasma Physics Conference, Loughborough, UK, 04/2019

- "Feasibility Study on the Use of Non-Thermal Plasma for a Cold Radio Blackout Experiment", presented by H. Jakob at 2020 AIAA SciTech Forum, Orlando, USA, 01/2020
- Kim, M, Keevil, C. W., Hervé, R. C., and Jakob, H. 2020. "Sterilisation of Endoscopes". United Kingdom Patent Application No. 2008127.9, filed May 2020. Patent Pending.

Signed: Date:

Acknowledgements

This thesis has been supported by a number of people, each in their own way. Firstly, I would like to thank Dr. Minkwan Kim. As my supervisor he has been my main support and motivator for my research. He has always provided guidance and encouragement throughout this process, and patiently helped me see the bigger picture and context when I was stuck.

I would also like to thank Dr. Rodolphe Hervé from the School of Biological Sciences, and Dr. John Lawson from the Aerodynamics and Flight Mechanics group at the University of Southampton. Working together with you both on collaborative projects allowed me to apply my research to interesting and exciting new fields and expand my horizon further. I am very grateful for your contribution to this thesis.

Thanks to my colleagues in plasma group, Tom, Ben, Johannes, James, Nathan and Xin, and the remaining Astro group. Working alongside you in the office and the lab, and lunch breaks filled with interesting and fun discussion, have made this journey so much more enjoyable.

A special thanks goes to my friends Matt, Chris and Silvia. You have been been such an amazing support throughout this whole time and especially the past few month your friendship has been invaluable. Thank you for our numerous London-Weekends and to hopefully many more exciting weekend trips to come.

Finally, I would like to thank my family, my parents, my two sisters and my grandparents. You have always supported and encouraged me these past five years no matter the distance. But mainly I would like to thank you for allowing me to become this person, curious about the world and its wonders, which inspired me to step on this research path in the first place. Danke.

Chapter 1

Introduction and literature review

Plasma is referred to as the fourth state of matter, besides the other three states: solid, liquid and gas. Figure 1.1 shows schematically the four states of matter, where transition between the states is achieved by energy increase in the system. The energy input can be in the form of thermal energy or introduced as electrical or electromagnetic radiation energy [1]. For the transfer from gas to plasma, the increased energy results in ionisation of the gas molecules, meaning a portion of electrons are stripped of the atoms and/or molecules and are free-flowing within the system. This ionisation procedure leads to a number of particles within the plasma, such as free-flowing electrons, positive and negative ions and various reactive species. The presence of positive and negative particles leads to plasma acting as an electrically conductive material, which can be influenced through electric and magnetics fields [2]. Although the presence of positive and negative particles in the plasma can result in localised net charges, the total charge balance over a given volume of the plasma is neutral, thus defined as "quasi neutral".

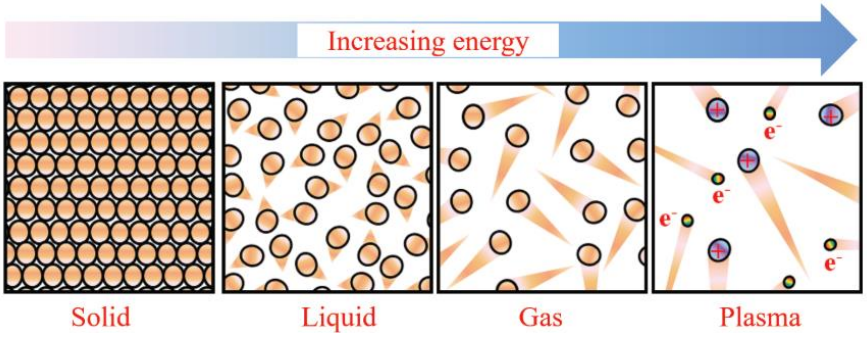

FIGURE 1.1: Schematic of the four states of matter (brown = neutral particles; violet = positive charge ions; iridescent =negative electrons) [3]

1.1 Non-thermal plasma

Plasma can be categorised based on the balance of the inherent particle temperatures [1, 4, 5]. It is defined through its gas temperature T_g and the electron temperature T_e. Figure 1.2 shows a schematic of thermal ("hot") and cold plasma, where positive ions and negative electrons are moving separately within the plasma. The gas temperature is dominated by the temperature of the large heavy particles within the plasma, namely the ions and neutral particles. When the temperature of all particles is equal, the plasma is in the complete thermodynamic equilibrium state ($T_e = T_g$). A local thermodynamic equilibrium (LTE) plasma is also called a "hot" plasma, with electron and heavy particles being in a thermal equilibrium ($T_e \approx T_g$) with values ranging up to 10^4 K. Compared to a hot plasma, a cold plasma, also known as non-thermal plasma, is in a non-equilibrium thermodynamic state, meaning electron temperatures are much larger than heavy particles temperature ($T_e >> T_g$). The actual gas temperature of these kinds of plasma is therefore cold/ambient, going down to as low as room temperature [4].

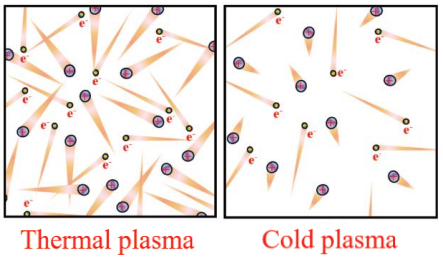

FIGURE 1.2: Schematic of thermal and non-thermal plasma (violet = positive charge ions; iridescent =negative electrons) [3]

Non-thermal plasma can be generated by applying an electric field to a gas at various pressure levels. The electric field accelerates the small and lightweight electrons much more strongly than the heavy ions [6]. This movement leads to inelastic collision between electrons and heavy particles, resulting in a relatively large number of free-flowing electrons in the range up to 10^{20} m^{-3} [5]. Further the collision of these electrons with the surrounding gas atoms and/or molecules lead to an unique plasma chemistry with negative and positive ions, neutral particles, and reactive species molecules. In comparison to the electrons, heavy particles within the plasma are less susceptible to the electric field and only few elastic collisions occur. The overall gas temperature is mainly determined by the average kinetic energy of these heavy particles [4]. Consequently, the few elastic collisions of heavy particles result in only minimal heating, thus creating an overall low gas temperature close to room temperature of the non-thermal plasma [4, 5].

1.2 Applications of non-thermal plasma

The unique physical and chemical characteristics of non-thermal plasma, namely its low temperature and its variety of reactive species, bring a broad spectrum of potential plasma applications. Two fields of applications, the aerospace field and biomedical field will be focused on more in the framework of this thesis.

1.2.1 Aerospace applications

During space missions, interplanetary contamination, such as contamination of a celestial body with earthly organisms (forward contamination) or the contamination of earth with extra-terrestrial agents (backward contamination), has to be prevented [7, 8]. Contamination of moon and other celestial bodies can compromise the success of current and future scientific exploration missions. For example, the search for extraterrestrial organisms on Mars can be hindered when the search rover itself is highly contaminated with earthly organisms. In order to avoid or minimize contamination, cleanrooms and spacecraft components undergo a sterilizing procedure prior to launch to minimize the bioload. This bioload can consist of a number of viable micro-organisms, such as bacterial, virus, fungus or mould [9]. Current sterilization methods include heat and the use of chemicals to reduce the bioload on spacecraft components [10, 11]. Additionally, UV radiation of the sun during exposure in space can aid in the sterilization of the spacecraft after launch during the mission.

However, these current sterilizing procedure can result in damage for advanced materials and sensitive electronics used in spacecrafts. Even minor changes of a spacecraft materials can results in changed properties and performance of the respective component and affect the mission success [8]. As an alternative method, non-thermal plasma has been proposed due to its ability to decontaminate biological organisms at a low temperature, low cost and the absence of chemical toxicity or damage to materials [8, 9, 12]. Studies of different contaminated spacecraft material samples have shown significant reduction in viable bacteria after direct treatment with non-thermal plasma [9]. Also indirect non-thermal plasma treatment of spacecraft materials has demonstrated significant reduction of bacterial concentration [8]. Studies have reported successful decontamination of bacterial load, reaching a 6-log reduction, which is equivalent to the reduction in viable bacteria seen after the dry heat decontamination method [12]. As the reactive species can potentially reach and treat more complex structures of spacecraft components, indirect non-thermal plasma treatment could be a more viable solution for the decontamination of spacecraft components.

Another potential application of non-thermal plasma is the experimental modelling of the radio blackout phenomenon. Figure 1.3 shows a schematic of a hypersonic vehicle during atmospheric re-entry. The radio blackout is a communication interruption caused

by a plasma sheath forming around a vehicle during hypersonic flight [13]. This plasma sheath is generated through an increase in thermal energy, which leads to the onset of dissociation and ionisation of air molecules. The process results in a large number of free-flowing electrons, thus forming a plasma with a given electron density. As the electrons around a vehicle can absorb or reflect radio signals, the communication is interrupted.

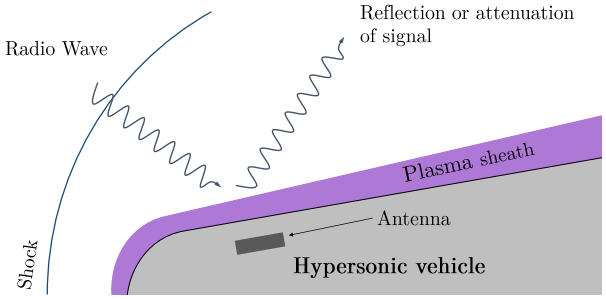

FIGURE 1.3: Schematic of radio blackout on re-entry vehicles through reflection or attenuation of electromagnetic waves in the plasma sheath

The communication interruption occurs when the frequency of an incoming and/or outgoing electromagnetic wave is smaller than the plasma frequency expressed as:

$$f_{plasma} = \frac{\omega_e}{2\pi} = \frac{1}{2\pi}\sqrt{\frac{e^2 n_e}{\varepsilon_0 m_e}} \tag{1.1}$$

where n_e is the electron density, e is the electron charge, ε_0 is the permittivity of vacuum and m_e is the electron mass. Through the plasma frequency, the critical electron density is identified as the key parameter for the onset of a radio blackout. During a re-entry, the electron density around a vehicle can reach about 10^{15} m^{-3} to 10^{19} m^{-3}, which is causing communication interruption for signals using frequencies from 0.3 GHz up to 30 GHz. However, also below a critical electron density, an electromagnetic signal is subjected to attenuation. The electron density in the plasma sheath follows a spatial gradient, thus having layers of varying electron densities [14]. Within one layer the refractive index is dependent on the electron density, and incoming signals can get deflected or fully reflected within that layer. For an accurate analysis of the radio blackout, it is therefore important to account not only for the maximum critical electron density, but also for the spatial gradient within the plasma sheath.

Although the radio blackout is a phenomenon well known since the early space programs [15] [16], vehicles still experience communication interruption during re-entry. The radio blackout occurs for all vehicles travelling at hypervelocity, such as the space shuttle, re-entry capsules and robotic spacecrafts entering the atmospheres of other planetary bodies. The radio blackout phase can last from only a few seconds up to 16 minutes, depending on atmospheric properties, vehicle shape or re-entry angle [17]. Alleviating

the radio blackout is particularly important to ensure the safety of a vehicle because it can travel thousands of miles without guidance from a ground station or GPS satellites.

Investigation of the radio blackout and the re-entry plasma sheath in experimental studies is challenging. Hypersonic ground test facilities, such as shock tubes, shock tunnels or plasma wind tunnels, can replicate certain characteristics of the re-entry conditions. Although shock tubes and shock tunnels can reach Mach numbers up to 30, these conditions can only be maintained for a few milliseconds and the achieved enthalpy is not large enough to initiate ionisation [18]. Arc-heated plasma wind tunnels achieve high temperature re-entry conditions, however the flow can be contaminated with particles and the high temperature conditions require specialised and complex set-ups and measurement equipments to characterise the plasma and the radio blackout [19]. Some investigations of the radio blackout and the re-entry plasma sheath outside of theses facilities have been reported. A helicon plasma source in vacuum is used to generate cold plasma for radio blackout testing [20, 21]. However, these studies focus on the generation of a single electron density and cannot capture the spatial electron density gradient of the re-entry plasma sheath.

1.2.2 Biomedical applications

Non-thermal plasma contains a number of different particles, such as radicals, charged particles (electrons and ions), reactive oxygen species and reactive nitrogen species [22]. Especially the oxygen-based and nitrogen-based reactive species affect the outer structures of cells, provoking surface lesions that cannot be repaired sufficiently quickly [23, 24]. Therefore, in combination with its low temperature at atmospheric pressure, non-thermal plasma can be used for various applications within the biomedical field, such as wound healing, dentistry and oncology, which will be described further [25, 26].

Some of the activities can be grouped together according to their aims for decontamination of biofilms in general, other activities use the decontamination capability for specific areas, such as within the field of dentistry [27]. Biofilms are formed from a group or colony of microorganisms, such as bacteria, adhering to a surface. The biofilm can grow and spread quickly to other regions, thus resulting in contaminated areas within the vicinity of the original colony. Consequently, biofilms can, through increasing contamination, lead to bacterial infections and to potentially life-threatening diseases [22]. Employing non-thermal plasma to eradicate biofilms has been successfully performed [28–30], achieving significant removal of viable bacteria, reaching up to a 6-log reduction.

Non-thermal plasma has also been employed for general wound healing procedures on skin, where the decontamination effect of non-thermal plasma is used. Studies are available for in-vitro testing looking at general decontamination of bacteria and biofilms

[31, 32]. Further ex-vivo studies, using contaminated human skin samples, have demonstrated effective elimination of bacteria after a few minutes of exposure to non-thermal plasma [33, 34]. Actual in-vivo testing with patients in clinical trials have also successfully demonstrated 4 - log reduction of artificially contaminated skin areas [35, 36]. Further clinical trials have used non-thermal plasma on patients to treat actual chronic wounds [37] or diabetic foot ulcers [38] on patients, where a reduction in size and accelerated wound healing has been reported. Figure 1.4(a) shows as an example the kINPen, a hand-held device producing a thin localised jet of non-thermal plasma for wound healing [31]. The commercially available device has demonstrated bactericidal efficiency, while providing low risk of skin damage for patients during the treatment.

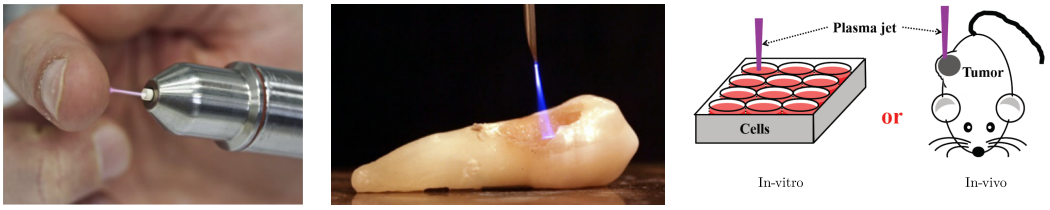

(a) Plasma pen (b) Teeth treatment (c) Cancer plasma treatment

FIGURE 1.4: Various plasma sources (a) Plasma pen (kINPen MED) for wound healing [31]; (b) Plasma applied to teeth [27]; (c) Direct plasma treatment on cancer cells (in-vitro) or tumours in mice in-vitro [3]

Within the field of dentistry the main focus of using non-thermal plasma is the removal of biofilms on tooth surfaces. Figure 1.4(b) shows the plasma treatment of a contaminated tooth, where significant reduction of biofilms of up to 4-log were reported [27, 39]. Other applications within the dentistry field aim at the sterilisation of dental cavities before filling [40], or the disinfection of root canals, to eliminate infection and prevent reinfection, where eradication of all colonies could be demonstrated [41].

Another application within the biomedical field is the treatment of medical devices [42, 43]. Medical devices get contaminated during usage and require a reprocessing procedure. This procedure includes sterilisation to eradicate biofilms before using the device on other patients to avoid cross contamination [44]. Usual methods, such as heat treatment and chemical cleaning, can result in surface degradation [22] of the sensitive medical equipment, while chemicals can additionally provoke toxic reactions in patients or healthcare workers and come along with an increased environmental impact [42, 45]. Studies using non-thermal plasma for the sterilisation of medical device have demonstrated successful eradication of biofilms in medical devices, such as endoscope channels [46, 47]. The complex geometries of medical devices for various application in the biomedical field require highly adaptive non-thermal plasma to ensure sufficient treatment of all areas.

Employing non-thermal plasma within the field of cancer treatment has also been investigated [48–51]. Inactivation of cancer cells is reported either in-vitro or in-vivo on numerous studies using mice, see schematic in Figure 1.4(c). In-vivo studies on cancer cells demonstrated inactivation of skin cancer cells while avoiding damage to healthy tissue and cells after short treatment times with non-thermal plasma [48, 49]. In further in-vivo studies, mice were infected with bladder cancer and subsequently treated with non-thermal plasma [49, 50]. A reduction in tumour size and delayed regrowth compared to control groups has been demonstrated. In-vivo studies as part of clinical trials on patients with head and neck cancer ulceration have used non-thermal plasma as a palliative treatment of cancer illness [52]. Studies with cancer patients for actual tumour treatment using non-thermal plasma are currently undergoing clinical trials. One clinical trial [53] investigating the reduction of cervical dysplasia, a mostly benign cell growth which can lead to cervical cancer. Another study [54] uses a non-thermal plasma spray after tumour removal in the remaining surgical margin area for a number of different tumours (lung, breast, kidney, ovarian). Previous in-vitro studies with the same device on cancer cells (Pancreatic, Ovarian, Kidney) have proven successful in the reduction of viability of the cancer cell line [51], however results of clinical study have not been published yet.

1.3 Methods to generate non-thermal plasma

Non-thermal plasma can be generated in various ways. Figure 1.5 shows the schematics of a few methods to generate non-thermal plasma. All configuration are powered through a high electrical voltage applied between at least two electrodes. The electrodes are of various shapes and can be separated by a dielectric material. Depending on the non-thermal plasma systems, it can be operated at environmental conditions, including pressure, temperature and gasses, to control the physical and chemical properties of the generated non-thermal plasma. Table 1.1 provides an overview of four methods to generate non-thermal plasma, which are the corona discharge (CD), micro hollow cathode discharges (MHCD), atmospheric pressure plasma jet (APPJ) and the dielectric barrier discharge (DBD).

1.3.1 Corona discharge (CD)

Figure1.5(a) shows a schematic of a corona discharge. As can be seen, a corona discharge develops on an asymmetric electrode configuration, when a pulsed high voltage signal is applied. Corona discharges are commonly used as ozone generators [55], particle precipitators [59], surface treatments [60] and biomedical applications [28]. Usually, a needle like electrode is used as the powered high voltage electrode, whereas a flat plate or blunt shape forms the ground electrode [55]. With the applied high voltage, an electric field

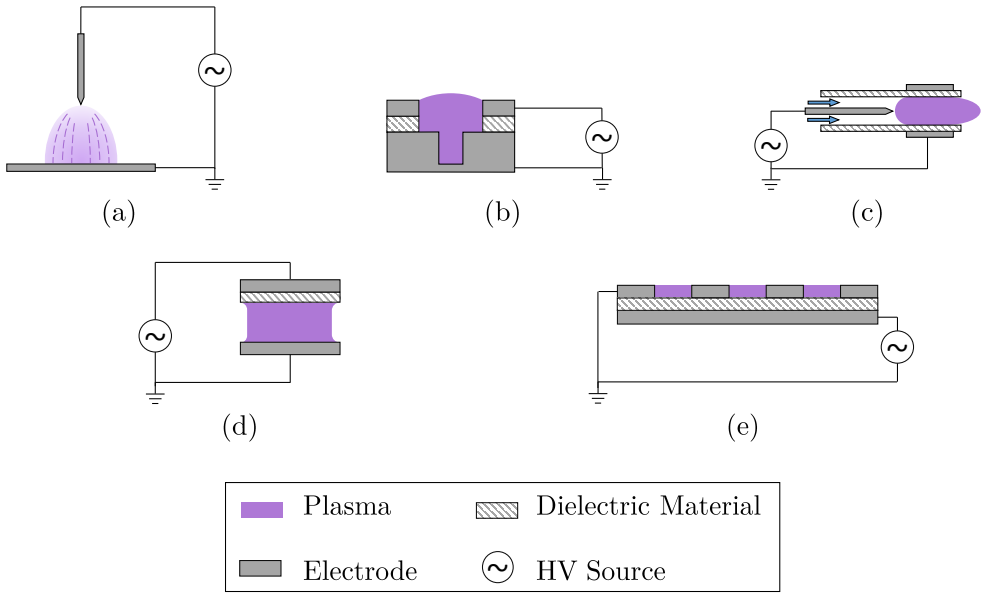

FIGURE 1.5: Schematics of various non-thermal plasma sources: (a) Corona discharge; (b) Micro hollow cathode discharges; (c) Jet plasma; (d) Volume dielectric barrier discharge; (e) surface DBD plasma source

	CD	MHCD	APPJ	DBD
Electrode Configuration	Sharply pointed electrode	Micro Hollow cathode	Coaxial electrodes with gas flow	Electrodes covered by diel. materials
Ignition method	Pulsed DC	DC	Pulsed DC / RF	Pulsed DC / AC / RF
Operating pressure	Atmospheric pressure	Atmospheric pressure	Atmospheric pressure	Atmospheric pressure
Breakdown Voltage	10 ∼ 50 kV	0.2 - 0.7 kV	0.05 ∼2 kV	1 ∼10 kV
Operating gas temperature	300 K	1200 K	300 - 1000 K	300 K
Shield gas requirement	No	Yes	Yes	No
Scalability	No	Yes	Yes	Yes

Table 1.1: Overview of plasma discharge properties for corona discharge (CD) [55], micro hollow cathode discharges (MHCD) [56], atmospheric pressure plasma jets [57], dielectric barrier discharge (DBD) [58]

forms on the powered needle electrode. Due to the sharpness of the needle, the electric field is concentrated and sufficiently strong at the needle tip, to induce ionisation in the surrounding air [59]. The corona discharge is generating a small volume of active plasma region within a critical radius around the needle tip [55]. With increasing distance from the needle, the electric field is not strong enough for self-sufficient plasma. Here secondary processes, such as transport of the charge carried from the high electric field region induce plasma also at larger distances from the needle towards the ground

electrode [61]. The operating voltage required for the corona discharge are in a range of $10 \sim 50$ kV [55]. Corona discharges are simple and robust methods for the generation of non-thermal plasma, however, the high voltage requirements (in comparison to other methods), can add safety concerns for their applications. Additionally, the localised nature of the corona discharge is limiting for applications where non-thermal plasma generation is needed over large geometries.

1.3.2 Micro hollow cathode discharge (MHCD)

A micro hollow cathode discharge (MHCD) develops in a small cavity situated in an arrangement of two electrodes and a dielectric material, see Figure 1.5(b) [62]. MHCD form a highly localised plasma mostly confined within the bore or near the vicinity of it. It can reach temperatures up to 2000 K [56, 62]. MHCD sources can be used in array-like structures to cover larger areas [63] and series arrangements of MHCD can increase the generation of plasma species [64]. The plasma properties are controlled through the dimension of the Micro Hollow Cathode, namely the bore diameter and the thickness of the dielectric material and environmental conditions, such as gas pressure [56].

The MHCD plasma sources benefit from very low operating voltages and the simple geometry allows for simple fabrication methods [65]. However, due to their highly localised plasma generation and high temperatures, they are not suitable for applications requiring lower temperatures, such as those involving thermally sensitive materials such as those used in the biomedical or aerospace field.

1.3.3 Atmospheric pressure plasma jet (APPJ)

Figure 1.5(c) shows an atmospheric pressure jet plasma source, which consist of a set of electrodes, which in combination with a gas flow generates a plasma jet structure [57]. One common arrangement is a coaxial configuration of the electrodes in and around a dielectric tube, although slit like configurations also exist [58]. Figure 1.5 (c) shows the schematic of an atmospheric Pressure Plasma Jet system. One electrode is placed centrally within the dielectric tube, whereas the other is placed as a ring electrode on the outer side of the tube. With an applied high voltage between the two electrodes, plasma will form in the area between both electrodes within the tube. The gas flow will transport the generated plasma within the flow direction along the tube, thus expanding the plasma towards the outside of the tube to form the plasma jet.

The localized plasma jet and its low operating temperature brings many advantages, commonly used for biomedical applications [66] [67], such as cancer treatment [52] and wound management [38] [31]. The plasma properties can be controlled through the

operating conditions [57], or gas composition [67]. However, plasma jet only provides localised plasma generation and the need of a gas supply increases system complexity and therefore, the operating cost of these non-thermal plasma sources are also increased.

1.3.4 Dielectric barrier discharge (DBD)

A DBD plasma source consists of two electrodes separated by a dielectric material. The two electrodes and the dielectric material of a DBD plasma source can be arranged in various configurations [58]. Figure 1.5(d) and 1.5(e) show two arrangements, the volume DBD plasma source and a surface DBD plasma source. In a volume DBD plasma source, both electrodes are arranged to form an air volume in-between them. In a surface DBD plasma source, as shown in Figure 1.5(e), the two electrodes are placed on either side of a dielectric layer. Usually, the powered electrode (bottom in Figure 1.5(e)) is encapsulated in the dielectric or insulated with dielectric tape, whereas the ground electrode (top in Figure 1.5(e)) remains exposed to the surrounding air.

For all arrangements of DBD plasma sources, the same working principles apply. Once a high voltage AC is applied to the electrodes, free electrons, and ions in the air between the two electrodes are affected by the electrical field [68]. The ions are accelerated towards the cathode and the electrons towards the anode. The ions are bigger in size and mass compared to the electrons and consequently only gain little energy during the acceleration. The lightweight and small electrons are able to gain higher energies and collide with atoms and molecules during the acceleration towards the anode. If the gained energy is higher than the ionization energy of the molecules, the molecules will be ionized, leaving a free electron and a positive ion. The new freed electron will lead to further ionisation events on its path towards the anode, called the Townsend avalanche. During the ionisation process, electron avalanches create a localized charge, adding to the existing electric field in this location. The avalanche process gets enhanced and forms into a plasma discharge channel.

The presence of the dielectric material between the two electrodes leads to the accumulation of charge at the surface of the dielectric material [68]. The accumulated surface charges induce an electric field, which is in the opposite direction of the initial electric field. Then the strength of the initial electric field will be weakened by the induced electric field and eventually gets extinct. This results in an extinction of the plasma generation. Consequently, the dielectric layer helps to limit the charge being deployed into the air between the electrodes. Without the dielectric, the Townsend avalanche process would continue further and lead to spark or arc discharge. Thus, the dielectric limits the temperature of the plasma, keeping it in a non-thermal, ambient temperature regime[58, 69].

1.4 Technical limitations of current non-thermal plasma source

The previously discussed applications in the biomedical or the aerospace field require highly adaptable non-thermal plasma sources, in order to achieve successful performance. Most applications currently use atmospheric pressure jet plasma sources for a localised generation of non-thermal plasma. In the biomedical field, jet plasma sources have been developed for clinical trials [70], where they can be used as hand-held devices to manually treat larger surfaces areas. Surface DBD plasma sources can offer a suitable method to generate non-thermal plasma uniformly across larger areas. They can be operated without a shielding gas and at low temperatures. Flexible design options of the electrodes in combination with simple fabrications methods promote applications in various fields. Surface DBD plasma sources have also been employed and can be developed as hand held devices [35] or as small patches [33, 34, 36] for plasma treatment and are mainly used to promote wound healing in the biomedical field.

The remaining challenge of DBD plasma systems is the uniform generation of non-thermal plasma over large and complex surfaces [25]. In particular the combination of a truly scalable and flexible plasma source is needed. Fabrication of fully scalable and flexible DBD plasma sources to generate uniform plasma, can further improve the effectiveness of non-thermal plasma application, such as surface treatment or decontamination method. Large scale plasma sources allow treatment of larger areas simultaneously, without a need for manual movement as with hand-held plasma jet device. Thus, large scale DBD plasma system can reduce the overall treatment time, allowing a more time efficient implementation of non-thermal plasma technology. Furthermore, the treatment success can depend sensitively on the gap distance between plasma layer and the treated surface [32, 70]. Therefore, flexible devices are needed to ensure adaptation of the electrode systems to complex geometries such as the human body.

1.4.1 Scalability

The uniform generation of non-thermal plasma across large areas is an ongoing technical challenge. Multiple DBD electrode systems can be used in an assembly to achieve larger sizes of plasma generation [71, 72]. This approach has been introduced in the flow control community, where mostly simple 1-D line configuration are used as electrode systems. The assembly approach has the benefit of using the individual systems to achieve localised control of the plasma generation [72]. Using DBD plasma sources for surface treatment or decontamination, most current systems are for the treatment of small flat areas. Figure 1.6(a) shows a hand-held plasma device for the indirect treatment of bacterial decontamination on skin [35]. The device itself has a treatment area of about 6 cm^2 and can only be used manually for the treatment of larger areas. Treatment of

larger areas has been proposed through a larger box using a DBD electrode system as a medical device for hand disinfection in the hospital environment [73], see Figure 1.6(b). Although the system reaches a total electrode area of 200 cm^2, the electrode system remains rigid and can not be flexibly adapted to curved or complex shapes.

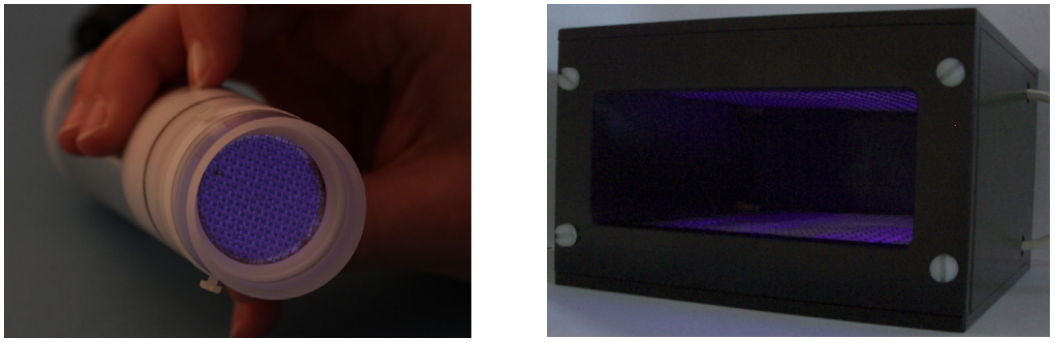

(a) (b)

FIGURE 1.6: DBD plasma sources solutions for larger scale non-thermal plasma generation: (a) Hand-held plasma treatment device [35]; (b) Plasma dispenser for hand sterilization [73]

1.4.2 Flexibility

Conventional surface DBD plasma sources are mostly still limited to being used as a flat and rigid electrode system. They consist of a rigid dielectric material, such as glass, quartz, ceramics, or polymer, which limits flexibility of the DBD system [74]. Few methods have proposed flexible DBD plasma devices to overcome the rigidity [32–34, 36]. Figure 1.7(a) shows a proposed flexible electrode array arrangement, consisting of independently movable pin like electrodes (see 1 in Figure 1.7(a)) [32]. The flexible movement of the individual electrodes promotes the treatment of curved shapes (see 3 in Figure 1.7(a)). Figure 1.7(b) shows another proposed method, a plasma patch, to generate non-thermal plasma over curved surfaces [33]. The plasma patch uses a flexible dielectric and electrode material, thus the device can be shaped around surfaces, such as the human body, to promote wound healing. Even though the device was demonstrated successfully for bacterial inactivation in clinical trials, no detailed performance analysis for varying, specifically small bending curvatures has been reported.

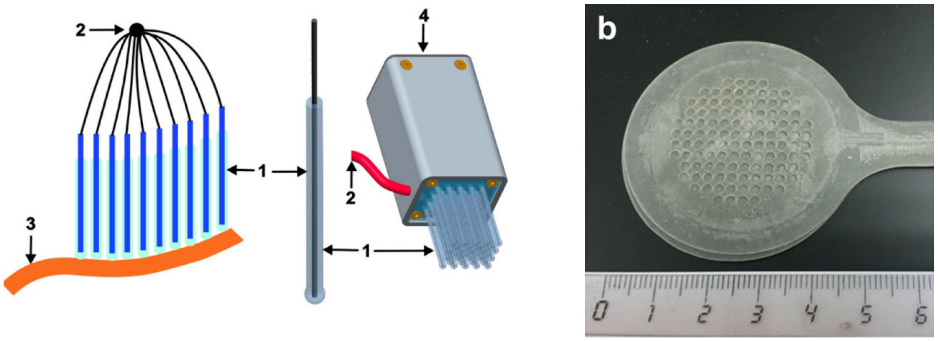

(a) (b)

FIGURE 1.7: DBD plasma sources solutions for flexible non-thermal plasma generation: (a) Flexible electrode array [32]; (b) Plasma pad to promote wound healing [36]

1.5 Aims and objectives

The overarching aim of the project is to investigate and develop a fully scalable and flexible plasma source, to advance the implementation of non-thermal DBD plasma technology in various applications, such as in the biomedical field and the space sector. The specific objectives of this study are to:

- Develop a truly scalable and flexible DBD electrode system to generate uniform non-thermal plasma over large and complex surfaces using printed electronics techniques.
- Develop a validated simulation model of a surface DBD plasma source generating non-thermal plasma to assist in the optimisation of design and operating parameter.
- Advance the findings of the investigation on truly scalable and flexible non-thermal plasma sources and demonstrate the feasibility of printed surface DBD plasma sources in the aerospace and biomedical field.

1.6 Overview of thesis

The following section provides an overview of this thesis and how the defined objectives were executed in this research project. Figure 1.8 schematically shows the overview of this thesis.

The first chapter has introduced non-thermal plasma with its unique physical and chemical properties. Various applications within the biomedical field and aerospace sector

have been discussed, highlighting the importance of further engineering advancement of non-thermal plasma sources. Several non-thermal plasma sources have been presented and their technical limitations have been discussed.

The second chapter introduces the fabrication method for surface DBD plasma sources using printed electronics techniques to promote scalability and flexibility. Two printing methods are presented, and their advantages are discussed. Furthermore, the experimental setup to power the plasma sources is presented. An overview of the diagnostic tools, consisting of electrical and optical diagnostic methods, including optical emission spectroscopy, is provided.

Chapter three demonstrates the scalability and flexibility of printed DBD plasma sources using the two previously presented printing methods. The results of electrical diagnostics tools are discussed to assess the electrical characteristics and performance of the DBD plasma sources. The optical diagnostics tools allow an analysis of the intensity and uniformity of the generated plasma across the surface DBD plasma sources.

The fourth chapter proposes a newly developed electrical simulation model of a surface DBD plasma source with complex electrode designs. The electrical model provides a tool to assist in the design optimisation of surface DBD plasma source and their operating parameters. The proposed electrical model is validated through a comparative study of printed plasma sources.

The fifth chapter provides short feasibility studies, using printed non-thermal plasma sources for applications within the aerospace sector and biomedical field. A new "Cold Radio Blackout Testing" solution is proposed using the high electron density generated by the developed printed plasma sources. Furthermore, the printed plasma sources are used as a decontamination system for medical equipment during the COVID-19 pandemic. The last feasibility study presents a thin and narrow plasma source, the plasma yarn, for the sterilisation of medical devices, such as endoscopes.

The final concluding chapter highlights the research outcomes of this project and proposes future work within the discussed topic.

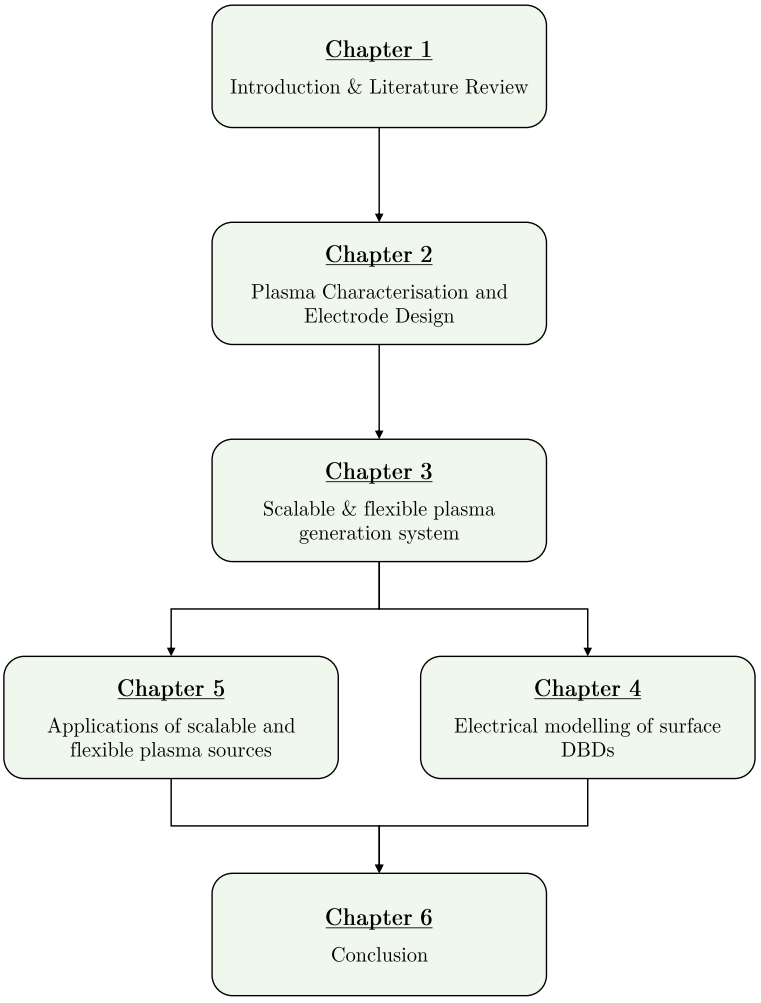

FIGURE 1.8: Overview of thesis

Chapter 2

Plasma characterisation and electrode design

The electrode geometry of surface DBD plasma sources can be manufactured by various approaches, depending on the desired application and requirements on the plasma generation system. A simple form is the application of copper tape on a dielectric substrate material. Here, thin polyamide film, such as Kapton, or rigid and thicker substrates, such as FR-4 (woven glass and epoxy resin laminate), glass or ceramic, can be used as the dielectric [75]. Copper tape is cut to the desired shape and applied on the substrate to form the electrode of the DBD plasma source. The method is cost- and time-effective, however due to the hand made nature the electrode it is limited to simple and mostly 1-D strip-like geometries with low precision and repeatability [75]. Additionally, even when using thin and flexible polyamide film as dielectric, the copper tape itself results in a high rigidity of the fabricated plasma source, making it unsuitable for flexible applications.

A method which overcomes some of the limitations of the copper tape method is the fabrication through etching of a printed circuit board (PCB). This is the same approach as used to fabricate electronic circuit boards. This method can involve a number of steps and allows more complex electrode geometries. PCB etching is performed using a dielectric substrate, which has a copper clad on either side. The copper later functions as the electrode and a desired electrode pattern is masked off, for example with photolithography. A subsequent chemical etching procedure leads to the desired copper circuit on the dielectric substrate. Usually, thick ($\sim$ 1 to 2 mm) and rigid FR-4 material is used to fabricate the PCB-based plasma sources, although thin and flexible PCB have become more and more available in recent years. Due to the number of steps and the need for a mask for each electrode design, PCB etching is advantageous and cost-effective for the production of large quantities of plasma sources. However, feasibility studies for plasma sources requiring prototyping and/or parameters studies require a more dynamic

fabrication approach. Direct electronics printing techniques can be used as an alternative fabrication method for surface DBD plasma sources. Conductive inks are used on flexible dielectric substrate for the fabrication method. Printed electronics techniques are widely used for wearable electronics, such as for health monitoring purposes [76–78]. These printing methods can be more advantageous for parameter and feasibility studies as they allow for a quick and cost-effective approach for prototyping.

In this chapter, two printing techniques are employed and assessed for the generation of non-thermal plasma sources. The first section discusses the electrode geometry and configuration of the surface DBD plasma sources. Section 2.2 presents manufacturing methods of the electrode system using printed electronics techniques. Two different printing methods are detailed: inkjet printing and dispenser printing, using conductive inks of varying viscosities. The fourth part of the chapter presents the experimental setup. This includes the components required to provide the high voltage power signals to generate non-thermal plasma with the fabricated surface DBD plasma sources. The last part of this chapter provides an overview of the employed diagnostics tools and methods to assess the fabricated non-thermal DBD plasma sources.

2.1 Electrode geometry and configuration

The geometry of the electrode has an important role in generating uniform plasma over large areas [32]. The geometry defines, where the plasma is generated and how it is distributed across the plasma source. When designing large electrode geometries for large surfaces, individual units of basic polygon structures are used to form a large pattern. Firstly, the plasma generation on a single unit of a surface DBD plasma sources is shown. Figure 2.1 shows one unit of a surface DBD plasma source, schematically showing the electric field lines and the region of plasma generation. As can be seen, the plasma forms in the edge region on the top laying air exposed electrode. With a decreasing linewidth, the area of air exposed dielectric increases. This in turn results in a larger proportion of one individual unit of an electrode pattern, on which plasma generation can occur.

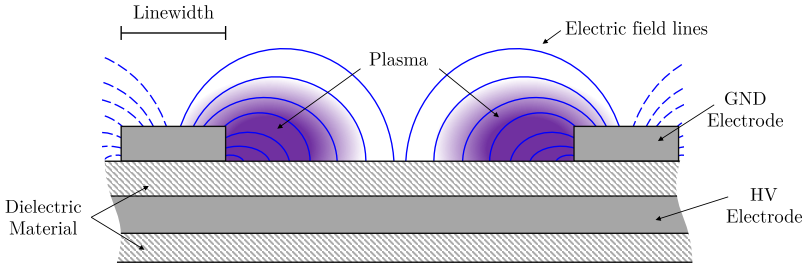

FIGURE 2.1: Schematic of single unit of a surface DBD plasma source pattern, showing electric field lines and region of plasma generation

A number of smaller polygons can be used to cover a larger area. This will allow to achieve a more uniform plasma generation across a large area. A uniform geometric pattern can be formed using a circle or three base polygon shapes, which are a triangle, square or a hexagon. Patterns using other polygon structures (pentagon, heptagon or higher) require a distorted polygon or combination of polygons to generate a large uniform pattern. All four patterns are formed with a polygon of the same unit size and linewidth. When deciding on the linewidth of a pattern, the material requirements have to be considered, as well as the possible printing precision. With a larger linewidth, the electrode becomes bulkier to withstand potential erosion, whereas a smaller linewidth offers a larger area with in an individual unit for plasma generation. The linewidth is chosen to be 0.3 mm. This is the thinnest possible printing linewidth of the employed printing methods, which are explained further in chapter 2.2. The unit size is chosen to be 2 mm, as this allows a sufficiently area within the unit in combination with the linewidth, to generate a strong plasma across the unit, thus also generating an overall uniform plasma across a larger patch of a printed electrode. Figure 2.2 shows four electrode geometry patterns using a circle, triangle, square and hexagon as the base polygon shape, which all covering an area of 21 mm by 21 mm.

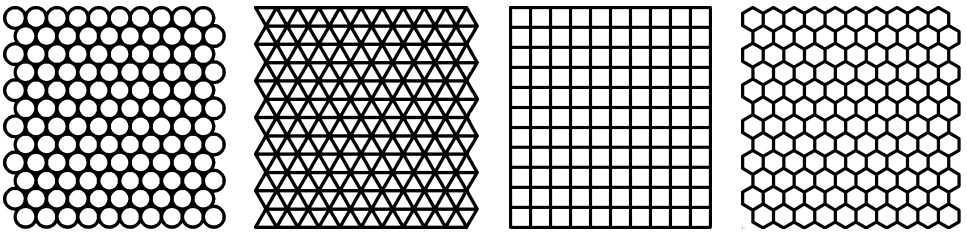

(a) Circle (b) Triangle (c) Square (d) Hexagon

FIGURE 2.2: Schematics of electrode pattern formed from various polygon shapes: (a) Circle; (b) Triangle; (c) Square; (d) Hexagon

When comparing the electrode patterns, the ratio between electrode covered area and air exposed area, is relevant. A smaller ratio refers to more area over the dielectric to be exposed to air, a larger area where plasma generation can occur. Additionally, a smaller ratio refers to less electrode area, thus less electrode material, which is an important parameter to consider with printing methods. With a reduced electrode area, the overall ink usage can be reduced, thus making the fabrication of the plasma sources more time and cost effective. Using a circular pattern leads to 36 % percent of the area being covered by the electrode. As can already be seen, using a triangle polygon leads to a large proportion of the area being covered by the electrode. With the shown triangle polygon pattern, 48 % of the surface of the pattern is covered by the electrode, whereas only 31 % are covered when using a squared pattern. Using a hexagon pattern results in the lowest ratio, with 28 % of the pattern is covered by the electrode. Consequently, a hexagonal unit has been chosen as the base polygon shape for the electrode pattern, as it provides the largest area for plasma generation at minimal electrode material.

Figure 2.3 shows a schematic top and cross-sectional view of a hexagonal pattern of a surface DBD plasma source. The ground (GND) electrode follows a hexagonal pattern. The high voltage (HV) electrode can be designed in various ways, for example to cover the full area, as shown in Figure 2.1, or only covering smaller areas, by following the same pattern as the ground electrode. In this thesis, the majority of the fabricated plasma sources have a hexagonal high voltage electrode pattern, as can be seen in Figure 2.3. This results in a reduced amount of material required for printing of the high voltage electrode, thus a more cost-effective fabrication of the overall plasma source. The linewidth (LW) of the ground electrode pattern is smaller than the linewidth of the high voltage electrode pattern, such that the plasma forms on the ground electrode pattern.

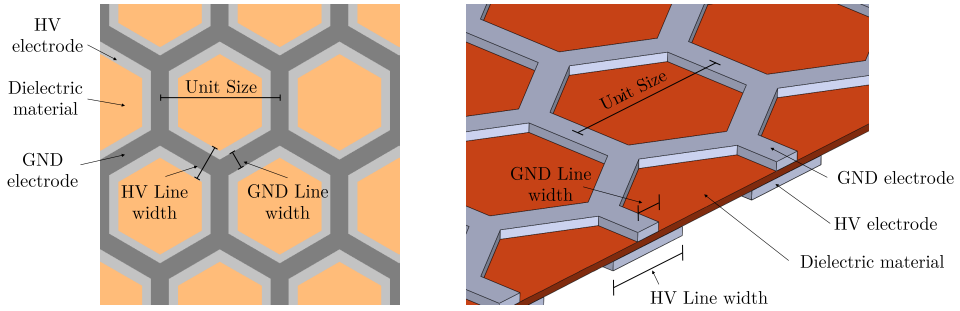

FIGURE 2.3: Overview of a hexagonal electrode pattern: (a) Top view; (b) Cross section

The hexagonal baseline unit is used to generate electrode patterns across a number of different surfaces, depending on the desired application. In this thesis a number of different electrodes are fabricated. Figure 2.4 shows examples of how the hexagonal unit is used to cover rectangular or square areas (Figure 2.4(a) and 2.4(b)), approximately circular areas (Figure 2.4(c)) or strip-like structures (Figure 2.4(d)) to cover long and thin geometry areas.

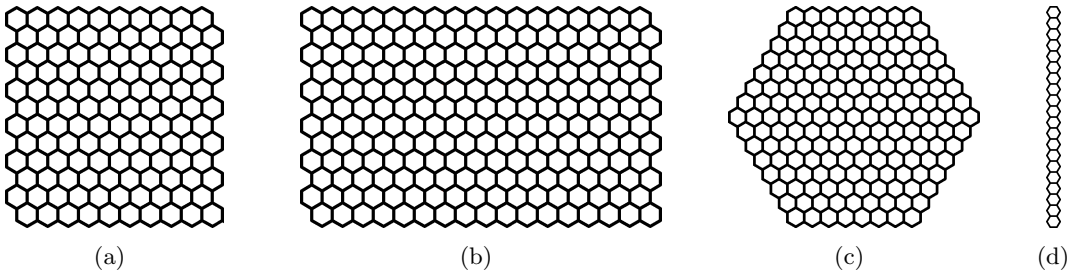

FIGURE 2.4: Schematics of pattern formed to form larger areas as: (a) Square; (b) Rectangular; (c) Circular; (d) Line

2.2 Manufacturing method of electrode systems

Printed electronics techniques are employed for the manufacturing of non-thermal DBD plasma sources. Common non-contact printing techniques include inkjet printing, aerosol jet printing, electrohydrodynamic jet printing, and dispenser printing [79]. Inkjet printing uses a piezoelectric actuator to generate and eject small droplets through a thin nozzle and print the desired circuit pattern. It is a method suitable for lower viscosity inks, which usually come along with a low conductive metal (silver) content. Thus, the printed circuit can have a lower conductivity and higher resistance. Aerosol jet printing has a coaxial nozzle with an air jet to aerosolize the ink and generate a focused jet stream to print the circuit pattern. Similarly, this method requires ink with low to medium viscosity. In electro-hydrodynamic jet printing an added electric field between nozzle and substrate is generated to increase the print resolution and precision. However, the method comes with a high complexity due to the required electric field and requires low viscosity inks with a low proportion of conductive material. Dispenser printing is suitable for inks with a large conductive metal/silver content, with high viscosity. This method uses a controlled actuation force to extrude ink through the fine nozzle to form the circuit pattern. The following part presents the two employed printing methods, inkjet printing and dispenser printing method, which are used for the manufacturing of the electrode systems.

2.2.1 Inkjet printing

Two inkjet printing methods are tested for the fabrication of non-thermal plasma sources. A low viscosity ink is used to print the electrode of the plasma sources using the Epson ET 2700 printer, and a medium viscosity ink is used with the Dimatix Materials Printer DMP2831.

2.2.1.1 Conductive ink with low viscosity

A piezo-electric inkjet printer can be used with conductive ink to fabricate electrode patterns for non-thermal plasma sources. Inkjet printers require low-viscosity ink. This study uses the Epson inkjet printer ET 2700 to print low-viscosity conductive ink (3 - 5 cP) with silver nano-particles (Novacentrix JS-B25P). This ink has a silver content of 25 % and a curing process of 24 hours at room temperature is recommended to achieve full strength and conductivity of the printed pattern [80].

Figure 2.5(a) shows a fabricated electrode using the Epson inkjet printer system with a low-viscosity ink. The ground electrode pattern is printed on photo-paper as the dielectric substrate. The printed electrode has a thickness of approximately 1 μm. For this plasma source, the high voltage electrode is fabricated using copper tape on the

backside of the substrate. Figure 2.5(b) shows the generated non-thermal plasma from the fabricated plasma source. As can be seen, plasma can be generated uniformly across the printed electrode. Figure 2.5(c) shows images of a time-series of generated plasma using the fabricated plasma source over 10 minutes. As can be seen, the intensity of the generated plasma decreases within 1 minute and the distribution of the plasma across the printed electrode becomes uneven. With ongoing time, this effect becomes more pronounced, where only a weak plasma is generated after 10 minutes. This reduced performance is caused by a high level of erosion due to the high bombardment of reactive species on the dielectric material and the thin electrode. This erosion can result in changed capacitance of the DBD system and ultimately affect its lifetime.

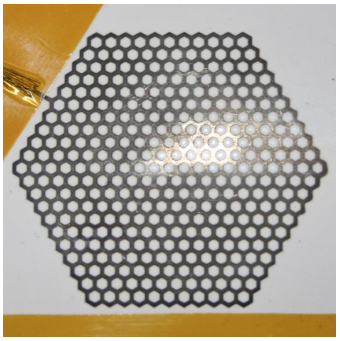

(a) Before

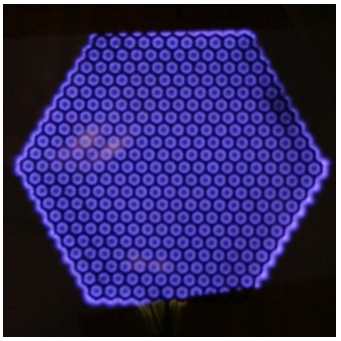

(b) During Ignition

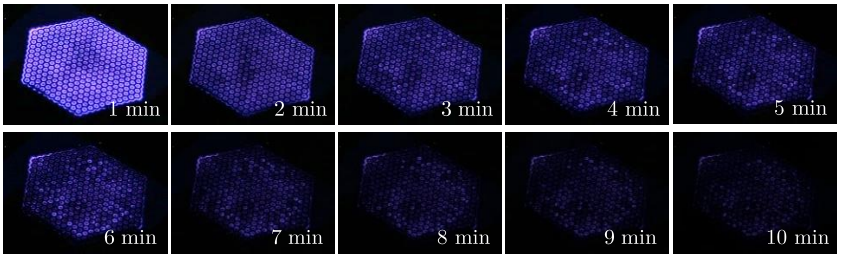

(c) Timeline over 10 minutes

FIGURE 2.5: Printed plasma source with Epson inkjet printer ET 2700

Although this printing method can fabricate DBD plasma sources and plasma generation is achieved, it provides limited capability to fabricate reliable and long-lifetime plasma sources. Additionally, the printer does not allow fabrication of both, ground and high voltage electrode, as printed electrodes, since no alignment option is available. Furthermore, the conductive ink results in clogging of the printer head and feeding system. A high level of maintenance, including a large number of cleaning and purging procedures, are required for reliable operation.

2.2.1.2 Conductive ink with medium viscosity

The Dimatix Materials Printer DMP2831 is used for electrode fabrication using conductive ink of medium viscosity (10 - 13 cP). The printer uses a piezoelectric actuator to generate a superimposed acoustic wave to eject droplets through a row of nozzles [79, 81]. Figure 2.6 shows the printer and ink cartridge used in the print procedure. The substrate is placed on the print bed and secured using a built-in air-suction system. The ink cartridge is secured in the printer head and moves horizontally over the print bed. The printer head deposit conductive silver ink though the nozzles directly on the substrate, where it can function as the ground electrode of the DBD plasma source. The printer head is fitted with a 10-pL piezoelectric cartridge with a total ink capacity of 1.5 ml.

(a) Overview (b) Ink Cartridge

FIGURE 2.6: Dimatix Materials Printer DMP2831 [82]: (a) Overview ; (b) Ink Cartridge

Figure 2.7 shows a printed electrode on flexible Kapton film. The Kapton film has a thickness of 127 μm. The ground electrode pattern of the non-thermal plasma sources is fabricated using conductive silver ink (SunTronic U5714, SunChemical) containing 40 % silver nano-particles. The ink requires a curing procedure of 30 minutes at 150 °C to achieve full strength and conductivity. The printed electrode has a thickness of approximately 2 $\sim$ 5 μm. The thin Kapton film offers a high level of flexibility and a high dielectric strength. Adhesive copper tape with a thickness of 88 μm is used as the high voltage electrode.

Figure 2.8 shows an ignited plasma source fabricated using the Dimatix printer system. As can be seen, a strong plasma can be generated at the printed electrode system. However, a small section of lower intensity can be identified. This can be traced back to print imperfections caused during the printing procedure. The printer head moves across the substrate in a horizontal path, during which a small horizontal section of the electrode pattern is printed. The cartridge requires a purging and cleaning procedure to avoid clogging of the printer nozzles. Even during these purging and cleaning procedures small misalignment to the calibration of the printer head position can occur, which then leads to imprecisions when continuing the printing procedure with the next section of the electrode pattern.

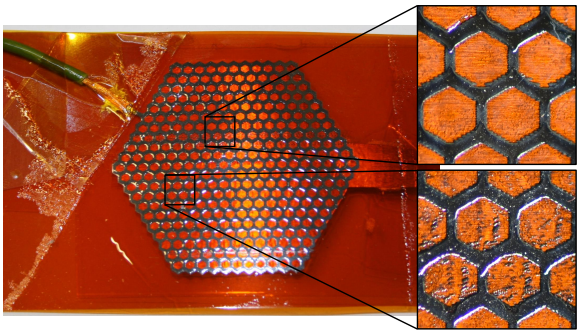

FIGURE 2.7: Printed plasma source using inkjet printing method (Dimatix Materials Printer DMP2831)

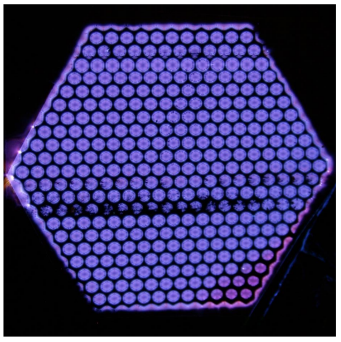

FIGURE 2.8: Ignited plasma source fabricate on the Dimatix Materials Printer DMP2831

Although the Dimatix printer system can be used to successfully fabricate plasma sources, the procedure has some disadvantages. The Dimatix printer system provides a realignment option. This would allow for an aligned print of the high voltage electrode on the back side of substrate already containing the ground electrode. However, achieving a good alignment remained challenging. Additionally, the nozzles were prone to clogging despite continuous purging and cleaning procedures of the cartridge. This led to frequent replacement of cartridges, which proved to be expensive, when considering the high cost of the cartridge alone (excluding cost for the conductive ink).

2.2.2 Dispenser printing

Dispenser printing techniques offer a number of advantages over ink-jet printing procedures for the development of plasma sources. Dispenser printers are used with higher viscosity inks, which results in a thicker electrode with a higher aspect ratio [79]. A thicker electrode offers a minimized power loss due to improved resistance and can therefore improve the performance/efficiency of the plasma source. Furthermore, the bulkiness of a dispenser printed electrode can improve the lifetime of the plasma source. During operation, erosion on the electrode leads to an ongoing reduction of material and consequently a bulkier electrode with a higher silver content will provide a longer lifetime.

In this project the Voltera V-One printer is used as a dispenser printer for the fabrication of plasma sources. Figure 2.9 shows the overview of the printer system, with the main parts being the print platform, the carriage to hold probe and dispenser and the calibration switches. The print bed has a maximum size of 128 mm by 116 mm, and additionally functions as a heated bed for the curing process of conductive inks. The dielectric printing substrate is fixed on the printing platform using clamps. In Figure 2.9(b) a detailed view of the carriage and the calibration switches are shown. The carriage holds the probe and the ink dispenser. The probe's main function is to position the to-be-printed electrode pattern to the substrate and generate a height map of the substrate. This height map is used as a reference for the subsequent print procedure. The ink dispenser contains the ink cartridge, onto which a nozzle with a diameter of 230 μm is attached. The dispenser releases the ink through the nozzle by applying pressure on a plunger.

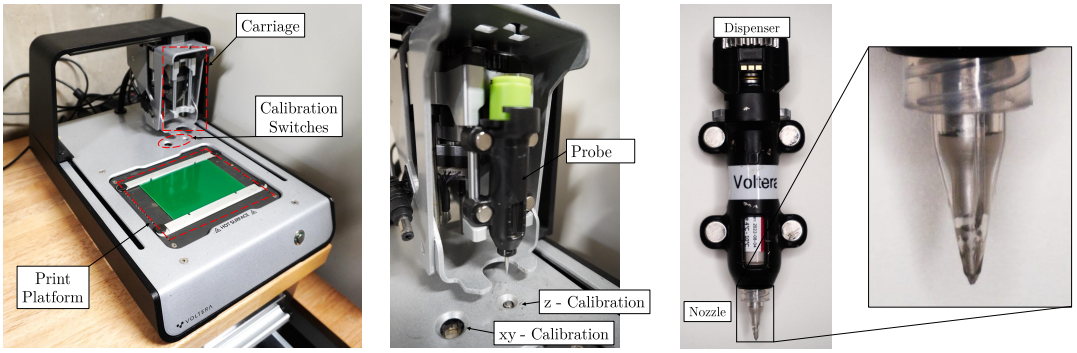

(a) Voltera V-One (b) Carriage (c) Ink Dispenser & nozzle

FIGURE 2.9: (a) Voltera V-One dispenser printing system; (b) Carriage and Calibration switches of Voltera V-One; (c) Ink Dispenser & nozzle

Figure 2.10 shows a printed electrode on flexible Kapton (75 μm) using a high viscosity conductive ink with a silver content of 75 % ("Voltera - Flex 2"). The flexible substrate is secured on a rigid board using Kapton tape to avoid smudging or print imprecisions of the electrode pattern caused through uneven substrate. Subsequent to the printing procedure, the conductive ink is cured using the built-in heating function in the printing platform. A curing procedure of 30 minutes at 160 °C ensures the strength and conductivity of the ink. Using the dispenser printing method results in an electrode thickness of approximately 20 μm. The dispenser printer system offers the advantage of printing electrode patterns on both sides of the substrate due to the alignment option. Following the print and curing of the powered electrode of the surface DBD plasma source, the ground electrode is printed on the other side of the flexible substrate.

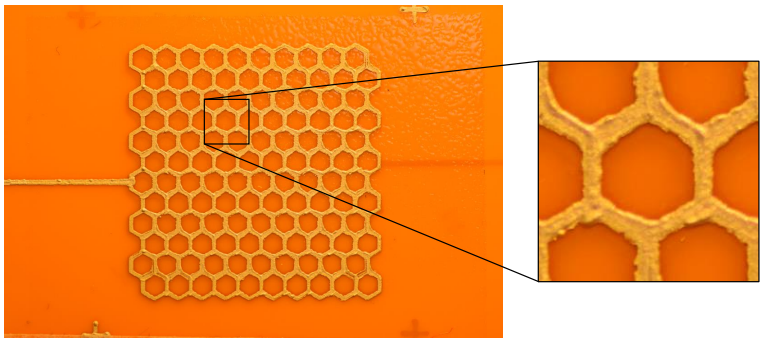

FIGURE 2.10: Printed plasma source with hexagonal pattern using dispenser printing method

2.2.2.1 Print precision

The quality of the printed electrode pattern can affect the capacitance of the surface DBD plasma source and thus its performance. The capacitance of a plasma source is linearly proportional to the directly facing area of both electrodes ($C \propto A$). Thus, small differences in for example the linewidth of the printed electrodes can directly affect the plasma source capacitance. During the printing procedure, print imprecisions can be caused by settings of the printer, or orientation and quality of the substrate fixture. This can lead to a deviation of electrode pattern from the theoretical geometry. Additionally, uneven edges can have small sharp section. These sharp sections of the electrode can result in a concentration of the local electrical field. These regions can experience an increased plasma activity and as such make it more prone to damage through erosion.

The print and alignment quality of the printed plasma source can be assessed through high-resolution images. Figure 2.11 shows small sections of a high resolution image obtained with a macro lens from two printed electrode patterns (print sample #1 and #2). The images show the thinner ground electrode pattern in silver on top, and the wider high voltage electrode is seen faintly through the orange Kapton substrate. Both patterns are printed using the exact same electrode geometry, with identical linewidth and alignment procedure. Nevertheless, the images show a difference in the resulting print quality and alignment. Print sample #1 shows good alignment between the ground and high voltage electrode, whereas a misalignment between the ground and high voltage electrode can be seen for print sample #2. The high voltage electrode is shifted slightly down and left, therefore not fully overlapping with the top lying ground electrode. Secondly the ground electrode of print sample #1 (Figure 2.11(b)) has a distinctly narrower linewidth than the ground electrode in print sample #2 (Figure 2.11(b)). This can be the results of varying printer settings, such as print height or plunger pressure. Both misalignment and print imprecisions, can result in a changed capacitance value. As the capacitance is calculated by the parallel overlapping area of the electrode pair, high

print quality of both electrodes is crucial and has to be ensured for all fabricated plasma sources.

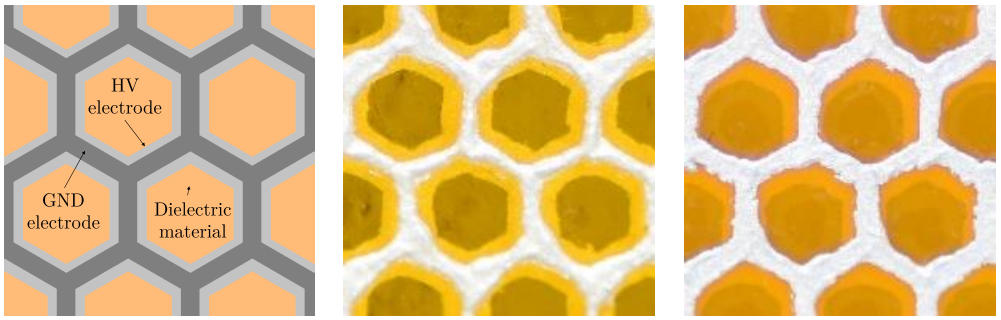

(a) Reference geometry (b) Print Sample #1 (c) Print Sample #2

FIGURE 2.11: Images and schematics of print alignment using the dispenser printer system: (a) Print pattern; (b) Print Sample #1 ; (c) Print Sample #2

The precision of a printed electrode can be further assessed through an image processing approach using Matlab. Figure 2.12 schematically shows the applied image processing procedure. The overview only shows a small section focusing on one single hexagon, but the image processing procedure is applied to the full picture of a printed electrode. An image is composed from the primary colours, red (R), green (G) and blue (B) (Step 1). Each pixel in the respective RGB image component is defined through a value between 0 and 255, where 0 is equivalent to no intensity and a value of 255 is equivalent of full intensity. The coloured image is converted to a grey-scale image (Step 2), which allows a clear distinction of the bright electrode pattern from the substrate. The grey-scale image is converted to a binary black and white image by defining a threshold value (Step 3). This value is chosen for each image, as it depends on the specific lighting conditions the image was taken with. In this study, threshold values between 10 and 50 have been used. A binary image only consists of pixels with two values, either 0 for a black pixel or 1 for a white pixel. The binary image is used to obtain the actual outline of the printed electrode using an edge detection method (Step 4). In this study the *Canny* edge detection method has provided the best results, as can be seen in the overview image in Figure 2.12. The last image section shows a comparison of the obtained, actual outline of the printed electrode (black line), in comparison to the theoretical outline defined for the printing process (Step 5). As can be seen, in the print sample shown in Figure 2.12, the actual printed outline slightly exceeds the theoretical outline.

The image processing procedure to obtain the outline of the printed electrode pattern can be used to calculate a print precision scaling factor, f_{pp} as:

$$f_{pp} = \frac{A_{print}}{A_{theo.}} \tag{2.1}$$

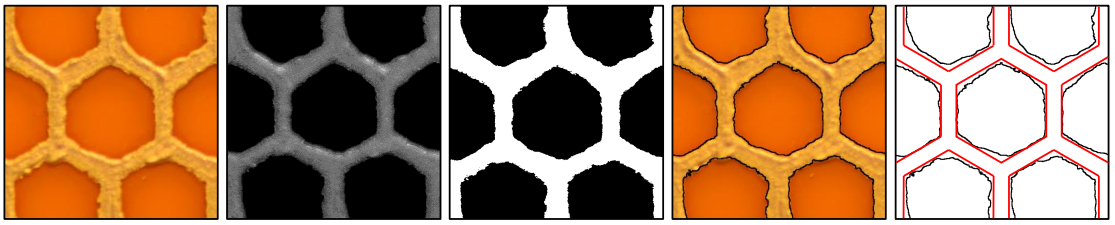

FIGURE 2.12: Overview of image processing to obtain area of printed electrode

where A_{print} is the area of the printed electrode and $A_{theo.}$ the theoretical area of the electrode design. The scaling factor, f_{pp}, is calculated for all printed plasma sources and is listed in the respective sections. It is taken as reference for the calculation of the capacitance of plasma source.

2.2.3 Comparison on printing methods

In the framework of this thesis two printing methods for the fabrication of DBD plasma sources have been assessed. Table 2.1 provides an overview of the two employed inkjet printing method using a low and medium viscosity ink. The dispenser printing method can be used with high to very-high viscosity inks.

	Inkjet Printing		Dispenser Printing	
	Low visc. ink	Medium visc. ink	high visc. ink	very high visc. ink
Printer	Epson ET 2700	Dimatix DMP2831	Voltera V-One	Voltera V-One
Ink	Novacentrix	SunTronic	Voltera	Inkron
	JS-B25P	U5714	Flex-2	IPC-114
Scalability	Good	Medium	Good	Poor
Double sided	No	No	Yes	Yes
Ink viscosity	3 - 5 cP	10 - 13 cP	5000 - 10000 cP	50000 cP
Thickness	< 2 μm	$2 \sim 5$ μm	~ 20 μm	~ 25 μm
Silver	25 %	40 %	75 %	70 %
Resistance	60 - 70 mΩ/sq	25 - 150 mΩ/sq	12 mΩ/sq	< 15 mΩ/sq

Table 2.1: Comparison of printing methods for printed DBD plasma sources

The overall performance of a printed plasma source is a balance of achievable printed quality and material properties of the electrode. Both printing methods can fabricate printed DBD plasma sources on thin and flexible substrates to successfully generate non-thermal plasma. The viscosity of the different used inks directly affects the thickness of the printed electrode. Using a low-viscosity ink results in thin electrodes, whereas an increased viscosity leads to a thicker electrode. The employed inkjet printer methods fabricate large scale electrodes with thicknesses of approximately $1 \sim 5$ μm, whereas the dispenser printing method results in thicknesses of approximately $20 \sim 25$ μm. The thickness of the electrode can affect the lifetime and performance of the plasma source.

A thicker electrode better withstands the high level of bombardment of reactive species, causing erosion on the electrode. However, using ink with a very high viscosity on the dispenser printer can result in an overall lower print quality. The very high viscosity ink (Inkron IPC-114) has been tested with the dispenser printer. However, the ink does not properly shear off the nozzle during printing procedure, resulting in streaking and smudging of the print and thus a poor print quality for larger electrode patterns.

Another aspect of comparing printed electrodes is the silver content of the conductive ink, which has a direct effect on the resistance of the electrode. The low and medium viscosity ink have a silver content of 25 % and 40 % respectively, whereas the high-viscosity and very-high viscosity inks has a concentration of 75 % and 70 % of silver respectively. This directly leads to high sheet resistance up to 150 mΩ/sq for printed electrode using the low or medium viscosity ink and low sheet resistance of approximately 12 mΩ/sq for printed electrode using the high-viscosity ink. The sheet resistance is inversely proportional to the conductivity of the electrode, thus can result in power losses within the plasma source.

In the present thesis, some initial test campaigns were carried out using the inkjet printing method (Dimatix DMP2831) using medium-viscosity ink (SunTronic U5714) to demonstrate the feasibility of a subsequent detailed analysis. For this subsequent analysis, the main focus is placed on the plasma sources fabricated using dispenser printing method (Voltera V-One) with high-viscosity ink (Voltera Flex-2) for the fabrication of the electrodes. The Voltera V-One is a low-cost and low-maintenance printer system tailored specifically for flexible prototyping of printed metallic circuits. The fabricated plasma sources combine high precision of the print pattern for both ground and high voltage electrodes, on flexible and thin dielectric materials. Using the high-viscosity conductive ink with a high silver content results in thick and highly conductive electrodes.

2.3 Experimental setup

The experimental setup consists of two main components, a high voltage power supply and diagnostics tools to measure electrical characteristics, optical intensity, and chemical composition of the generated plasma. Figure 2.13 shows a schematic of the experimental setup including the high voltage power supply and required diagnostics systems for monitoring and controlling of the plasma source. In this study early testing has been carried out using a Trek Model 20/20C-HS high-voltage amplifier. This system can supply up to 20 kV at frequencies up to 20 kHz. However, the amplifier system is limited when supplying power to larger capacitive loads, as this study aims to investigate. Hence a custom-made high voltage power supply was built and presented in this section. The diagnostics methods will be addressed in the subsequent section 2.4.

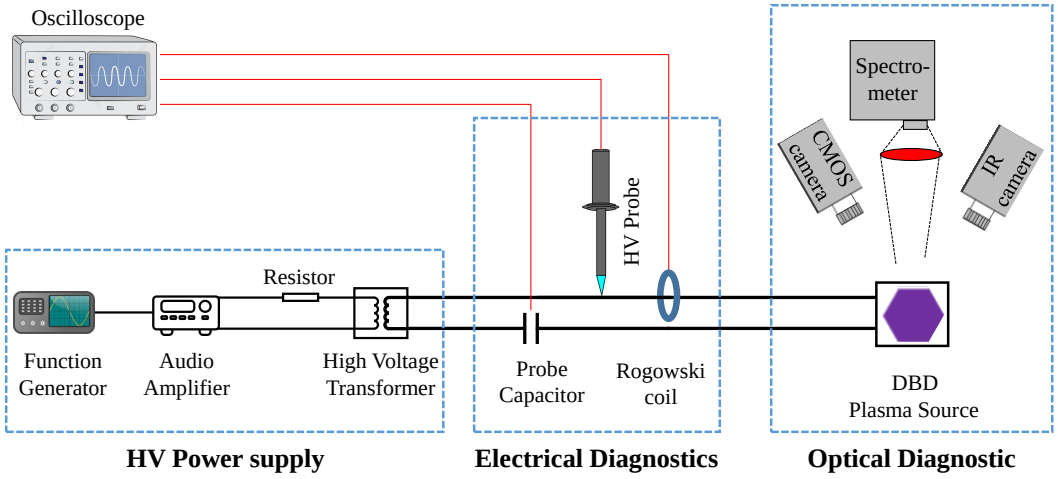

FIGURE 2.13: Schematic of the experimental setup with the high voltage power supply, electrical diagnostics and optical diagnostics

Figure 2.14 shows a schematic of the high voltage power supply systems. It consists of three main components: a function generator, an audio amplifier and a high voltage step-up transformer. This arrangement allows a step wise amplification of a low amplitude input signal to large amplitude power signal. The high voltage end of the power supply setup is placed in a safety enclosure made of Perspex to improve the safety of the experimental setup. The safety enclosure fully shields any high voltage components from the lab user. It provides access through a door to set up the to-be-tested plasma source and diagnostics. However, during operation of the high voltage power, the door must remain closed as per the risk assessment. The enclosure contains a number of smaller access holes to allow cable feed troughs for electrical diagnostics and larger openings to allow visual access for optical diagnostic tools.

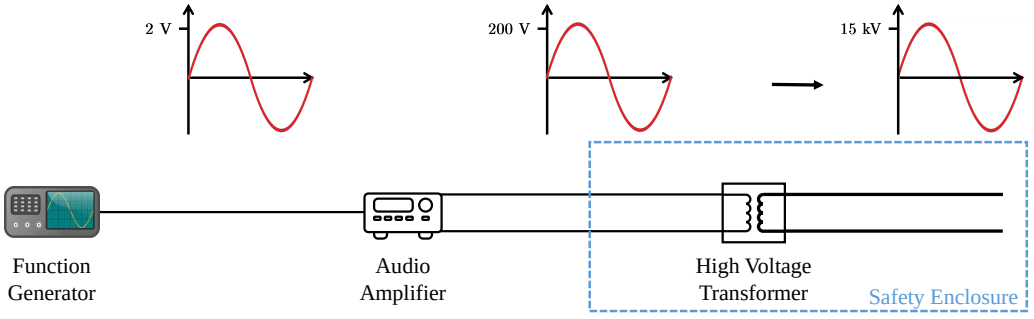

FIGURE 2.14: A schematic of the high voltage power supply with components and signal path

The initial signal for the power supply system is provided through the arbitrary waveform generator (AWG) of a PicoScope 4824, which simultaneously is also used as the data acquisition system for the electrical diagnostic tools. The role of the AWG is solely to provide a high accuracy input signal, but does not provide the power needed to sustain a high voltage signal for the plasma generation. The AWG can provide a maximum

output voltage of ± 2 V and a frequency up to 1 MHz with a DC accuracy of ± 1 %. The signal from the AWG is led to the audio amplifier through a shielded BNC cable. In the framework of this thesis, a sinusoidal waveform is used as an input signal.

The sinusoidal signal provided from the function generator is fed into the signal input port of the audio amplifier CDi 2|600 from Crown Audio Inc.. The audio amplifier functions as the main power provider of the high voltage power supply system. The amplifier is powered through a mains connection and acts as an intermediate step in the build power supply system. The low amplitude input signal of 4 Vpp is amplified according to the chosen amplification setting on the audio amplifier. At maximum setting the system can provide up to 285 Vpp as an output signal. The output signal is provided from the output terminal at the rear of the audio amplifier. As the audio amplifier is intended for audio equipment with a load of 4 Ω to 8 Ω, a sufficiently high load has to be ensured when connecting the audio amplifier stage to the second amplification stage of the high voltage step up transformer. As the step-up transformer only has a very low impedance of 0.032 Ω, a power resistor is implemented at the output of the audio amplifier. A power resistor of 4 Ω with a power rating of 100 W is chosen to provide a sufficient load to the audio amplifier.

The power signal provided from the intermediate audio amplifier stage is led into an enclosure containing the high voltage step-up transformer. A transformer coil is a passive electrical component to transfer energy between circuits. It consists of a magnetic core with two sets of windings from a metallic conductor wound around the core. These two sets of windings make the primary and secondary side of a transformer. The winding on the primary side, N_p, is smaller than the winding on the secondary side, N_s. The transformer converts a low voltage signal on the primary side, V_p, to a higher voltage signal on the secondary side, V_p, with a given turn ratio n:

$$n = \frac{N_p}{N_s} = \frac{V_p}{V_s} \tag{2.2}$$

The presented power supply system uses a high voltage step up transformer Model No. 5012 from Corona Magnetics, Inc.. Figure 2.15 shows the high voltage transformer in the enclosure. The connecting cables for both primary and secondary side can be seen. The transformer coil has a turn ratio of 1:137.5 and has a maximum input voltage of 100 Vrms at 12 kHz on the primary side and a maximum output voltage of 13.75 kVrms. The ferromagnetic core of the transformer coil is designed with a gap, which allows for adjustment of the core gap distance, see Figure 2.15.

Optimizing the efficiency of the power supply setup and reducing power losses requires impedance matching/optimization of the system. This impedance matching process achieves the operation of the system in the resonance point. In this condition, the power delivery from the audio amplifies over the resistor and HV transformer to the

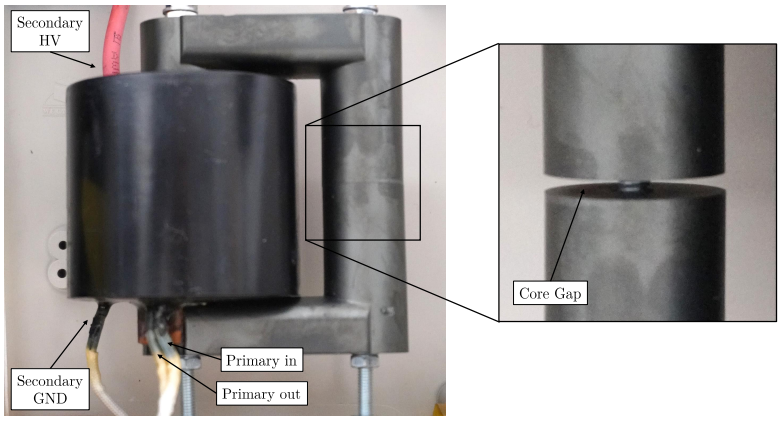

FIGURE 2.15: High voltage step up transformer with core cap

load, the DBD plasma source, will be optimized. An impedance mismatch leads to large proportions of the power getting reflected back from the HV transformer to the audio amplifier [83]. This high power loss due to the impedance mismatch, leads to low efficiency of the power supply system, which can ultimately result in an expensive and over-rated power supply system [83]. An optimized system can be achieved by implementing a matching circuit in either the primary or secondary side of the HV transformer to compensate for varying impedance. However, both options place high demands on the individual components of the matching circuit. A primary side matching circuit requiring components capable of handling high currents, and a secondary side matching circuit requires components to withstand high voltages [84].

Another approach to improve the efficiency of the power supply system is adjusting the impedance in the system by varying the core gap distance of the HV transformer. As described above, the transformer coil implemented in the power supply system has an adjustable gap distance of the magnetic core material. Varying this gap distance leads to a varying magnetic flux through the magnetic core, which results in a varying inductance of the coil. With the ability to adjust the transformer inductance, the impedance in the system can be adjusted to achieve operating in the resonant point with optimal power delivery to the DBD plasma source. The optimal core gap distance can be determined by monitoring the voltage drop across the power resistor between audio amplifier and HV transformer. A minimum voltage drop across the resistor indicates minimal losses within the systems and operation in the resonant point. In this thesis, the impedance of the power supply system is optimized through identification of the optimal core gap distance in the high voltage transformer coil. The impedance is dependent not only on the operating frequency, but also the capacitance [84]. Thus, calibration tests are performed at various operating frequencies and for different plasma sources with varying capacitances. Before each test of a new plasma source, the core gap distance is stepwise increased, while monitoring the voltage drop across the power resistor. While performing a step wise increase of the core gap distance, the voltage drop across the power resistor

is monitored, where a minimal voltage drop indicates the possible optimal impedance for the given conditions.

Figure 2.16 shows the operating envelope with regards to operating voltage and frequency of the build power supply system, which is defined through its various components. A red dashed box in Figure 2.16 highlights the operating frequency and voltage range. The high voltage transformer coil is saturated at 4 kHz, which marks the lower range of the operating frequency. The maximum operating frequency is defined by the maximum operating frequency of the audio amplifier as 20 kHz. The maximum operating voltage is limited at 20 kV_{RMS} through the maximum input voltage of the high voltage probe. Overall, the power supply system has a maximum output power of 100 W, limited by the load resistor between audio amplifier and high voltage transformer.

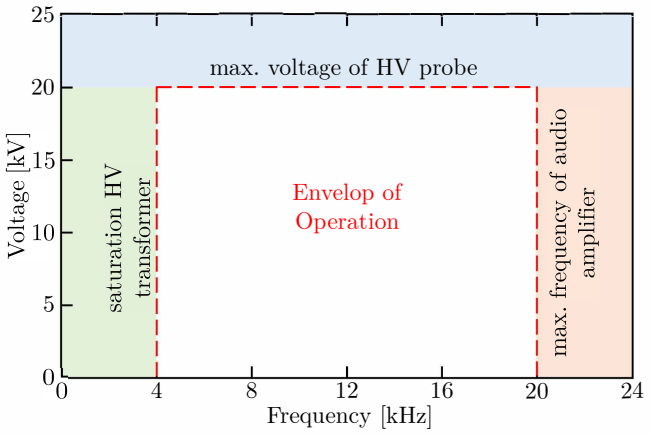

FIGURE 2.16: Envelope of operating conditions of built high voltage power supply system

2.4 Diagnostics

The printed DBD plasma sources fabricated in the framework of this thesis are assessed through two main diagnostics methods, electrical characteristics, and optical characteristics of the generated plasma. The electrical diagnostics provides crucial information about the discharge power of the DBD plasma source, but can also be used for more detailed analysis of the breakdown voltage and characteristic of the microdischarge pattern. With the optical diagnostics, the overall intensity, and the uniformity of the generated plasma across the surface DBD plasma source can be assessed. The following section introduces the diagnostics tools employed in this study and presents how key parameters are obtained for comparative studies presented in the following chapters of this thesis.

2.4.1 Electrical diagnostics

The electrical behaviour of a non-thermal plasma can be characterised by measuring three main quantities: applied voltage, current and charge [85]. The three electrical quantities methods allow the assessment of various electrical characteristics of a non-thermal plasma source, such as the discharge power, values such as breakdown voltage and characteristic discharge patterns. In this study, the discharge power will play an important role and the following shall present the electrical diagnostic tools implemented within the electrical circuit and the derivation of the discharge power.

The high voltage signal is monitored used a high voltage probe. A high voltage probe provides a scaled down measurement of a high voltage using a voltage divider circuit. In this study, two high voltages probes were used to measure the high voltage, Testec TT-HVP 15HF and Tektronix P6015A. The current measurement is carried out using two methods, through a shunt resistor or using an inductive coil. The shunt resistor uses a known resistance (100 Ω) in series to the load, the DBD plasma source, and the circuit ground. Monitoring the voltage drop, across shunt resistor allows to calculate the current. The choice of its resistance is a balance between accuracy of the measurement and minimizing the affect the implemented shunt resistor has on the overall circuit. A large resistance provides a good accuracy of the current measurement. However, it results in a large voltage drop relative to the voltage drop across the actual load, the DBD plasma source. This can affect the remaining circuit and reduce the accuracy of the voltage measurement. Choosing a very small resistance minimizes this affect but also reduces the accuracy of the current measurement. A second method to measure the current passing through the DBD plasma source, I_{DBD}, is using an inductive Rogowski coil (Pearson Current Monitor Mode 6585). The coil obtains the AC current as the integral of a magnetically induced voltage caused by the passing current. The Rogowski coil is measuring the current on the high voltage side of the plasma source. A probe capacitor can be used to monitor the charge transfer on the electrodes in the DBD plasma source [86]. The probe capacitor is placed in series, between the DBD plasma source and the circuit ground. The charge, Q_{DBD}, can be calculated according to:

$$Q_{DBD}(t) = C_p \cdot V_{CP}(t) \tag{2.3}$$

where V_{CP} is the measured voltage drop across the probe capacitor and C_P its capacitance (10 nF). The current through the probe capacitor is the same as through the DBD plasma source, due to the series the series arrangement and can be be calculated as:

$$I_{DBD} = C_P \cdot \frac{dV_m(t)}{dt} \tag{2.4}$$

The choice of the capacitance of the probe capacitor is based on the capacitance of the DBD plasma source. As it is placed in series, it carries the ability to influence the capacitive behaviour of the circuit. To ensure the probe capacitor has negligible effect, it is recommended to be at least three orders of magnitude above the capacitance of the DBD plasma source [86].

The measurement of the electrical characteristics is used to obtain the discharge power of DBD plasma sources. The discharge power is an important parameter in comparative studies of different electrode designs. A meaningful comparison of different DBD electrode designs is only possible when constant power levels are considered [87]. The discharge power plays a crucial role for a cost benefit analysis of DBD plasma sources. For example, in the flight actuator community, light-weight high-voltage power supplies are required. Additionally, studies are using the discharge power as way of health monitoring of DBD actuators [88]. Therefore, a correct assessment of the discharge power is crucial. In this thesis, the discharge power is used as a comparative parameter to assess various operating conditions and design parameters of printed DBD plasma sources.

Figure 2.17 shows an exemplary measurement of one period of the voltage, current and charge measurement obtained from a printed DBD plasma source. As can be seen in Figure 2.17(a), the voltage follows a sinusoidal signal with a peak-to-peak voltage of 3.6 kV and a frequency of 8 kHz. Once the applied voltage exceeds a certain limit, ionisation start occurring and non-thermal plasma will start forming. This limit is known as the breakdown voltage. The current waveform clearly indicates the active plasma region in the positive and negative half period with the microdischarges being visible as numerous high frequency and large amplitude signals, the microdischarges. Figure 2.17(b) shows the voltage-charge characteristic, the Lissajous graph.

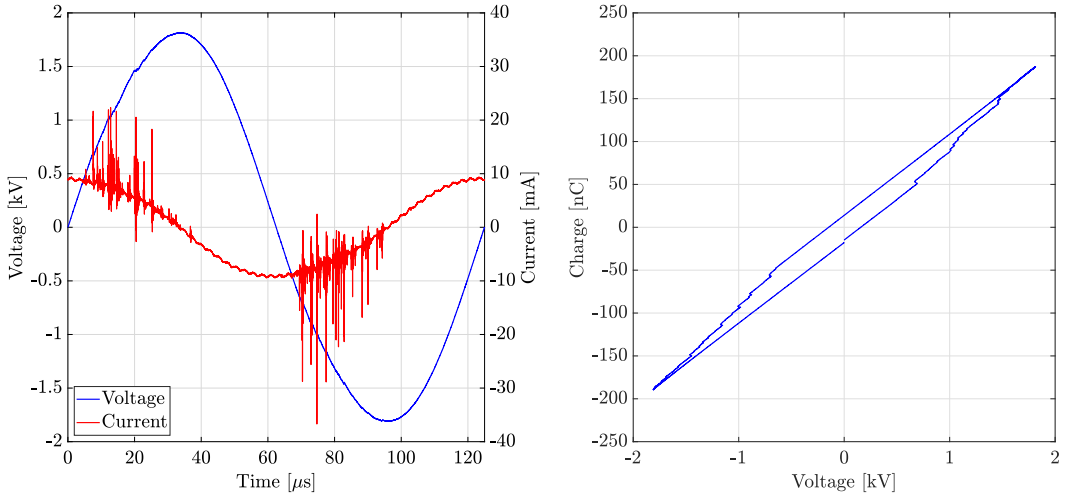

(a) (b)

FIGURE 2.17: Electrical measurements: (a) Voltage and current measurement; (b) Voltage-charge characteristics (Lissajous graph)

The discharge power of the DBD plasma sources can be obtained through two separate methods. The first method uses voltage and current measurement to calculate the instantaneous power, $P_{inst.}(t)$, as:

$$P_{inst.}(t) = V_{DBD}(t) \cdot I_{DBD}(t) \tag{2.5}$$

From the instantaneous power, the discharge power over one period, P_T, can be calculated as:

$$P_T = \frac{1}{T}\int_0^T P_{inst.}(t)dt = \frac{1}{T}\int_0^T V_{DBD}(t) \cdot I_{DBD}(t)dt \tag{2.6}$$

The second method uses the Lissajous graph to obtain the discharge power over one period [85]. The discharge power can be described as the area within the Lissajous graph as:

$$P_T = \frac{1}{T}\int_0^T V_{DBD}(t) \cdot I_{DBD}(t)dt \tag{2.7}$$

Using equation 2.4 for the current through the plasma source and equation 2.3 for the charge measurement based on the capacitance of the probe capacitor, C_p, and the measured voltage drop across the probe capacitor, V_m, the discharge power can be obtained as:

$$\begin{aligned} P_T &= \frac{1}{T}\int_0^T V_{DBD}(t) \cdot C_p \cdot dV_{CP} \\ &= \frac{1}{T}\int_0^T V_{DBD}(t) \cdot dQ_{DBD} \end{aligned} \tag{2.8}$$

Obtaining the discharge power through the capacitor measurement presents a more accurate measurement [86, 89]. Due to the integration of the current through the capacitor, the microdischarges are captured more accurately, consequently providing a more accurate discharge power. This description of the discharge power for both methods (equation 2.6 and 2.8) provides the discharge power over one period of the driving signal. However, the electrical date is recorded over several milliseconds, therefore capturing several period of the sinusoidal signal, depending on the operating frequency. The average power of the DBD plasma source, P_{ave}, can be expressed as the average over the full obtained signal as:

$$P_{ave} = \sum_{n=1}^{k} P_T \tag{2.9}$$

where k is the total number of periods captured for one measurement. The standard deviation of P_{ave} will be shown as the error bars for the respective measurement in the following chapters to highlight the uncertainty of the measurements.

2.4.2 Optical diagnostics

Analysis of the optical properties of the generated plasma can provide important information about the DBD plasma source. Previous studies have highlighted correlations between the time-resolved light intensity and the discharge current [90]. This indicates that the discharge power in a DBD plasma source can be correlated to the light intensity. The relationship between both the discharge power and light intensity can be understood as an efficiency of the DBD plasma source. The discharge power represents the energy input into the systems and the light intensity indicates the plasma intensity. In this thesis, the light intensity of the generated plasma is assessed with two methods, an optical image processing approach and Optical Emission Spectroscopy (OES), both further explained in the following sections.

2.4.2.1 Image processing

As an optical diagnostics tool, image processing is used to assess not only the overall intensity but also the uniformity of the generated plasma across the printed electrode system. The plasma generation from the printed DBD electrode systems is captured using a DLSR camera. A Nikon D5600 camera with macro lens is used to obtain high resolution images of the plasma generation across the full DBD surface. To obtain high quality images with the whole electrode surface in focus, the camera is ideally positioned normal to the surface of the DBD plasma source. However, the second optical diagnostics, the OES setup, is being kept with a viewing angle normal to the plasma source. Thus, the images obtained with the DSLR camera are recorded under a small angel as a trade off.

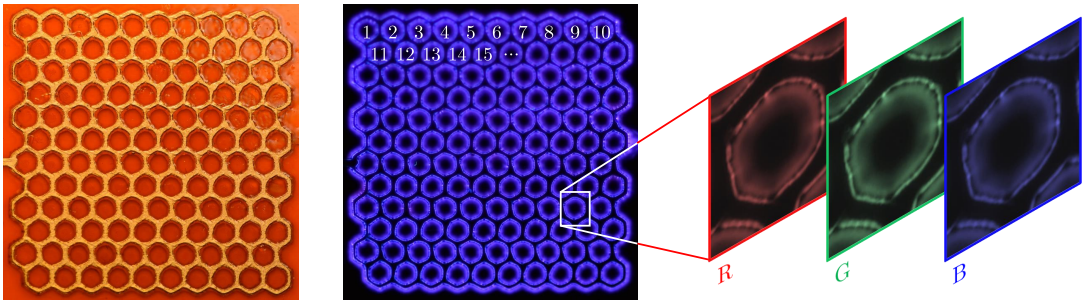

FIGURE 2.18: Overview of image intensity and uniformity assessment, schematically showing RGB component of generated plasma

Figure 2.18 shows an image of the printed plasma source and a typical image of the generated plasma. Quantifying the image intensity and the uniformity is performed by dividing the image in numerous sections following the geometry pattern of the electrode. Figure 2.18 shows exemplary a hexagonal electrode pattern of 20 mm x 20 mm with an

unit size of 2 mm and a total number of hexagons of k =120. The position of the centre of each hexagon is calculated by calibrating the image through referencing to the known dimensions of the printed electrode geometry. The pixel position of the upper and lower extend, as well as the left and right position of the electrode is obtained from the image. Based on these positions, the pixel position and size of each hexagonal unit can be calculated. Each hexagonal unit section has the same dimension. Within each image section, s_k, the image intensity value, I_{img,s_k}, is obtained as:

$$I_{img,s_k} = \sum_{i=1}^{n}\sum_{j=1}^{m} R_{k,ij} + \sum_{i=1}^{n}\sum_{j=1}^{m} G_{k,ij} + \sum_{i=1}^{n}\sum_{j=1}^{m} B_{k,ij} \tag{2.10}$$

where $R_{k,ij}$, $G_{k,ij}$ and $B_{k,ij}$ are the pixel intensities of the respective RGB part (red, green, blue) of the image section and n and m the width and height of the image section respectively. Within each RGB image components, the pixels have values between 0 for low intensity and 255 for high intensity. I_{img,s_k} is therefore the total pixel-sum within each image section.

The image intensity within each section, I_{img,s_k}, is normalized through a reference image with full intensity values of the same dimension, I_{ref}. This reference image contains the maximum pixel value of 255 for all three RGB image component over the full section dimension and is calculated as:

$$I_{ref} = \sum_{i=1}^{n}\sum_{j=1}^{m} 255 + \sum_{i=1}^{n}\sum_{j=1}^{m} 255 + \sum_{i=1}^{n}\sum_{j=1}^{m} 255 \tag{2.11}$$

The average image intensity of the plasma generation over the full printed plasma source can be expressed as:

$$I_{img} = \sum_{i=1}^{k} \left(\frac{I_{img,s_k}}{I_{ref}}\right) \tag{2.12}$$

Consequently, I_{img} defines the image intensity as a percentage of an image with maximum brightness. This mean image intensity, I_{img}, quantifies the overall intensity of the generated plasma as a percentage over the full electrode geometry. The uniformity of the plasma generation, σ_{img}, can be expressed as the image intensity deviation by calculating the standard deviation as:

$$\sigma_{img} = \sqrt{\frac{\sum_{i=1}^{k}(I_{img,s_k} - I_{img})^2}{k}} \tag{2.13}$$

It shall be noted, that this assessment does not provide any qualitative information of the plasma generation, but allows for a quantitative comparison of different electrode systems and operating conditions within the presented studies of this thesis. Camera settings parameters, such as shutter speed and aperture have to be maintained constant,

to allow relative comparison between different plasma sources. Both the mean image intensity, I_{img}, and the image intensity deviation, σ_{img}, are used to quantify the plasma generation of the printed electrode systems. The mean image intensity, I_{img}, allows comparison of the emission intensity of plasma generation within the visible wavelength band. A larger image intensity, I_{img}, is indicative of a stronger plasma generation. A low image intensity deviation, σ_{img}, represented similar image intensity within each hexagonal section and consequently indicates a high level of uniformity of the generated plasma across the electrode surfaces. An increase of the image intensity deviation points to a non-uniform plasma generation across the electrode, with individual sections of the recorded image having a stronger or weaker plasma generation.

2.4.2.2 Optical emission spectroscopy

The chemical properties of the generated plasma are analysed with optical emission spectroscopy (OES) as a simple and non-invasive diagnostic technique. The optical emission spectroscopy in air at atmospheric pressure mainly measures the intensity of nitrogen emission of the plasma and allows characterisation of the physical and chemical properties of the generated non-thermal plasma. Additionally, it can provide an estimation of plasma parameters such as electron temperature and electron density n_e. Figure 2.19 shows a detailed set-up of the OES system. A collimating lens (OceanOptics 74-UV collimating lens) is used to collect the emitted light from the generated plasma and lead through an optical fibre (600 nm diameter) to the spectrometer (OceanOptics HR4000CG-UV-NIR). The spectrometer is equipped with an entry slit of 5 μm and a CCD detector (linear array of 3648 pixels) and obtains emission in the wavelength range 200 - 1100 nm with an optical resolution of 0.5 nm. The software OceanView (by OceanOptics) is used for displaying the recorded spectra and identification of spectral lines in real time and for saving spectra for further post-processing.

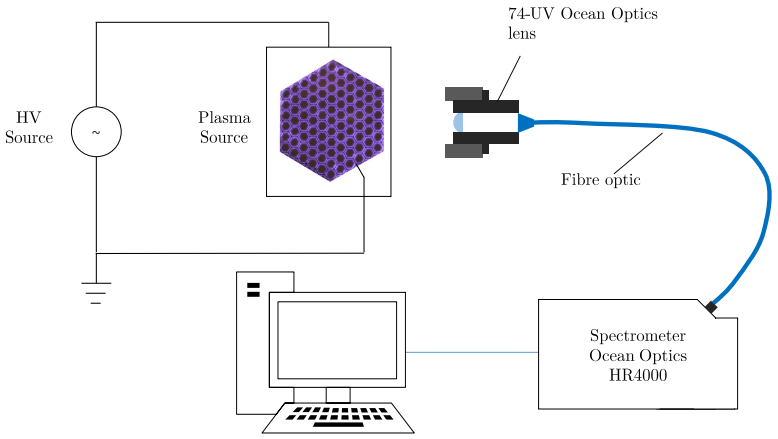

FIGURE 2.19: Schematic of the setup of the optical emission spectroscopy system

Figure 2.20 shows an example of the recorded spectra from the plasma emission from a printed electrode system. As can be seen, the spectrum is characterised by strong emission peaks in the wavelength band from 300 to 440 nm. The dominant emission peaks can be assigned to the second positive system of N_2 ($C^3\ \Pi_u$ - $B^3\ \Pi_g$), and the first negative system of N_2^+ ($B^2\ \Sigma_u^+$ - $X^2\ \Sigma_g^+$). Table 2.2 lists the major emission peaks of both systems. As atmospheric non-thermal plasmas have mean electron energies in the range of few eV, only a small fraction of electrons posses energies that exceed these elementary processes. Therefore, the relative low intensity of N_2^+ ($B^2\ \Sigma_u^+$ - $X^2\ \Sigma_g^+$) at 391 nm is indicative of this small number of highly energetic electrons. The emission of atomic oxygen can currently not be detected, even though the required energy for these transitions is well below the threshold for emission at 391 nm. This is mainly due to high quenching rates from collisions with N_2 and O_2 molecules. Quenching from N_2 and O_2 is one of the main depopulation process of in atmospheric plasma [91].

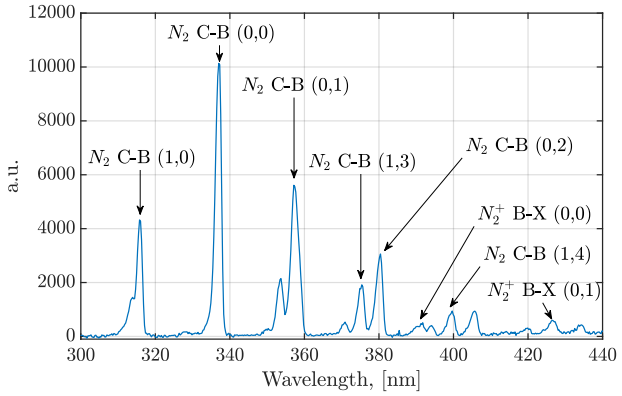

FIGURE 2.20: Typical emission spectra of printed DBD plasma source with the major emission peaks indicted

Species	System	Peak [nm], (v', v")
N_2	2^{nd} Pos. ($C^3\ \Pi_u$ - $B^3\ \Pi_g$)	316 (1, 0); 337 (0, 0); 357 (0, 1); 375 (1, 3); 380 (0, 2); 400(1, 4)
N_2^+	1^{st} Neg. ($B^2\ \Sigma_u^+$ - $X^2\ \Sigma_g^+$)	391 (0, 0); 428 (0, 1)

Table 2.2: Major observed emission peaks in wavelength range from 300 to 450 nm

The obtained emission spectra can be compared to spectra found in literature. Figure 2.21 shows a typical spectra of a printed DBD plasma source in addition to three spectra of atmospheric air plasma from literature [66, 92, 93]. As can be seen, the recorded major emission peaks of the second positive system of N_2, and first negative system, N_2^+, overlay with the peaks found from literature.

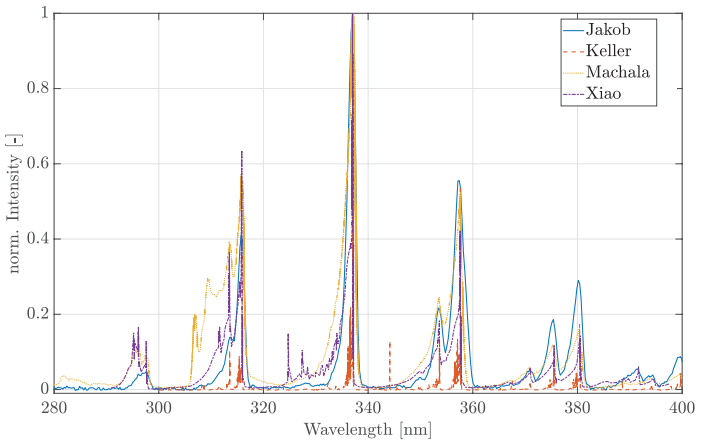

FIGURE 2.21: Typical emission spectra of printed DBD plasma source compared to literature: Keller [92]; Machala [93]; Xiao [66]

The emission spectra of the plasma generated for various plasma sources is quantified with regards to their overall spectral intensity of the recorded spectrum within the wavelength band of the major emission peaks of the second positive system of N_2 ($C^3\ \Pi_u$ - $B^3\ \Pi_g$), and the first negative system of N_2^+ ($B^2\ \Sigma_u^+$ - $X^2\ \Sigma_g^+$). The overall emission intensity, I_{spec}, is quantified by deriving the integrated spectral intensity as:

$$I_{spec} = \int_{250nm}^{450nm} I(\lambda) d\lambda, \tag{2.14}$$

where $I(\lambda)$ is the spectral intensity at the respective wavelength, λ. Obtaining the integrated spectral intensity allow for a relative comparison between the varying electrode configuration and power conditions.

An optical diagnostics set-up requires calibration in order to ensure a reliable and precise characterisation of plasma properties. Figure 2.22 shows a printed plasma source mounted in the plasma test chamber with optical diagnostic system. As can be seen, a plasma source is mounted on an adjustable platform to analyse the influence of viewing angles between the plasma source and the lens axis. A schematic of the calibration set-up can be seen in Figure 2.22 (b).

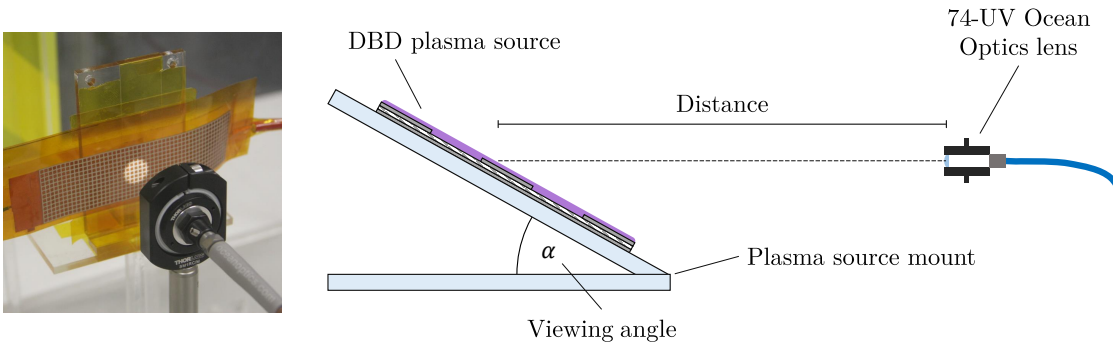

FIGURE 2.22: (a) Setup of optical diagnostic (b) Schematic of calibration setup

Table 2.3 gives the details for the respective parameters for the calibration activities of the optical diagnostic, including the viewing angle (α), the distance (d), between plasma source and lens, the lens focus settings (f_{FOV}) integration time (t_{int}), and the number of scans to average (StA).

	Description	Variation
α	Angle between lens axis and plane of the plasma source.	10° / 20° / 90°
d	Distance between lens and plasma source.	4 cm/5 cm/8 cm/12 cm
f_{FOV}	Variation of the field of view (FOV)	f (focused), c (collimated), w (wide)
t_{int}	Time the detector in the spectrometer monitors the incoming photons.	5 s / 10 s / 15 s
StA	Number of discrete spectral acquisitions used to generate an averaged spectrum.	1 / 10

Table 2.3: Assessed parameters for calibration of OES system

Figure 2.23(a) to 2.23(c) shows the spectra for varying integration time (5s; 10s; 15s) for the three different viewing angles (10°; 20°; 90°). The spectra show the second positive system and first negative system of excited nitrogen in the range from 300 nm to 400 nm with varying intensities for the respective calibration configuration. Figure 2.23(a) shows the spectra for a viewing angle of 10°. As can be seen, some of the emission peaks are reaching the saturation limit at approximately 14500 counts, which is the saturation limit of the OES system. Therefore, the emission peaks at 337 nm and 357.4 nm can not be clearly identified. However, the emission peaks at 316 nm are clearly visible for all three integration times. Therefore, it is important to account for the saturation limit during the experimental activities, in order to accurately characterise the plasma.

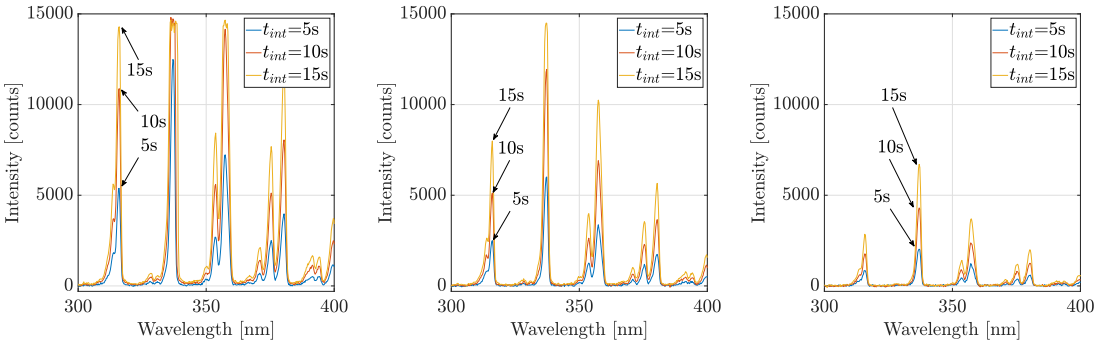

(a) α=10° (b) α=20° (c) α=90°

FIGURE 2.23: Spectra with variation of integration time for varying viewing angles

As can be seen in Figures 2.23(a) to 2.23(c), the recorded spectra intensity of a plasma increase is proportional to the integration times. This means the spectra intensity for the integration time of 15 sec increases by factor of three, compared to spectra using the integration time of 5 sec. This is due to a larger number of photons reaching the CCD chip of the spectrometer for longer exposure times. The intensity scaling effect of integration time comes with an approximately 5% error. Moreover, the comparison of Figures 2.23(a) to 2.23(c) demonstrate that a decreased viewing angle leads to a higher spectra intensity. This results in the highest recorded intensity peaks for the smallest viewing angle of 10°. A 90° viewing angle gives the lowest spectral intensity because an optical emission spectroscopy (OES) is a line-of-site measurement.

As shown in Figure 2.24, the spectra intensity is related to a relative thickness, t' along the viewing axis rather than an actual plasma layer thickness, t. It can be expressed as:

$$sin(\alpha) = \frac{t}{t'} = \frac{I_{\perp}}{I_{\alpha}} \tag{2.15}$$

where α is the viewing angle, $I_{\perp}$ is the spectral intensity with the viewing angle, and I_{α} the spectral intensity with the plasma layer normal to the lens axis.

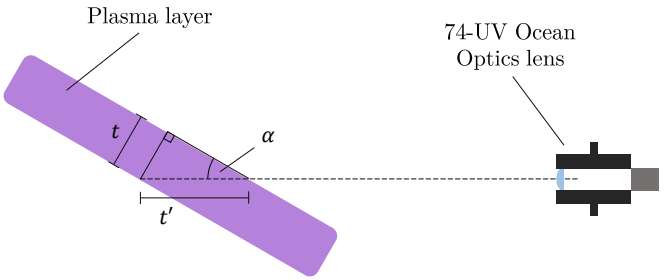

FIGURE 2.24: Schematic of spectral intensity and viewing angle relation

Using the measured spectra data, correction factors for viewing angles and integration times can be derived. For a viewing angle of 10°, the measured spectra intensity is approximately 6.05 times higher than a normal viewing angle. The correction factor calculated using equation 2.15 is 5.76. For a 20° viewing angle, measured correction factor is 2.83, and the calculated correction factor is 2.92. This deviation of the scaling factor of below 5 % demonstrates, that the viewing angle can be chosen as an active method to influence the recorded spectral intensity. A plasma with an anticipated weaker intensity can be recorded with a smaller viewing angle, in order to obtain a spectrum with sufficiently high signal to noise ratio.

Different lens settings are also investigated. Figure 2.25(a) shows an image of the three different lens settings (focused, collimated and wide) used to record spectra. Figure 2.25(b) shows the measured spectra with the three different lens settings where the distance, the viewing angle and the integration time are kept constant. As can be seen, the spectra intensity remains similar for varying lens setting. As confirmed with the measurement of various viewing angles and also shown in Figure 2.24, the spectra intensity is mainly dependent on the plasma along the lens axis within the plasma layer. Therefore, various lens settings only result in a negligible influence on the recorded spectra intensity.

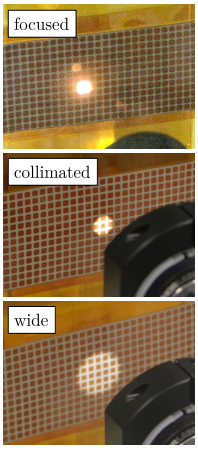

(a) Field of view images

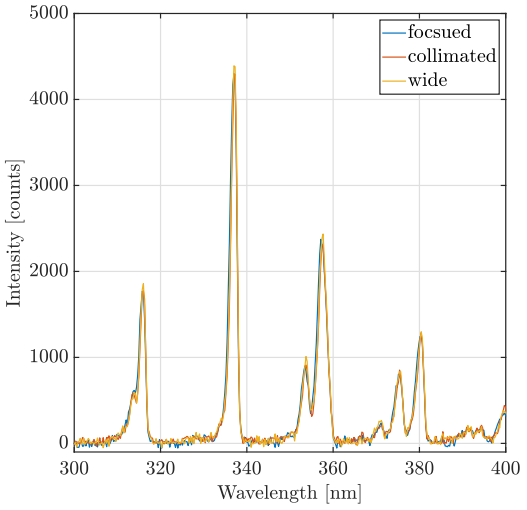

(b) Field of view

FIGURE 2.25: Variation of optical lens setting (a) Field of view for focused, collimated and wide lens setting; (b) Spectra with various lens settings

The recorded spectra at three different distances between plasma source and lens are analysed in Figure 2.26(a). As can be seen, the measured spectra intensity is not sensitive in terms of distance to a plasma source. Figure 2.26(b) shows two spectra with constant calibration configuration but varying number of “Scans to average”. For both a constant integration time of 5 s was used. No major affect can be recognized in the spectra when

comparing a recording using 10 scans to average compared to only one scan. Yet, an improvement of the signal to noise ratio can be measured.

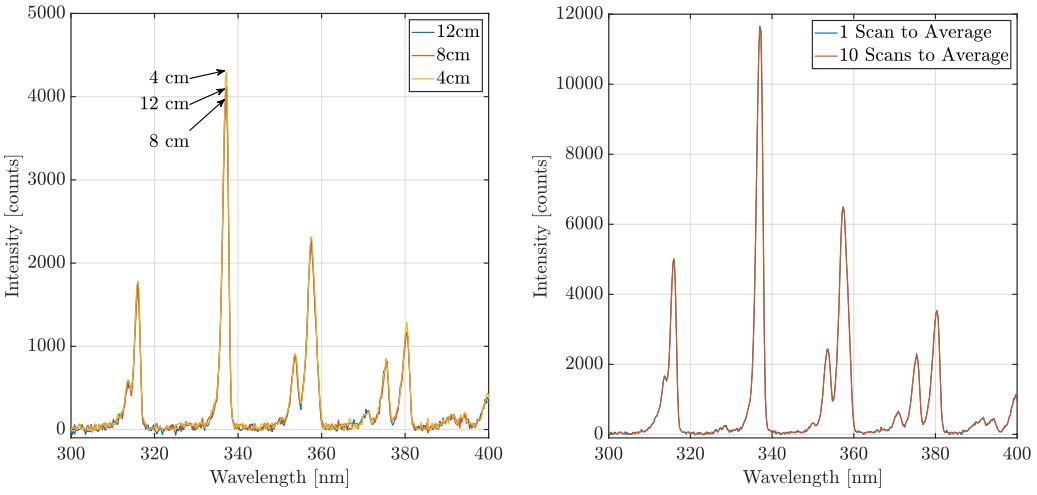

(a) Distance

(b) Scans to Average

FIGURE 2.26: Spectra with (a) varying distance between plasma source and lens; (b) varying number of scans to average

Chapter 3

Scalable and flexible plasma generation systems

This chapter presents a comprehensive analysis of printed electrode systems and their performance as a scalable and flexible plasma generation system. Section 3.1 describes a preliminary test campaign that was carried out and which investigated the performance of printed plasma sources fabricated with the ink-jet printer method (Dimatix DMP2831). The ink-jet printer system was selected because it can print electrodes on a thin and flexible dielectric material. Section 3.2 shows a comprehensive test campaign, which investigated the performance of printed plasma sources fabricated using the dispenser printing method (Voltera V-One). The dispenser printing method uses high-viscosity ink, resulting in thicker and more robust electrodes. Printed plasma sources using both printing methods were subjected to lifetime testing, performance evaluation under varying operating conditions and a scalability and flexibility assessment. With the lifetime testing, the printed plasma sources are assessed in terms of damage from erosion after an extended operating time. Analysing the performance under varying operating voltages and frequencies allowed for the definition of the operating envelope, which plays a crucial role in the design and optimisation procedure of non-thermal plasma sources. The scalability and flexibility assessment demonstrates the versatility of printed electrode systems for varying applications that are required to treat large and/or complex surfaces.

3.1 Ink-jet printed electrodes

3.1.1 Surface erosion of printed electrodes using inkjet printing

During discharge, electrodes can be eroded and oxidised due to the high power density and bombardment of high-energy particles in the plasma. The erosion of electrodes can

result in the change of electrode geometry and can limit the lifetime of a printed plasma source [58]. Therefore, the efficiency and reliability of a plasma source will be limited by the erosion and oxidation of electrodes for long-term operations [94].

Assessment of the lifetime of the printed plasma sources fabricated with medium-viscosity conductive ink using the inkjet printing method are carried out. Figure 3.1 shows the fabricated plasma source with a microscope image and additionally highlighting the print quality. The electrode geometry is a linear hexagon pattern. As can be seen, the printed hexagon-shaped electrode has slightly uneven edges, with thin lines being identified. This is due to the individual nozzles in the printer head. In combination with the medium viscosity of the conductive ink, this results in short streaking lines on the edge of the printed electrode [95, 96]. A better regularity of the printed edges can be achieved by adjustment of ink droplet size and placement of the inkjet printer nozzle head.

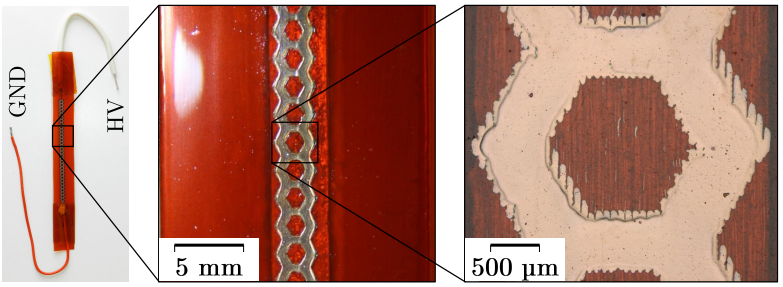

FIGURE 3.1: Inkjet-printed plasma source using medium-viscosity conductive ink on a flexible dielectric material

The lifetime assessment of the printed plasma source is carried out at an operating voltage of 6 kV at a frequency of 3 kHz for a total operating test time of 15 minutes. Figure 3.2(b) shows the surface of the printed electrode after the operating test time. As can be seen the printed electrode has been eroded near the edge region of the hexagonal pattern, mainly located at the short streaking lines. The remaining electrode surface is also subjected to erosion, as can be seen by an overall discolouration of the electrode. Since the local electric field is strongest in the edge region, erosion is most prominent in this region and reduces towards the central areas of the printed electrode.

The erosion and oxidation of the printed electrodes can be minimized by preventing direct contact between the electrode and the plasma [97]. Applying a protective coating on the electrode minimizes the effect of the bombardment of high-energy particles on the electrode material. The coating material acts as a buffer layer, which can reduce the erosion of the electrode material. The thickness and material properties of the coating define the level of protection from erosion. However, they can also affect the performance of a plasma source. The coating will act as an additional dielectric later on the plasma source, thus a thicker coating and/or higher relative permittivity will increase the capacitance of the plasma source and can increase the power consumption.

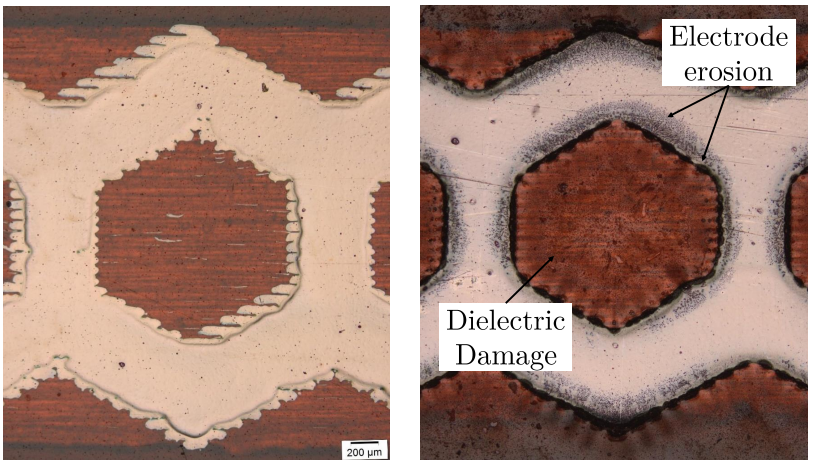

(a) (b)

FIGURE 3.2: Microscope images of printed electrodes; (a) unused printed electrode; (b) printed electrode after operation for 15 minutes without surface coating

Two protective coatings are assessed in terms of their protective capability, an aerosol silicone resin coating (Modified Silicone Conformal Coating) and an oil-based silicone coating (Polydimethylsiloxane - PDMS). Table 3.1 shows an overview of the specifications of both employed coatings. The aerosol silicone resin coating is an aerosol spray coating, which cures in air after 2 hours and forms a solid and rigid layer with a dielectric strength of 90 kV/mm. The oil-based silicone coating is a highly vicious oil coating, which requires application with a brush. The coating does not cure and remains as a viscous layer on the electrode with a dielectric strength of approximately 100 kV/mm. As both coating materials have high dielectric properties, low reactivity, and high thermal and oxidative stability, they can protect the surface of printed electrode [75].

	Aerosol silicone resin coating	Oil-based coating
Density	0.78 g/ml	0.98 g/ml
Curing Time	2 hours 20 °C	N/A
Dielectric Strength	90 kV/mm	100 kV/mm

Table 3.1: Specifications of the chosen protective coatings

Figures 3.3 shows microscope images from printed electrode with the aerosol silicone resin and oil-based silicone coatings after 15 minutes of operation. As can be seen, the aerosol silicone resin coating forms a uniform layer over the electrode and significantly reduces the erosion of printed electrodes. The printed electrode shows some erosion near the edge, however only minimal erosion is visible across the electrode surface. Using an oil-based silicone coating on the printed electrode achieved a significant level of protection of the electrode material. No dark erosion spots are visible at the edge region and no surface discolouration, indicating erosion across the surface, are visible.

However, the oil-based silicone coating forms a less uniform thickness, as can be seen in the bottom area in Figure 3.3(b). This uneven distribution of the coating layer can potentially affect the local electric field distribution due to the dielectric property of the coating. This can result in a non-uniform plasma generation and therefore the efficiency when using the plasma source in an application.

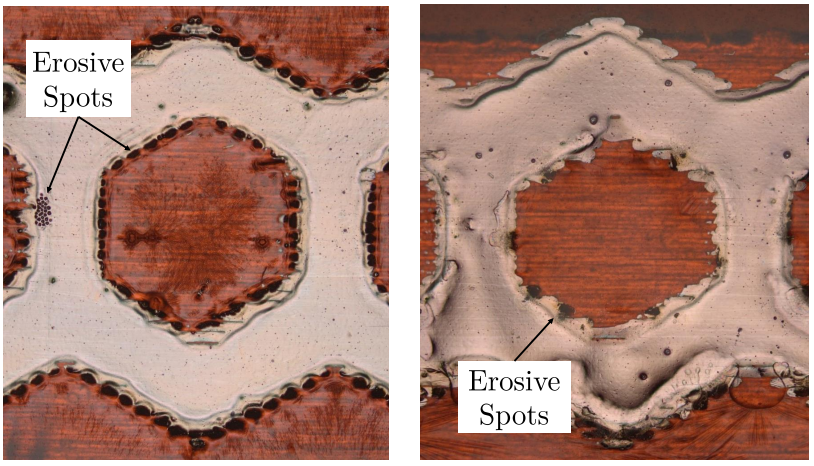

(a) (b)

FIGURE 3.3: Microscope images of printed electrodes with (a) Aerosol silicone resin coating after operation for 15 minutes (b) printed electrodes with PDMS coating after operation for 15 minutes

he assessment of surface erosion on printed electrodes using inkjet printing concluded that an inkjet printed electrode is subjected to erosion for increased operating times. Employing protective coating methods can alleviate the electrode erosion and dielectric damage. The aerosol silicone resin coating can be applied as a rigid layer of uniform thickness and will therefore be employed for the future studies using inkjet printed electrodes.

3.1.2 Electrical characteristics

Figure 3.4(a) shows the measured voltage and current from the printed plasma source for the operating voltage of 6 kV and operating frequency of 2 kHz. The electrical data is recorded for a total time of 0.2 s, which covers a total of 400 cycles, however the signal shown is covering one period of the sinusoidal waveform. On the current measurement, the active plasma region can be clearly distinguished in the positive and negative half period. Within the active plasma phase, the microdischarge current is superimposed to the current signal and characterised through high frequency and large amplitude current spikes. Figure 3.4(b) shows the Lissajous graph with the voltage-charge characteristics. From the Lissajous graph, the discharge power can be obtained from the area within the voltage-charge-characteristics. Deriving the discharge power over the full length of the recorded signal provides an average discharge power of $P_{ave} = 5.4$ W with a

corresponding standard deviation of the discharge power of $\sigma_{P_{ave}}$=11% over the 400 cycles.

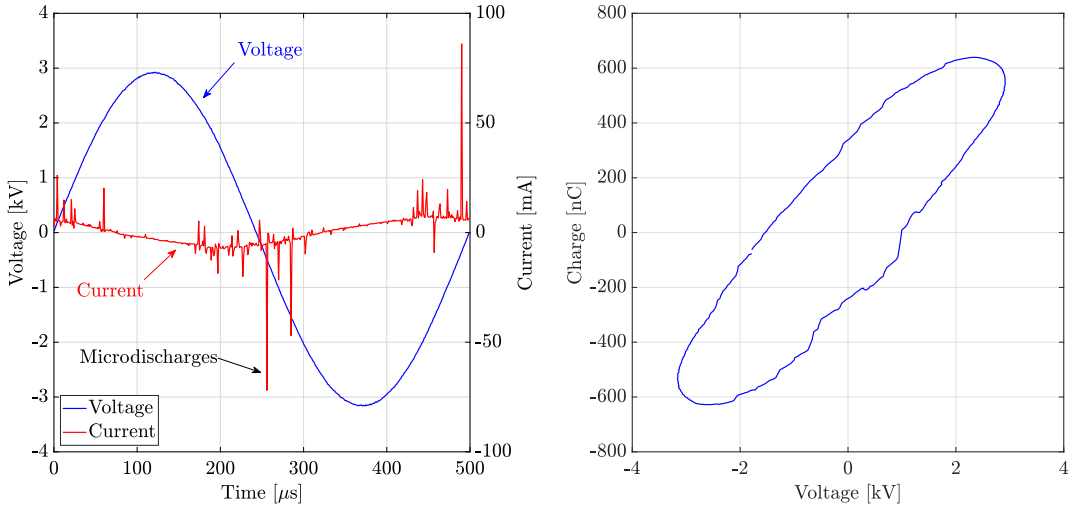

(a) Voltage and current measurements (b) Lissajous graph

FIGURE 3.4: Electrical Characteristics of printed plasma source using inkjet printing method: (a) Voltage and current measurements; (b) Lissajous graph

3.1.3 Scalability

The scalability of the printed plasma source is assessed using electrical and optical diagnostics. Plasma sources of three different length scales (64 mm, 128 mm and 256 mm) are fabricated using the inkjet printer method. Figure 3.5(a) shows a schematic of the fabricated plasma sources of varying lengths. Figure 3.5(b) shows the images of the plasma emission for operating conditions of 6 kV and 2 kHz. The images show only a small section of the actual full length of the respective electrode system. In addition Figure 3.5(b) shows qualitatively that the overall intensity of the plasma emission across the printed DBD plasma source remains constant.

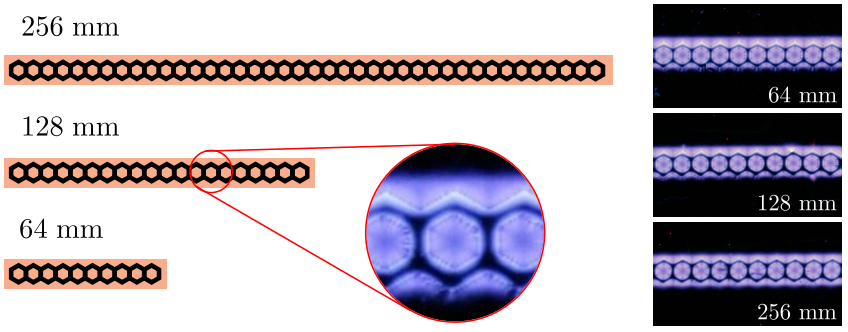

(a) (b)

FIGURE 3.5: (a) Schematic of printed plasma source of varying lengths (b) Air plasma emission images of plasma sources of varying lengths

Quantification of the intensity and uniformity of the plasma emission is performed by obtaining the relative image intensities from the images, as presented in section 2.4.2. The image intensity value is obtained in each individual hexagon of the printed plasma source. The average image intensity,I_{img}, is derived as the mean across all hexagons of the respective plasma source. The standard deviation, σ_{img}, is derived as a measure of the uniformity of the plasma generation across the plasma source. Table 3.2 shows the derived relative plasma intensity and uniformity values for different lengths of the printed plasma source. The image intensity shows only small variation for different length scales, with values ranging from 56 % to 62 %, whereas the intensity deviation, σ_{img}, remains below 2 %. This small value in the standard deviation indicates a highly uniform generation of plasma across the electrodes.

	64 mm	128 mm	256 mm
Image Intensity I_{img}[%]	57	56	62
Image Uniformity σ_{img} [%]	2	1.6	0.9

Table 3.2: Image intensities and uniformities of inkjet printed plasma source of varying length

The power per unit length, P_L, is used to assess the electrical characteristics of the printed plasma source of varying lengths, which can be obtained as:

$$P_L = \frac{P_{ave}}{L} \tag{3.1}$$

where P_{ave} is the obtained average discharge power and L the length of the respective plasma source, which provides the power per unit length in W/m. Table 3.3 shows this power per unit length, P_L, for plasma sources of varying lengths. As can be seen, the normalised discharge power for a 64 mm short printed plasma source is 22.32 W/m, a 128 mm medium long plasma source 21.3 W/m and a long 256 mm long printed plasma source is 21.06 W/m. This confirms that the power scales linearly with the length of a printed plasma source. The spectral emission intensity of the generated plasma of the printed plasma sources of varying lengths is analysed through the integrated spectral intensities, I_{spec}, as presented in 2.4.2. Table 3.3 shows the spectral intensities, I_{spec}, for different lengths of the printed plasma source, which are ranging from 8613 to 9587. As can be seen, the spectral intensity is mostly unchanged for varying lengths of the printed plasma sources, with fluctuations in a range of +/- 6 %.

	64 mm	128 mm	256 mm
Power per unit length P_L [W/m]	22.32	21.3	21.06
Spec. Intensity I_{spec} [-]	9587	8738	8613

Table 3.3: Power and spectral intensity of inkjet printed plasma source of varying length

Through the assessment of electrical and optical diagnostic it can be concluded that the printed plasma source using the inkjet printing method can be used as a highly scalable solution to generated non-thermal plasma. The plasma emission remains constant for varying length of plasma systems, while the electrical performance, power per unit length, is maintained.

3.1.4 Flexibility

Adequate flexibility performance of printed plasma sources is achieved when the obtained image and spectral intensity remain constant for the same operating conditions. The flexibility assessment is carried out using the linear plasma source of 256 mm length, presented in the previous section. Figure 3.6(a) shows the printed plasma source bend around a nylon rod for flexibility assessment and Figure 3.6(b) shows nylon rods of three different diameters (6 mm, 10 mm and 20 mm) used in this study. Similarly to the scalability assessment, the flexibility of inkjet printed plasma sources is assessed through electrical and optical diagnostics. The electrical and optical characteristics are assessed in reference to a flat plasma source. The flexibility assessment is carried out at an operating voltage of 6 kV and an operating frequency of 2 kHz.

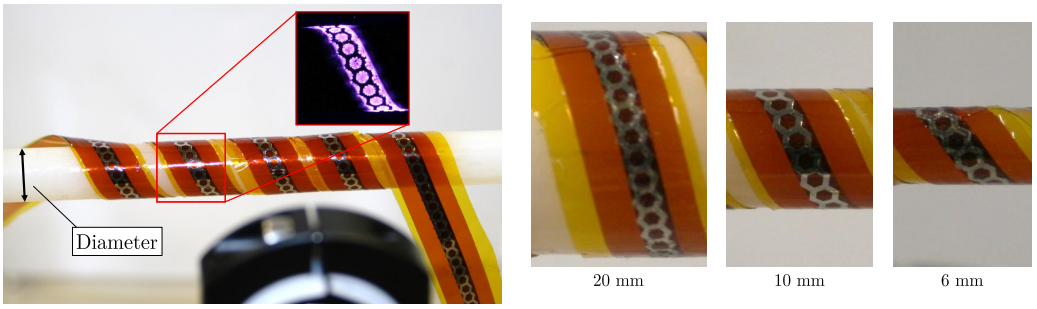

FIGURE 3.6: (a) Inkjet printed plasma source around nylon rod (b) Variation of Diameter of 20 mm, 10 mm and 6 mm

Figure 3.7 shows the generated plasma emission images over various curvatures in reference to a flat plasma source. The images qualitatively show that the overall intensity of the plasma emission across the printed DBD plasma source remains similar for varying curvatures. The images are used to quantify the average image intensity, I_{img}, and standard deviation, σ_{img}, as an uniformity measure.

The intensity within each hexagonal unit is obtained in order to derive the average image intensity, I_{img}, and standard deviation, σ_{img}, as a measure of the uniformity of the plasma generation. Due to the deformation of the plasma source, not all hexagonal units can be included in the assessment. Especially for small curvatures, the image shows only a distorted view of the hexagonal units near the edge region of the nylon rod. Therefore, only hexagonal units within the central region of the nylon rod are included

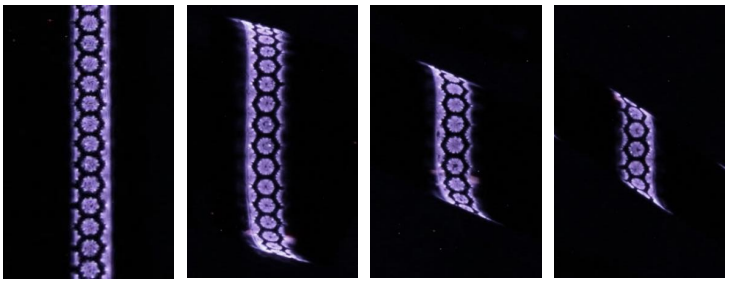

FIGURE 3.7: Emission images of the inkjet printed plasma sources over non-flat surfaces having various curvatures

to obtain I_{img} and σ_{img}. Table 3.4 shows the obtained image intensity and uniformity values of the plasma generation by printed electrodes over varying curvatures. The average intensity for varying curvatures ranges between 56 % - 62 % whilst the standard deviation remains below 2 %. This demonstrates that the plasma source can reliably generate uniform plasma over curved surfaces.

	Flat	20 mm	10 mm	6 mm
Image Intensity I_{img} [%]	62	58	56	62
Image Uniformity σ_{img} [%]	0.9	1.9	0.9	1.3

Table 3.4: Relative image intensities and uniformities of inkjet printed plasma sources using the various curvatures

Table 3.5 lists the obtained power per unit length of the printed electrode system for various curvatures. The power intensity remains constant for varying curvatures, ranging between 20.7 W/m and 20.06 W/m. Additionally, listed in table 3.5 is the integrated spectral intensity, I_{spec}, which ranges from 8237 to 9999 and fluctuates by +/- 10% for varying curvatures of the printed electrode system.

	Flat	20 mm	10 mm	6 mm
Power per unit length P_L [W/m]	21.06	20.77	20.69	20.24
Spec. Intensity I_{spec} [-]	8613	8237	9300	9999

Table 3.5: Power and spectral intensity of inkjet printed plasma source of varying curvatures

The assessment of electrical and optical diagnostics show that the printed plasma source using the inkjet printing systems can be used as a highly flexible solution to generate non-thermal plasma of curved surfaces. It is demonstrated that the plasma emission remains constant for varying bending curvatures of the plasma sources, while the electrical performance is maintained.

3.2 Dispensing printed electrodes

3.2.1 Surface erosion on printed electrodes using dispenser printing

The electrode and dielectric material of a printed plasma source are subjected to the high power density plasma and bombardment of high-energy particles. The electrode and dielectric material therefore can suffer from erosion and oxidation, which can affect the life and performance of a plasma source [98]. Therefore, a detailed analysis of the main design parameters affecting the erosion is necessary to ensure reliable performance of a plasma source over extended operating times.

3.2.1.1 Simplified 1-D line electrode

The effects of erosion of printed plasma sources using the dispenser printing method are assessed using a simplified 1-D line geometry. Figure 3.8 shows a schematic and an image of the simplified 1-D line geometry with a length of 20 mm. The linear geometry generates a uniform electric field distribution along the printed electrode edges. This allows for the assessment of erosion on the printed electrode material independently of geometrical effects of the electrode pattern.

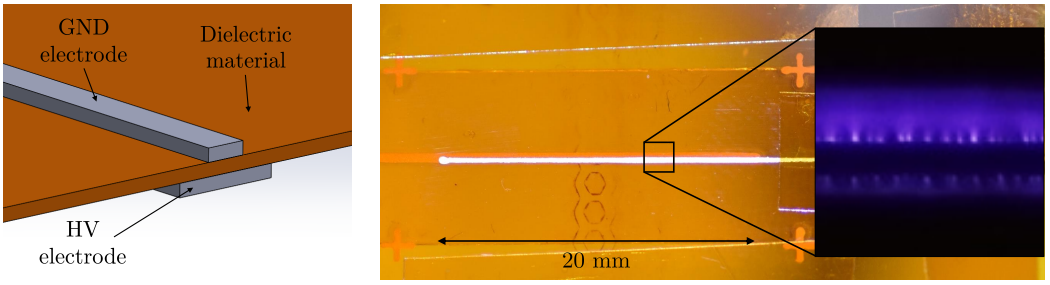

(a) (b)

FIGURE 3.8: (a) Schematic of simplified 1-D line geometry electrode (b) Picture of simplified 1-D line geometry electrode for lifetime analysis

The simplified plasma source geometry is defined by three main parameters, which are ink composition, dielectric material, and dielectric thickness. The capacitance of a printed plasma source can be calculated as:

$$C = \varepsilon_0 \cdot \varepsilon_r \cdot \frac{A}{t} \tag{3.2}$$

where ε_0 is the permittivity of vacuum, ε_r is the permittivity of the dielectric material, A is the total area of the printed electrode, t is the thickness of the dielectric material. From equation 3.2 it is evident that the dielectric constant and the dielectric thickness can affect the capacitance and consequently can affect the electric field distribution of the

plasma sources. Within this study, three different dielectric materials and four different thicknesses of the dielectric are tested. Table 3.6 shows specifications of the different dielectric materials. Polypropylene has a dielectric constant of $\varepsilon_r = 2.1$, Kapton HN has a dielectric constant of $\varepsilon_r = 3.4$ and Kapton MT $\varepsilon_r = 4.2$. A larger dielectric constant results in an increase in capacitance and reduced local electric field strength on the dielectric surface. The analysis of the effect of the dielectric thickness is carried out using the Kapton HN as the dielectric material, with varying thicknesses of 25 μm, 50 μm, 75 μm and 127 μm. An increasing dielectric thickness results in a reduced capacitance and reduced local electric field on the dielectric surface.

	Polypropylene	Kapton HN				Kapton MT
Thickness [μm]	75	25	50	75	127	75
Dielectric constant ε_r	2.1	3.4	3.4	3.4	3.4	4.2

Table 3.6: Specifications of dielectric material to fabricate printed electrodes [99–101]

The electrode material is printed using two different ink compositions, the Voltera Flex-2 ink [102] and the Inkron IPC-114 ink [103]. Table 3.7 lists the specifications of both inks. The Voltera Flex-2 ink consists of 75 % silver and 25 % of solvents, whereas the Inkron ink contains of 70 % silver and 30 % solvents. A plasma source using a thin copper strip will be fabricated to analyse the effect of the metal content on the lifetime in reference to the printed electrodes.

	Voltera - Flex-2	Inkron - IPC-114
Ink viscosity	5000 - 10000 cP	50000 cP
Thickness	$\sim$ 20 μm	$\sim$ 15 μm
Silver %	75 %	70 %
Resistance	12 mΩ/sq	$<$ 15 mΩ/sq

Table 3.7: Specifications of conductive ink used to fabricate printed electrodes using the dispenser printing method [102, 103]

Table 3.8 shows an overview of the fabricated plasma sources with the varying parameters with a respective electrode ID for referencing. The electrodes are operated continuously for 1 minute, after which a microscope image of the electrode is recorded to allow a qualitative analysis of the progression of erosion and/damage on the electrode or dielectric material. All electrode samples are operated at 6 kHz and at an operating voltage between 2.3 kV and 4.1 kV. The operating voltage is chosen as the minimum voltage for which a uniform plasma is generated across the electrode.

Electrode ID #	Material	Thickness	Electrode Material	Voltage
#1	Kapton HN	75 μm	Copper tape	4.2 kV
#2	Kapton HN	75 μm	Voltera ink	4.1 kV
#3	Kapton HN	75 μm	Inkron ink	4.1 kV
#4	Kapton HN	127 μm	Voltera ink	4.1 kV
#5	Kapton HN	50 μm	Voltera ink	2.9 kV
#6	Kapton MT	75 μm	Voltera ink	3.2 kV
#7	Kapton HN	25 μm	Voltera ink	2.3 kV
#8	Polypropylene	75 μm	Voltera ink	4.1 kV

Table 3.8: Overview of fabricated 1-D Line electrodes for the lifetime assessment

Effect of electrode material on lifetime The effect of the electrode material on the lifetime of the plasma source is carried out through comparing electrodes #1 to #3. Figure 3.9 shows the microscope images of the plasma sources with the three different electrode materials, which are the thin copper tape, the Voltera Flex-2 ink and the Inkron IPC-114 ink. The microscope images are shown before operation, after 1 minute, 5 minutes, 10 minutes and 15 minutes of operation.

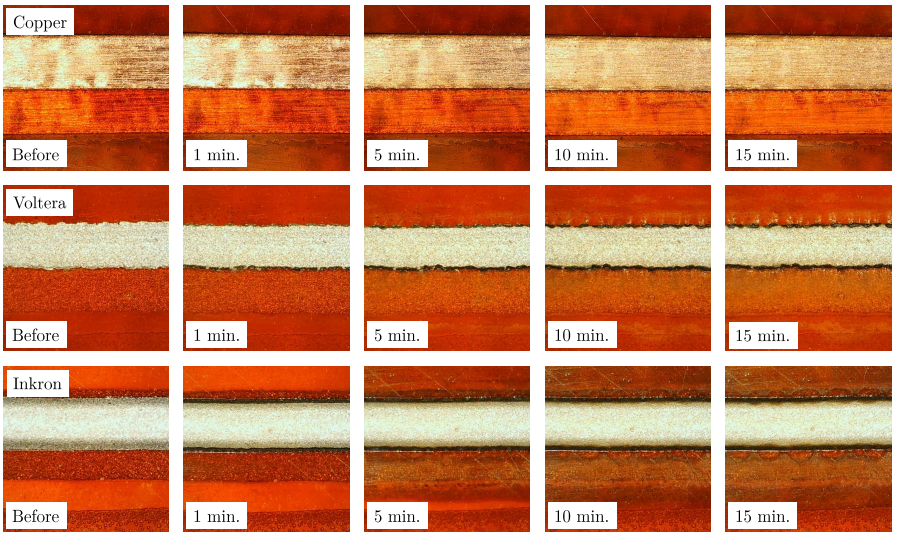

FIGURE 3.9: Microscope images comparing different electrode material (Electrode ID#1, #2 and #3)

The microscope images of the copper electrode (Electrode ID #1) show no signs of erosion on the electrode material and no damage to the dielectric material can be identified after the total operating test time of 15 minutes. In comparison the plasma source using a printed electrode (Electrode ID #2 and #3) show signs of damage to the electrode and dielectric material after a test time of 1 minute. The damage can be distinct in two components: (1) Erosion on the electrode and (2) damage to the dielectric material.

The printed electrode using the Voltera Flex-2 ink shows signs of erosion to the electrode edge of printed plasma sources after a test time of 1 minute. The erosion is visible as dark spots near the printed electrode edge and appears more pronounced at small print imprecisions. These imprecisions result in a concentration of the local electric field. Plasma particles are affected by the electric field, thus these regions have an increased bombardment of high-energy particles, which can result in a higher degree of erosion. Additionally, the overall colour of the printed electrode is darkened after approximately 5 minutes test time. The electric field strength is weaker on the electrode surface, thus resulting in a less heavy bombardment of high-energy particles compared to the edge region. Thus, the surface erosion appears only as a discolouration of the electrode material and is most pronounced after the full test time of 15 minutes. The bombardment of high-energy particles also causes damage to the dielectric material. The damage is visible as darker spots and regions from a test time of 5 minutes onwards. The erosion of the electrode edge and surface region and the damage to the dielectric material is more pronounced with increasing operating time.

Although the printed electrodes using the Inkron ink results in a precise edge finish with minimal edge imprecisions, erosion still occurs after 1 minute of operation. Similarly, this is characterised by dark erosion spots in the edge region, as well as a discolouration of the overall electrode surface. The dielectric material shows visible signs of damage as well. The effect of erosion on the electrode and dielectric material is increased with ongoing operating time. In comparison to the electrode fabricated from the Voltera Flex-2 ink, the electrode from Inkron IPC-114 ink shows stronger signs of erosion at an earlier test time. This is likely caused by the difference in silver content and solvent composition of the inks. With a lower silver content, the Inkron IPC-114 ink is more prone to erosion in comparison to the Voltera Flex-2 ink.

Effect of dielectric material on lifetime The effect of the dielectric material on the lifetime of the plasma source is assessed by comparing electrodes #2, #6 and #8. Figure 3.10 shows the microscope images of the simple electrode geometry printed on three different dielectric materials, which are Polypropylene, Kapton HN and Kapton MT, which have dielectric constants of $\varepsilon_r = 2.1$, $\varepsilon_r = 3.4$ and $\varepsilon_r = 4.2$ respectively. The electrodes for all three are printed using the Voltera Flex-2 ink and the thickness of the dielectric material is 75 μm.

The microscope images from the electrodes made using different dielectric materials, seen in Figure 3.10, show similar effects of erosion on the electrode material and damage to the dielectric material. Erosive spots can be identified on the printed electrode for all three dielectric materials after 1 minute of test time. Discolouration to the surface of the electrode material and to the dielectric material become visible from approximately 5 minutes onwards. Both erosion of the electrode material and damage to the dielectric

material become more pronounced with increasing test time. No major difference in electrode erosion and damage to dielectric material was determined.

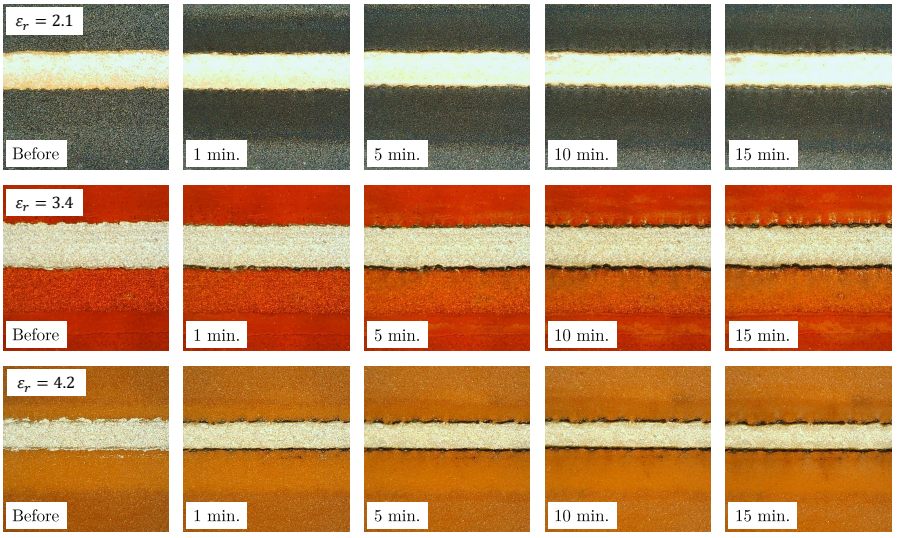

FIGURE 3.10: Microscope images comparing different dielectric material of varying dielectric constant, which are $\varepsilon_r = 2.1$, $\varepsilon_r = 3.4$ and $\varepsilon_r = 4.2$ (#8 #2 #6)

Effect of dielectric thickness on lifetime The effect of the dielectric thickness on the lifetime of printed plasma sources is determined by assessing four 1-D electrodes printed with the Voltera Flex-2 ink on Kapton HN dielectric material with various different thicknesses, which are 25 μm, 50 μm, 75 μm and 127 μm (Electrode IDs #7, #5, #2 and #4 respectively). Figure 3.11 shows the microscope images over a 15 minutes test time.

On the microscope images, large regions of erosion are visible after 1 minute of operation for a dielectric thickness of 25 μm. Dark spots of erosion at the edge region of the electrode and an overall discolouration of the electrode can be seen and become more pronounced with increasing operating time. Additionally, damage to the dielectric material is visible as darker regions, after test time of approximately 5 minutes. Electrode systems with a thicker dielectric material also show signs of electrode erosion and dielectric surface damage. However, the effects scale with the dielectric thickness. With an increase in dielectric thickness, the electrode erosion, both near the edge region and on the surface of the electrode, is minimised. The electrode systems using a 127 μm thick dielectric material show few erosion spots and less visible discolouration of the electrode. Additionally, less damage to the dielectric material can be seen with an increasing thickness of the dielectric material.

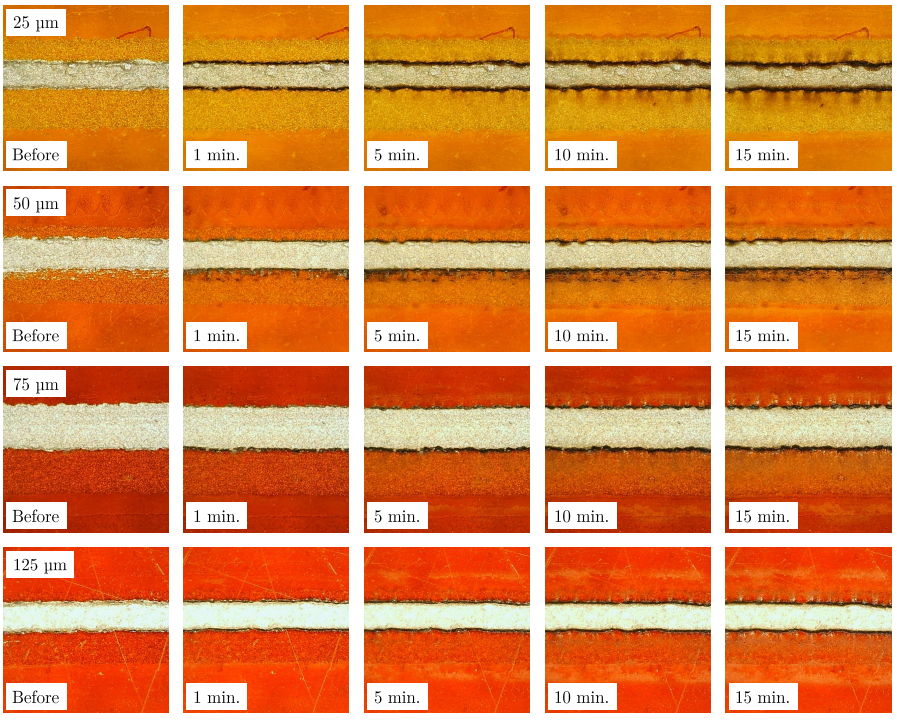

FIGURE 3.11: Microscope images comparing different dielectric thickness, which are 25 μm, 50 μm, 75 μm and 127 μm (IDs #7, #5, #2 and #4 respectively)

Main Findings on 1-D Line Electrode The study of the simplified 1-D line electrode has identified the effects of the key design parameters of printed plasma sources on their lifetime. Although electrode erosion and damage to the dielectric still occurred within the total operating test time of 15 minutes, a printed electrode using the Voltera Flex-2 ink on 75 μm Kapton HN dielectric material resulted in only moderate signs of erosion and damage. Therefore, this combination is selected as the preferred material combination for subsequent testing. Alleviation from the effect of erosion and damage can be achieved by applying protective coatings to the surface of the DBD plasma source, which act as an additional dielectric layer between the electrode, dielectric material and the high reactive species in the generated plasma.

3.2.1.2 Effectiveness of protective coating

The assessment of coating to protect the printed electrode surface from erosion and damage is carried out using a larger and more complex electrode geometry. Figure 3.12 shows a schematic and an image of the surface DBD plasma source using a hexagonal electrode pattern. An electrode covering a larger area allows for a better assessment of uniformity of the plasma generation across larger areas and the effect of the coating methods on such. One hexagonal unit of the of the electrode design measures 2 mm and the overall size of the plasma source is 441 mm^2. The geometry of the electrode pattern

can be found in Appendix A.1. The electrodes are printed using the Voltera Flex-2 ink on 75 μm Kapton HN dielectric material.

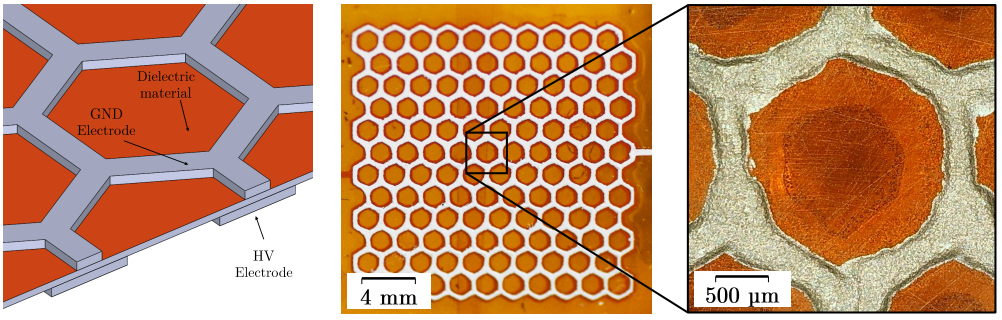

(a) (b)

FIGURE 3.12: (a) Schematic of hexagonal geometry electrode (b) Picture of hexagonal geometry electrode for lifetime analysis

Table 3.9 provides an overview of the fabricated surface DBD plasma sources. An uncoated plasma source is used as reference to assess electrode erosion and damage to the dielectric material. Four plasma sources are coated with the aerosol silicone resin coating (Modified Silicone Conformal Coating) and the coating is cured at ambient temperatures in 2 hours. Improved performance can be achieved with a subsequent heat cure at 90 °C. During the heat treatment, additional evaporation of the coating material takes place, thus increasing the resistance of the coating film. Consequently, a heat cured coating can show a high resistance to external factors, such as the bombardment of high-energy particles from a plasma. Three plasma sources underwent additional curing at 90 °C for 1 hour, 2 hours and 3 hours (IDs #11, #12 and #13 respectively). All plasma sources are operated at the same operating conditions of 4.2 kV at 6 kHz for a total operating test time of 15 minutes. The total test time is split up into 1 minute increments to retrieve the microscope image for the assessment of electrode erosion and damage on the dielectric material of the plasma source.

Electrode ID	Thickness	Coating	Curing
#9	75 μm	no	-
#10	75 μm	yes	2 h amb.
#11	75 μm	yes	2 h amb. + 1 h 90 °C
#12	75 μm	yes	2 h amb. + 2 h 90 °C
#13	75 μm	yes	2 h amb. + 3 h 90 °C

Table 3.9: Overview of fabricated hexagonal printed electrodes for coating assessment

Figure 3.13 shows microscopy images of the plasma sources without a protective coating layer. As can be seen, after one minute of operation dark spots of erosion appear

at the printed edge region. The surface of the electrode shows discolouration, which indicates erosive damage to the overall electrode surface. The dielectric material shows signs of damage from approximately 5 minutes test time onwards. These observations are similar to the findings in the microscope images of the 1-D line electrode. On the complex electrode geometry, the signs of electrode erosion and damage to the dielectric material also increase with ongoing test time.

FIGURE 3.13: Time series of microscopy images from plasma source using 75 μm Kapton HN without coating (Electrode ID #9)

Figure 3.14 shows a time series of microscope images from the surface DBD plasma source with the silicone resin coating applied. The coating is visible as a shiny and reflective layer, providing an even protective layer over the printed electrode and dielectric material. After one minute of operation, few dark spots of erosion can be identified in the edge region of the printed electrode. With increasing test time a few more erosion spots appear on the electrode edge and small regions of discolouration on the coating can be identified. These regions grow from spots of erosion on the electrode edge, normal towards the centre of the hexagonal unit. Stemming from the erosive spots, small particles of electrode and coating material are expelled and can be deposited on the top surface of the coating material, where they are visible as small circles of discolouration. After the total operating time of 15 minutes, some erosion spots can be seen at the electrode edge region, whilst the overall colour of the electrode only shows moderate change in colour. However, the severity of the erosion is less than compared to an uncoated plasma source.

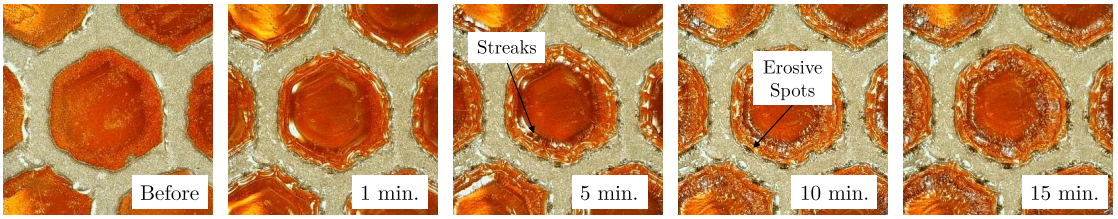

FIGURE 3.14: Time series of microscopy images from plasma source using 75 μm Kapton HN with silicone resin coating (Electrode ID #10)

Another effect observed in the microscope images is a change in the coating structure with extended test time. A change in coating distribution can be observed after 1 minute of operation, which is recognisable through a different reflective pattern of the coating on the microscope images. Further thin streak lines become visible in the coating after an operating time of approximately 5 minutes. These streak lines form perpendicular to the edge of the printed electrode. These lines are likely caused by strong electric field lines between the ground and high voltage electrode. Although the coating is cured at ambient temperature and forms a rigid layer, it has a lower density of 0.78 g/ml compared to the dielectric material with 1.42 g/ml. Thus, the coating materials remains softer and can align along strong electric field lines.

Figure 3.15(a) to 3.15(c) shows the times series of microscope images from printed electrodes with the coatings cured at 90 °C for 1, 2 and 3 hours, respectively. As can be seen, erosion spots become visible only after an operating time of 5 minutes. No major change to the structure of the coating material, such as streaks, are recognized prior to this time. Compared to a coating without heat curing, these microscope images show less sever signs of electrode erosion and damage to the dielectric material at a later test time. After the total operating time of 15 minutes, several eroded spots on the printed electrode edge and discoloured circles on the coating surface are visible on all three plasma sources. However, it can be seen that an increased curing time of 3 hours, provides the highest level of protection, indicated through fewer erosive spots and less surface damage to the coating material.

The analysis of protective coatings on printed plasma sources highlighted their importance to alleviate erosion on a printed electrode and damage to the dielectric material. Carrying out an additional heat curing procedure for the coatings at 90 °C for an increased time can further improve their performance, thus provides added protection on the electrode and improve the overall lifetime of printed plasma sources.

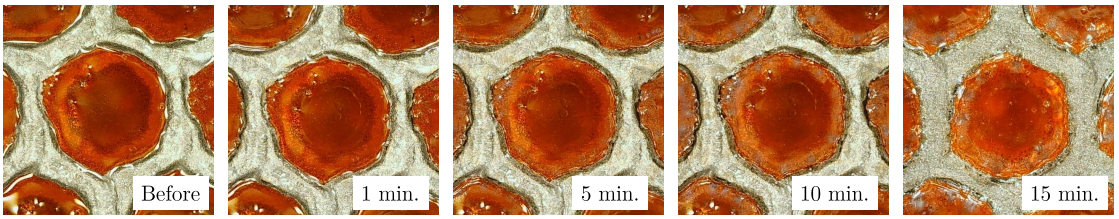

(a) 75 μm Kapton with coating 1h heat curing

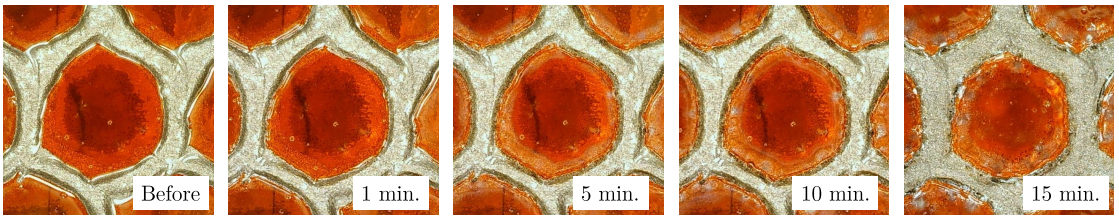

(b) 75 μm Kapton with coating 2h heat curing

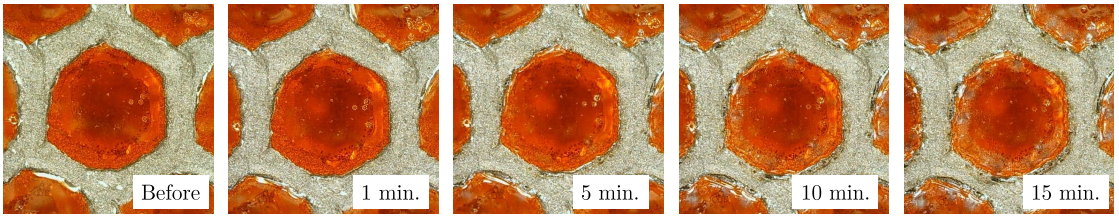

(c) 75 μm Kapton with coating 3h heat curing

FIGURE 3.15: Time series of microscopy images from plasma source using (a) 75 μm Kapton without coating (b) 75 μm Kapton with coating (c) 127 μm Kapton with coating cured at 90 °C for (a) 1 hour, (b) 2 hours (c) 3 hours

3.2.2 Operating conditions

Effect of operating conditions can play a crucial role in the design and optimization procedure of DBD plasma sources. It is therefore important to carry out a broad assessment of the DBD plasma source performance over a larger number of operating conditions, including the operating voltage and frequency. In this study, a sinusoidal waveform will be used with varying levels of operating voltage, ranging from 2 to 7 kV and operating frequencies ranging from 6 to 12 kHz. Table 3.10 provides an overview of the plasma sources analysed in this section. Additionally, Table 3.10 includes the obtained print precision scaling factor, f_{pp}, for each respective electrode system. The same hexagonal electrode design as in the previous section is used, see Figure 3.12. . The electrodes are printed on dielectric material, Kapton HN and Kapton MT, with varying thickness, ranging from 25 μm and 125 μm. All five electrodes are protected with an aerosol silicone resin coating (cured for 3 hours at 90 °C) to minimize electrode erosion and damage to the dielectric material during testing. Images of the fabricated plasma source can be found in Appendix B.1

Electrode ID	Material	Thickness	f_{pp}
#14	Kapton HN	25 μm	1.25
#15	Kapton HN	50 μm	1.32
#16	Kapton HN	75 μm	1.29
#17	Kapton MT	75 μm	1.32
#18	Kapton HN	127μm	1.30

Table 3.10: Overview of printed plasma sources for variation of operating condition testing

3.2.2.1 Electrical characteristics

Figure 3.16(a) shows the measured voltage and current at an operating voltage of 5 kV and a frequency of 8 kHz for a plasma source using a 75 μm thin Kapton HN dielectric material (electrode ID #16). The operating voltage follows the sinusoidal waveform and on the current waveform the active plasma region is clearly visible in the negative and positive half period. Figure 3.16(b) shows the voltage-charge characteristics, also known as the Lissajous graph, over one cycle for the corresponding operating conditions of 5 kV at 8 kHz. Additionally, the Lissajous graph for a different operating frequency of 10 kHz at the same operating voltage of 5 kV is shown. As can be seen, both Lissajous graphs align closely with each other, enclosing a similar area. This indicates that the dissipated energy per cycle is constant. Consequently, at constant voltages, the discharge power scales in proportional level with the operating frequency. An overview of Lissajous graphs can be found in Appendix C.1, where the Lissajous graphs are shown over varying operating conditions electrode exemplary for IDs #16.

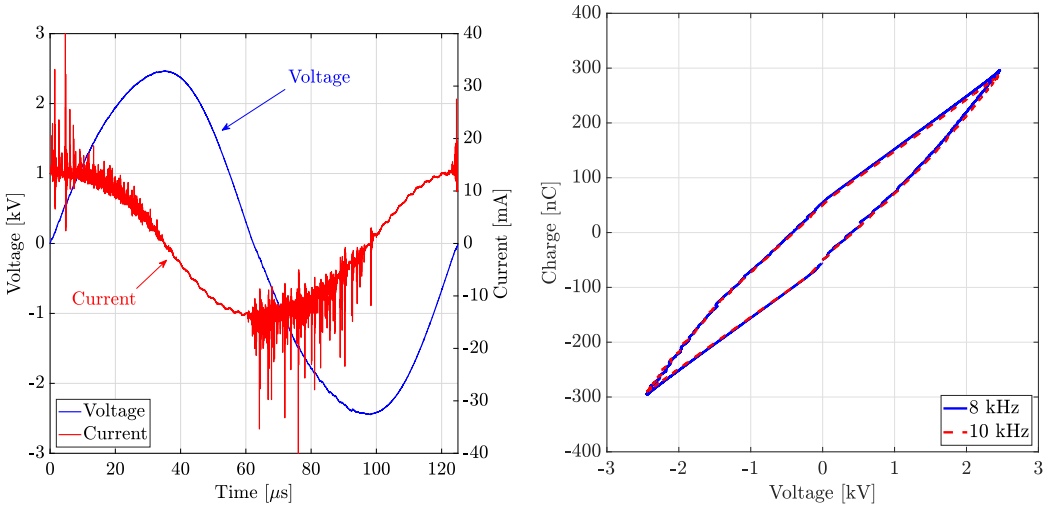

(a) (b)

FIGURE 3.16: Electrical Characteristics of printed plasma source using dispenser printing method: (a) Voltage and current measurements; (b) Lissajous graph

The Lissajous graph can be used to derive the discharge power as the area within the curve. Figure 3.17 shows the derived discharge power for electrode IDs #14 to #18 over varying operating voltages and frequencies. As can be seen for examples in Figure 3.17(a), plasma is generated from an operating voltage of approximately 2 kV onwards for all frequencies. With increasing voltage, the discharge power increases. Similarly, an increasing trend is seen for increasing operating frequency. The behaviour is observed for the other electrodes with varying dielectric thickness and material, electrode IDs #15 to #18 in Figure 3.17(b) to 3.17(e). Comparing the smallest voltage at which plasma is generated between the different electrodes, shows that an increasing voltage is needed for thicker dielectric materials. A thin dielectric material of 25 μm (ID #14 in Figure 3.17(a)) plasma is generated at operating voltages of approximately 2 kV. In contrast, a thicker dielectric material of 125 μm (ID #18 in Figure 3.17(e)) requires approximately 4 kV to initiate plasma generation. This behaviour is due to the local electric field strength on the plasma source surface, which reduces with an increasing dielectric thickness when the operating voltage remains constant. Consequently, a larger operating voltage is required to achieve a sufficiently strong local electric field for plasma generation.

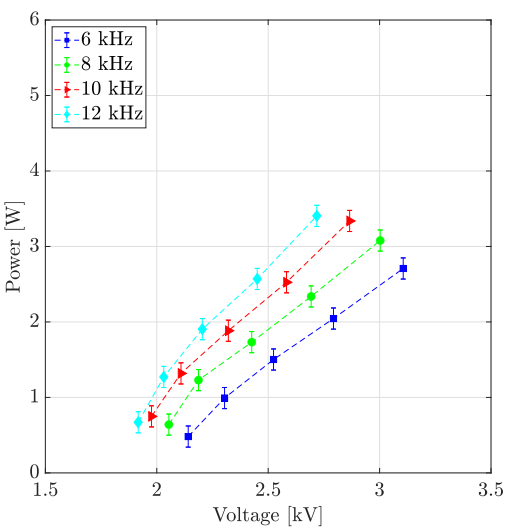

(a) 25 μm Kapton HN

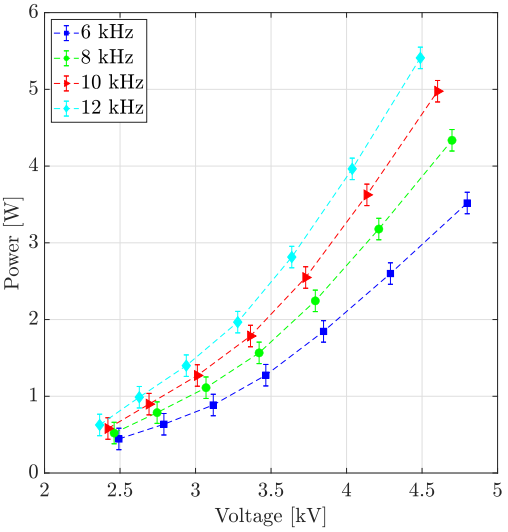

(b) 50 μm Kapton HN

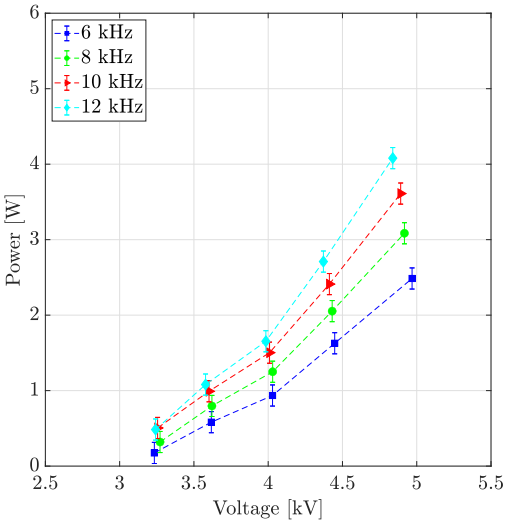

(c) 75 μm Kapton HN

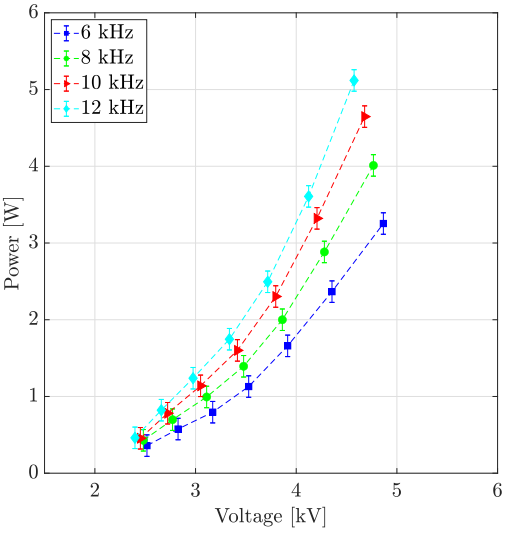

(d) 75 μm Kapton MT

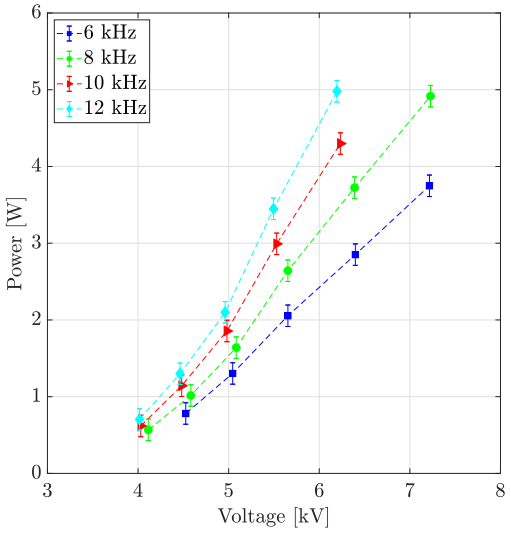

(e) 125 μmKapton HN

FIGURE 3.17: Measured average discharge power, P_{est}, for printed plasma sources using varying dielectric substrates: (a) 50 μm Kapton HN, (b) 50 μm Kapton HN, (c) 75 μm Kapton HN, (d) 75 μm Kapton MT, (e) 75 μm Kapton HN

Figure 3.17(c) and 3.17(d) shows the discharge power from plasma sources using two different dielectric materials, which are Kapton HN ($\varepsilon_r = 3.4$) and Kapton MT ($\varepsilon_r = 4.2$). It can be seen that the plasma source using a dielectric material with a larger dielectric constant results in a larger discharge power at the same operating voltage and frequency. This is linked to the difference in dielectric constant and the resultant local electric field strength. As the dielectric constant is linearly proportional to the capacitance, a plasma source using Kapton MT as dielectric material has a larger capacitance. With this increase in capacitance, the local electric field reduces and the discharge power is increased.

The comparison between plasma source with different dielectric thicknesses and materials show a slight variation in trend of the operating power with increasing voltage. A plasma sources with a thinner dielectric tends to follow a more linear trend, whereas a plasma source with a thicker dielectric follows a more exponential trend. This behaviour could indicate a difference in plasma generation regime, which in turn has an influence on the charge transfer, thus the discharge power. However, a definitive assessment of a specific discharge regime requires a more detailed optical analysis of the generated plasma.

The discharge power can be modelled using a power law, as proposed in several literatures [86, 104–108]. The power scaling law provides a tool for the estimation of the discharge power based on the operating and design parameters of the plasma source. The dependency on, for example the operating voltage is described in literature as a power law following:

$$P_{ave} \propto V_{pp}^{a} \quad \text{with} \quad 1 < a < 3.5 \tag{3.3}$$

where P_{ave} is the average discharge power normalised [86, 104–108]. Exponents of the power law ranging from 1 to 3.5 are reported in literature and can be a result of varying material, electrode geometry or also experimental setup.

The relationship between discharge power and operating frequency has often been described as a linear relationship ($P_{ave} \propto f$) by most research groups [104, 105, 107–110]. A large proportion of the proposed power scaling laws are presented from the flight actuator community [88, 111]. These applications often use simple 1-D line electrodes generating plasma to introduce a force vector on airfoils for improved performance. Within the community, a comparison between different 1-D line electrodes is performed by defining the discharge power per unit length, P_L as:

$$P_L = \frac{P_{ave}}{L} \tag{3.4}$$

where the L is the length of the tested 1-D line electrode. This normalisation is fundamentally a normalisation by capacitance, due to the proportionality of the capacitance to the electrode area and therefore the length ($C \propto A \propto L$). The plasma sources in this study do not follow a simple 1-D line geometry, but are of a complex electrode geometry.

Therefore, this study uses the complete capacitance, C, of a plasma source to propose a new power scaling law for complex geometries. The relationship between discharge power, capacitance, operating voltage and frequency is described in the scaling number, Θ_P, as:

$$\Theta_P = \frac{P_{ave}}{f \cdot C \cdot V_{pp}} \tag{3.5}$$

where f is the operating frequency, C the capacitance of the plasma source and V_{pp} the operating voltage. The scaling number, Θ_P, accounts for the variation of dielectric thickness and material through the capacitance, C, for each developed electrode, which can be calculated as:

$$C = \varepsilon_0 \cdot \varepsilon_r \cdot \frac{A \cdot f_{pp}}{t} \tag{3.6}$$

where ε_0 is the permittivity of vacuum, ε_r is the permittivity of the dielectric material, A is the total area of the electrode geometry, t is the thickness of the dielectric material and f_{pp} the print precision factor. The total printed electrode area is ideally the same for all printed plasma sources analysed within in this study, as the electrode geometry is constant. However, as presented in section 2.2.2.1, the actual printed electrode geometry deviates from the theoretical geometry due to print imprecisions. To account for these geometry deviations, the print precision factor, f_{pp}, is added to the area definition in the capacitance calculation.

Figure 3.18 shows the scaling number, Θ_P, over the applied voltage for electrode IDs #16 to #18 for all operating frequencies. As can be seen, the curves for all five tested electrodes over the full envelope of operating conditions collapses onto one trend line. It can be seen that for each electrode, some data points at lower operating voltages fall slightly below the overall trend line. This is likely due to the non-uniform plasma generation at the tested conditions. At these low operating voltages, plasma is not yet uniformly generated over the full surface of the plasma source. This can affect the calculation of the discharge power, since the plasma itself acts as a current source during operation, and thus significantly affects the electrical characteristics of the plasma source.

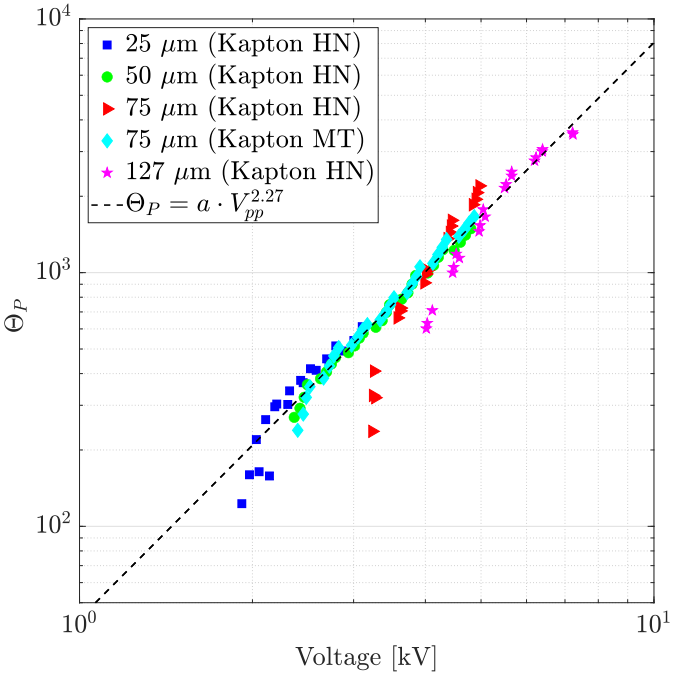

FIGURE 3.18: Scaling number, Θ_P against operating voltage for DBD plasma source with varying dielectric thickness and material

The trend shown in Figure 3.18 can be approximated through a power law as:

$$\Theta_P \approx 6.65 \cdot V_{pp}^{2.27} \tag{3.7}$$

where V_{pp} is the operating voltage. The approximation has a coefficient of determination of $R^2 = 0.96$, thus a high degree of confidence. The approximation for Θ_P in equation 3.7 can be combined with the definition for the scaling number, Θ_P, in equation 3.5 as:

$$\Theta_P = \frac{P_{ave}}{f \cdot C \cdot V_{pp}} \approx 6.65 \cdot 10^{-6} \cdot V_{pp}^{2.27} \tag{3.8}$$

Rearranging and solving equation 3.8 provides an estimation of the discharge power, P_{est}, in terms of the operating conditions (f and V_{pp}), and design parameters of the plasma source (C calculated through t and ε_r) as:

$$P_{est} \approx 6.65 \cdot f \cdot C \cdot V_{pp}^{3.27} \tag{3.9}$$

Equation 3.9 proposes a proportionality between discharge power, operating and design parameters of printed plasma sources. The estimated discharge power is described as a linear relationship to the operating frequency, f, due to the proportionality $P_{est} \propto f$. Similarly, the capacitance, C, influences the estimated discharge power in a linear correlation due to the proportionality $P_{est} \propto C$. The relationship between the estimated discharge power and the operating voltage, V_{pp}, is described through a power law with

the exponent of 3.27 and therefore a proportionality of $P_{est} \propto V_{pp}^{3.27}$. Thus, the operating voltage is identified as the most influential parameter amongst the included operating (V_{pp} and f) and design parameters (t and ε_r) of plasma sources. These proportionality relationships can be taken into account for a prediction of the discharge power in the design and optimization procedure of printed DBD plasma sources.

Figure 3.19 shows the measured discharge power, as previously shown in Figure 3.17. In addition, the estimated discharge power, P_{est}, using equation 3.9 is plotted, to confirm the modelling of the discharge power through a scaling law. As can be seen, the estimated discharge power, P_{est}, shows good agreement with the measured discharge power. This behaviour is expected, as the presented data set is directly used to retrieve the estimated discharge power, P_{est}, in equation 3.9. The robustness of the estimated discharge power, P_{est}, through the scaling law will be demonstrated further in the following sections 3.2.3 and 3.2.4, where the scalability and flexibility of printed plasma sources are assessed.

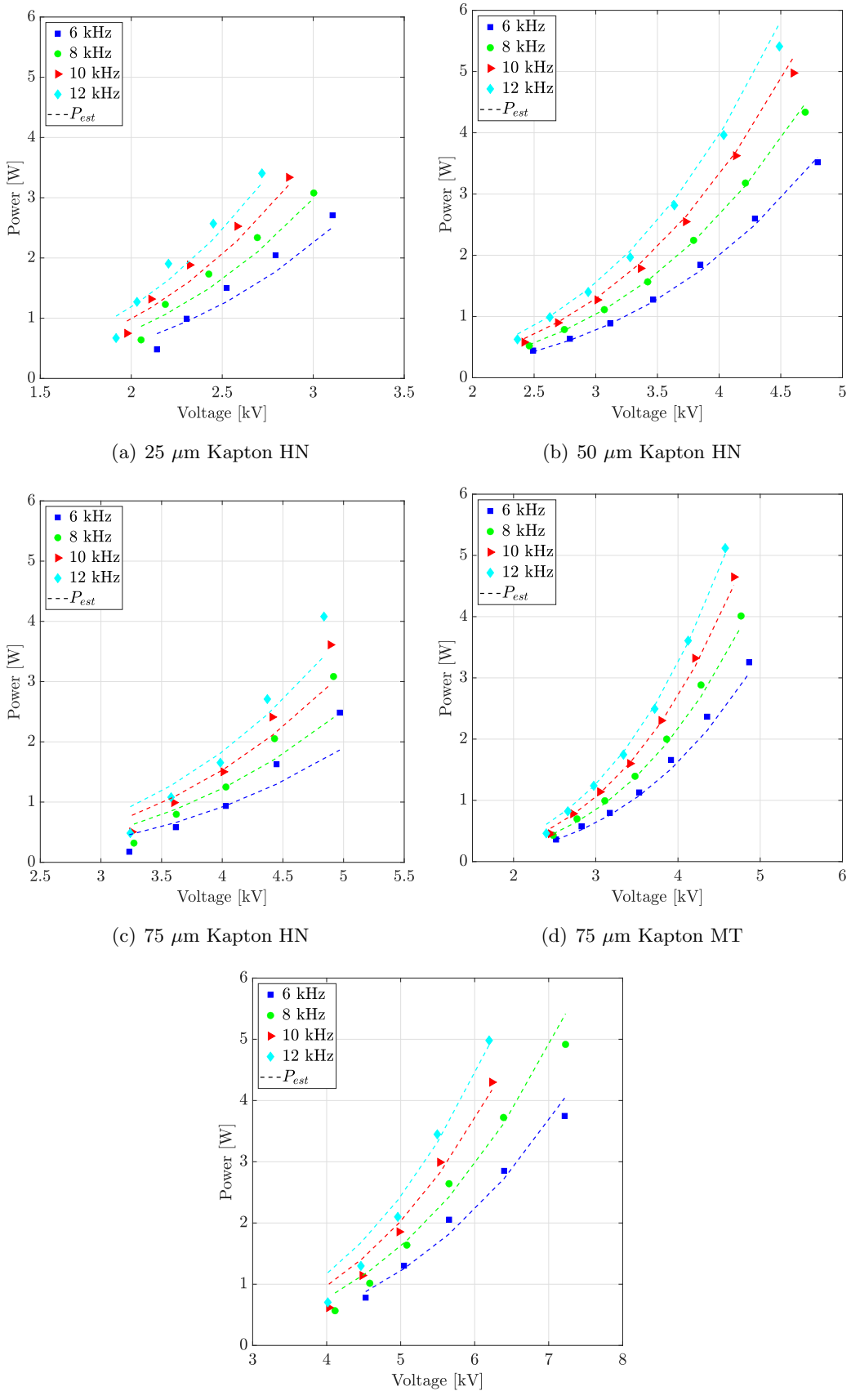

(a) 25 μm Kapton HN

(b) 50 μm Kapton HN

(c) 75 μm Kapton HN

(d) 75 μm Kapton MT

(e) 125 μm Kapton HN

FIGURE 3.19: Estimated discharge power, P_{est}, for printed plasma sources using varying dielectric substrates: (a) 50 μm Kapton HN, (b) 50 μm Kapton HN, (c) 75 μm Kapton HN, (d) 75 μm Kapton MT, (e) 75 μm Kapton HN

3.2.2.2 Optical characteristics

The optical diagnostics can be used to assess the intensity of the generated plasma on the printed DBD systems. Figure 3.20 shows the emission images of the generated plasma produced by the printed plasma source using a 75 μm Kapton HN dielectric material at 6 kHz over varying operating voltages. The images shown in Figure 3.20 shall serve as an example to qualitatively assess the plasma generation over the electrode and the trend with increasing operating voltage. As can be seen in Figure 3.20, at a low operating voltage of 3.2 kV, the plasma is not generated uniformly over the electrode yet. The majority of the electrode area is only showing very weak or no plasma generation. With increasing operating voltage up to 3.6 kV, plasma is generated across the full electrode. Further increasing operating voltage shows an increase in intensity of the generated plasma.

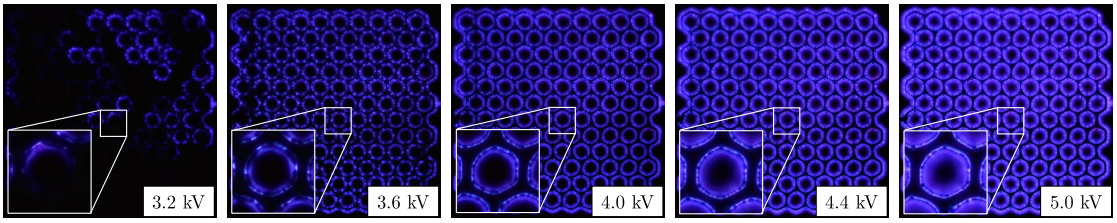

FIGURE 3.20: Emission images of electrode using 75 μm Kapton HN at 6 kHz for varying operating voltages

A detailed view in Figure 3.20 shows the plasma generation in one hexagonal unit. As can be seen at low operating voltages of 3.2 kV, a weak plasma is generated near some edges of the printed electrode. This area, the edge region of the printed electrode is characterised through a strong electric field, thus plasma will start forming here first. With increasing operating voltage, plasma is generated around all edges. Increase of the operating voltage, results in a growing electric field strength reaching further in the centre of the hexagonal unit. Thus plasma will start forming further in the centre. At an operating voltage of 5 kV it can be seen that the plasma generation stretches much further into the centre of the hexagonal unit, in comparison to a low operating voltage for example at 3.6 kV.

The emission images of the printed electrodes (ID#14 to #18) are used to quantify the image intensity, I_{img}. As presented in section 2.4.2.1 the image intensity, I_{img}, is used to quantified the overall plasma intensity. The uniformity of the plasma generation, σ_{img}, is derived as the standard deviation of the image intensity across the total number of observed hexagons. Thus the uniformity is shown as the errorbars and provides a measure of the uniformity of the plasma generation across the electrode.

Figure 3.21 shows the image intensity, I_{img}, over the applied power for the printed electrodes using Kapton HN and Kapton MT of varying thickness. As can be seen, the image intensity increases with increasing operating power for all dielectric thicknesses and materials. At small operation powers, a steep increase in image intensity is shown, whereas the trend flattens with increasing power. With an increase in power, the electric field grows closer to the centre of a hexagonal units. Consequently, the central region is characterised through a colliding electric field from all edges of the electrode. Thus the electric field strength can not grow further and plasma generation stagnates, indicated by a flattening trend in the image intensity.

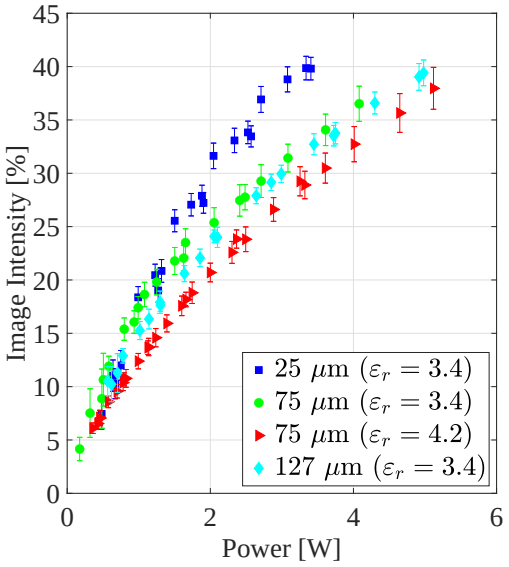

FIGURE 3.21: Image Intensity against power for DBD plasma source with varying dielectric thickness and material

The image intensity is a measure of the plasma intensity and in literature a correlation between emission intensity and operating voltage has been reported [88, 112]. In this study a correlation between the operating power, P_{ave}, and the image intensity, I_{img}, is observed, which can be interpreted as an efficiency of the DBD plasma source. The power is the energy input into the electrode systems, whereas the obtained image intensity is related to the plasma intensity. Thus the relationship indicates how much of the input energy has been converted into plasma. The correlation of operating power, P_{ave}, and the image intensity, I_{img}, can be described using a power law as:

$$I_{img} = f(P_{ave}) = \alpha \cdot (P_{ave})^n \tag{3.10}$$

This power law can be used to describe the trend of the image intensity, I_{img}, for electrode using varying dielectric thicknesses and materials. Figure 3.21 shows these trend lines, with the coefficients α and n being listed in table 3.16. Additionally, the

respective coefficient of determination, R^2, is listed, which indicates the confidence of the respective fit.

	25 μm Kapton HN	75 μm Kapton HN	75 μm Kapton MT	125 μm Kapton HN
α	17.01	16.61	12.66	15.13
n	0.74	0.57	0.69	0.61
R^2	0.99	0.99	0.99	0.99

Table 3.11: Scaling parameter from $I_{img} = \alpha \cdot (P_{ave})^n$ for plasma sources of varying dielectric thickness and material

The coefficient listed in Table 3.11 can be used to compare the efficiency of the respective electrode system. A similar efficiency, thus conversion of input power (P_{ave}) into generated plasma intensity (measured through I_{img}), is achieved when the coefficient α is constant. An increasing value of α relates to a steeper curve, relating to a higher plasma intensity and thus indicating a better efficiency of the electrode systems.

As can be seen in Table 3.11, the coefficient α is largest for the electrode systems with a 25 μm dielectric with a value of 17.01 . With increasing thickness, the coefficient decreases down to values of 16.61 and 15.13 for an electrode systems with a 75 μm and 125 μm dielectric respectively. Thus, the efficiency of an electrode systems scales with the dielectric thickness. A similar behaviour is seen when comparing the dielectric material. The coefficient α decreased from a value of 16.61 for an electrode with dielectric material Kapton HN (ε_r=3.4) down to a value of 12.66 for the electrode with the dielectric material Kapton MT (ε_r=4.2) respectively. This decrease indicates a lower efficiency in the electrode system using the dielectric with a higher dielectric constant.

An additional approach to quantify the plasma intensity can be achieved through measurement of the spectral intensity. The spectral intensity is calculated as an average intensity over the second positive and first negative system of the nitrogen emission peaks in the recorded emission spectra. Thus the spectral intensity provides an indication of the plasma strength. Figure 3.22 shows the recorded total spectral intensity over the applied power for the printed plasma sources using Kapton HN and Kapton MT of varying thickness. As can be seen, the spectral intensity scales with the applied operating power, indicating increasing plasma strength for increasing applied power.

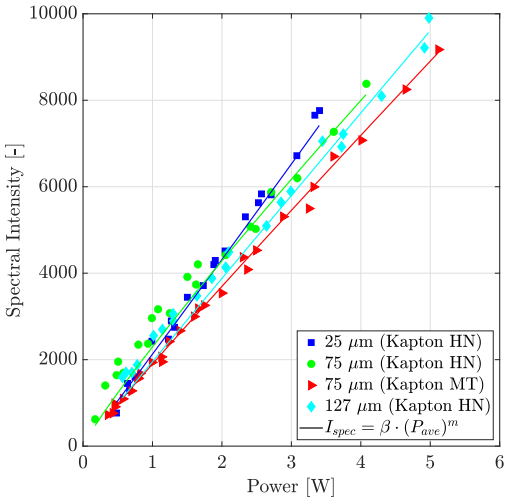

FIGURE 3.22: Spectral Intensity against power for DBD plasma source with varying dielectric thickness and material

The correlation of spectral intensity, I_{spec}, to the operating power, P_{ave}, can be similarly expressed through a power law as:

$$I_{spec} = \beta \cdot (P_{ave})^m \tag{3.11}$$

Similarly, this power law can be used to describe the trend of the spectral intensity, I_{img}, for electrodes using varying dielectric thicknesses and materials. Figure 3.22 shows these trend lines, with the coefficients β and m being listed in Table 3.12.

	25 μm Kapton HN	75 μm Kapton HN	75 μm Kapton MT	125 μm Kapton HN
β	2352	2185	1917	2084
m	0.95	0.97	0.96	0.93
R^2	0.99	0.97	0.99	0.99

Table 3.12: Scaling parameter from $I_{spec} = \beta \cdot (P_{ave})^m$ for plasma sources of varying dielectric material

Table 3.12 shows that the exponent of the power law $I_{spec} = \beta \cdot (P_{ave})^m$ is close to 1, indicating a near linear relationship of the power to the spectral intensity. The coefficient β allows a comparison of the efficiency of the respective electrode system. The coefficient β is largest for the electrode systems with a 25 μm dielectric with a value of 2352. With increasing thickness, the coefficient decreases down to 2185 and 2084 for an electrode systems with a 75 μm and 125 μm dielectric respectively. A similar decrease in the coefficient β is seen in relation to the dielectric material. The coefficient β decreases from 2185 to 1917 for an electrode with dielectric material Kapton HN (ε_r=3.4) and Kapton MT(ε_r=4.2) respectively.

These trends of the spectral intensity for varying dielectric thickness and materials, are similar to trends observed for the image intensity. Therefore, the trends can be equally interpreted as the efficiency of the respective DBD plasma source. The efficiency of an electrode systems increases with decreasing dielectric thickness and decreasing dielectric constant. Both parameters, dielectric thickness, t, and dielectric constant, ε_r, affect the capacitance of the DBD plasma source. Thus it can be concluded, that the efficiency of the electrode system is proportional to the capacitance of an electrode system. An electrode system with a lower capacitance, for example through a thinner dielectric, has shown higher efficiency. However, it has to be noted that a thinner dielectric also suffers from an increasing level of erosion, as has been observed in the microscope images in the previous section. A high level of erosion can result in a reduced lifetime of the electrode system. For the design optimization of an electrode system both, the efficiency of the system but also lifetime of the electrode have to be accounted for.

3.2.3 Scalability

For the following scalability assessment, two aspects of scaling are considered. Figure 3.23 shows a schematic of the printed plasma sources with different length and area scales. The plasma sources of varying length scale consist of a row of connected hexagonal units with a unit size of 2 mm. Four different length scales of plasma sources are fabricated, which are 10 mm, 20 mm, 40 mm and 80 mm. For the area scaling assessment, three different plasma sources are fabricated, where the hexagonal units are arranged over a square area of 10 mm x 10 mm, 20 mm x 20 mm and 40 mm x 40 mm, covering a total area of 100 mm^2, 400 mm^2 and 1600 mm^2 respectively. The electrode geometries can be found in Appendix A.1 and images of the fabricated plasma source can be found in Appendix B.2.

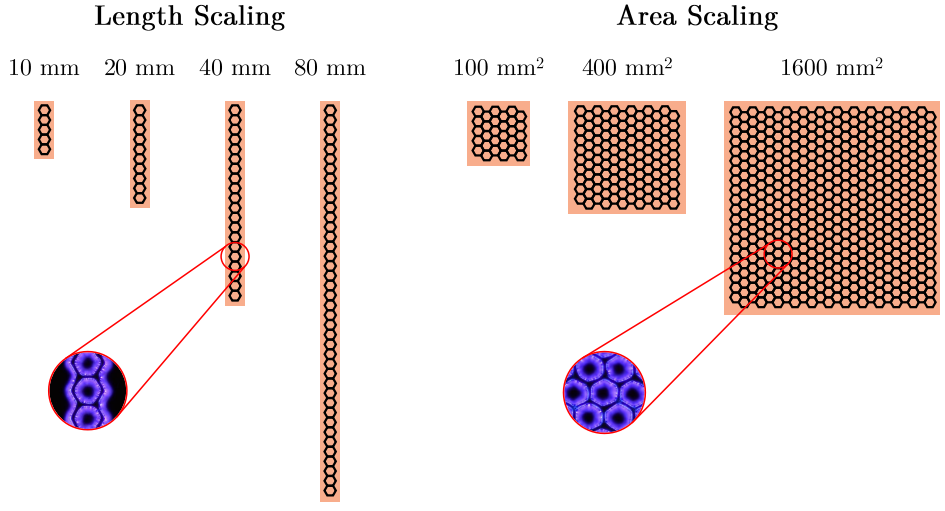

FIGURE 3.23: Schematic of scalability assessment with two aspects, length and area scaling

Table 3.13 provides an overview of the fabricated plasma sources for the scalability assessment. All plasma sources are printed on Kapton HN dielectric material with a thickness of 75 μm with silver ink using the dispenser printer method. The hexagonal geometry of the ground electrode is printed with a linewidth of 0.3 mm and the high voltage electrode with a linewidth of 0.6 mm. All fabricated plasma sources are coated with a protective aerosol silicone resin coating, which is cured at 90 °C for 3 hours to improve the protective quality of the coating. All tests are carried out at a constant frequency of 6 kHz and with varying operating voltages.

Electrode ID	Geometry	Dimensions	f_{pp}
#19	Line	10 mm	1.03
#20	Line	20 mm	1.11
#21	Line	40 mm	1.10
#22	Line	80 mm	1.22
#23	Square	10 mm x 10 mm	1.03
#24	Square	20 mm x 20 mm	1.22
#25	Square	40 mm x 40 mm	1.19

Table 3.13: Overview of fabricated plasma sources of different length and area scales

3.2.3.1 Electrical characteristics

Figure 3.24 shows the derived discharge power for different lengths of the fabricated printed plasma sources over varying operating voltages. As can be seen, the discharge power follows an increasing trend with increasing operating power. Longer plasma sources show a larger discharge powers. The dotted line shows the estimated power, P_{est}, using the derived equation 3.9 from the previous section. As can be seen, the estimated discharge power matches the measured discharge power well, demonstrating the robustness of the prediction method using equation 3.9.

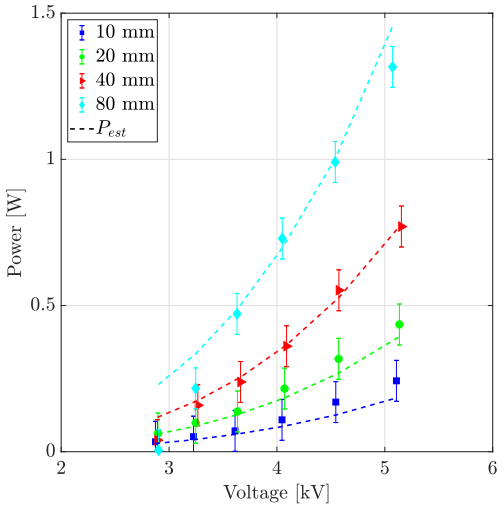

FIGURE 3.24: Discharge power, P_{ave}, for plasma sources with varying length

Figure 3.25 shows the discharge power per unit length P_L in [W/m] for all four electrodes of varying lengths. As can be seen, the discharge power per unit length follows a constant trend over varying operating voltage for the different length scales of the fabricated plasma sources. This is due to the scaling of the discharge power with the capacitance of the plasma source. For the presented plasma sources (IDs #19 to #23), the capacitance scales with the area of the electrodes, as the remaining parameters for the capacitance calculation (thickness t and relative permittivity ε_r) remain constant in this scalability study. Consequently the length is the only variable parameter affecting the capacitance, thus the power per unit area remains constant.

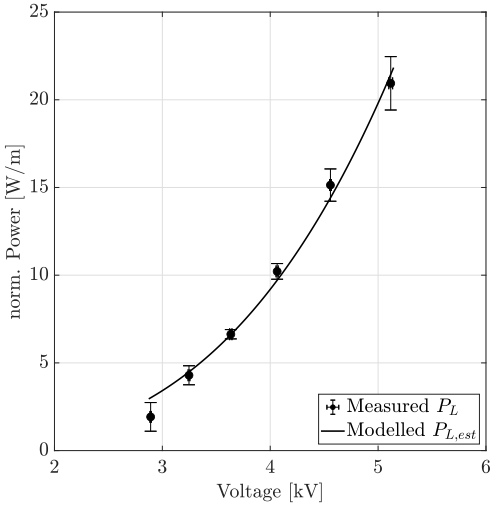

FIGURE 3.25: Discharge power per unit length, P_L, of plasma sources with varying length

The correlation of discharge power per unit length, P_L, and voltage can also be expressed over a power law as:

$$P_{L,est} \propto (V_{pp})^{3.35} \tag{3.12}$$

This proportionally follows a power law with an exponent of 3.35. This is similar to the correlation presented in the estimated power, P_{est}, using equation 3.9 from the previous section, where exponent was concluded to be 3.27. Therefore, the concluded correlation of $P_{L,est} \propto (V_{pp})^{3.35}$ shown in Figure 3.25 is good agreement with power estimation presented in the previous section.

Figure 3.26 shows the discharge power for varying area sized plasma sources. Here a similar behaviour can be seen, with the discharge power following an increasing trend for varying area sized of the plasma sources. A plasma source with a larger area has a higher discharge power. This can be attributed again to the scaling effect through the electrode area. A larger area results in an increased capacitance, thus an increased

discharge power. The dotted line shows the estimated discharge power using equation 3.9, which provides a satisfactory fit to the measured discharge power.

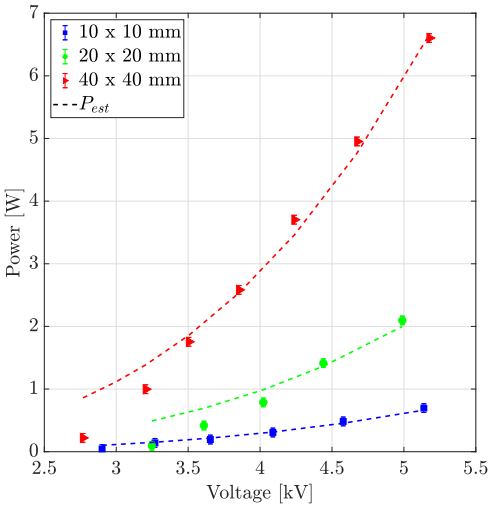

FIGURE 3.26: Discharge power, P_{ave}, for plasma sources with varying area

Figure 3.27 shows the discharge power per unit areas P_A in kW/m^2, for the three different sizes of plasma sources. As can be seen, the discharge power per unit area follows a constant trend for the different sizes of the plasma source. The correlation of discharge power per unit length, P_A, and voltage can again be expressed using a power law as:

$$P_{A,est} \propto (V_{pp})^{3.45} \tag{3.13}$$

The correlation follows a power law with an exponent of 3.45, which is larger than the exponent of 3.27 used in the calculation for the estimated power, P_{est}, in equation 3.9 from the previous section. This deviation can be likely traced back to the larger proportion of print imprecision across larger areas. The used printing procedure is able to generate small patterns at high print precision, however with increasing area of the printed electrode, imprecision become more common. This is due to the flexible dielectric material, which is taped down during the printing procedure. A larger flexible dielectric material is more susceptible to warping, which can consequently lead to a varying linewidth throughout the printed electrode.

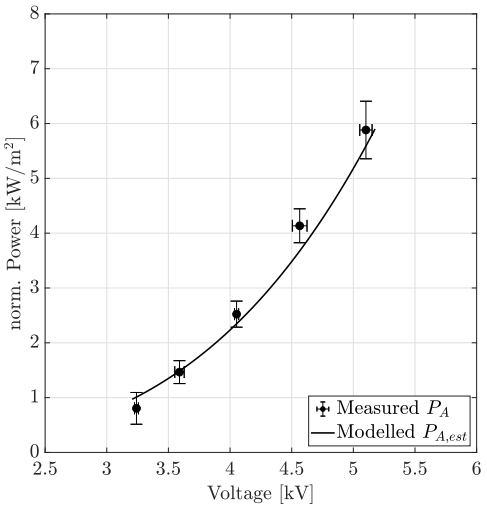

FIGURE 3.27: Discharge power per unit area, P_A, of plasma sources with varying area

3.2.3.2 Optical characteristics

Optical diagnostics on the DBD plasma sources are used to assess the intensity of the generated plasma. Figure 3.28 shows the recorded emission images of the different length scales at an operating voltage of 5.1 kV. The images only show a small section of the actual full electrode. As can be seen, the plasma forms similarly across hexagonal electrodes of different length scales.

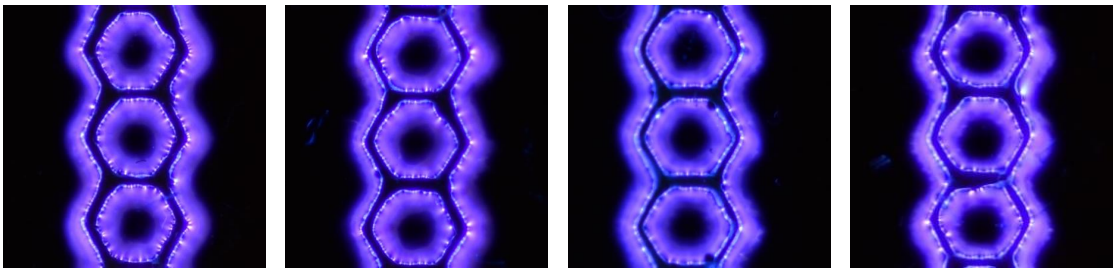

FIGURE 3.28: Emission images of plasma sources with varying lengths at an operating voltage of 5 kV

The recorded emission images are used to derive the image intensity across the different length scales of the printed plasma sources. Both image intensity, I_{img}, and uniformity, σ_{img}, are derived using a similar approach to that presented in the previous section. Figure 3.29 shows the image intensity derived from different length scales of plasma sources over the discharge power per unit length, P_L. As can be seen, the image intensity increases with increasing power, P_L.

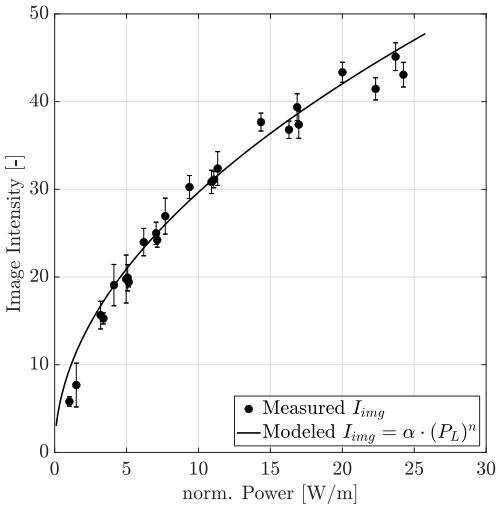

FIGURE 3.29: Image intensities, I_{img}, over power per unit length, P_L, on plasma sources of varying lengths

The correlation between the power per unit length, P_L, and the image intensity, I_{img}, has previously been interpreted as an efficiency of the plasma source. The power is the energy input into the electrode systems and the image intensity is related to the plasma intensity, thus how much of the input energy has been converted into plasma. Similarly, the correlation of operating power per unit length, P_L, and the image intensity, I_{img}, can be described using a power law as:

$$I_{img} = f(P_L) = \alpha \cdot (P_L)^n \tag{3.14}$$

The power law can be used to describe the trend of the image intensity, I_{img}, for electrodes of varying lengths. Figure 3.29 shows these trend lines, with the coefficients α and n being listed in table 3.14.

	10 mm	20 mm	40 mm	80 mm
α	8.79	9.37	8.39	10.38
n	0.51	0.53	0.56	0.54
R^2	0.99	0.99	0.99	0.98

Table 3.14: Scaling parameter from $I_{img} = \alpha \cdot (P_L)^n$ for plasma sources of varying lengths

Table 3.14 shows that the coefficients of the power law from equation 3.14 for plasma sources of varying lengths. It can be seen that the exponent, n, ranges between 0.51 and 0.56. This is in good agreement with the exponent observed for a plasma source with 75 μm Kapton HN as dielectric material, which is 0.57 (see table 3.11). The coefficient α allows a comparison of the efficiency of the respective electrode system. A similar level of efficiency is achieved when the coefficient α remains constant for varying lengths of a plasma source. As can be seen, the coefficient α ranges between 8.39 and 10.38, with a standard error of 8 %. This indicates that plasma sources of varying lengths

are of similar efficiencies. Therefore, good scalability of printed plasma sources can be concluded through the assessment of the image intensity.

A similar assessment of the plasma intensity and efficiency of a plasma source can be carried out using the spectral intensity, I_{spec}. Figure 3.30 shows the obtained spectral intensity on plasma sources of different length scales. As can be seen, the spectral intensity scales with the power per unit length.

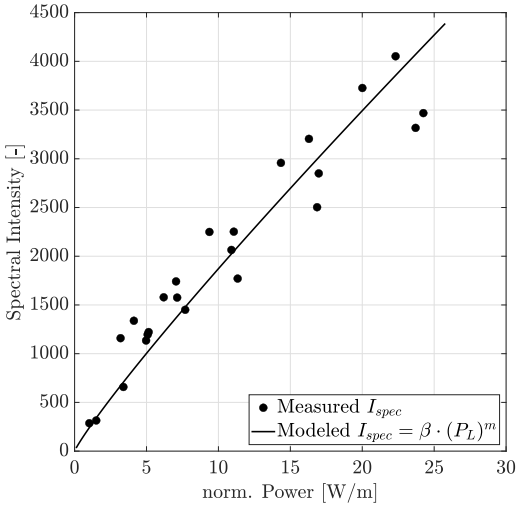

FIGURE 3.30: Image intensities, I_{spec}, over power per unit length, P_L, on plasma sources of varying lengths

A power law is again used to describe the correlation of spectral intensity, I_{spec}, and power per unit length, P_L, as:

$$I_{spec} = \beta \cdot (P_L)^m \tag{3.15}$$

Table 3.15 lists the respective coefficients β and m. The exponent, m, ranges between 0.92 and 0.97, which is in good agreement with the exponent observed in the previous sections for a plasma source with 75 μm Kapton HN as dielectric material, which is 0.97 (see Table 3.12). The coefficient β ranges between 216 and 269 with a standard error of 9 %. This indicates similar efficiency for plasma sources of varying lengths and is in accordance with the observation of the image intensity, I_{img}.

	10 mm	20 mm	40 mm	80 mm
β	216	259	269	266
m	0.95	0.97	0.92	0.91
R^2	0.94	0.96	0.96	0.97

Table 3.15: Scaling parameter from $I_{spec} = \beta \cdot (P_L)^m$ for plasma sources of varying lengths

In addition to the line scalability, the area scalability is assessed using plasma sources of three different areas. Figure 3.31 shows the recorded emission images of plasma sources with three different area scales at an operating condition of 5.1 kV. The images show only a small section of the actual full image of the electrode. It can be seen that the plasma generates uniformly across the shown electrode region over different area scales.

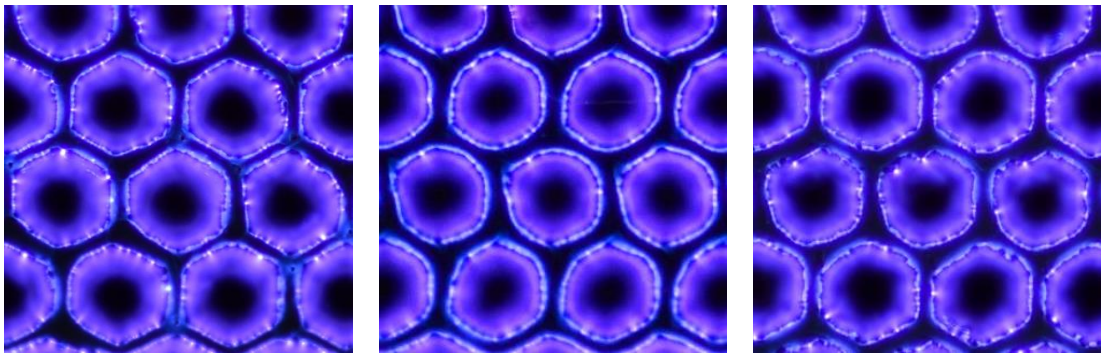

FIGURE 3.31: Emission images of plasma sources with varying area at an operating voltage of 5 kV

The recorded emission images are used to derive the image intensity across the different area scales of the printed plasma sources. Figure 3.32 shows the image intensity derived from different area scales of plasma sources over the discharge power per unit area, P_A. As can be seen, the image intensity increases with increasing power per unit area, P_A.

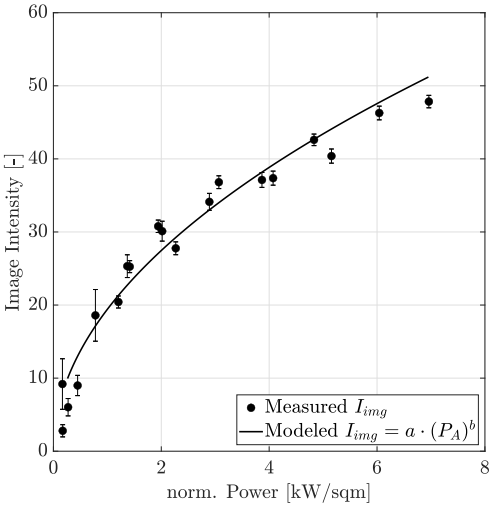

FIGURE 3.32: Image intensities, I_{img}, over power per unit area, P_A, on plasma sources of varying area

The correlation is again described using a power law show in Figure 3.32 and is defined as:

$$I_{img} = f(P_A) = \alpha \cdot (P_A)^n \tag{3.16}$$

Table 3.16 lists the respective coefficients, α and n, for the plasma sources of varying areas. The exponent, n, ranges between 0.49 and 0.56. This is in good agreement with the exponent observed for a plasma source with 75 μm Kapton HN as dielectric, which is 0.57 (see table 3.11). The coefficient α is again used as indicator of efficiency of the respective electrode system. As can be seen, the coefficient α ranges between 17.51 and 19.6 with a standard error of 7 %. This indicates that plasma sources of varying areas are able to generate a similar plasma intensity per power per unit area.

	10 mm x 10 mm	20 mm x 20 mm	40 mm x 40 mm
α	19.6	17.51	19.7
n	0.49	0.56	0.50
R^2	0.92	0.99	0.96

Table 3.16: Scaling parameter from $I_{img} = a \cdot (P_A)^n$ for plasma sources of varying area

A similar assessment of the plasma intensity and efficiency of a plasma source can be carried out using the spectral intensity, I_{spec}. Figure 3.33 shows the spectral intensity on plasma sources of different area scales. As can be seen, the spectral intensity scales with the power per unit area, P_A.

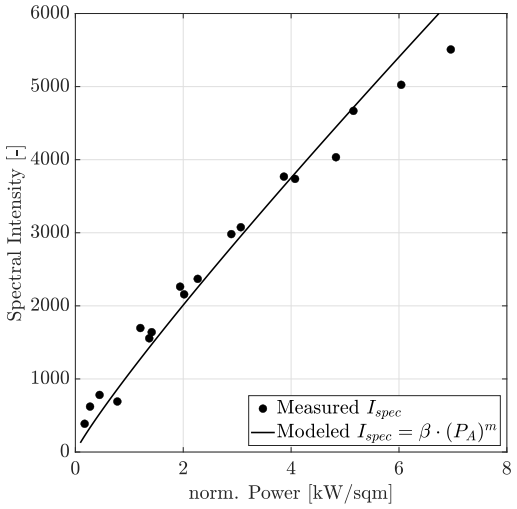

FIGURE 3.33: Image intensities, I_{spec}, over power per unit area, P_A, on plasma sources of varying area

A power law is again used to describe the correlation of spectral intensity, I_{spec}, and power per unit area, P_A, as:

$$I_{spec} = \beta \cdot (P_A)^m \tag{3.17}$$

Table 3.17 lists the respective coefficients. The exponent, m, ranges between 0.89 and 0.97, which is in good agreement with the exponent observed for a plasma source with 75 μm Kapton HN as dielectric, which is 0.97 (see Table 3.12). The coefficient β ranges between 1109 and 1211 with a standard error of 8 %. This indicates similar efficiencies

for plasma sources of varying areas and is again in accordance with the observation of the image intensity, I_{img}.

	10 mm x 10 mm	20 mm x 20 mm	40 mm x 40 mm
β	1109	1211	1208
m	0.91	0.92	0.89
R^2	0.96	0.91	0.99

Table 3.17: Scaling parameter from $I_{spec} = \beta \cdot (P_A)^m$ for plasma sources of varying area

The scalability assessment has demonstrated that dispenser printed plasma sources can be used as a highly scalable solution to generated non-thermal plasma. The assessment of electrical and optical diagnostic of plasma sources of varying length and area scales has demonstrated, that the plasma intensity, quantified through the obtained image intensity and spectral intensity, remains similar per power per unit length/area.

3.2.4 Flexibility

The flexibility assessment of printed plasma sources using the dispenser printing method is carried out using the linear plasma source of 80 mm length (Electrode ID #22), presented in the previous section. Small bend diameters can result in cracking of the printed electrode, thus in a loss of the electrical connection on the plasma sources. Cracking is observe during handling of the plasma sources in the fabrication procedure and is observed as very small diameters. Figure 3.34(a) shows the printed plasma source bend around a nylon rod and Figure 3.34(b) shows the three different rod diameters used in this study, which are 6 mm, 10 mm and 20 mm. Similarly to the scalability assessment, the flexibility of printed plasma sources is assessed through electrical and optical diagnostics. The electrical and optical characteristics are assessed in reference to a flat plasma source. The flexibility assessment is carried out at a constant frequency of 6 kHz and with varying operating voltages.

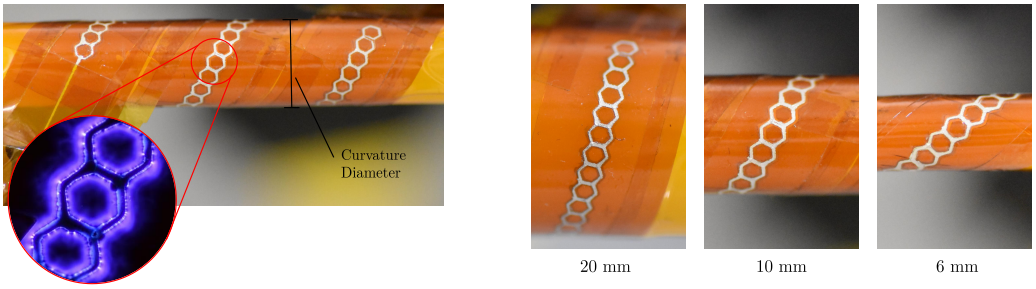

(a) (b)

FIGURE 3.34: (a) Printed plasma source using dispenser printing around nylon rod (b) Variation of diameter of 20 mm, 10 mm and 6 mm

3.2.4.1 Electrical characteristics

Figure 3.35 shows the discharge power of the plasma sources over varying curvatures. The discharge power of a flat plasma source is shown as reference for the flexibility assessment. As can be seen, a plasma source curved over a larger radius of 20 mm shows only a small effect of the obtained discharge power over varying operating conditions. Bending the plasma source over curvatures of 10 mm and 6 mm results in a small reduction of power at higher voltages. A reduction in discharge power due to a reducing curvature diameter can be caused by a change in the local electric field distribution of the plasma source. Bending the plasma source can affect the geometric configuration of dielectric material and the electrodes. This results in a changed local electric field distribution and change of the capacitive behaviour of the plasma source, which will affect the discharge power.

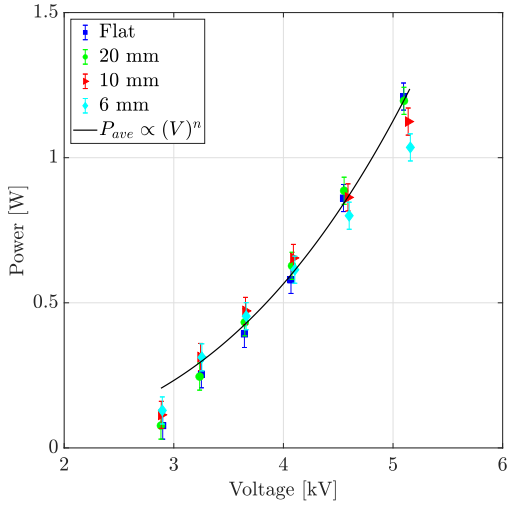

FIGURE 3.35: Discharge power for plasma sources over varying curvature

The overall trend of the discharge power, P_{ave}, over the operating voltage, V_{pp}, can be estimated using a the power law correlation as:

$$P_{ave} \propto (V_{pp})^{3.1} \tag{3.18}$$

Figure 3.35 shows the correlation $P_{ave} \propto (V_{pp})^n$, which follows a power law with an exponent of 3.1. This is similar to the correlation presented in the estimated power, P_{est}, using equation 3.9 from the previous section, where exponent was concluded to be 3.27. Therefore, the concluded correlation of $P_{ave} \propto (V_{pp})^{3.1}$ shown in Figure 3.35 is in good agreement with power estimation presented in the previous section.

3.2.4.2 Optical characteristics

Figure 3.36 shows the emission images of the plasma sources over varying curvatures for an operating voltage of 5.1 kV. As can be seen, uniform plasma is generated across the electrode for all curvatures and the visual plasma emission remains at similar level compared to the flat reference plasma source.

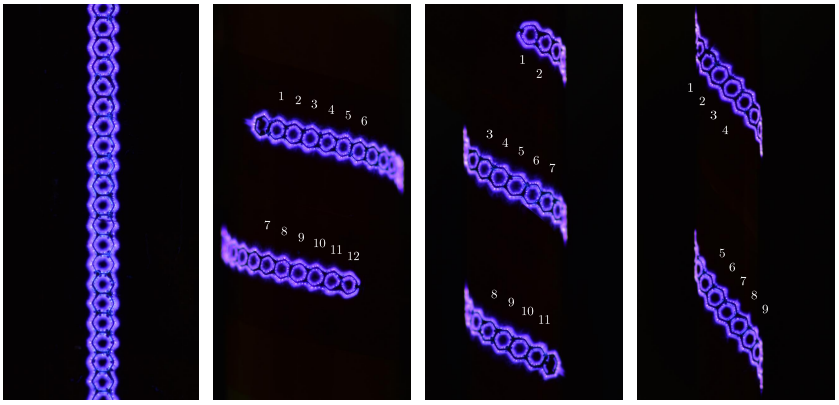

FIGURE 3.36: Emission images of printed plasma sources using dispenser printing method over varying curvature

Quantifying the image intensity, I_{img}, is performed similarly as presented previously, by analysing the pixel sum within the individual hexagonal units of the printed plasma source. The included hexagons are noted in Figure 3.36. Figure 3.37 shows the obtained average image intensity, I_{img}, over the discharge power for varying curvatures of the plasma source. As can be seen, the image intensity increases with the discharge power, a similar trend as seen previously. As can be seen, the image intensity for a curved plasma source lies below the image intensity for a flat plasma source. This reduction is likely caused by the distorted viewing angle on hexagons curving away from the optical camera. The plasma emission in these hexagons is captured under a distorted view, thus not capturing the full emission intensity. Consequently the averaged image intensity on curved plasma sources reduces.

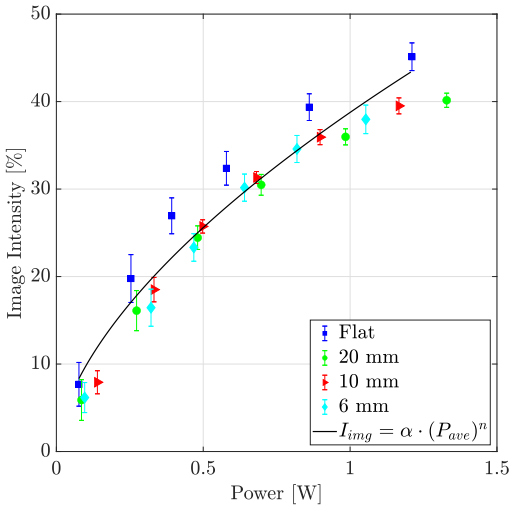

FIGURE 3.37: Image intensity for plasma sources over varying curvature

The correlation between the power, P_{ave}, and the image intensity, I_{img}, has been interpreted as an efficiency of the plasma source. The relationship of power, P_{ave}, and the image intensity, I_{img}, can be described through a power law as:

$$I_{img} = \alpha \cdot (P_{ave})^n \tag{3.19}$$

Table 3.18 lists the coefficients of the power law from equation 3.19 for plasma sources of varying curvatures. It can be seen that the exponent, n, ranges between 0.54 and 0.64. This is in good agreement with the exponent observed for similar plasma sources in the previous section (see table 3.11). The coefficient α allows a comparison of the efficiency of the respective electrode system. As can be seen, the coefficient α for a flat plasma source is 42.0, and reduces to a range of 35.5 to 38.7 for curved plasma sources. This relates to an average reduction of 11 % from a flat to a curved plasma source. This would indicate a drop in efficiency of the curved plasma sources. However, it is more likely that this effect is dominated by the distorted viewing angle, as described above.

	Flat	20 mm	10 mm	6 mm
α	42.0	35.5	37.1	38.7
n	0.54	0.58	0.64	0.59
R^2	0.98	0.97	0.96	0.97

Table 3.18: Scaling parameter from $I_{img} = \alpha \cdot (P_{ave})^n$ for plasma sources over varying curvatures

The spectral intensity can be used as an additional measure of the plasma intensity. The spectra are obtained only from a small section on the curved plasma source, thus the distortion effect observed with images will be minimized. Figure 3.38 shows the obtained

spectral intensity over discharge power for plasma sources with varying curvatures. The spectral intensity follows an increasing trend with increasing discharge power for a flat plasma source, as well as plasma sources operated under varying curvatures. It can be seen that the obtained spectral intensity for curved plasma sources lies below the spectral intensity for a flat plasma source.

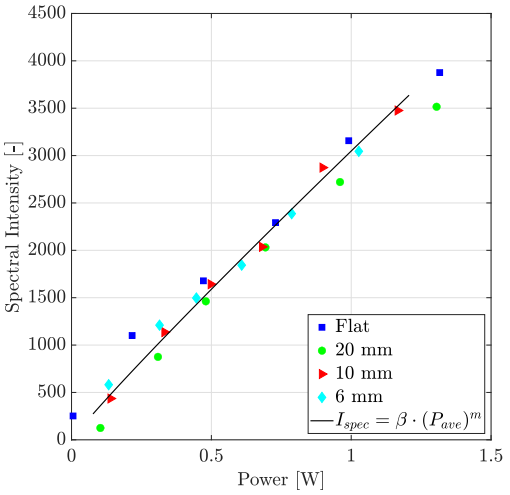

FIGURE 3.38: Spectral intensity for plasma sources over varying curvature

Similar to the image intensity, the correlation between the power, P_{ave}, and the spectral intensity, I_{spec}, can be interpreted as an efficiency of the plasma source. The relationship of power, P_{ave}, and the spectral intensity, I_{spec}, can be described through a power law as:

$$I_{spec} = \beta \cdot (P_{ave})^m \tag{3.20}$$

Table 3.19 lists the coefficients of the power law from equation equation 3.20 for plasma sources of varying curvatures. It can be seen that the exponent, m, ranges between 0.91 and 1.05. This is in good agreement with the exponent observed for similar plasma sources in the previous section (see table 3.12). The coefficient β allows a comparison of the efficiency of the respective electrode system. The coefficient β for a flat plasma source is 2897, and reduces to a range of 2593 to 2823 for curved plasma sources. This relates to an average reduction of 5 % from a flat to a curved plasma source. Thus a smaller reduction is observed in the spectral intensity in comparison to the reduction observed in the image intensity, which was 11 % This would support the explanation of the distorted viewing angle having an effect on the image intensity measurements.

	Flat	20 mm	10 mm	6 mm
β	2897	2779	2823	2593
m	0.91	0.99	1.05	0.93
R^2	0.98	0.97	0.96	0.97

Table 3.19: Scaling parameter from $I_{spec} = \beta \cdot (P_{ave})^m$ for plasma sources over varying curvatures

The flexibility assessment has demonstrated that dispenser printed plasma sources can be used as a flexible solution to generated non-thermal plasma. The assessment of electrical and optical diagnostic of plasma sources bend over varying curvatures has demonstrated, that the plasma intensity, quantified through the obtained image intensity and spectral intensity, remains similar for varying curvatures.

3.3 Summary

DBD plasma sources fabricated using printed electronics techniques can generate non-thermal plasma across large and complex geometries. Two printing methods have been used, ink-jet printing using low-viscosity ink and a dispenser printing technique using a high viscosity ink. DBD plasma sources fabricated using the ink-jet printing method have been used to demonstrate the capability of printing techniques for scalable and flexible plasma sources. A more comprehensive study has been carried out using the dispenser printing method, as it is able to print thicker electrodes with a high silver content. A lifetime analysis of printed plasma sources identified the need for protective coating methods to minimized the effects of electrode erosion and damage to the dielectric material. A parameter study of printed plasma sources with varying operating conditions (frequency f, voltage V_{pp}) and design parameters (dielectric thickness t, dielectric constant ε_r) allowed the proposal of a scaling law for the discharge power, image intensity and spectral intensity.

A comprehensive scalability and flexibility study has been carried out to demonstrate reliable plasma generation over large and complex surfaces using printed plasma sources. Plasma sources of various scales offer stable plasma intensity properties, measured through image and spectral intensities, while maintaining constant discharge power per unit length (or unit area). A flexibility assessment has shown the capability to generate stable and reliable non-thermal plasma when bending the electrode system over small curvatures. Therefore, is has been demonstrated that printed plasma sources can be used for applications where a non-thermal plasma generation is required for complex geometries.

Chapter 4

Electrical modelling of surface DBD plasma sources

A fully scalable and flexible plasma source can require a complex electrode geometry to be successfully used in an application. Therefore, in conjunction with the experimental study, a new electrical model is developed for complex electrode designs. An electrical model can play a key role in the design process of non-thermal plasma sources and assist in the optimisation of design and operating parameters. Although a few electrical models for surface DBD plasma sources have been developed, these models are limited to simple and mostly linear electrode designs. This chapter presents a new electrical model for surface DBD plasma sources with complex electrode geometries. The developed model employs a fractional segmentation of an electrode surface into a discharge and non-discharge area with a time-variable plasma discharge propagation length. The model is validated through comparing key electrical parameters, such as the discharge power, for four different complex electrode designs over a large range of operating conditions. Parts of this chapter have been previously published in the IEEE Transactions on Plasma Science [113].

4.1 Introduction

DBD plasma sources have gained growing interest in numerous application fields, including flow control [114], water purification [115] and cancer treatment [49, 52]. As various non-thermal plasma applications require different plasma properties or design parameters, it is important to optimise a plasma source in the development of non-thermal plasma technology. Current optimisation procedures of plasma sources rely on experimental data to identify relevant design parameters affecting their performance [116–118]. However, it is difficult to obtain experimental data over the wide range of design parameters due to time and cost constrains. Therefore, predicting the electrical

behaviour of DBD plasma sources is essential to optimise surface DBD plasma sources for the desired plasma properties.

The electrical characteristics of DBD plasma sources can be described using an electrical model, which is based on the design of an equivalent electrical circuit with analogous electrical components [119]. These components can represent specific physical parts of a DBD plasma source, electrical characteristics of their behaviour, as well as the components and behaviour of the experimental set-up, such as circuit impedance. Previously, various electrical models have been developed for volume DBD plasma sources [97] or variations of these, such as coaxial DBD plasma sources [120]. Figure 4.1 shows a schematic of a volume DBD, one of the most simple and common configuration of a DBD plasma source, and a simplified equivalent electrical circuit [97]. As can be seen, the physical components of the DBD plasma sources, the gas cap between both electrodes and the dielectric material, are modelled using a series arrangement of capacitors, C_g and C_d, respectively. In this simplified model, the characteristic behaviour of the plasma discharge is modelled by introducing a microdischarge resistance using a time varying resistor, $R(t)$, parallel to the gas gap capacitor. The time at which the plasma discharge occurs can be controlled through a switch.

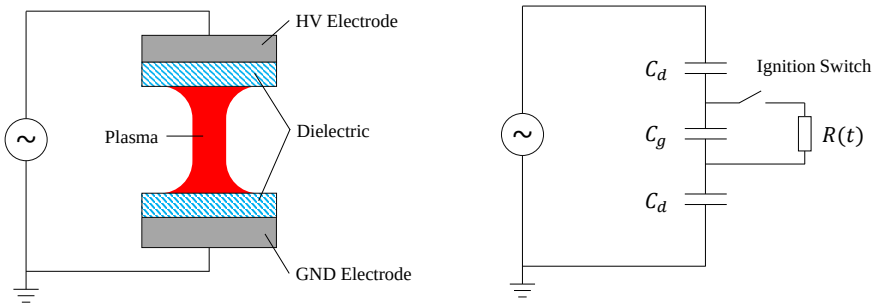

FIGURE 4.1: Volume DBD Plasma Source and a simple equivalent electrical circuit model, where C_d is the capacitance of the dielectric material, C_g is the capacitance of the gas gap and $R(t)$ resistance of the microdischarge

The behaviour of the actual plasma discharge within the electrode volume can be modelled in various approaches, such as using a variable resistor with rapidly changing resistance to describe microdischarges [97, 121]. Alternatively, Zener diodes can be implemented to model the discharge and account for effects such as the breakdown voltage, memory effects and the power dissipated in the discharge [122, 123]. Instead of variable components, the non-linearity of the discharge behaviour can be modelled through implementation of a voltage-controlled-current-source into the circuit [120, 124–127]. A voltage controlled current source superimposes a discharge current onto the displacement current to model the microdischarge. The discharge current can either be calculated by employing Kirchhoff's circuit laws [120, 124, 125, 127], or controlled through a function of the voltage using a power law [55, 126].

Compared to a volume DBD plasma source, electrodes in a surface DBD plasma source are planar, which results in a different characteristic electric field distribution. These kinds of plasma sources are widely used for flow control in the plasma actuator community [128–131]. Most developed electrical models for surface DBD plasma sources use similar approaches as volume DBD plasma sources by using variable resistors [106, 107] or voltage controlled current sources [124, 132]. Other approaches for surface DBD plasma sources include partitioning of the surface [133–136], thus assuming two distinct sections, the discharge and non-discharge section [134, 135] or defining an infinite chain of sections representing infinite sections of the discharge region [133, 136]. However, the majority of the electrical models presented for surface DBD plasma sources are limited to simple and mostly linear electrode designs, commonly used for flow actuators. The existing models, therefore, are not suitable for complex electrode configurations or geometries of surface DBD plasma sources.

In this chapter an electrical model is proposed to predict the electrical characteristics and performance of a surface DBD plasma source with a complex electrode geometry. The proposed model divides the surface of a plasma source into a discharge and non-discharge region. This segmentation is achieved by calculating the respective discharge and non-discharge area of the surface of the DBD plasma source. The microdischarge behaviour is modelled through superposition of a discharge current onto the displacement current by implementing a voltage-controlled-current-source. As the discharge and non-discharge area over a plasma source surface varies with temporal behaviour of the voltage, the ratio of discharge to non-discharge area is consequently also a time varying parameter. Therefore, the proposed electrical model is expanded by a semi-empirical study of the time varying discharge propagation length. This is used in the calculation of the discharge and non-discharge area. The proposed electrical model is validated through a comparative analysis of electrical key characteristics, such as the discharge current and the discharge power of several complex electrode configurations over a larger range of operating conditions.

4.2 Equivalent electrical circuit model

The key part of the proposed electrical model is the segmentation of the DBD plasma surface into a discharge and non-discharge area. The following section will explain the segmentation in detail, how it accommodates for complex geometries and how it is transferred into an equivalent electrical circuit.

4.2.1 Segmentation of the surface DBD plasma source

Segmentation of the surface DBD plasma sources allows for accounting of complex electrode geometries by calculating the specific areas. In this chapter, a hexagonal electrode

pattern is used as the baseline design. Figure 4.2(a) shows the top-down and Figure 4.2(b) shows the cross-sectional view of the hexagon unit of the surface DBD plasma source. As can be seen, the surface DBD plasma source has a hexagonal electrode with different regions of an electrical model: the dielectric capacitive region (A), discharge region (B) and non-charge region (C). The region where both electrodes are directly opposed to each other is called the dielectric capacitive region. As can be seen, the generated plasma forms near the edge of a ground electrode, called the discharge region. In the discharge region the distance between both electrodes is minimal, resulting in a strong local electric field. The area of the discharge region is defined by the discharge propagation length, $p_d(t)$, the distance of how far plasma ranges to the centre of the hexagonal unit. Towards the unit centre, the field strength reduces with the increasing distance between both electrodes and only weak or no plasma is formed in the central region of a hexagonal unit. This region is called the non-discharge region.

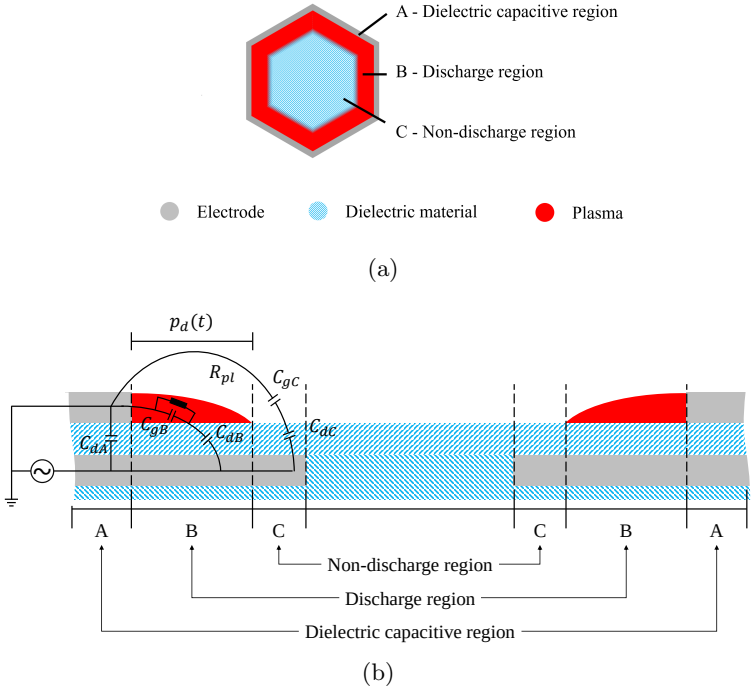

FIGURE 4.2: (a) Top-view of one unit of hexagonal electrode patten (b) Equivalent electrical components in segmented surface DBD plasma source (Colours: Grey: Electrode; Blue: Dielectric material; Red: Plasma)

The dielectric capacitive region covers the area of a ground electrode. This region is solely defined by the capacitance of the dielectric material between high voltage and ground electrode. Therefore, it can be described with a single capacitor, $C_{d,A}$. The discharge region covers the area above the dielectric material, where plasma discharge is occurring. The equivalent electrical characteristics of the discharge region, B, can be described using a series arrangement of dielectric capacitance, $C_{d,B}$, and equivalent electrical components to model the plasma, R_{pl} and $C_{g,B}$. The equivalent components of plasma consist of a capacitor, $C_{g,B}$, and a resistor, R_{pl}. The capacitor, $C_{g,B}$, models

the capacitance of the remaining gas and the resistor, R_{pl}, describes the resistance of the microdischarge. The non-discharge region, C, is the remaining area between both electrodes, where no discharge is occurring, and can be described with a dielectric capacitance, $C_{d,C}$, and a gas capacitance, $C_{g,C}$. The proportion of discharge area to non-discharge area is a function of the discharge propagation length, $p_d(t)$, and can be defined by the discharge area fraction, $\alpha(t)$, as:

$$\alpha(t) = f(p_d(t)) = \frac{A_B(t)}{A_B(t) + A_C(t)} \tag{4.1}$$

where $A_B(t)$ is the area of a discharge region and $A_B(t)$ is the area of a non-discharge region. An area discharge fraction of $\alpha(t) = 1$ refers to a full ignition across the entire electrode surface. An area discharge fraction of $\alpha(t) = 0$ means no plasma ignition is being present on a surface DBD plasma source. The area discharge fraction $\alpha(t)$, is a time-dependent parameter, because the discharge area is changing during operation. The operating voltage is a sinusoidal AC signal, which causes a time varying local electric field. At the beginning of each period, the voltage potential across both electrodes is small. Once the operating voltage reaches the breakdown voltage, the local electric field is strong enough to ionize the air. Then plasma starts forming in the edge regions, where the local electric field is strongest. With increasing operating voltage, the electric field grows stronger towards the centre of the hexagonal unit and accordingly the discharge area propagates towards the centre.

4.2.2 Discharge propagation

The discharge propagation length can be estimated using analytical and numerical methods [137, 138]. In literature experimental studies can be found, which analyse the propagation length on simple electrode geometries. Studies shown that increasing permittivity of a dielectric material reduces the discharge propagation length [117, 139]. For pulse signals, further correlation between the steepness of a voltage pulse signal and the propagation length have been reported, with increasing propagation length for larger voltage gradients [139]. Previous numerous studies demonstrated that a rise in applied voltage, leads to an increase of discharge length, with values ranging between a few millimetres up to a few centimetres [133, 138, 140–142].

The dependency of the discharge length on the applied voltage can be further analysed using the open-source program SDBDDesigner [137, 143, 144]. The SDBDDesigner allows to calculate discharge characteristics of surface DBD plasma sources based on design parameters. Using the parametric analysis in the SDBDDesigner, the 2D and 3D discharge lengths are calculated for operating voltages ranging from 0.7 kVrms to 1.7 kVrms. Remaining design parameters are kept constant (Dielectric thickness $t_{diel} =$

$75\mu m$, dielectric constant $\varepsilon_r = 3.4$, gas pressure $p = 101325\ Pa$, gas temperature $T = 300K$).

Figure 4.3 shows the obtained discharge length over the applied voltages. As can be seen, the discharge length is calculated in a 2D and 3D approximation, with both discharge propagation curves follow an exponential trend with the base e and the same exponent of 0.7. However, the 2D and 3D approximation have different coefficients, which are 0.07 and 0.3 respectively, resulting in the 2D approximation having larger discharge lengths.

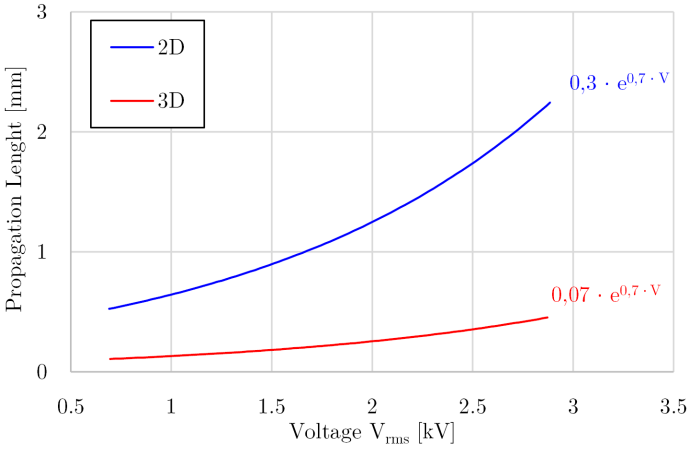

FIGURE 4.3: Discharge propagation length from SDBDDesigner using 2D and 3D approximation

On the basis of the exponential trend derived from the SDBDDesigner an empirical study has been carried out. This study analyses the discharge propagation length using a simple 1-D line electrode geometry. The electrode is operated at a frequency of 10 kHz and for operating voltages, V_{rms}, from 0.85 kV to 3.2 kV. Figure 4.4 shows the 1-D line electrode and a series of recorded images for various operating voltages. As can be seen, the average discharge length increases with rising operating voltage

The recorded images can be used to estimate the discharge propagation length. The propagation length is analysed by estimating the extent of the visual plasma ignition from the image recordings. As the camera shutter speed is 1 seconds, the recorded image contains the average discharge behaviour over 10000 cycles (with the operating frequency of 10 kHz). Therefore, the derived discharge propagation length in the images is only a representation of the average propagation length. The average propagation length is estimated using an image processing approach. The obtained images are calibrated by defining a reference length of a known distance in the image.

Figure 4.5 shows the image intensity per row over the pixel length at an applied operating voltage of 2.6 kVrms. The pixel count starts at the electrode edge and runs down vertically, perpendicular to the printed electrode. As can be seen, the image intensity is large near the printed electrode and reduces with increasing distance from the electrode.

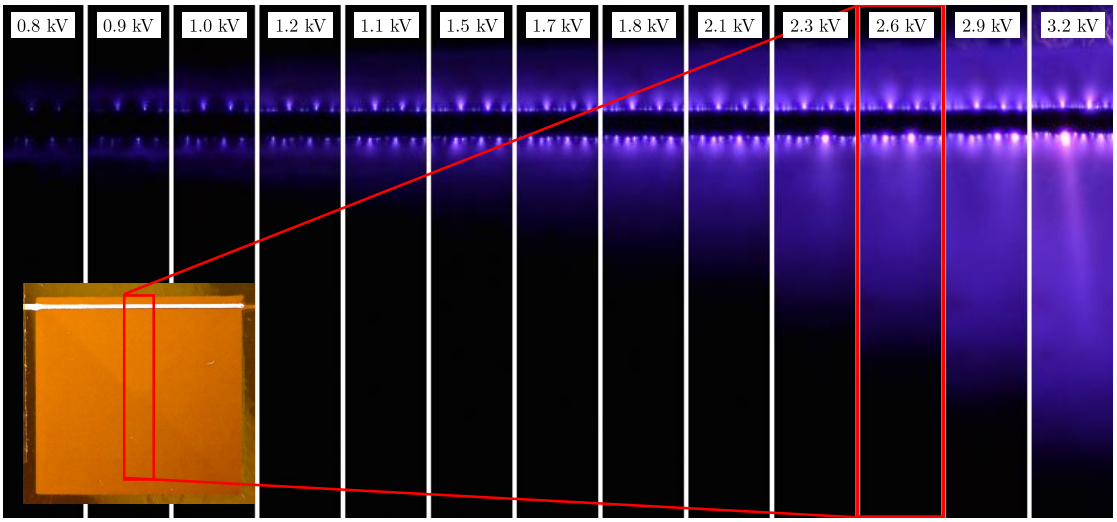

FIGURE 4.4: Images of the discharge propagation length on a 1-D line electrode for varying operating voltages

The discharge propagation length was derived at the length of a 95% reduction in image intensity, indicated as the red dashed line in Figure 4.5.

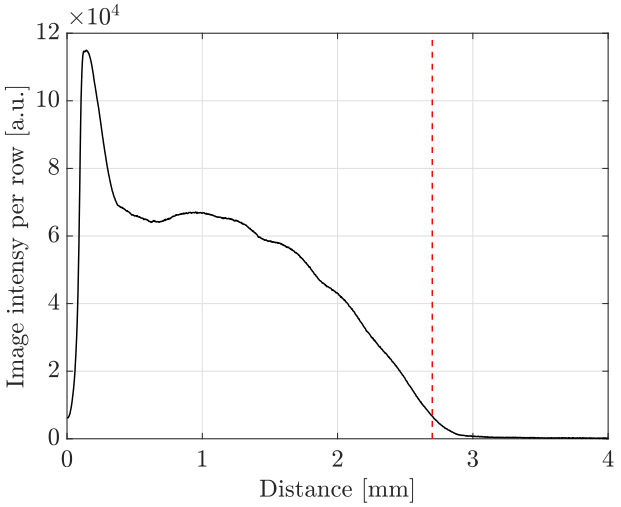

FIGURE 4.5: Obtained image intensity over distance from electrode on 1-D line geometry for an operating voltage of 2.6 kVrms

Figure 4.6 shows the obtained average propagation lengths for all tested operating voltages. The obtained propagation length can be approximated using an exponential function with the base e, similar to the one calculated in the open source program SDB-Designer. The discharge propagation length, $p_d(t)$ therefore can be approximated as (confidence: $R^2 = 0.9902$):

$$p_d(t) = 0.3 \cdot e^{0.9 \cdot V(t)} \tag{4.2}$$

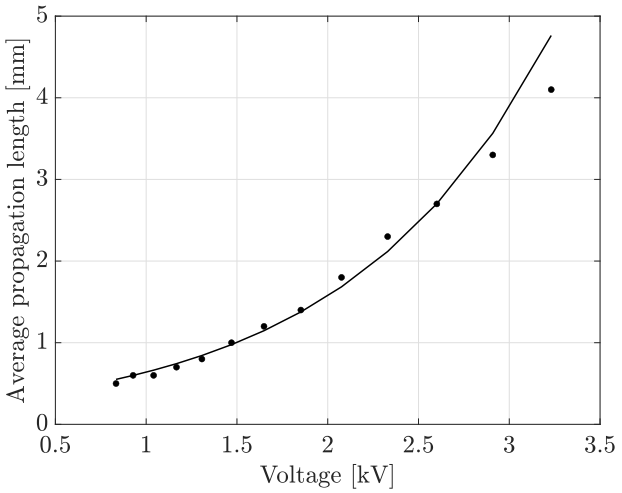

FIGURE 4.6: Estimated discharge propagation length, $p_d(t)$ over varying operating voltages

4.2.3 Equivalent electrical circuit

Equivalent analogous electrical components are defined for the surface DBD plasma source and are transferred into an equivalent electrical circuit model. Figure 4.7 shows the equivalent electrical circuit model based on the segmentation approach, where the three regions, dielectric capacitive region, discharge region, and non-charge region are highlighted. The applied voltage for the circuit is provided by the AC voltage source shown on the left side of the circuit and $I_{DBD}(t)$ is the total current passing through the plasma source. The dielectric capacitive region (A) contains a single capacitance $C_{d,A}$ representing the dielectric material between both electrodes. The discharge region (B) contains the dielectric capacitance $C_{d,B}$ and two inversely operating switches SW1 and SW2 alternate to incorporate two different regions of the circuit. Switch SW2 is closed when no discharge is occurring, which includes a circuit path containing the gas capacitance $C_{g,B}$ in region B. Once the applied voltage exceeds a threshold breakdown voltage, V_{bd}, plasma is formed and SW1 will close, causing SW2 to open simultaneously. This disconnects the gas capacitance $C_{g,B}$ and instead incorporates the microdischarge resistance R_{pl} and a voltage controlled current source. The voltage controlled current source superimposes a plasma discharge current, I_{CCS}, to the circuit, which represents the current passing through the microdischarges during the plasma phase. In the non-charge region (C), no plasma is present and the gas and dielectric capacitance are represented through a series arrangement of two capacitors, $C_{g,C}$ and $C_{d,C}$.

Applying Kirchhoff's voltage and current law to the circuit shown in Figure 4.7, the applied voltage V_a and the total current, I_{DBD} can be described as:

$$V_a(t) = V_A(t) = V_B(t) = V_C(t) \tag{4.3}$$

$$I_{DBD}(t) = I_A(t) + I_B(t) + I_C(t) \tag{4.4}$$

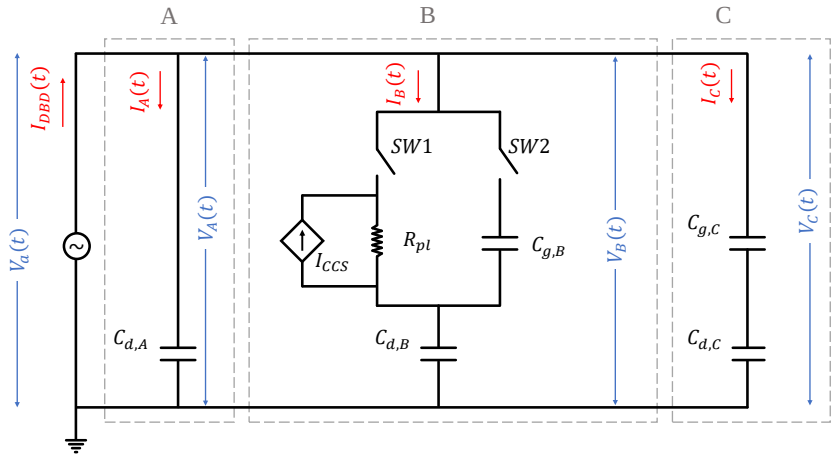

FIGURE 4.7: Schematic of equivalent electrical circuit model

where $V_A(t)$, $V_B(t)$ and $V_C(t)$ are the voltages in the dielectric capacitive region, discharge region, and non-charge region, respectively. $I_A(t)$, $I_B(t)$ and $I_C(t)$ are the currents passing through the respective regions. The current in the dielectric capacitive region (A), $I_A(t)$, and in the non-discharge region (C), $I_C(t)$, can be described as:

$$I_A(t) = C_{d,A}\frac{dV_A(t)}{dt} = C_{d,A}\frac{dV_a(t)}{dt} \tag{4.5}$$

$$I_C(t) = \frac{C_{g,C}(t)\cdot C_{d,C}(t)}{C_{g,C}(t)+C_{d,C}(t)}\frac{dV_C(t)}{dt} = \frac{C_{g,C}(t)\cdot C_{d,C}(t)}{C_{g,C}(t)+C_{d,C}(t)}\frac{dV_a(t)}{dt} \tag{4.6}$$

where $C_{d,A}$ is the capacitance of the dielectric capacitive region, $C_{d,C}(t)$ is the dielectric capacitance, and $C_{g,C}(t)$ is the gas capacitance in the non-discharge region. During discharge the current passing through the discharge region (B) is assumed as $I_B(t) = I_{CCS}(t)$ and by substituting equations 4.5 and 4.6 into equation 4.4 the plasma discharge current, $I_{CCS}(t)$, can be expressed as:

$$I_{CCS}(t) = I_{DBD} - \left(C_{d,A} + \frac{C_{g,C}(t)\cdot C_{d,C}(t)}{C_{g,C}(t)+C_{d,C}(t)}\right)\frac{dV_a(t)}{dt} \tag{4.7}$$

This derived equation for the plasma discharge current I_{CCS}, is used to define the voltage controlled current source in the model.

The total dielectric capacitance of the surface DBD plasma source, $C_{d,tot}$, is defined as:

$$C_{d,tot} = C_{d,A} + C_{d,B} + C_{d,C} = \varepsilon_0 \cdot \varepsilon_{diel}\frac{A_{Hex}}{t_{diel}} = \varepsilon_0 \cdot \varepsilon_{diel}\frac{A_A + A_B(t) + A_C(t)}{t_{diel}} \tag{4.8}$$

where ε_0 is the permittivity of vacuum, ε_{diel} is the permittivity of the dielectric material, A_{Hex} is the total area of one hexagonal unit, and t_{diel} is the thickness of the dielectric material. The area A_A of the dielectric capacitive region is defined by the geometry of the printed electrode pattern and remains constant as a time-independent variable. The areas of the discharge and non-discharge region, $A_B(t)$ and $A_C(t)$ are time varying and

can be described as a function of the total area, A_{Hex}, and the time-independent area of the dielectric capacitive region, A_A, and the discharge area fraction, α, as:

$$A_B(t) = (A_{Hex} - A_A) \cdot \alpha(t) \tag{4.9}$$

$$A_C(t) = (A_{Hex} - A_A) \cdot (1 - \alpha(t)) \tag{4.10}$$

The fractional dielectric capacities in the discharge and non-discharge region, $C_{d,B}(t)$ and $C_{d,C}(t)$, are defined as:

$$C_{d,B}(t) = \varepsilon_0 \cdot \varepsilon_{diel} \frac{A_B(t)}{t_{diel}} \tag{4.11}$$

$$C_{d,C}(t) = \varepsilon_0 \cdot \varepsilon_{diel} \frac{A_C(t)}{t_{diel}} \tag{4.12}$$

Similarly the time-dependent fractional capacitances $C_{g,B}(t)$ and $C_{g,C}(t)$ are calculated as:

$$C_{g,B}(t) = \varepsilon_0 \cdot \varepsilon_{air} \frac{A_B(t)}{t_{air}} \tag{4.13}$$

$$C_{g,C}(t) = \varepsilon_0 \cdot \varepsilon_{air} \frac{A_C(t)}{t_{air}} \tag{4.14}$$

where ε_{air} is the permittivity of the air, and t_{dis} is the discharge zone thickness, and t_{air} is the thickness of the air layer above the surface DBD. The thickness of the discharge zone is reported in various studies as ranging from 10 to 100 μm ([138, 143, 145]). In this thesis the discharge zone thickness is approximated as 50 μm.

Figure 4.8 shows a characteristic waveform of a DBD plasma source, where the active plasma phase is indicated in the negative and positive half period of the current signal. Once the applied voltage, $V_a(t)$, exceeds a breakdown voltage, V_{bd}, discharge is initiated and will be maintained until $dV_a(t)/dt = 0$. The active plasma phase in the positive half period is present from $t_1 < t < t_2$. In the negative half period, the active plasma phase is defined as lasting for $t_3 < t < t_4$. The specific times, t_1 to t_4, are calculated based on the sinusoidal voltage waveform, $V_a(t) = A \cdot sin(\omega t)$ as:

$$t_1 = \frac{1}{\omega} sin^{-1}\left(\frac{V_{bd}}{A}\right) \tag{4.15}$$

$$t_2 = \frac{\pi}{2\omega} \tag{4.16}$$

$$t_3 = \frac{1}{\omega} sin^{-1}\left(\frac{-V_{bd}}{A}\right) \tag{4.17}$$

$$t_4 = \frac{3\pi}{2\omega} \tag{4.18}$$

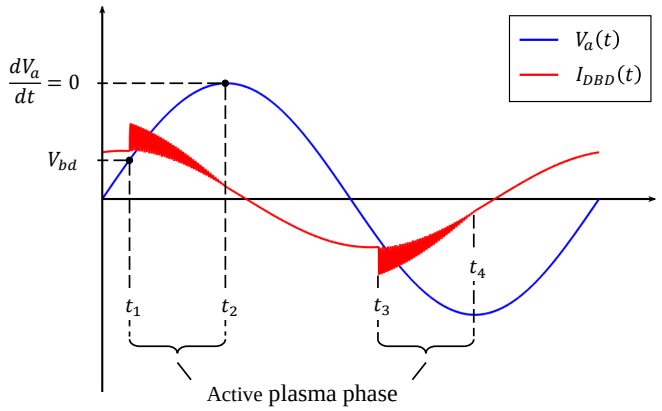

FIGURE 4.8: Theoretical voltage and current signal with the active plasma phase highlighted

4.3 MATLAB Simulink model

A MATLAB Simulink model has been developed using the equivalent electrical circuit. This developed model is illustrated in Figure 4.9 consisting of the main circuitry and three controlling blocks. The main circuitry is powered by an AC voltage source block, which is controlled with the operating voltage and frequency. The three distinct regions of the surface DBD plasma sources are highlighted, which are the dielectric capacitive (A), discharge (B) and non-discharge region (C). Additionally, a variable discharge propagation block (VDP) is included in the model. The VDP block calculates the area discharge fraction, $\alpha(t)$, based on the plasma propagation length, $p_d(t)$. With the time dependent area discharge fraction $\alpha(t)$, areas $A_B(t)$ and $A_C(t)$ are calculated according to equations 4.9 and 4.10. The respective time dependent capacitance values $C_{g,B}(t)$, $C_{g,C}(t)$, $C_{d,B}(t)$ and $C_{d,C}(t)$ are calculated with equations 4.11 to 4.14. Subsequent to the VDP block, a "Pulse" block is implemented, which acts as a switch between non-discharge and discharge time ($t_1 < t < t_2$ and $t_3 < t < t_4$) according to equations 4.15 to 4.18. The pulse signal will remain zero when no discharge is occurring, once the breakdown voltage is reached, the pulse signal will be one until the extinction of the discharge at $dV_a/dt = 0$. The pulse block operation is applied to the time-variable capacitance values $C_{g,B}(t)$, $C_{g,C}(t)$, $C_{d,B}(t)$ and $C_{d,C}(t)$, before each being led into the variable capacitor blocks.

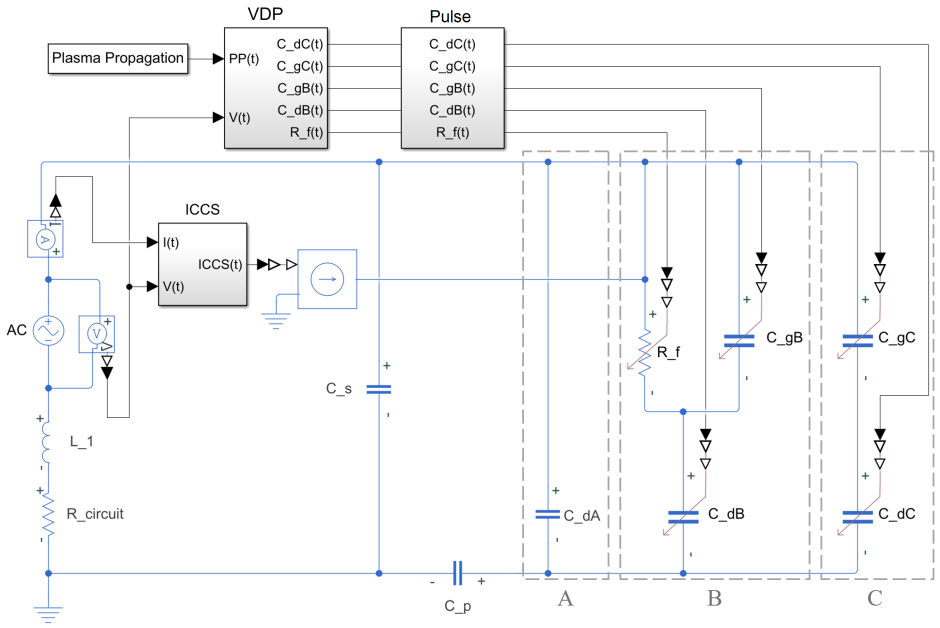

FIGURE 4.9: MATLAB Simulink model of equivalent electrical circuit model

The "voltage-controlled-current-source" block (ICCS) applies the calculated discharge current $I_{CCS}(t)$ to the circuit according to equation 4.7 to the circuit. Figure 4.10 shows a detailed view of this circuit block, where the total circuit current I_{DBD} and the differential of the operating voltage $dV_a(t)$ are multiplied with the respective gains according to equation 4.7. The resulting value is further multiplied with a pulse signal and sine signal. The pulse signal switches between discharging and non-discharge time, similarly to the Pulse block in the main circuit model. The sine wave signal is superimposed to model the behaviour of the microdischarge. The microdischarges are characterised by numerous high frequency signals. The frequency of the microdischarges is obtained using FFT analysis of the experimental data. Across multiple electrode configurations and operating conditions, the microdischarge frequency remains constant at approximately 3.8 MHz. The microdischarge resistance, R_{pl}, can not be derived analytically or measured experimentally. It is selected as 25 kΩ, because this results in the highest correlation between experimental and simulated results across all electrode configurations and power conditions. The electrical model further contains a capacitor, C_s, to account for parasitic capacities within the circuit. Its values can be estimated from the capacitance when no discharges on the plasma source is present and is estimated with $C_s = 20$ pF. A probe capacitor, C_p with a value of 10 pF is added in the circuit, to measure the charge characteristics of the modelled plasma source. Additionally, the circuit contains a resistance R_{circut} and an inductance L_1 to account for the impedance of the power supply system. Both values are measured from the experimental setup, which are $R_{circut} = 0.553$ kΩ and $L_1 = 10$ μH, respectively.

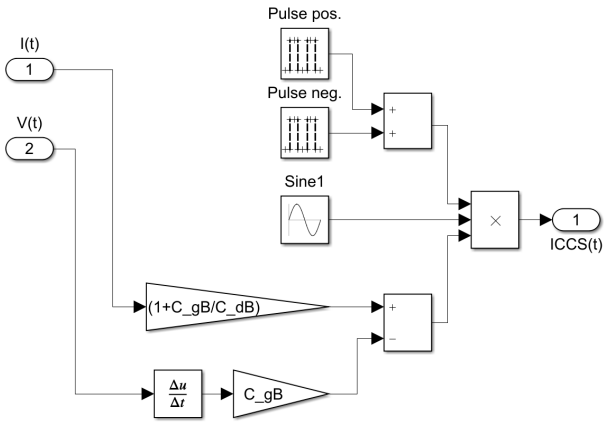

FIGURE 4.10: MATLAB Simulink model of "voltage controlled current source" block (ICCS)

4.3.1 Breakdown voltage

The breakdown voltage of a plasma discharge defines the onset of the plasma discharge, thus the time parameters t_1 to t_4 defining the active plasma region from equations 4.15 to 4.18. The breakdown voltage depends on various parameters, such as air composition, humidity and relative permittivity of dielectric material [120]. As the breakdown voltage itself cannot be measured, it needs to be derived from experimental data or estimated with analytical or empirical methods. In this thesis, the breakdown voltage is obtained from electrical data at the time of first occurrence of a micro discharge.

Figure 4.11 shows the voltage and current measurement obtained by the Rogowski coil for a voltage of 3.3 kV and frequency of 10 kHz. As can be seen in Figure 4.11(b), the plasma discharge region is clearly distinct from the remaining current signal as a region with superimposed high frequency and large amplitude signals. Within each half period of the sinusoidal current signal, the first occurrence of this micro discharge region is identified by obtaining the time at which the current amplitude exceeds the noise level by a factor of 2. The breakdown voltage in the negative, $V_{bd,neg.}$, and the positive half period, $V_{bd,pos.}$, are given by the voltage measurement at the same time. A value is obtained for numerous cycles over the recorded electrical data and then averaged.

Figure 4.12(a) and 4.12(b) shows the breakdown voltage for the positive and negative half period obtained from the electrical measurement. The breakdown voltage is shown over the applied voltage for varying frequencies ranging from 6 kHz to 12 kHz. As can be seen, the breakdown voltage follows a linear trend, with larger values ranging around 300 V for small applied voltages. With an increasing operating voltage, the breakdown voltage decreases down to 0 V, all the way down to -600 V for the largest operating voltages. The breakdown voltage obtained in the negative half period follows a similar trend, ranging from -600 V for small operating voltage up to 600 V for large operating voltages. Note that the inverted sings due to the breakdown voltage obtained from

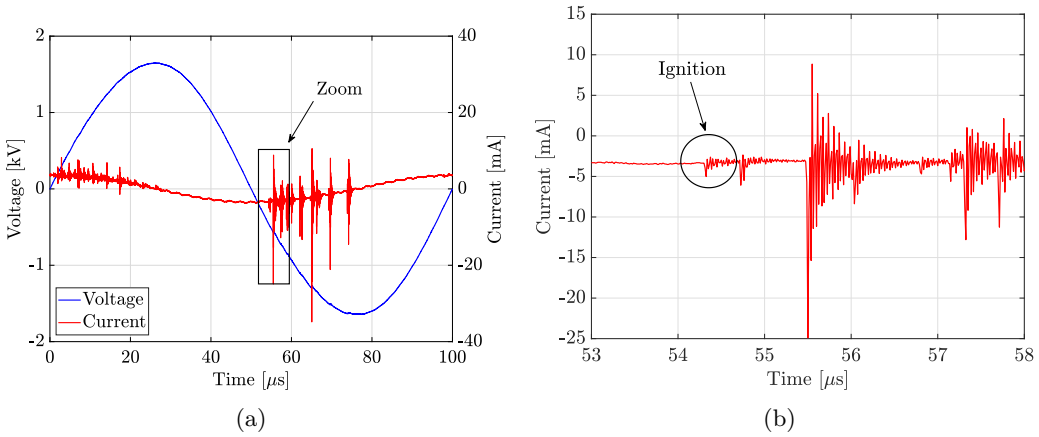

(a) (b)

FIGURE 4.11: Obtaining breakdown voltage from (a) Current measurement with micro discharge region (b) Zoom of micro discharge identifying ignition

the positive and negative half period. The appearance of negative breakdown voltages (or positive for the negative half period) can be attributed to the memory effect of surface DBD plasma sources. This is due to the accumulation of memory charge at the dielectric material from a previous half period [119, 140, 146]. The memory charge results in an increased charge density at specific locations on the dielectric surface and leading to changes in the local electric field distribution. Consequently, the required voltage to induce discharge is reduced and the occurrence of the first microdischarge correlates with a time step at which the applied voltage is negative. The memory effect is more pronounced at larger operating voltages. An increased operating voltage results in a stronger local electric field across the dielectric surface, leading to a larger area to accumulate charge.

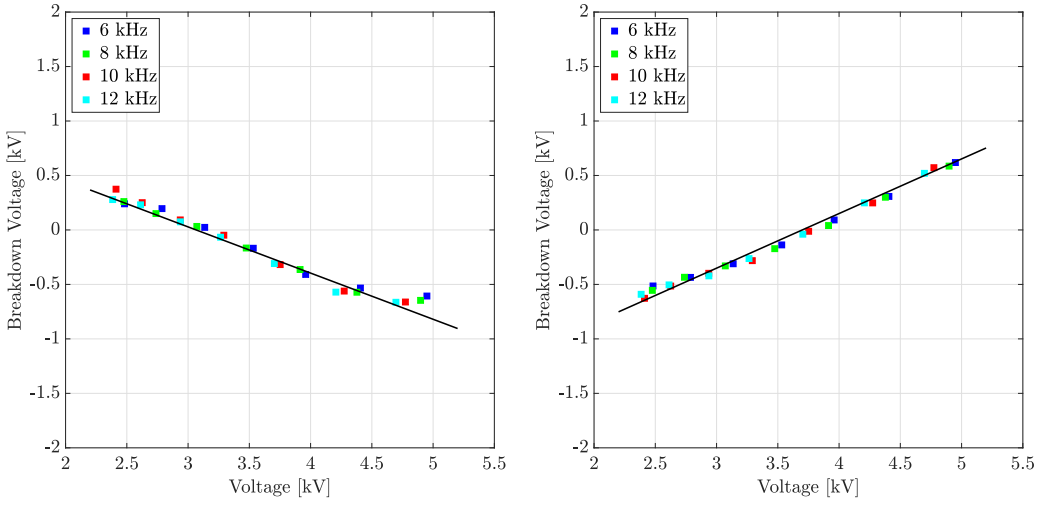

(a) (b)

FIGURE 4.12: Obtained breakdown voltage against operating voltage over varying frequency for (a) positive half period (b) negative half period

The obtained breakdown voltages for the negative and positive half period can be approximated using a linear curve fitting (see black line in Figures 4.12(a) and 4.12(b)) to define an empirical relation of breakdown voltage to operating voltage, V_{pp}, as follows:

$$V_{bd,pos.} = -0.424 \cdot V_{pp} + 1300 \tag{4.19}$$

$$V_{bd,neg.} = 0.5014 \cdot V_{pp} - 1855 \tag{4.20}$$

As part of this study no correlation between breakdown voltage and operating frequency has been observed. The empirical equation (equations 4.19 and 4.20) for the breakdown voltages for the negative and positive half period are implemented in the electrical model, in order to improve the accuracy of the model.

An analytical estimation of the breakdown voltage can be obtained using the open-source program SDBDesigner [144]. The breakdown voltage is provided for a given set of input parameters, including applied voltage, frequency, dielectric thickness and material. For the electrode samples and operating conditions presented in this chapter a breakdown voltage of 560 V is derived from the program. The analytical estimation does not show any dependency of the breakdown voltage on the operating voltage or frequency and no differentiation between the negative and positive half period is provided. The analytically derived breakdown voltage is only in agreement with the experimentally obtained breakdown voltage at low operating voltages. This can be interpreted as an indication that the analytical estimation does not account for the memory voltage due to accumulated surface charge, as this effect is minimal at small operating voltages.

4.4 Validation of the electrical model

4.4.1 Electrode configurations

The developed electrical model is validated against 4 different electrode configurations. The electrode configurations have been designed to analyse the effect of varying electrode geometry on the electrical characteristics and electric field distributions. The ratio of the linewidth (LW) of ground and high voltage electrode size, r_{ELR}, is varied in the four different configurations, which is defined as:

$$r_{ELR} = \frac{LW_{HV}}{LW_{GND}} \tag{4.21}$$

where LW_{HV} is the linewidth of the high voltage electrode and LW_{GND} the linewidth of the ground electrode. In all four configurations, the electrodes are printed using dispenser printer, on a dielectric substrate, Kapton HN, with thickness of 75 μm. Figure 4.13 shows the schematic of the four electrode configurations with the pictures of the fabricated electrodes. The exact electrode geometries can be found in Appendix A.2.

The ground electrode is kept at a constant linewidth of 0.3 mm for all four configurations. Configuration #1 has the same ground electrode and high voltage electrode pattern, thus an electrode linewidth ratio r_{ELR} is 1. Configurations #2 and #3 have high voltage electrodes with a size of 0.95 mm ($r_{ELR} = 3.2$) and 1.6 mm ($r_{ELR} = 5.3$) respectively. Therefore, the central area in each hexagonal unit is not covered by any electrode. Configuration #4 has a high voltage electrode covering the full hexagonal unit, and consequently the largest ratio r_{ELR} of 6.6. The variation of the electrode size ratio leads to different distributions of the electric field at in the centre of the hexagonal units. Configuration #1 has an electric field concentrated towards the edge regions closer to the ground electrode. With increasing electrode line width ratio, the electric field grows stronger within the centre of the hexagons. The electric field of configuration #4 is fully extended to the centre. Therefore, all four configurations have different electric field distributions at the centre of electrodes.

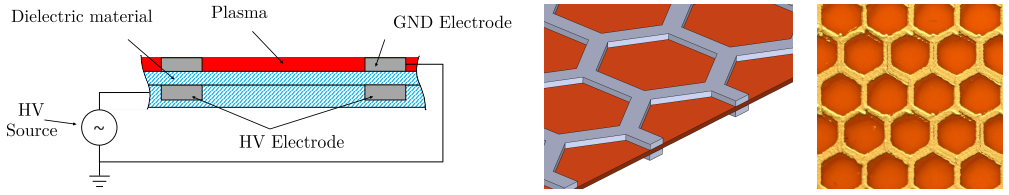

(a) Configuration #1

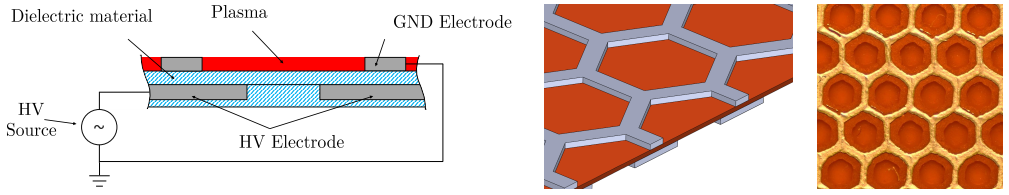

(b) Configuration #2

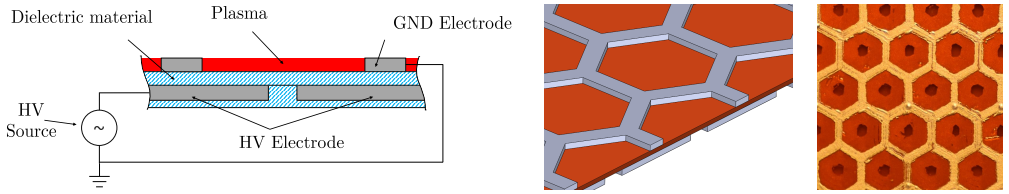

(c) Configuration #3

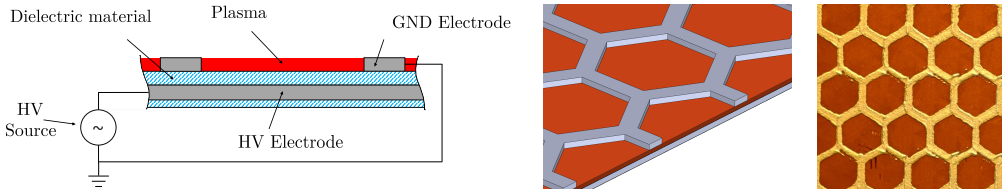

(d) Configuration #4

FIGURE 4.13: Schematic cross section view, schematic side view and top view of printed electrode configurations #1 to #4

HV Thickness	Electrode Linewidth Ratio	Area Ratio	Description
0.27 mm	1	0 %	Configuration #1
0.95 mm	3.2	63 %	Configuration #2
1.6 mm	5.3	95 %	Configuration #3
2 mm	6.6	100 %	Configuration #4

Table 4.1: Geometrical details for electrode configurations #1 to #4

4.4.2 Model validation

The electrical model is validated by experimental results using current and voltage measurements from the four surface DBD configurations presented in the previous section. The experimental studies are carried out for a larger range of operating conditions, with voltages ranging from 2.5 kV to 5 kV and frequencies ranging from 6 kHz up to 12 kHz. The average discharge power, P_{ave}, is derived from the experimental data and predicted using the developed electrical model for a comparative analysis in order to assess the accuracy of the electrical model.

Figure 4.14(a) shows the experimental measurements of voltage $V(t)$ and current $I(t)$ for electrode configuration #2 with operating conditions of 3 KV at 10 kHz. As can be seen, the voltage measurement follows the sinusoidal waveform, however shows a slight distortion due to non-optimised impedance-matching in the experimental setup. In the current measurement, the active plasma phase in the positive and negative half period is clearly distinct by the presence the microdischarges. These microdischarges are numerous high frequency and large amplitude signals superimposed onto the sinusoidal waveform. Figure 4.14(b) shows the experimentally obtained Lissajous graph. The shape of the Lissajous curve can give an indication of the discharging behaviour in the plasma volume. Volume DBD plasma sources usually have a stable and only minimally changing discharge volume and a Lissajous curve in the shape of a parallelogram. Surface DBD plasma sources in comparison have constantly changing discharge volume [86, 117], which is indicated in the bluntness of the Lissajous curve, which is then usually described as almond shaped [88, 107, 136]. The shape of the Lissajous curve presented in Figure 4.14(b) can be described as a parallelogram with rounded off edges especially in the blunt corners. An overview of the Lissajous graph of the four different electrode configurations can be found in Appendix C.1, where the Lissajous graphs are exemplary shown for varying operating voltages at constant operating frequency of 6 kHz.

Figure 4.15(a) shows the voltage and current signal predicted with the developed electrical model. Both signals display a high level of correlation to the experimentally obtained voltage and current signals. Figure 4.15(b) shows the simulated voltage-charge characteristic. In comparison to the experimental Lissajous curve, the model slightly under-predicts the charge and the shape of the curves shows more rounded off edges. The inaccuracy in the charge prediction can be attributed to the approximation of discharge

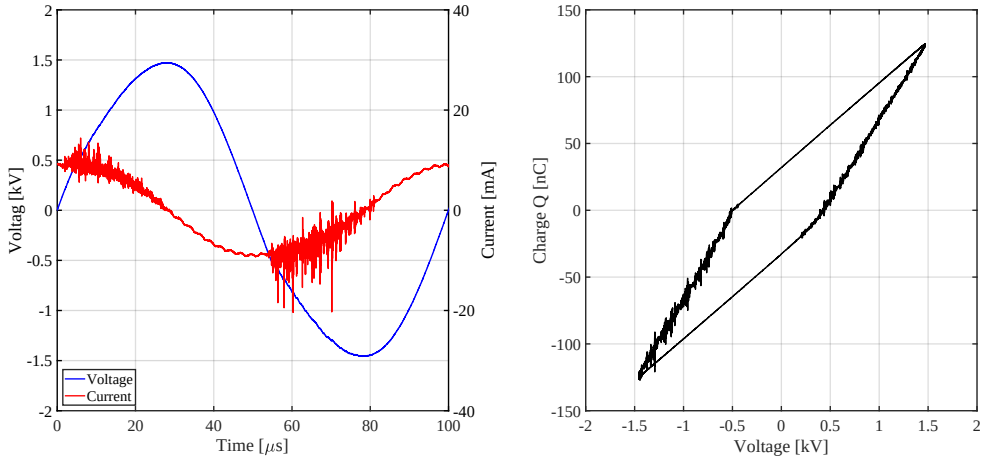

(a) (b)

FIGURE 4.14: Experimental results with 3 kV at 10 kHz (a) Voltage and current reading; (b) Lissajous graph

area in comparison to the actual discharge area. The discharge area in the electrical model is based on the semi-empirical definition of the discharge propagation, thus only an approximation of the actual discharge propagation. Consequently, the area across which plasma is predicted to be present is likely slightly different, which affects the charge transfer on the surface DBD plasma source. Additionally, the discharge volume itself is an approximation, and a more rounded off shape of the Lissajous curve is an indication of an under-prediction of the dynamic behaviour of the discharge volume. The abrupt pulse signal to simulate the transition between discharge and non-discharge phase, introduces an inaccuracy of the discharge dynamics.

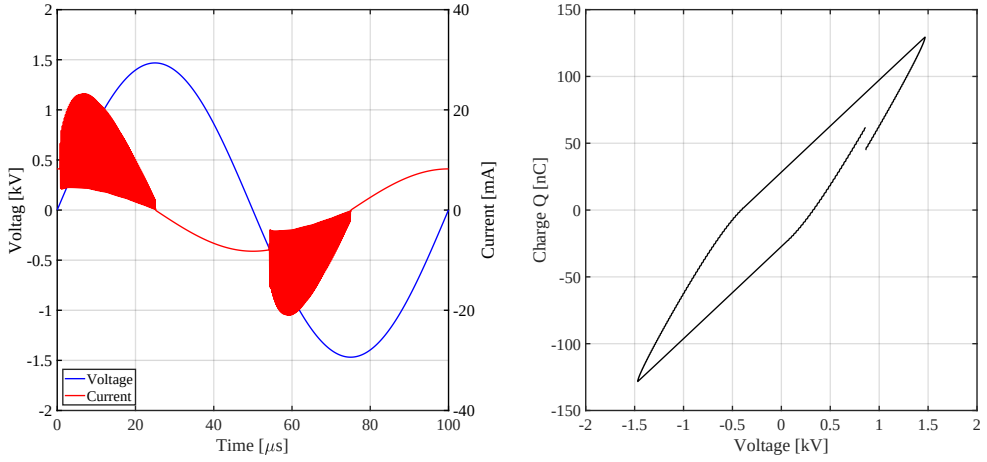

(a) (b)

FIGURE 4.15: Simulated results with 3 kV at 10 kHz (a) Voltage and current reading; (b) Lissajous graph

Assessing the accuracy of the electrical model over a large range of power conditions

and electrode configurations is achieved by analysing the experimental and predicted discharge power, P_{ave}. The discharge power is obtained from the area of the respective Lissajous graph as:

$$P_{ave} = \frac{1}{T} \oint_T V(t) dQ \tag{4.22}$$

where $V(t)$ is the applied voltage and Q the charge measured with the probe capacitor.

Figure 4.16(a) to 4.16(d) shows the average discharge power for electrode configuration #1 to #4 over the applied voltage for varying frequencies. As can be seen across all electrode designs, the discharge power scales with both the operating voltage and frequency, where an increase in either voltage or frequency results in an increasing discharge power. Comparing the four different electrode design it can be seen that the discharge power increases with an increasing electrode line width ratio.

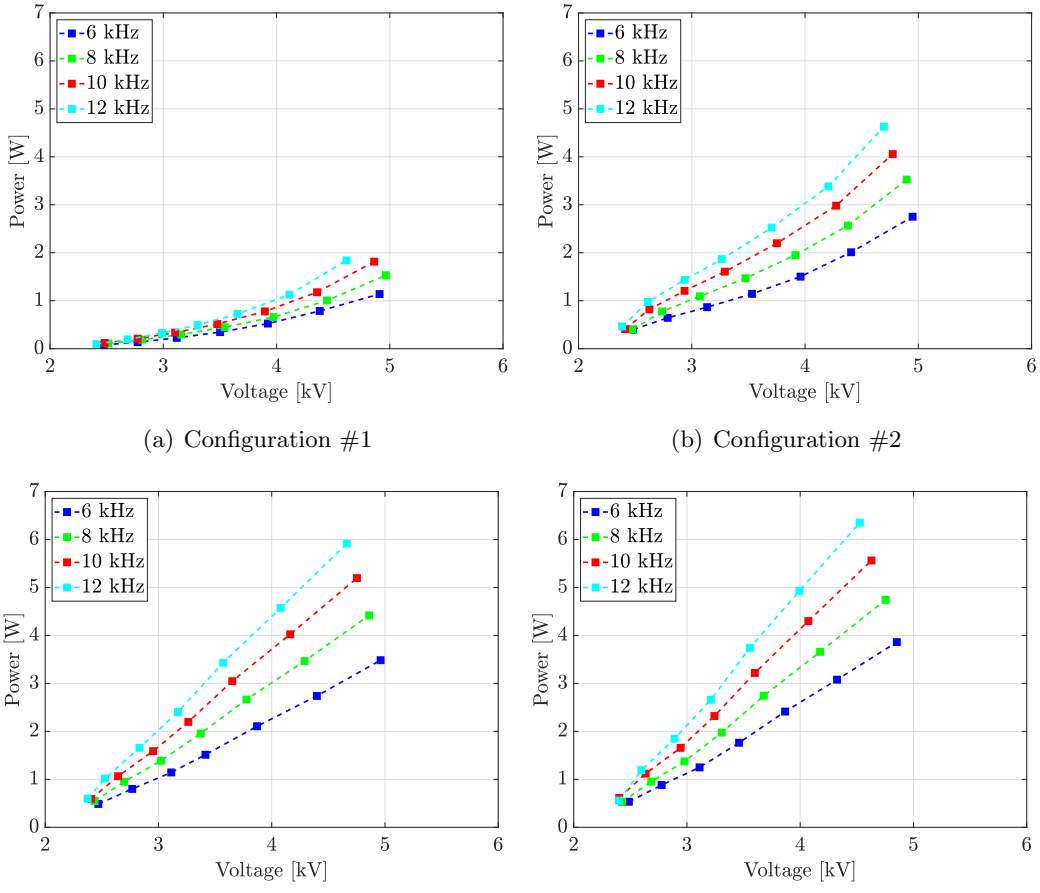

(a) Configuration #1

(b) Configuration #2

(c) Configuration #3

(d) Configuration #4

FIGURE 4.16: Experimental discharge power of electrode configuration #1 to #4

Figure 4.17 shows the images of the four different electrode configurations at the same operating conditions. For a line width ratio of one, as in electrode configuration #2, the ground and high voltage electrode have the same thickness and the local electric field is concentrated towards the edge region of one hexagonal unit. The discharge occurs

predominately within this edge region and will not stretch/exceed far into the centre of the hexagonal unit. Consequently, the discharge area is smaller, which results in a reduced discharge power. With increasing electrode line width ratio, the high voltage electrode reaches further into the centre of the hexagonal units. Similarly, the local electric field expands further towards the centre for electrode configuration #4. With this stronger electric field, the discharge area is expanded, resulting in an increase in discharge power. Additionally, charge can be deposited in the central region. Despite the electric field not being strong enough to initiate discharge here, the charge accumulation can add up to an increase in discharge power.

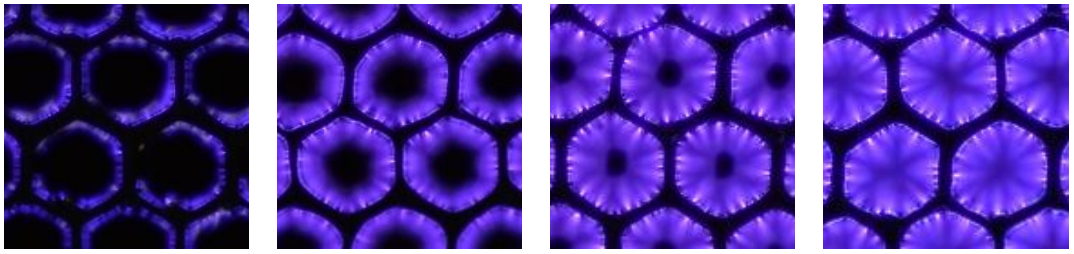

(a) (b) (c) (d)

FIGURE 4.17: Images of plasma ignition across hexagonal unit for printed electrode configurations #1 to #4 all at 4.4 kV and 6 kHz

Figure 4.18 shows additionally the comparison of the experimental and predicted discharge powers. As can be seen, the developed electrical model simulates discharge powers with good agreement to the experimentally obtained power across all electrode configurations and power conditions. For electrode configuration #1, the electrical model predicts the overall range of the discharge power reasonably well. Similar results can be observed for all four electrode configurations, where the absolute discrepancy between experimental and predicted discharge power remains constant and below a value of 0.6 W. The correlation of increasing discharge power with increasing operating voltage and frequency is predicted by the model. However, the model over-predicts the discharge power at small operating voltages and under-predicts the power for larger operating voltages. This behaviour can again be a result of inaccuracy in the definition of the discharge area/volume. Especially for small discharge power values, as seen for electrode configuration #1, a small inaccuracy in the predicted discharge volume can result in a larger relative discrepancy between experimental and predicted discharge power. It also has to be kept in mind, that the discharge propagation length, which ultimately defines the discharge volume, is only derived for an operating frequency of 10 kHz. The SDBDDesigner used for the initial assessment of the discharge propagation length, did not indicate a dependency on the operating frequency. However, for pulse signals, a dependency on the voltage gradient was reported [139], which in turn could be related to the voltage gradient in AC signals of varying frequencies. Consequently, a frequency

dependency of the discharge propagation length could have a direct impact on the discharge area/volume, thus the discharge power. Similar as discusses in chapter 3.2.2, a difference in plasma regime can also result in a varying trend of the discharge power. However, the regime characteristics of plasma generation are challenging to model, and are not included in the presented electrical model.

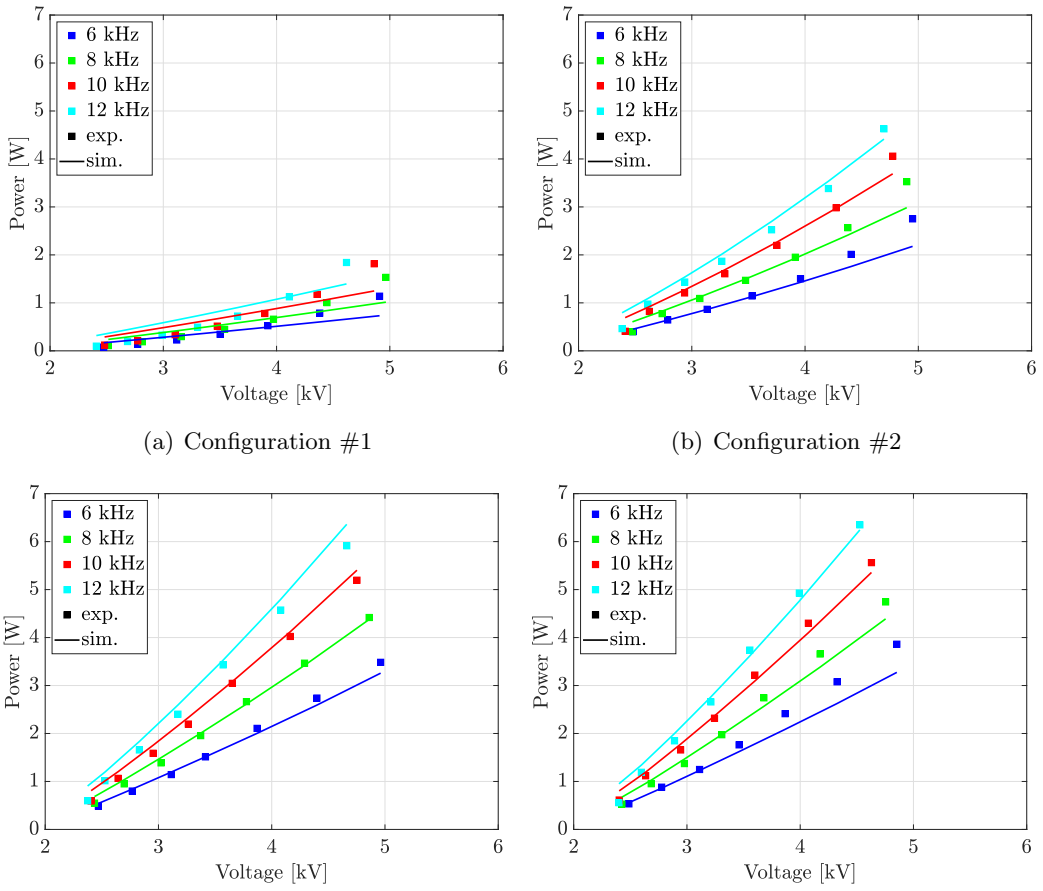

(a) Configuration #1

(b) Configuration #2

(c) Configuration #3

(d) Configuration #4

FIGURE 4.18: Experimental and simulated discharge power of electrode configuration #1 to #4

4.5 Summary

The new developed electrical model uses a segmentation approach to split the surface DBD plasma source into a discharge and non-discharge area by implementing a semi-empirical equation for the time-variable plasma discharge propagation length. The validation of the developed electrical model shows a good agreement when comparing experimental and predicted voltage and current signals, as well as prediction of the Lissajous curve. Moreover, the discharge power is derived across four presented electrode configuration and operating conditions cover a range of 2.4 to 5 kV and 6 to 12 kHz.

However, the developed electrical model has a few limitations. The model describes the transition between discharge and non-discharge phase with a sharp pulse signal, albeit the physical transition is characterised by an onset of numerous appearing microdischarges. The electrical model uses an approximation to describe the discharge propagation length of the surface DBD plasma source. This approximation is used to define the discharge area fraction and the plasma volume within the hexagonal units. The developed model relies on a semi-empirical estimation of the propagation length, which combines an analytical calculation with an estimation of the average propagation length from image recordings. As presented, the plasma volume has a direct impact on the predicted discharge power, consequently the propagation length is a key parameter for the accuracy of the electrical model.

Chapter 5

Applications of scalable and flexible plasma sources

This chapter explores three feasibility studies of surface DBD plasma sources, which significantly benefit from using printed fabrication technique. As printed electrode systems offer flexible and highly adaptive electrode geometry design, the plasma generation can be easily tailored to the different requirements of the applications. The first section, 5.1, proposes a new "Cold Radio Blackout Testing" solution using the high electron density generated by the developed plasma sources. Section 5.2 presents the use of printed DBD plasma sources as a decontamination system for PPE and medical equipment during the COVID-19 pandemic. The last section, 5.3, presents a thin and narrow plasma source, called plasma yarn, for sterilisation in narrow spaces, such as endoscopes.

5.1 Cold plasma experiment for radio blackout testing

5.1.1 Radio blackout

During atmospheric re-entry the electron density within the plasma sheath around a re-entry vehicle can causes a communication interruption, known as a radio blackout. Although the radio blackout is a phenomenon well known since the early space programs, vehicles still experience communication interruption during re-entry today [147]. Developing a strategy to maintain continuous communication during a radio blackout phase requires a clear understanding of the plasma layer around a re-entry vehicle and its interaction with electromagnetic waves.

Within the plasma sheath during re-entry flight, the electron density reaches about 10^{15} m^{-3} to 10^{19} m^{-3} [148], where a critical electron density defines the onset of the radio blackout. However, even below the critical electron density, an electromagnetic signal is

subjected to attenuation due to the spatial density gradient of the electron density. This spatial gradient can lead to incoming signals being deflected or fully reflected within a specific layer. For an accurate analysis of the radio blackout, it is important to account for the maximal, critical electron density, as well as the spatial gradient character of a re-entry plasma sheath.

Using novel printed DBD plasma sources, a new ground testing method of the radio blackout, called "Cold Radio Blackout Testing" can be proposed. The "Cold Radio Blackout Testing" procedure includes an electron density controllable non-thermal plasma source to reproduce the spatial electron density gradient of the re-entry plasma sheath. The spatial electron density gradient, which forms during hypersonic flight, can be reproduced with a "Multi-Layer DBD Plasma Source" using thin printed surface DBD plasma sources. Aiming to use thin printed surface DBD plasma sources allows to model curved and more complex re-entry vehicle shapes. Figure 5.1 shows a schematic of a plasma layer over a hypersonic vehicle surface, which can be discretised in a defined number of layers. Within each layer the plasma properties are assumed to be constant.

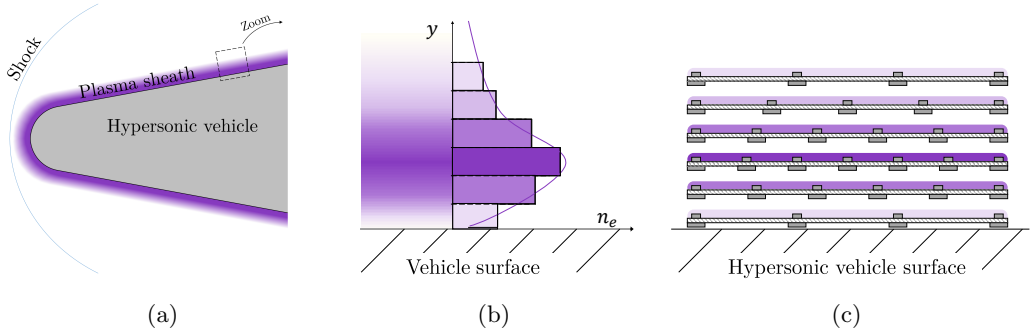

FIGURE 5.1: Schematic of discretising plasma layer using multilayer-DBD sources (a) Electron density gradient over hypersonic vehicle surface (b) multilayer-DBD sources over hypersonic vehicle surface

A stacked assembly of surface DBD plasma sources, as seen in Figure 5.1(c), can be used to generate the spatial electron density gradient. Within each layer the electron density is constant. To achieve various electron densities for the individual layers, several approaches, such as variation of geometrical configuration and operating conditions can be employed. This multilayer DBD plasma source will allow an accurate modelling of the re-entry conditions, by accounting not only for the critical electron density, but also the spatial gradient within a re-entry plasma sheath. The feasibility of the "Cold Radio Blackout Testing" is demonstrated in three main steps:

1. Electron Density measurement: Demonstrate that a printed DBD plasma source is able to generate similar electron density levels as seen during atmospheric re-entry.

2. Radar Transmissivity of printed electrode systems: Demonstrate that sufficient EM transmissivity is provided by optimising the electrode geometry of printed DBD plasma sources.

3. Controllable non-thermal plasma sources over curved re-entry vehicle: Demonstrate generation of non-thermal plasma over a scaled down version (1:35) of the ExoMars re-entry lander.

5.1.2 Electron density Estimation

Parts of the following section have been previously presented as a conference paper at the 2020 AIAA SciTech Forum in Orlando, USA [149]. The electron density of a plasma can be measured and estimated through various methods, including Langmuir probe, laser Thomson scattering and stark broadening. A Langmuir probe can offer very localised measurement of electron density, however due to the intrusive nature of the measurement technique, it is not well suited for atmospheric pressure plasmas [150, 151] and small plasma regions, such as the thin plasma layer on the surface DBD plasma sources [66]. Laser Thomson scattering is a non-intrusive measurement technique allowing high accuracy and precision measurement of the electron density, however the measurement requires a complex and expensive optical setup [152]. Stark broadening also provides a non-intrusive measurement of the electron density, using a simple setup optical emission spectroscopy setup. However the available OES system does not provide the required resolution for a successful measurement with the Stark broadening method [150, 153]. Nevertheless, the available OES can be employed to estimate the electron density of the non-thermal plasma using the line-ratio method presented by Xiao et al. [66]. The method uses optical emission spectra of atmospheric pressure air plasma, specifically the dominant nitrogen emissions of N_2(C - B), N_2^+ (B - X) and N_2(B - A). These emission states are excited by direct or step-wise electron impact as follows:

$$N_2(X^1\Sigma_g^+) + e \longrightarrow N_2(C^3\Pi_u) + e \tag{5.1}$$

$$N_2(X^1\Sigma_g^+) + e \longrightarrow N_2(A^3\Sigma_u^+) + e \tag{5.2}$$

$$N_2(A^3\Sigma_u^+) + e \longrightarrow N_2(C^3\Pi_u) + e \tag{5.3}$$

$$N_2(X^1\Sigma_g^+) + e \longrightarrow N_2(B^3\Pi_g) + e \tag{5.4}$$

$$N_2(X^1\Sigma_g^+) + e \longrightarrow N_2^+(B^2\Sigma_u^+) + 2e \tag{5.5}$$

$$N_2(A^3\Sigma_u^+) + e \longrightarrow N_2^+(X^2\Sigma_g^+) + 2e \tag{5.6}$$

$$N_2^+(X^1\Sigma_g^+) + e \longrightarrow N_2^+(B^2\Sigma_u^+) + e \tag{5.7}$$

The emission intensity of excitation state N_2(C - B) at 337 nm and N_2^+ (B - X) at 391 nm are defined as:

$$I_{N_2}(C-B,0-0) = Q_{N_2(C)} \cdot N_{N_2} \cdot k_{N_2(C)} \cdot V_{plasma} \cdot n_e, \tag{5.8}$$

$$I_{N_2^+}(B-X,0-0) = Q_{N_2^+(B)} \cdot (N_{N_2} \cdot k_{N_2^+(B)} + N_{N_2^+} \cdot k^+_{N_2^+(X)}) \cdot V_{plasma} \cdot n_e, \tag{5.9}$$

where Q are the quenching factors, k are the excitation rate coefficients, N is a number density, V_{plasma} is the plasma volume and n_e is an electron density. The excitation rate coefficients $k_{N_2(C)}$, $k_{N_2^+(B)}$ and $k^+_{N_2^+(B)}$ are obtained with the open-source program BOLSIG+ [154]. The program uses the electron energy distribution function (EEDF ($f_v(E)$)) and excitation cross section σ_{exc} for the calculation of the excitation rate coefficients:

$$k_{exc} = 4\pi\sqrt{2}\int_0^\infty f_v(E)\sqrt{\frac{2e}{m_e}} \cdot \sigma_{exc}(E)dE, \tag{5.10}$$

where e is the elementary electron charge, m_e the elementary electron mass and E is the kinetic energy of electrons (in eV). The excitation cross sections for $k_{N_2(C)}$ and $k_{N_2^+(B)}$ are obtained from the Phelps database [155] and the excitation cross section for $k^+_{N_2^+(B)}$ from Crandall et al. [156]. The excitation rate coefficients are calculated as a function of the reduced electric field, $\frac{E}{N}$, using the BOLSIG+ code [154]. The magnitude of the reduced electric field $\frac{E}{N}$ is approximated as $\frac{V_{rms}}{N \cdot t}$, with the applied voltage to the plasma source, V_{rms}, the effective distance, t, between both the electrodes, and the background neutral density of $N = 2.504 \cdot 10^{25} m^{-3}$.

The quenching factors $Q_{N_2(C)}$ and $Q_{N_2^+(B)}$ are defined as:

$$Q_{N_2(C)} = \frac{A_{N_2(C)}}{A_{N_2(C)} + k_{qN_2}^{N_2(C)} \cdot N_{N_2}}, \tag{5.11}$$

$$Q_{N_2^+(B)} = \frac{A_{N_2^+(B)}}{A_{N_2^+(B)} + k_{qN_2}^{N_2^+(B)} \cdot N_{N_2}}. \tag{5.12}$$

where A are the Einstein coefficients [157] and N_{N_2} is the number density of nitrogen in air, $1.98{\cdot}10^{25} m^{-3}$. The Einstein coefficients are the probability of emission for the excited state and are obtained from the NIST data base [91] as $1.27 \cdot 10^8 s^{-1}$ and $7.56 \cdot 10^7 s^{-1}$, for $A_{N_2(C)}$ and $A_{N_2^+(B)}$ respectively. The rate coefficients $k_{qN_2}^{N_2(C)}$ and $k_{qN_2}^{N_2^+(B)}$ are for quenching of $N_2(C)$ and $N_2^+(B)$ due to collision with N_2. Their values can be found in literature as $k_{qN_2}^{N_2(C)} = 0.31 \cdot 10^{10} cm^3 s^{-1}$ [158] and $k_{qN_2}^{N_2^+(B)} = 8.84 \cdot 10^{10} cm^3 s^{-1}$ [159].

The electron density is estimated with the assumptions of a quasi-neutral plasma and the number density $N_{N_2^+}$ approximated as the electron density [66]. These assumption

with equations 5.8 to 5.12 deliver the following description for the electron density as a function of the line ratio $\frac{I_{N_2^+}(B-X,0-0)}{I_{N_2}(C-B,0-0)}$:

$$n_e = \frac{\frac{I_{N_2^+}(B-X,0-0)}{I_{N_2}(C-B,0-0)} \cdot Q_{N_2(C)} \cdot N_{N_2} \cdot k_{N_2(C)} - Q_{N_2^+(B)} \cdot N_{N_2} \cdot k_{N_2^+(B)}}{Q_{N_2^+(B)} \cdot k^+_{N_2^+(B)}}. \tag{5.13}$$

Equation 5.13 is used to estimate the electron density of surface DBD plasma source with a hexagonal electrode configurations. The electrode geometry is varied in unit size (1 mm, 2 mm and 4 mm) and linewidth (0.1 mm, 0.25 mm and 0.5 mm) to analyse the effect on the electron density. The operating conditions for the printed plasma sources are varied in a range from 4 to 12 kV and 2 to 4 kHz.

Figure 5.2 shows the estimated electron density n_e over the calculated power for varying geometrical configurations. As can be seen, the electron density ranges between $10^{17}m^{-3}$ and $10^{22}m^{-3}$, which coincides with the electron density range reached at atmospheric re-entry [148], thus can be used to model the physical phenomena related to the electron density in the re-entry plasma layer.

Figures 5.2(a) shows the electron density for varying unit size of the hexagonal pattern. As can be seen, small 1 mm unit sized plasma sources provide high estimated electron densities, ranging above $10^{22}m^{-3}$. However 4 mm unit sized plasma sources have electron densities ranging over a spectrum from $10^{17}m^{-3}$ up to $10^{22}m^{-3}$. Here the electron density increases with an increasing operating power, P_{ave}.

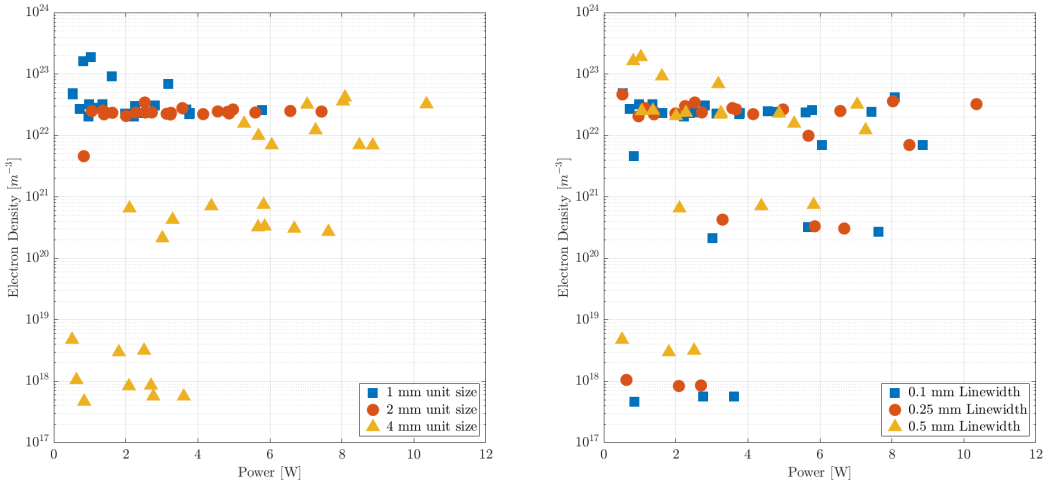

(a) (b)

FIGURE 5.2: Electron Density n_e over spectral intensity for varying power conditions and geometry configurations (a) varying unit size (b) varying line width

Increasing electron density, n_e, with smaller unit sizes, can be caused by a stronger electric field within one unit. Figure 5.3(a) shows a schematic of the plasma generation within hexagonal units. Case # 1 symbolises a hexagon cross section with a small unit, whereas Case # 2 has a larger unit size. Case # 2 and # 3 both have the same unit size and their difference only lies within the linewidth of the ground electrode pattern, with case # 3 having a smaller linewidth. Additionally, the electron density distribution is schematically shown in case # 1 to # 3 for similar power conditions and the electron density distribution $n_e(x)$ with the mean electron density $\overline{n}_e$ is shown in Figure 5.3(b). A smaller unit size (Case 1) leads to a strong electric field in the unit centre and a stronger ionization, resulting in a plasma with high electron densities. However, larger unit sizes or a smaller line width (Case # 2 and # 3)), give a weaker electric field in the centre of the unit. This consequently leads to a weaker plasma in the unit centre and therefore with a lower mean electron density.

Figure 5.3(c) shows the ignited plasma across a grid pattern plasma source, where the varying plasma intensity across one unit can be observed. As can be seen, the plasma intensity in the centre of a unit is notably decreased in comparison towards the edge region. Therefore, a desired mean electron density $\overline{n}_e$ can be achieved with the appropriate choice of unit size and line width of a printed electrode pattern.

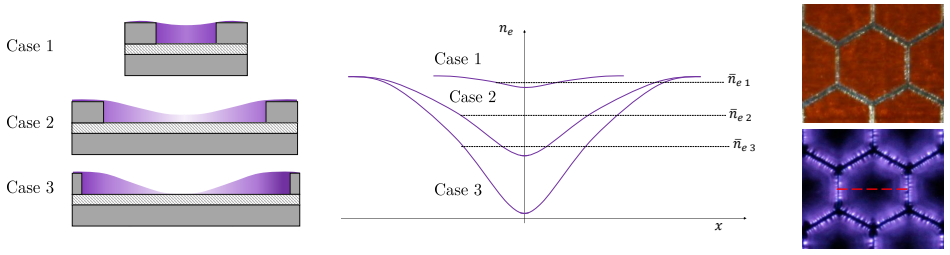

(a) (b) (c)

FIGURE 5.3: (a) Schematic of plasma and electron density distribution across plasma source units with varying geometrical configurations (b) Image of grid pattern plasma source generation with unit size 4 mm (c) Derived Image intensity profile across one unit

Based on the presented correlation, it can be concluded, that the mean electron density, $\overline{n}_e$, of printed DBD plasma sources can be controlled by changing geometrical configurations and/or operating power conditions.

5.1.3 Radar transmissivity of printed electrode

The electrode of the DBD plasma source is printed using conductive metallic ink, which can influence the propagation of electromagnetic (EM) waves. The signal attenuation induced by the metallic electrode depends on the frequency/wavelength of the used EM

signal and the dimension of the printed electrode geometry. The disturbance of the printed electrode on EM wave propagation is minimized by ensuring the wavelength of an EM signal is smaller than the characteristic dimension of the plasma source, such as the unit size of a hexagonal electrode geometry. Only with a characteristic electrode dimension larger than the wavelength, transmission through the plasma source can be achieved.

The transmissivity of printed electrode designs is assessed using radar sensor system from Acconeer. The Acconeer radar sensor system is a single chip system which offers minimal system complexity at low cost to measure the transmissivity. The A1 Acconeer radar sensor contains an embedded antenna for transmission and reception of the 60 GHz ($\lambda = 5$ mm) pulsed coherent radar signal. The beam opening of the sensor signal is 40° and 80° in E-plane and H-plane, respectively. Additional dielectric lenses can focus the beam opening down to 12° for both E-plane and H-plane. The transmitted radar signal is sent out up to a distance of several meters. The signal is reflected by any obstacle within the beam path and the amplitude and phase of the reflected signal is provided as output by the sensor system.

The radar transmissivity of metallic electrode is characterised using a semi-open small-scale anechoic chamber. Figure 5.4(a) shows the chamber setup, with the radar sensor fixed in a holder and positioned facing the target and the printed electrode design. Figure 5.4(b) shows the small-scale anechoic chamber build for the radar transmissivity testing.

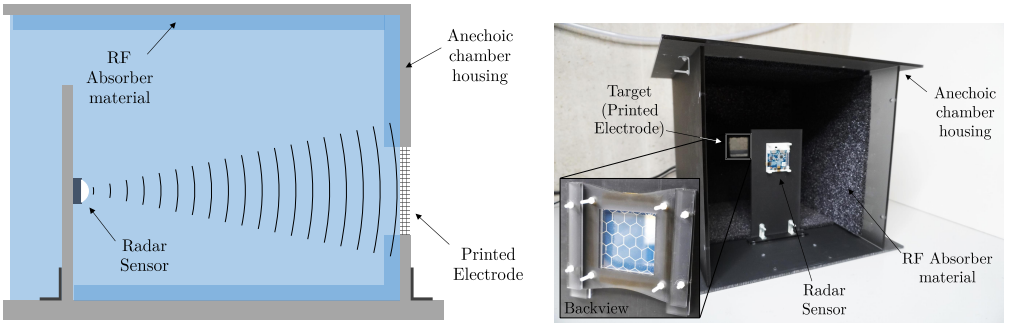

(a) (b)

FIGURE 5.4: (a) Schematic of anechoic chamber with radar sensor and printed electrode (b) Picture of anechoic chamber with backview of printed electrode

The samples of printed electrode designs are mounted in a holder, which can be placed into an opening in the back chamber wall. The distance, d, between the radar sensor and the target has to satisfy the far field condition with:

$$d \geq \frac{2 \cdot (L_{ant.})^2}{\lambda}, \tag{5.14}$$

where $L_{ant.}$ is the characteristic length scale of the antenna. Beyond the target holder a stainless steel metal plate is placed. The chamber is made of 5 mm acrylic sheets, which can lead to added reflection patterns of the radar signal. In order to minimize reflection foam absorbent material (Laird Eccosorb HR-10) is used to line the interior walls of the chamber. The absorber material provides signal attenuation of up to -24 dB at a frequency of 60 GHz.

Figure 5.5 shows all four different samples and in table 5.1 the different geometries, materials and their characteristics dimensions are listed. As these samples only assess the RF transmissivity, only a single layer printed electrode pattern is required. Additionally, one sample of the dielectric substrate is used as a reference sample and one sample using copper tape instead of a printed electrode pattern is assessed. Given the wavelength of the radar signal of 5 mm, a hexagonal printed electrode pattern with a unit size of 2 mm will act as a reflective surface and only larger units size of 8 mm and 12 mm will allow signal transmission. Using line pattern rather than a hexagonal pattern will allow signal transmission for larger wavelength bands.

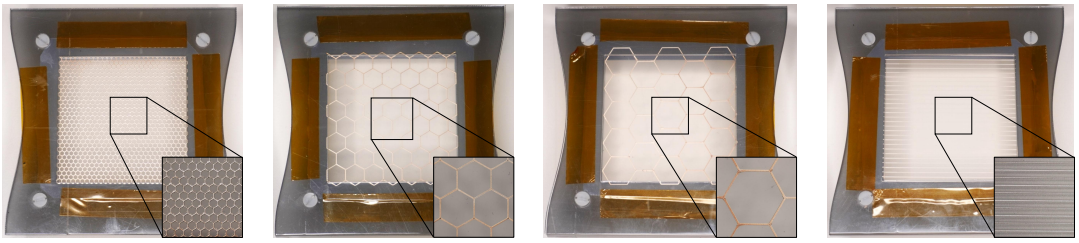

(a) Hexagon 2 mm (b) Hexagon 8 mm (c) Hexagon 12 mm (d) Line 2 mm

FIGURE 5.5: Printed electrode patterns (a) Hexagonal pattern with unit size of 2 mm (b) Hexagonal pattern with unit size of 8 mm (c) Hexagonal pattern with unit size of 12 mm (d) Line pattern with unit distance of 2 mm

Description	Geometry	Material	Characteristic Size
Substrate	none	none	none
Line 2 mm	Line pattern	Printed silver ink	2 mm
Hex 2 mm	Hex pattern	Printed silver ink	8 mm
Hex 8 mm	Hex pattern	Printed silver ink	12 mm
Hex 12 mm	Hex pattern	Printed silver ink	2 mm
Copper	Full coverage	Copper	-

Table 5.1: Radar transmissivity testing

Figure 5.6(a) shows the amplitude response of the RF signal for the different samples. The distance from sensor to the sample holder is at 36 cm, and to the metal back plate is 46 cm. As can be seen, the amplitude distributions are distinct by two peaks, one at

a distance of 36 cm and one at 46 cm. A thin copper film results in a large amplitude of the reflected RF signal at the target distance, whereas a dielectric substrate leads to a low amplitude of the reflected RF signal.

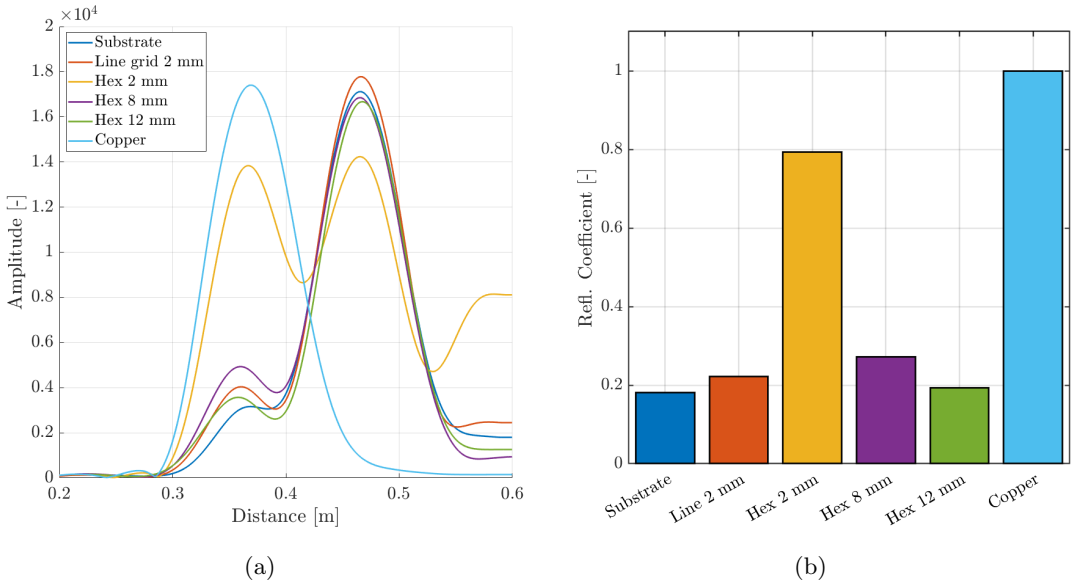

(a) (b)

FIGURE 5.6: Printed electrode patterns (a) Hexagonal pattern with unit size of 2 mm (b) Hexagonal pattern with unit size of 8 mm (c) Hexagonal pattern with unit size of 12 mm (d) Line pattern with unit size of 2 mm

Comparison of the printed electrode patterns shows the high amplitude response for a hexagonal pattern with a unit size of 2 mm. The wavelength of the RF signal with 5 mm is larger than the unit size of 2 mm, therefore no RF signal is transmitted through and the printed electrode pattern acts as a reflective surface. Electrode pattern with unit sizes larger than the wavelength of the RF signal (unit size of 8 mm and 12 mm), are characterised by low amplitudes at the specific distance, thus allow for RF transmission. The amplitude is used to define the reflective coefficient of the different samples as:

$$C_{refl.} = \frac{Amp_{Sample}}{Amp_{ref.}} \tag{5.15}$$

where Amp_{Sample} is the amplitude of the respective sample at the target distance and $Amp_{ref.}$ the amplitude of a metallic reference sample at the target distance. The amplitude response from the copper film is used as the metallic reference sample. Figure 5.6(b) shows the reflective coefficient for the different samples. As can be seen, the reflective coefficient for a substrate without any printed electrode pattern is low with a value of $C_{refl.} = 0.18$. Using a line pattern with 2 mm distance, leads to a small increase in reflective coefficient. However a hexagonal pattern with a 2 mm unit size results in a significant increase of the reflective coefficient of $C_{refl.} = 0.8$. Increasing the unit size and exceeding the RF wavelength, the reflective coefficient reduces significantly to

$C_{refl.} = 0.2$ for a 12 mm unit size. This demonstrates, that with an appropriate design of a printed electrode, the reflectivity can be significantly reduced to ensure transmission of RF waves.

5.1.4 Controllable non-thermal plasma sources over re-entry vehicle

The cold radio blackout testing uses a multilayer DBD plasma source to model the spatial electron density gradient over hypersonic re-entry vehicle. The generation of non-thermal plasma over a hypersonic re-entry vehicle is demonstrated using a printed electrode design over a scaled down version of the Schiaparelli EDM lander. The Schiaparelli EDM lander is a re-entry vehicle for the ExoMars programme of the European Space Agency (ESA) [160]. It is chosen due to its topicality and relevance in the European space sector. Figure 5.7 shows a 3D printed model of the ExoMars lander of a scale of 1:35. On the bottom side of the lander model, two plasma sources are attached, intending to resemble the plasma build up during atmospheric re-entry, see Figure 5.7(b). The plasma source electrodes are designed in accordance with the findings of EM transmissivity of printed electrodes. Using a closed pattern, such as a hexagonal pattern, it has to be ensured, that the characteristic length of the pattern is larger than the electromagnetic wavelength. Choosing a line pattern ensures transmission for a larger wavelength range. The electrode design shown in Figure 5.7(b) consists of two plasma sources with concentric lines.

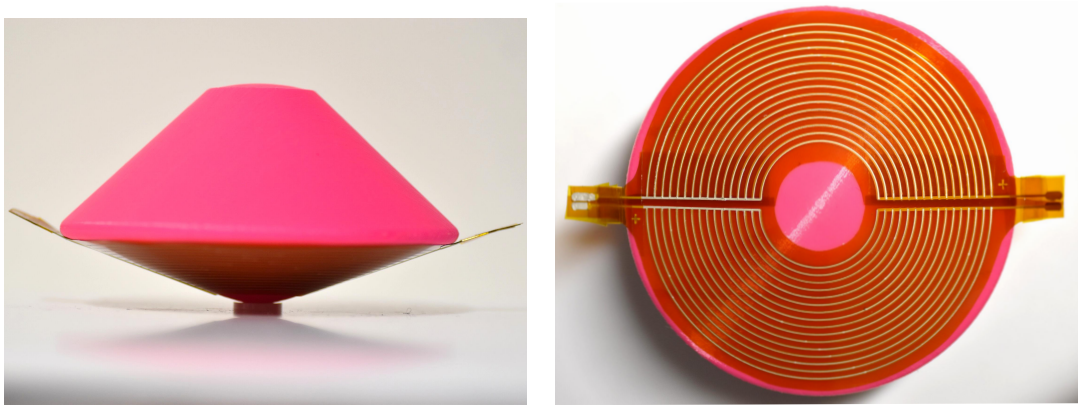

(a) (b)

FIGURE 5.7: 3D printed ExoMars model with plasma source attached

Figure 5.8 shows the ExoMars model with plasma generation. The plasma sources were ignited at 6 kHz for voltages ranging from 2 to 3 kV. As can be seen, the plasma generation is non-uniform at lower voltage and reached uniformity at an operating voltage of 2.6 kV. The electron density for the generated non-thermal plasma is estimated based on the method presented in section 5.1.2, with values ranging between $10^{18} m^{-3}$ to $10^{21} m^{-3}$.

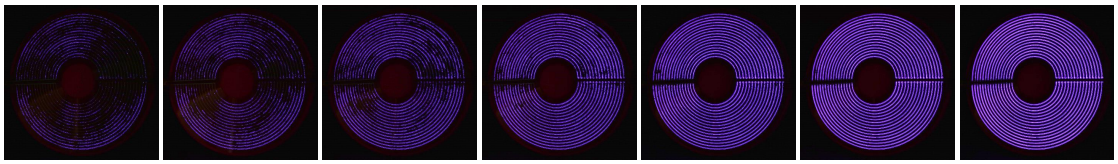

FIGURE 5.8: 3D printed ExoMars model with plasma generation for varying voltages

5.1.5 Summary

This section demonstrated the potential of printed non-thermal DBD plasma sources for a new "Cold radio blackout testing" method to model the spatial electron density gradient over hypersonic re-entry vehicle. The spatial electron density gradient plays an important role to accurately predict radio blackout through plasma and electromagnetic wave interaction. It was demonstrated that the electron density of a printed plasma source can be controlled through varying electrode geometries and operating conditions, reaching electron densities in a range of $10^{17} m^{-3}$ to $10^{22} m^{-3}$. As the DBD plasma source consists of two printed metallic electrodes, thus the propagation of electromagnetic waves can be influenced. The radar transmissivity of printed plasma source can be ensured by accounting for the wavelength of the electromagnetic signal in the design of the electrode pattern. A line pattern allows transmission for a large range of EM signals, whereas a closed pattern, such as a hexagonal pattern, can lead to high reflectivity when the unit size is below the size of the wavelength of transmitting EM signal. A printed DBD plasma source using a line electrode pattern is applied to a scaled down re-entry model (ExoMars), where a uniform plasma generation is achieved with electron densities ranging between $10^{18} m^{-3}$ to $10^{21} m^{-3}$.

5.2 Decontamination system for PPE and medical equipment

The presented research in the following section was carried out in cooperation with project partner from the Aerodynamics and Flight Mechanics group and the School of Biological Sciences of the University of Southampton and parts have been previously published in the journal AIP Advances [161]

5.2.1 Introduction

In times of a global pandemic, such as the COVID-19 pandemic, filtering facepiece respirators (FFRs) not only play crucial role for the protection of front-line healthcare workers, but also for the general public. N95 and N99 mask present a high filtration ability of >95 % [162] and have been highly recommend by the World Health Organization (WHO) and even been made mandatory in some nations [163]. The sudden spike in demand for the single-use FFRs resulted in a global shortage of FFRs and personal-protection-equipment (PPE) in general. This leaves especially healthcare workers at the front-line of the pandemic at an increased risk for infection [163]. Additional concerns have been raised due to the high environmental impact of single-use PPE the global pandemic has caused [164]. Addressing these concerns requires the reuse of PPE and to ensure no risk of contamination, a proper decontamination procedure is required.

Decontamination methods for PPE and FFRs in specific have been previously investigated, using ultraviolet germicidal irradiation (UVGI) [165, 166], vaporous hydrogen peroxide (VHP) [166], dry or moist heat [166, 167] and bleach [168]. Even though some of these methods show successful decontamination, some safety and performance concerns remain. Residues from for example decontamination using bleach or hydrogen peroxide can cause skin irritation, thus making these methods unsuitable for FFRs. Furthermore, heat and chemical treatment, such as ethanol, can result in physical damage to the mask itself. This results in loss of filtration efficiency and consequently making the mask unsuitable for reuse [169]. The use of non-thermal plasma as a decontamination method has been demonstrated previously, as it can inactive up to 99.9 % of various viruses [170, 171]. Non-thermal plasma generates reactive species, such as highly reactive hydroxyl ($OH^{\cdot}$), which is also produced by hydrogen peroxide. Decontamination with hydrogen peroxide is officially recognized as a SARS-CoV-2 disinfectant, however remains unsuitable due to its skin irritation risk. Consequently, non-thermal plasma presents as an interesting candidate for the decontamination for FFRs. With non-thermal plasma, no residue of reactive hydroxyl species remain due to fast recombination after the non-thermal plasma treatment.

This section presents the use of printed surface DBD plasma sources generating non-thermal plasma for the decontamination of FFRs. The project focuses on three main parts, the plasma decontamination system and the demonstration of decontamination and filtration efficiency tests:

1. Plasma Decontamination system: Design and fabrication of a compact and portable power supply unit and a non-thermal plasma generator using printed non-thermal plasma sources.

2. Decontamination efficiency tests: Demonstrate decontamination of SARS-CoV-2 on N95 and N99 mask samples using the compact and portable plasma decontamination system in a Bio-Containment Level 3 cabinet.

3. Filtration efficiency tests: Demonstrate filtration efficiency of plasma treated N95 and N99 mask samples through particle image velocimetry technique to ensure satisfying performance after the decontamination procedure.

5.2.2 Plasma decontamination system

The plasma decontamination of FFRs is carried out using printed non-thermal plasma sources. The surface DBD plasma sources are printed on polyamide film (Kapton, 75 μm) using conductive ink over an area of 38 x 38 mm^2 in a hexagonal electrode geometry to achieve a highly uniform plasma generation. A small sample is cut from the N95 or N99 mask and placed in mask holder and secured at a fixed distance to a surface DBD plasma source. Figure 5.9(a) shows a mask of type N99 (F631, JSP) used in this study. In Figure 5.9(b) the mask holder containing the mask sample of size of a size 38 x 38 mm^2 can be seen. During the filtration efficiency testing, the mask holder is placed on top of the planar plasma source for treatment. Figure 5.9(c) shows the mask holder in close proximity to the generated plasma.

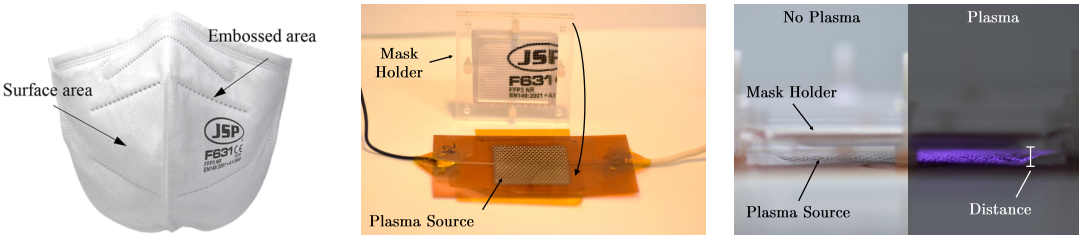

(a) (b) (c)

FIGURE 5.9: (a) Filtering facepiece respirators with highlighted surface and embossed area (b) Prepared mask sample in mask holder and plasma source (c) Mask holder placed on plasma source for treatment with plasma

The decontamination efficiency testing cannot be carried out in the plasma lab as the SARS-CoV-2 requires containment in a level 3 lab. Therefore, a portable and compact power supply system for the decontamination testing is designed. As the tests are carried out in a Bio-Containment Level 3 cabinet, specific requirements have to be met during the design and development steps. The Bio-Containment Level 3 cabinet uses an interlock system for access to the cabinet. The interlock systems pose size limitations on the maximum size of the power supply system, which is built inside a portable and compact polycarbonate enclosure of 300 mm x 300 mm x 180 mm. The enclosure is a fully sealed system with IP rating IP66/67, to withstand the formaldehyde fumigation cycle in the Bio-Containment Level 3 cabinet. The enclosure houses the power processing unit

(PPU), which is based on the same system components as the lab based power supply setup presented in chapter 2.3, see Figure 5.10(a). It consists of a signal generator (XR2206 Signal Generator Function, KKmoon), providing a sinusoidal signal. The signal is used as an input for a class D audio amplifier (UM60 Compact Mixer-Amplifier, Adastra), providing signal output up to 100 Vpp. The last stage consists of a high voltage step-up transformer (CMI-4967, Corona Magnetics) generating an output of up to 4 kVpp. All PPU components are mounted in the portable enclosure to ensure a fit through the interlock system of the Bio-Containment Level 3 cabinet. A plasma source mount is connected to the PPU through a double insulated power cord.

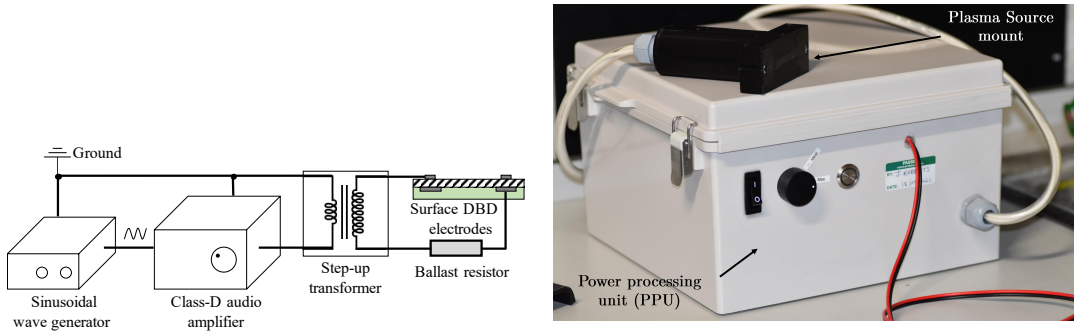

(a) (b)

FIGURE 5.10: Portable plasma decontamination system which consists of a power processing unit, plasma brush wand, and electrode cartridge: (a) Layout of a plasma brush decontamination system; (b) Picture of the assembled plasma decontamination system [161]

The plasma source mount is shown in Figure 5.11. It consists of a cylindrical handle and a push-fit attachment system for the electrode cartridge. Two spade connectors form the push-fit system, which allows easy exchange between different cartridges. The cartridge uses a sandwich system to hold the printed surface DBD plasma source and both spade connectors in position to ensure precise/correct mounting at the plasma source mount. Figure 5.10 shows the developed PPU including the plasma source mount and the electrode cartridge. The plasma source is consistent with the plasma source used for the filtration efficiency testing.

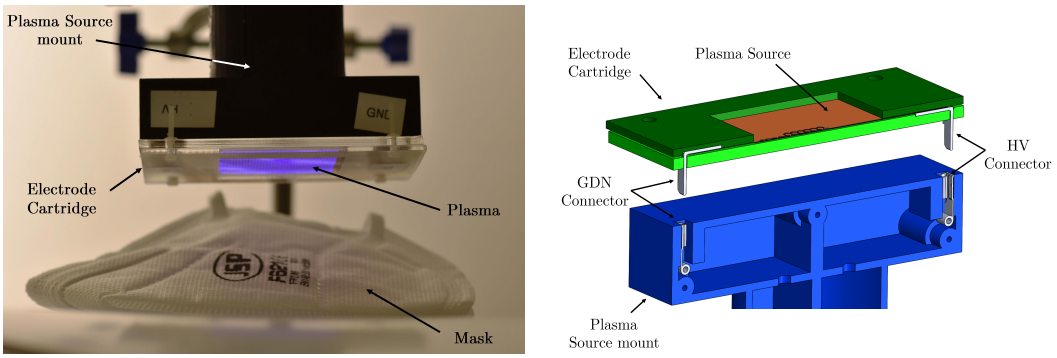

(a) (b)

FIGURE 5.11: (a) Plasma source mount and electrode cartridge; (b) Schematic of push-fit system [161]

5.2.3 Results

In this section the performance of the developed plasma decontamination system for FRRs is presented and both filtration and decontamination efficiency are assessed.

Plasma dose

During the filtration and decontamination efficiency testing it is necessary to ensure constant plasma conditions to allow reliable comparison. The performance of the plasma decontamination procedure is analysed by defining the plasma dose, D, to quantify the amount of plasma exposure during various treatment times. The plasma dose is defined as :

$$D = \frac{P_{ave} \cdot t_{treat}}{A_{treat}} \tag{5.16}$$

where P_{ave} is the time average discharge power, t_{treat} the treatment time and A_{treat} the area of the plasma source. Figure 5.12(a) shows the measured voltage and current from the plasma decontamination system. The plasma source is operated with 4 kV at 6 kHz. Figure 5.12(b) shows the Lissajous graph, with the typical parallelogram shaped curve having blunt edges. The time average discharge power is calculated as the area within the Lissajous curve, which is 5.45 W.

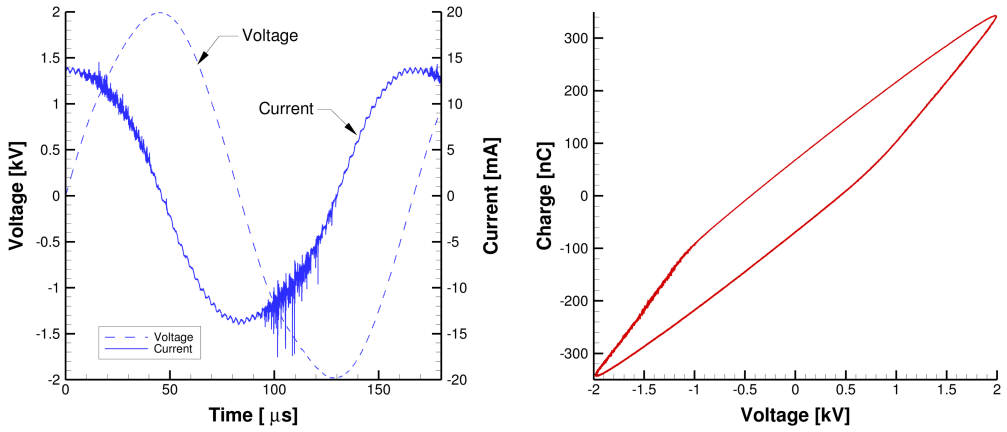

(a) (b)

FIGURE 5.12: (a) Measured voltage and current and (b) Lissajous figure of the plasma source [161]

During filtration and decontamination efficiency testing, the samples from the N95 and N99 mask are exposed to the non-thermal plasma for varying treatment times, which are 5 minutes, 10 minutes and 30 minutes With the three treatment times, the plasma dose is calculated to be 113.2 J/cm^2, 226.5 J/cm^2, and 679.4 J/cm^2, respectively.

Filtration efficiency

The filtration efficiency tests are carried out in the plasma lab using the high voltage power supply system presented in chapter 2.3. The filtration efficiency testing is performed by treatment of mask samples for various times. The plasma treatment is performed in the plasma lab, where they are exposed to the plasma dose stated in the previous section. Subsequently the mask samples are passed on the project partners from the Aerodynamics and Flight Mechanics group of the University of Southampton to assess the filtration efficiency. The filtration efficiency is quantified through planar particle image velocimetry (PIV) technique. The test procedure is performed based on the standard for Filtering testing for Respiratory Protective Devices (BS-EN 149 standard [172]). However due to difference in the system and setup, the obtained filtration efficiency is interpreted relative to a measured control mask sample, rather than direct comparison to the efficiencies provided in the standard. Figure 5.13 shows the filtration test setup, consisting of an aerosol generator injecting sodium chloride (NaCl) into a settling chamber. Here the aerosol is allowed to dry and with a fan assisted air system pressuring the chamber, the aerosol is driven into a square test section. Within the transparent test section, the mask sample is placed perpendicular to the flow, generating two regions, upstream and downstream of the mask sample. A 200 mJ pulsed Nd:YAG laser (Litron Bernoulli 200-15 PIV) laser system generates a planar laser sheet,

illuminating both the upstream and downstream region within the test section. Images of both regions are recorded using a CMOS camera.

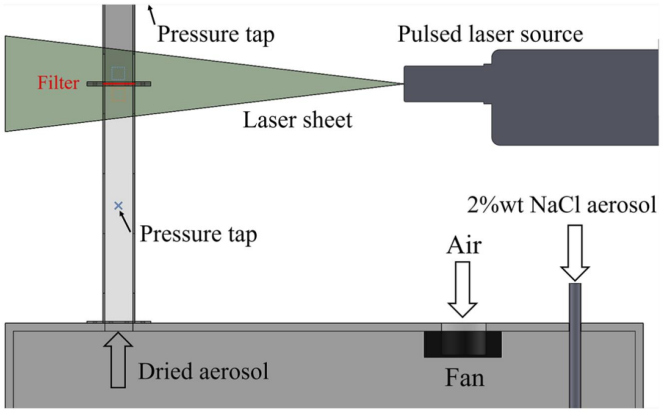

FIGURE 5.13: Schematic of filtration test setup [161]

Post-processing of the recorded images includes the identification of particles as local intensity maxima over a region of equal size upstream and downstream. The particle density in both regions is calculated as :

$$\rho = \frac{N_{PIV}}{A_{PIV} \cdot t_{LS}} \tag{5.17}$$

where N_{PIV} is the umber of particles averaged over 50 images, A_{PIV} the physical area of the region and t_{LS} the thickness of the laser sheet, which is $t_{LS} \approx 0.7$mm. The transmission T_{PIV} through a mask sample is calculated as the relative particle density between the downstream, ρ_{dow}, and upstream, ρ_{up} region as:

$$T_{PIV} = \frac{\rho_{dow}}{\rho_{up}} \tag{5.18}$$

The transmission with no filter in the test section is measured to be $T_{PIV} = 0.97 - 1.12$. Figure 5.14(a) shows the measured transmission for both N95 and N99 mask samples. As can be seen, the transmission of an untreated samples (0 minutes treatment time) fluctuates over various magnitudes, with some measurements showing a transmission of 1 % and 6 %, thus exceeding the thresholds (red dotted line) of the BS-EN 149 standard. This effect is likely linked to the difference filtration test procedure described above. For both, N95 and N99 mask samples, the transmission after a 5 minutes and 10 minutes plasma treatment is in the similar range as the untreated control mask sample. However it can be seen, that for both N95 and N99 mask samples, after a 30 minutes plasma treatment, the transmission ranges an order of magnitude above the transmission obtained from the respective control mask sample. It can be concluded, that the filtration efficiency remains constant for plasma treatment times of 5 minutes

and 10 minutes, however a 30 minutes plasma treatment inflicts changes to the mask samples resulting in a significant reduction of filtration efficiency.

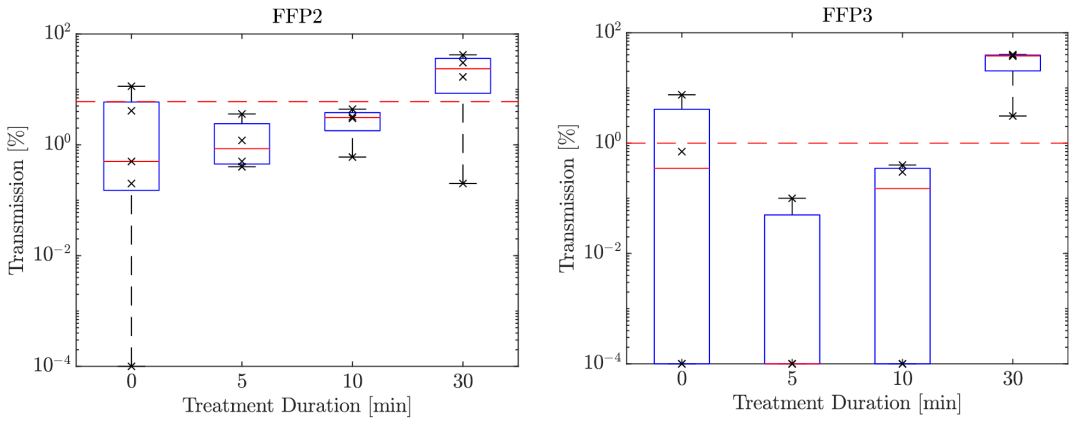

FIGURE 5.14: Aerosol transmission for (a) N95 masks (b) N99 masks [161]

Decontamination efficiency

The decontamination tests are carried out using the portable and compact plasma decontamination system presented in section 5.2.2. The systems as well as all mask samples are passed on the projects partners in the School of Biological Sciences from the University of Southampton, where the following tests are carried out. From both N95 and N99 mask, two samples are used each to represent the two distinct regions across the mask, see 5.9(a). One sample is taken from a flat surface area and one samples is taken from the embossed area on a mask, in order to assess potentially different behaviour of the decontamination procedure. The decontamination tests are carried out in Bio-Containment Level 3 cabinet using SARS-CoV-2 (B.1.1.7 strain) from Porton Down, UK. The N95 and N99 mask samples are contaminated by pipetting 2 μl virus stock on the sample (also called spiked, with "spike" representing a droplet) and left to dry for 1 h. The contaminated mask samples are secured on a plastic support for treatment. The treatment is performed by securing the plasma source mount with the electrode cartridge at a distance of 1 mm to the mask samples for treatment times of 2 minutes, 5 minutes and 10 minutes. After the plasma treatment, the spiked area is washed with infection medium which is then transferred onto a SARS-CoV-2 sensitive cell monolayer. During incubation for 3 days at 37 °C, any virus remaining after treatment infects a cell and replicates until breaking down (also called lysing) the infected cells. This leads to further infection in neighbour cells in the monolayer, creating an area of lysed dead cells termed plaque. Subsequently, the monolayer is stained to visualise the number of plaques and quantify the number of virions which survived treatment. Figure 5.15 shows exemplary wells from a 6-well microplate with the monolayer, where Figure 5.15(a) and 5.15(b) show the negative and positive control, respectively. Figure 5.15(c) shows a

monolayer from a N95 mask samples after 2 minutes of plasma treatment. A purple colour indicates and intact monolayer, whereas the absence of stained cells indicates contamination with SARS-CoV-2 and subsequent cytolysis spreading (disintegration of one cell) from one infected cell, forming a cytolysis plaque (white regions). The cytolysis plaques seen in Figure 5.15(c) indicate remaining contamination from a mask sample. In this region a virion surviving the plasma treatment was able to replicate during the incubation time. The decontamination efficiency is quantified by assessing the amount of cytolysis plaques in a monolayer relative to the negative control.

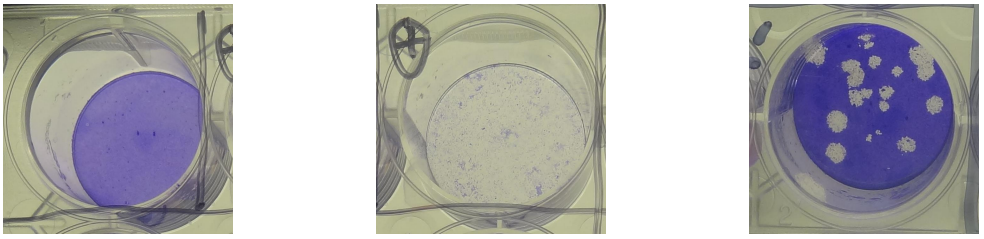

(a) (b) (c)

FIGURE 5.15: Pictures of cell monolayers in a 6-well plate (a) negative control (not contaminated) (b) positive control (contaminated) (c) N95 mask samples after 2 minutes of plasma treatment

Figure 5.16 shows the obtained decontamination efficiency for both N95 and N99 masks. As can be seen, a moderate reduction in viral load is obtained for mask samples after a treatment time of 2 minutes, whereas a plasma treatment time of 5 minutes resulted in a significant reduction in the residual viral load for all tested mask samples. After a treatment time of 10 minutes, no contamination could be detected. Comparison between the surface and the embossed mask areas, shows a reduced decontamination efficiency for embossed mask samples for treatment times of 2 and 5 minutes. As the embossment acts as an impression in the otherwise flat mask samples, the embossed area is at a slightly larger distance to the surface of the plasma source. Consequently, the embossed regions are potentially exposed to a reduced plasma dose. Nevertheless, after a plasma treatment of 10 minutes no contamination could be detected on the embossed mask areas, thus no bar plot is visible for the 10 minutes treatment time in Figure 5.16.

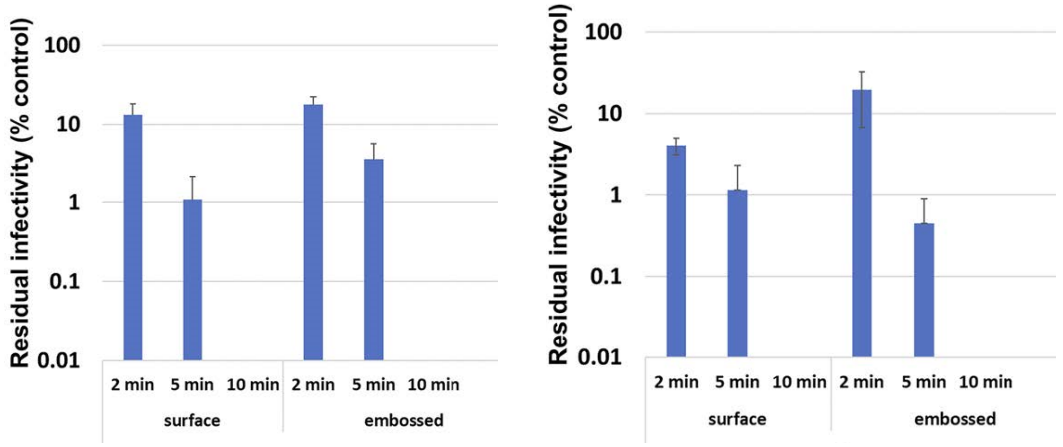

(a) (b)

FIGURE 5.16: Decontamination efficiency for (a) N95 masks (b) N99 masks [161]

5.2.4 Summary

A new decontamination system for the inactivation of SARS-CoV-2 on on N95 and N99 mask was presented. Decontamination and re-use of FFRs can play an important role especially during a global pandemic, to counter shortages of PPE and alleviate their environmental impact. Using printed electronic techniques, masks samples were treated with non-thermal plasma for the deactivation of SARS-CoV-2. Mask samples underwent filtration and decontamination efficiency testing, where a significant reduction of viral load after a treatment time of 5 minutes, without a reduction in filtration efficiency was demonstrated. However the decontamination efficiency test have also highlighted the importance of a constant distance between plasma layer and target surface. Small increase in distance showed a slight reduction in decontamination efficiency. This can be alleviated by using printed electrode systems for the plasma sources. Printed plasma sources allow for flexible substrates, thus can be accommodated for complex geometries and ensure constant treatment distances to the FFRs.

5.3 Decontamination system for narrow spaces

The presented research in the following section was carried out in cooperation with project partner from the School of Biological Sciences of the University of Southampton and parts have been previously published in the journal Plasma research Express [173] and presented at the 8th International Conference on Plasma Medicine in 2021 [174].

5.3.1 Introduction

Flexible endoscopes are used in a variety of medical procedures as a diagnostic or therapeutic tool [42, 175]. As a minimally invasive procedure, endoscopic intervention can reduce the risk of complications, such as bleeding or perforation, thus aid a faster recovery[176]. During the endoscopic intervention an endoscope is contaminated with a patients secretions [177, 178]. This requires a reprocessing protocol before reuse of the equipment on another patient.

Figure 5.17 shows an endoscope and detailed view of the channel cross section with its multiple internal channels [177, 178]. Endoscopes are difficult to reprocess due to the complex structure including the long and narrow tube. Due to the sensitive material composition of endoscope channels they are not suitable for heat sterilization using steam [179, 180]. The commonly applied reprocessing protocol mostly consist of three main steps: First bedside rinse immediately after the procedure; Second manual washing with detergent and specific brushes while the entire endoscope is immersed and a third automated washing and chemical-based high level disinfection prior to packaging and return to clinic [42]. However, chemical residues can remain in the equipment and provoke toxic reactions in patients or healthcare workers [42, 45]. Additionally, they can eventually lead to a material degradation, reducing the endoscope lifetime [22]. Moreover bacteria can remain in the long and complex geometry of the equipment and reuse of this contaminated equipment can cause infections in patients [42]. These healthcare associated infections (HCAIs) are a danger for patients and generate a large added economic cost in the healthcare sector [181].

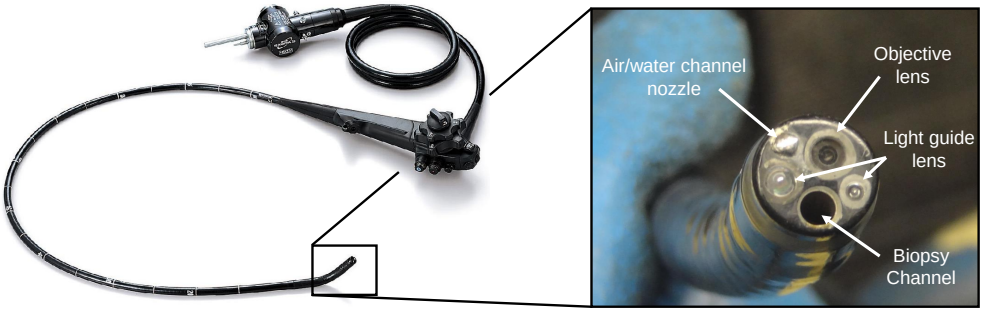

FIGURE 5.17: Endoscope with multiple internal channels, including, air/water channel, lens and light channel and a biopsy channel [176]

Reactive species generated by non-thermal plasma can eradicate biofilms [22] and has been previously proposed for the decontamination of medical devices [24, 43]. Compared to chemical cleaning procedures non-thermal plasma presents various advantages for the decontamination of endoscope channels. As it does not use toxic chemicals, it has a reduced environmental impact and can promote the safety of patients and healthcare workers otherwise exposed to toxic chemicals. It can also improve the lifetime of the

equipment as the sensitive equipment experiences reduced material degradation. Few methods using non-thermal plasma for the decontamination of narrow channels currently exist [46]. However most fail to ensure constant plasma properties along the full length of the narrow endoscope channels of approximately 2 m length with a 2.2 to 3.8 mm diameter.

Plasma jet sources have been used to supply plasma into narrow channels. These systems either inject plasma into the tube [182–185] or rely on continuous axial movement of the system to ensure the full length receives plasma treatment [186–189]. However ensuring stable and constant plasma properties across the full tube length remains a challenge and the need for gas supply increases the complexity of such systems. Further systems are developed, where external electrodes are arranged outside a modelled endoscope tube to generate plasma at the inside of the tube. These electrode systems can consist of planar flat electrodes [190, 191] or electrodes wrapped around a tube [179, 180, 192]. These approaches use mostly short tubes of dielectric material to model the actual endoscope channel. As the actual endoscope consists of additional metallic materials and casing [177], these methods are unsuitable for actual endoscope decontamination procedures.

In this section, a new plasma source configuration, known as the plasma yarn, is presented to overcome these limitations of non-thermal plasma for the decontamination of endoscope channels. The plasma yarn is designed in a coaxial electrode configuration and can generate constant and stable plasma properties over length up to 2 m. The plasma yarn can be fabricated using printed electronics technique to ensure a thin enough yarn, which can be directly inserted into long and narrow channels of endoscopes with diameters of $2 \sim 3$ mm. The generated plasma directly ionises the air inside the small gap between the outer layer of the yarn and the luminal surface of the channel-to-be-decontaminated, thus no gas supply is needed in this system. The following sections will present and discuss three different configurations for the plasma yarn. Further, an assessment of the bactericidal capability of the plasma yarn against biofilms in narrow channels in presented.

5.3.2 Decontamination system in narrow lumens

Three different configurations for the plasma yarn are developed for endoscope decontamination. All three plasma yarn configurations have a coaxial arrangement with the power electrode in the centre and are fully enclosed by dielectric material. The difference between the three different yarn configurations lies in the configuration and fabrication of the ground electrode and its attachment to the powered high voltage electrode.

5.3.2.1 Knitted plasma yarn (Configuration # 1)

Figure 5.18(a) shows a schematic of the plasma yarn using a knitted electrode. The high voltage electrode is in the centre of the coaxial arrangement and fully encased in the dielectric material. The ground electrode is on the exposed outer area of the dielectric material and is fabricated by knitting tinned copper wire around the dielectric material. The knitted ground electrode is solely secured by the knitted structure itself and no additional adhesive is required. The plasma generation mainly occurs in the air exposed area between dielectric material and in-between the knitted ground electrode. Figure 5.18(b) shows the fabricated knitted plasma yarn. A flexible dielectric material in combination with the knitted outer electrode allows for a highly flexible yarn configuration. This method allows a fast and reliable fabrication of a long length of the plasma yarn.

However, limitations of this configuration can occur in relation to the overall diameter of the yarn. Due to the thickness of the ground electrode and the knitted structure itself, the diameter is slightly larger when compared to other configurations presented in the next two sections. Furthermore, it requires special care when inserting the yarn, because the knitted outer electrode can inflict small scratches on endoscope channels consisting of softer materials.

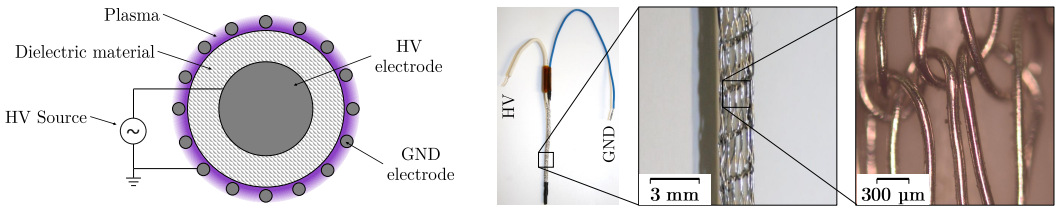

(a) (b)

FIGURE 5.18: (a) Schematic of knitted plasma yarn (b) Picture of manufacture knitted plasma yarn

5.3.2.2 Printed plasma yarn (Configuration # 2)

Plasma yarn configuration #2 consists of a printed ground electrode and a coaxial power electrode. Figure 5.19 shows a schematic of configuration #2 with a coaxial power electrode fully encased by a flexible dielectric material. The ground electrode is printed as a larger planar patch on a flexible substrate and wrapped around the coaxial core structure and is secured. The plasma generation occurs on the outer layer on the air exposed side of the ground electrode. A printed ground electrode can minimise the overall diameter of the plasma yarn. In addition, the smooth surface of a printed ground electrode reduces the risk of scratching when inserting the yarn into an endoscope channel. However, the overall flexibility of this configuration can be reduced due to the rigidity of the printed substrate of the ground electrode.

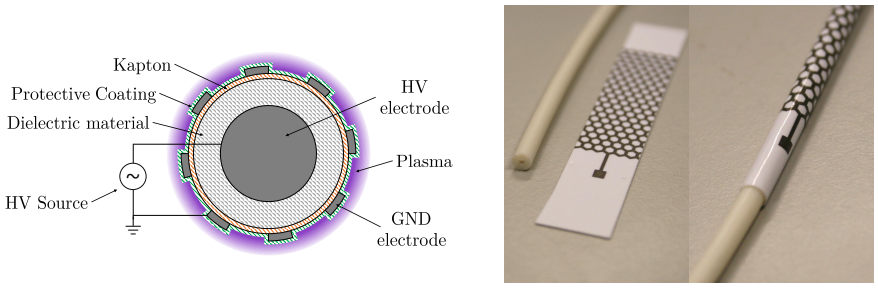

(a) (b)

FIGURE 5.19: (a) Schematic of printed plasma yarn (b) Picture of manufacture printed plasma yarn

5.3.2.3 Helical printed plasma yarn (Configuration # 3)

Plasma yarn configuration #3 is similar in design to configuration #2. Figure 5.20 shows a schematic of yarn configuration #2 with the coaxial arrangement of a power electrode. A ground electrode is printed in a thin strip on a flexible substrate. In this configuration a printed ground electrode is wrapped around the core structure in a helical direction to improve flexibility of the system. It also benefits from an overall reduced diameter and smooth surface finish when compared to a knitted electrode.

However, the fabrication of this configuration is similarly limited in size due to available printing capabilities and only short sections of plasma yarn configuration #3 can be manufactured. Furthermore, the fabrication requires precise alignment of the outer electrode to ensure uniform plasma generation. Both configurations, the printed plasma yarn and the helical printed plasma yarn, rely on an adhesive layer to secure the substrate with the printed ground electrode on the core structure. The substrate and the adhesive layer both act as an additional dielectric layer in the plasma source, increasing the power requirement of the plasma yarn.

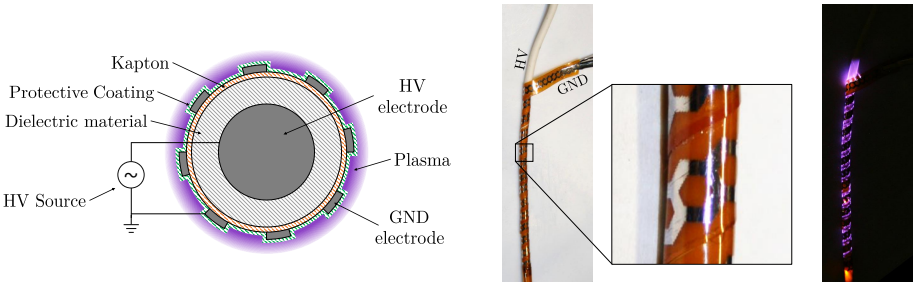

(a) (b) (c)

FIGURE 5.20: (a) Schematic of helical printed plasma yarn (b) Picture of manufacture helical printed plasma yarn (c) Ignited helical printed plasma yarn

5.3.2.4 Analysis of plasma yarn

The key parameters to assess the suitability of a plasma yarn for an endoscope sterilisation application are:

- Scalability of plasma yarn up to full length of endoscope channels
- Uniformity of plasma properties along full length of plasma yarn
- Flexibility in order to allow treatment in flexible endoscope channels

Plasma yarn configuration #1 is fabricated using industrial knitting technology, thus can be fabricated in large length and quantities with a constant and repeatable quality. Plasma yarn configuration #2 and #3 rely on a ground electrode being fabricated using printing method. Due to the printable size on the dispenser printer system, one continuous ground electrode is only achievable for a limited size of 5 $\sim$ 10 cm. This would require a modular assembly of several sections of plasma yarn to achieve the coverage of the full length of an endoscope channel. Furthermore, plasma yarn configuration #2 has a reduced flexibility, thus would not be able to be easily inserted into the flexible endoscope channel. In the framework of this thesis, plasma yarn configuration #1 is chosen for further analysis, as it fulfils all the above listed key parameters for endoscope sterilisation procedure.

Scalability:
The scalability assessment is carried out similarly to the assessment presented in chapter 3. Three different lengths of plasma yarn, which are 64 mm, 128 mm and 256 mm, are used to evaluate the scalability of the yarn. The plasma yarn samples of different length are analysed in their power density and the emission spectra. A fully scalable plasma systems is characterised by a constant power per unit length and shows similar spectral response across various different lengths. Figure 5.21(a) shows the plasma emission images for plasma yarn configuration #1 for the three different lengths. For a better comparison, the images only show a section of the full length plasma yarn. As can be seen, the visual plasma emission for the yarn of the three different lengths remains constant. Figure 5.21(b) shows the calculated power the different lengths of plasma yarn. As can be seen, the power scales linearly with the length of the plasma yarn. The power per unit length remains mostly constant with 3.75 W/m, 4.06 W/m and 4.22 W/m, for a 64 mm, 128 mm and 256 mm long plasma yarn, respectively. The spectral intensity shows fluctuations of up to 43 % between the different lengths of plasma yarn. Larger fluctuations in spectral intensity for the plasma yarn can be related to the geometrical configuration. As the ground electrode consists of a knitted mesh around the dielectric material, small and minimal gaps between the knitted electrode and the dielectric material can appear even in a straight, unbent configuration. These

small gaps can vary the local electric field distribution resulting in regions with stronger plasma, where the distance between electrode and dielectric is minimal, or weaker plasma generation, where the gap is larger.

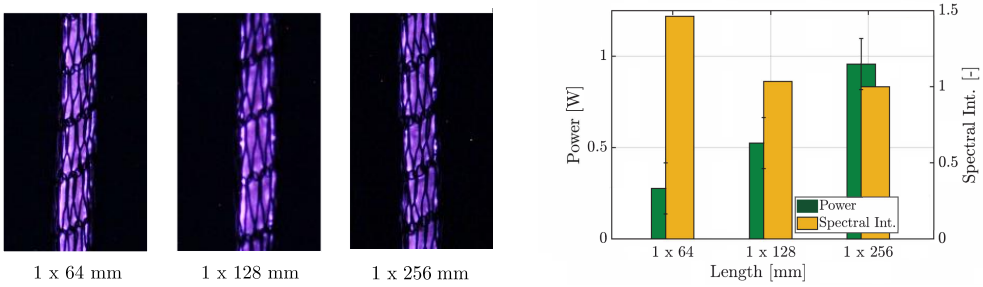

(a) Emission images of plasma yarn with varying length

(b) Power and spectral intensity of plasma yarn with varying length

FIGURE 5.21: Scalability assessment of plasma yarn: (a) emission images of plasma yarn for varying lengths; (b) Power and spectral intensity of plasma yarn for varying lengths

Flexibility:

The flexibility of the plasma yarn is evaluated by assessing its performance over non-flat surfaces. The plasma yarn is wrapped around nylon rods of three different diameters, which are 6 mm, 10 mm and 20 mm. Figure 5.22(a) shows the emission images from the flexibility assessment using the plasma yarn. As can be seen, the overall intensity of the generated plasma decreases for curved plasma yarns. With a decreasing diameter, the generated plasma appears patchy, with some areas across the yarn having a weaker plasma. This effect can be related to the geometrical configuration of the plasma yarn. With an increased curvature, the geometrical displacement between the outer knitted ground electrode and the dielectric material can be aggravated. Further gaps will be introduced by bending the plasma yarn, leading to changes in the local electric field, thus resulting in a weakened plasma generation in some areas. This effect can also be seen when analysing the power of the plasma yarn over varying curvatures, as shown in Figure 5.22(b). The power consumption is reduced for smaller curvatures, since only a smaller area of the plasma yarn is ignited. Figure 5.22(b) additionally shows the recorded spectral intensity, where a strong reduction of spectral intensity for smaller curvatures can be seen. The spectral intensity confirms the effect already seen in the recorded images.

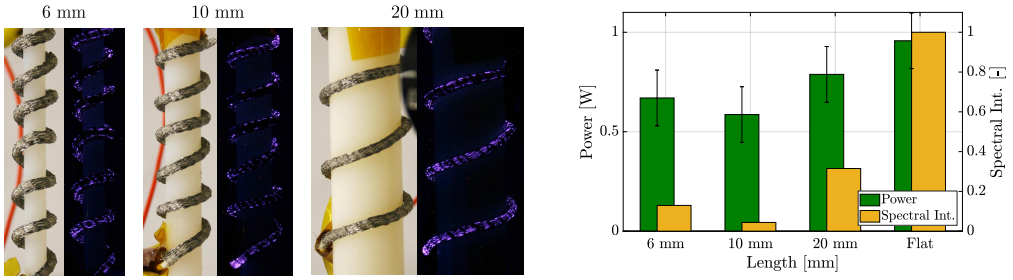

(a) Emission images (b) Power and spectral intensity

FIGURE 5.22: Flexibility assessment of plasma yarn: (a) emission images of plasma yarn for varying curvatures; (b) Power and spectral intensity of plasma yarn for varying curvatures

Uniformity:

The uniformity of the plasma yarn for endoscope sterilisation is important, as a constant plasma dose across the full length of the endoscope channel needs to be ensured. Plasma yarn configuration #1 can be fabricated with constant properties for a long length up to several meters, as it is industrially fabricated. Figure 5.23 shows plasma yarn configuration #1 over a length of 2 m, at voltage of 6 kV at 2 kHz. As can be seen, the yarn is ignited with a constant plasma intensity along the full length.

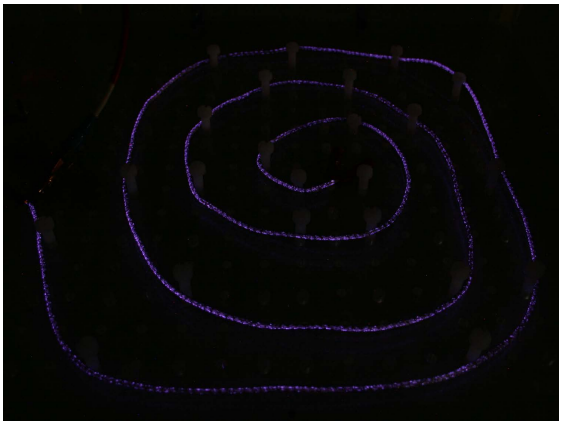

FIGURE 5.23: Plasma yarn of 2 m length at 6 kV at 2 kHz

The uniformity of the plasma generation across the plasma yarn is quantified by employing an image processing method. Figure 5.24(a) shows a section of the plasma yarn of 100 mm length. A repeating pattern can be seen, which is related to the knitting structure of the ground electrode. The image intensity is obtained in each pixel column along the full length of the yarn as:

$$I_{img}(i) = \sum_{j=1}^{m} R_{ij} + \sum_{j=1}^{m} G_{ij} + \sum_{j=1}^{m} B_{ij} \tag{5.19}$$

where R_{ij}, G_{ij} and B_{ij} are the pixel intensities of the respective RGB component of the image. Variables i and j are the pixel positions in x- and y-direction, respectively. Parameter m is the maximum pixel number across the height of each image section. Figure 5.24(b) shows the image intensity across the full length of the plasma yarn. As can be seen, the image intensity remains constant across the length of the plasma yarn. A fluctuation pattern of the intensity along the yarn length can be seen. This is related to the pattern in the knitted ground electrode. The intensity deviation across the yarn length is low with a relative percentage of 8 % and is mainly due to the intensity fluctuations due to the electrode pattern.

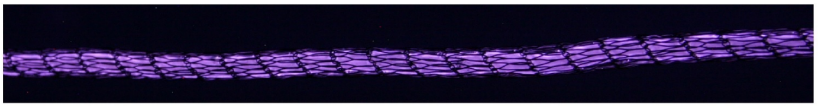

(a) Plasma yarn

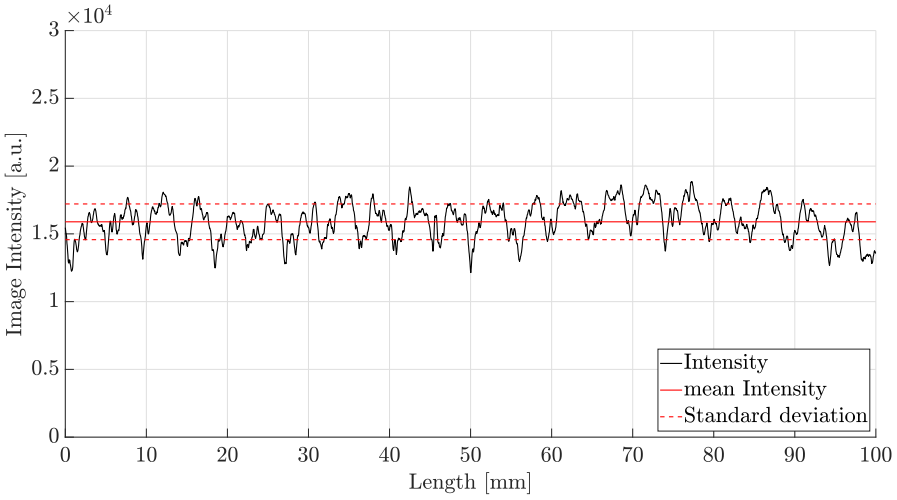

(b) Image intensity along plasma yarn

FIGURE 5.24: Uniformity of plasma yarn: (a) 100 mm long plasma yarn; (b) obtained image intensity over plasma yarn

5.3.3 Biological test and demonstration of efficacy

Real endoscope channels with an internal diameter of 2.5 mm and two different bacterial strains, Pseudomonas aeruginosa and Enterococcus faecalis, were used for the controlled contamination of endoscope channels. Contaminated endoscope channels are treated using the plasma yarn and assessed to investigate the feasibility of the plasma yarn for the sterilisation of endoscope channels. These tests have been carried out in cooperation with project partners in the School of Biological Science at the University of Southampton. Sections of endoscope channels have been sterilised and subsequently contaminated in a controlled procedure using liquid suspension. The bacterial suspensions were injected inside the channels using a sealed sterile syringe and were kept in contact for 1 hour to

allow adsorption of bacteria onto the luminal surface. Afterwards, the tubes are flushed with sterile water, leaving a contaminated film of adhering bacteria on the channel luminal surface. The contaminated channels are incubated at 37 °C for 72 hours, to allow the growth of a biofilm from any remaining bacteria inside the channel.

The plasma treatment is performed by inserting the yarn into the endoscope channel immediately after rinsing the excess contamination. Plasma yarn configuration #1 is chosen for the biological test series, as repeatable fabrication of different yarn section can be performed reliably. A negative control is carried out where the yarn is inserted into the channel, then removed before the application of plasma treatment. All treatment procedures are carried out with voltage of 6 kV at 6 kHz and the treatment time is varied from 1 to 10 minutes. After treatment, the yarn is removed and some channel is cut longitudinally to allow microscopic examination of the internal luminal surface. Treated channels and used yarn sections are suspended in growing media to assess any residual bacteria inside the channels or on the yarn itself.

Figure 5.25 shows falcon tubes with channel sections which were spiked with one of the two bacterial strains (Pseudomonas and Enterococcus) and treated with plasma for various durations before incubation in culture medium for 72 hours in Tryptic Soy Broth (TBS) as growing media. Tube #1 contains medium only and is used as a reference. The transparency of the suspension media is indicative of no contamination. Tubes #2 and #5 contain channel sections, which were inserted in endoscope channels contaminated with Pseudomonas aeruginosa and Enterococcus faecalis, respectively, where no plasma treatment delivered. As can be seen, the media is cloudy, indicating the contamination of the channel section. Tubes #3 and #4 contain channel sections contaminated with Pseudomonas aeruginosa and treated with 5 and 10 min plasma, respectively, before the 72 h incubation. It can be seen that the culture media has an improved transparency with a 5 minutes plasma treatment. A time of 10 minutes plasma treatment leads to no turbidity in the media, indicative of no bacterial growth. The turbidity is comparable to the reference media in tube #1, therefore it can be concluded that a maximum treatment of 10 minutes can result in successful decontamination of Pseudomonas bacteria. For contamination with Enterococcus faecalis, a treatment time of 5 minutes already results in a high transparency of the suspension medial, indicating that successful decontamination can be achieved from treatment times of 5 minutes.

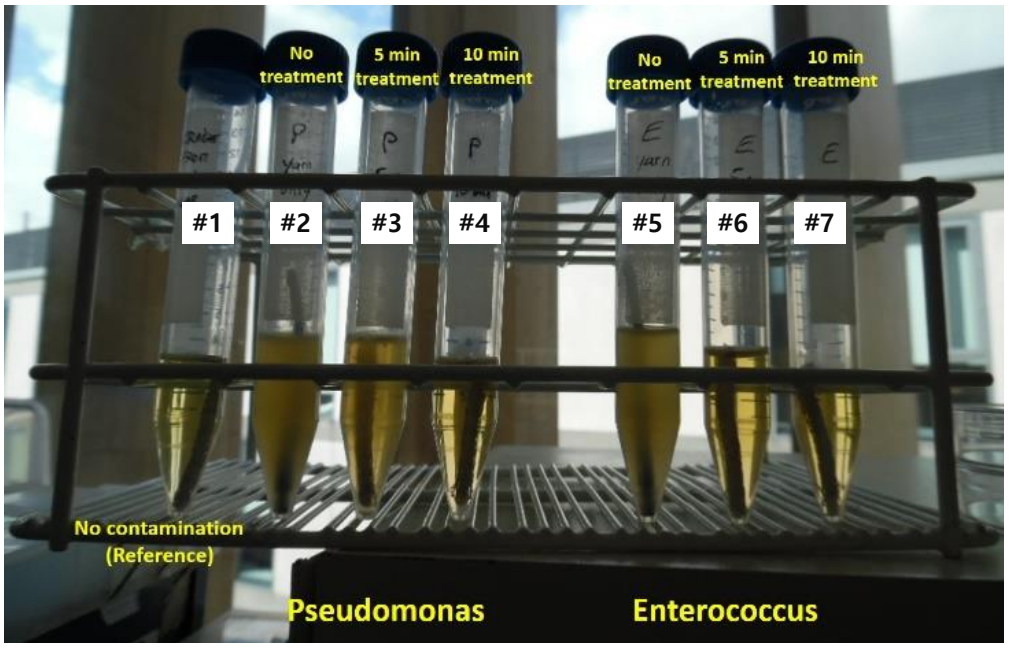

FIGURE 5.25: Results from plasma treatment of endoscope channels

Figure 5.26 shows the obtained results for the contaminated endoscope channels. Control and plasma treated channels are kept in liquid suspension cultures (TBS) for 24 or 72 hours after treatment to allow growth of a biofilm from remaining bacteria. Analysis of the decontamination efficiency of the plasma treatment in endoscope channels is performed through optical density (OD) measurement of the medium. The optical density measurement quantifies the turbidity in the growing media seen in the tubes in Figure 5.25. As can be seen in Figure 5.26(a), the optical density is highest for the positive reference sample channel. With an increased exposure time to non-thermal plasma from the plasma yarn, the obtained optical density is reduced. However Pseudomonas bacteria appear to recover when left for longer incubation time of 72 hours for 5 minutes treatment sample, whereas only minimal recovery can be observed for samples with a treatment time of 10 minutes. The decontamination capabilities of the plasma yarn are also tested against Enterococcus bacteria, see Figure 5.26(b). As can be seen, the optical density is reduced after only 2 minutes of plasma treatment using the plasma yarn. The obtained optical density is reduced down to the same level as a reference clean uncontaminated and untreated channel (see TBS reference).

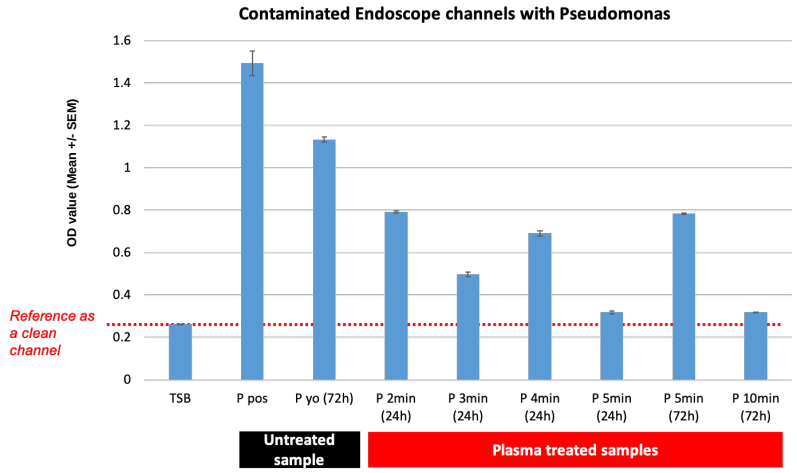

(a)

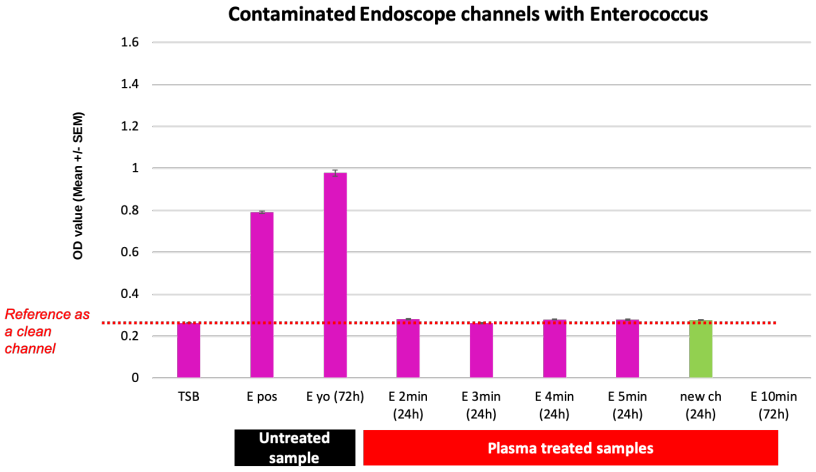

(b)

FIGURE 5.26: Optical density profiles from culture media at 24 or 72 hours incubation with channels treated for various duration after contamination: (a) Pseudomonas; (b) Enterococcus

5.3.4 Summary

In this section, a new method for endoscope decontamination using a new developed non-thermal plasma source, the plasma yarn, was presented. The plasma yarn is a simple coaxial DBD electrode design for direct insertion into long and narrow channels. Plasma and its containing reactive species are directly generated at the internal surfaces of endoscope channels, which is to be decontaminated. Three different plasma yarn configurations were presented and their benefits and current fabrication limitations were discussed and the scalability, flexibility and uniformity of the plasma yarn was demonstrated. The capability of the plasma yarn for endoscope decontamination was assessed by analysing contaminated (Pseudomonas and Enterococcus) endoscope channels after

treatment with the plasma yarn. It was demonstrated that plasma yarn can inactivate bacteria on the surface of endoscope channels after a few minutes of treatment time.

Chapter 6

Conclusion

This chapter provides a summary and review of the carried out studies, its main research findings and proposes potential future work to advance non-thermal plasma technology and its applications.

6.1 Summary and review

This study has investigated and developed a fully scalable and flexible plasma sources. In doing so, this has advanced the implementation of non-thermal plasma sources in various applications. The fabricated plasma sources have been considered for both aerospace and biomedical applications.

The first chapter provided an introduction of non-thermal plasma and its unique physical and chemical properties. The relevance of non-thermal plasma for various applications including biomedical and aerospace applications have been discussed. Furthermore, several methods of generating non-thermal plasma were discussed. In addition, the limitation of surface dielectric barrier discharge (DBD) plasma sources for the generation if non-thermal plasma over large and complex surfaces was identified.

In the second chapter, fabrication methods of surface DBD plasma sources using printed electronic techniques were presented. Two printing methods, focusing on low and high viscosity inks, have been employed. The dispenser printing method was identified as most favourable. The remaining part of the chapter presented the experiment setup and diagnostic tools used to assess the fabricated plasma source.

The third chapter assessed the scalability and flexibility of the fabricated printed DBD plasma sources. Using electrical and optical diagnostic methods, the printed plasma sources were assessed and a power scaling law was proposed. The power of printed plasma sources has been estimated based on various operating conditions and design

parameters using the proposed power scaling law. Further studies using various length and area scales of printed electrodes have demonstrated good performance as a scalable plasma source. A flexibility study of printed plasma sources concluded that uniform and stable plasma is generated when bending the electrode system over small curvatures. Through the assessment of scalability and flexibility of the printed electrode systems, it has been demonstrated that the surface DBD plasma sources can generate uniform non-thermal plasma over large and complex surfaces.

In chapter four, the thesis proposes a new electrical simulation model of a surface DBD plasma source with complex electrode designs. The proposed electrical model used a fractional segmentation of a surface DBD plasma source to account for the dynamic behaviour of the plasma discharge volume. The model was validated through a comparative study, where a good agreement was shown between experimental and predicted electrical characteristics of four different electrode configurations.

In chapter five short feasibility studies using printed non-thermal plasma sources for applications within the aerospace sector and biomedical field were presented. A new "Cold Radio Blackout Testing" solution was proposed, which uses the high electron density generated by the developed printed plasma sources to model a re-entry plasma sheath. In addition, the printed plasma sources were successfully employed as a decontamination system of SARS-CoV-2 contaminated personal protective equipment (PPE). Finally, a newly developed thin narrow plasma source, a plasma yarn, was proposed and successfully used for the sterilisation of endoscope channels.

6.2 Contributions and Limitations

The presented study resulted into a number of research contributions for non-thermal plasma technology. The following section will highlight these research contributions, but also provide a brief discussion of their limitations and how these could be addressed.

6.2.1 Discharge power scaling law

A discharge power law can be employed as a predictive tool for printed plasma sources in the design and optimisation procedure of non-thermal plasma sources in various applications.

A scaling law for the discharge power of printed surface DBD plasma sources is proposed. The discharge power of printed DBD plasma source can be estimated based on design parameters of the DBD plasma source, as well as the driving conditions of the DBD plasma source. The design parameters included in the scaling law are the thickness, t, of the dielectric material and the relative permittivity, ε_r, of the dielectric material of

the surface DBD plasma source. Through t and ε_r, the capacitance, C, of the DBD plasma source is calculated. The driving conditions included in the scaling law are the frequency, f, and applied voltage, V_{pp}. The discharge power scaling law proposed a linear relationship of discharge power to the operating frequency ($P \propto f$). A linear relationship is also concluded for discharge power the plasma source capacitance ($P \propto C$). The operating voltage is proportional to the discharge power through the power law of ($P \propto V^{3.27}$), which is in good agreement with literature. The discharge power scaling law is derived within a defined parameter envelope, thus is limited to the behaviour of printed plasma sources within this envelope. Therefore, a closer Additionally, the approach does not assess other influential factors such as erosion on the electrode material, which can in turn affect the capacitance, thus the electrical behaviour of a plasma source.

6.2.2 Scalability of printed plasma sources

Thin printed DBD plasma source generate non-thermal plasma with constant plasma intensity per unit area.

The scalability study assessed printed plasma sources of varying length and area scales using electrical and optical diagnostics tools. The study demonstrated that that stable plasma generation is achieved, measured through image and spectral intensities, while constant discharge power per unit length (or area) was maintained. The study verifies the scalability of printed plasma source, thus proposing its capability for various applications requiring non-thermal plasma generation across large surfaces. The scalability assessment has been performed for individual plasma sources, however plasma generation across larger scales can also be achieved using a modular approach, operating several plasma sources in parallel. Thus, the application of printed plasma sources can be further expanded using a modular approach.

6.2.3 Flexibility of printed plasma sources

Thin printed DBD plasma source generate non-thermal plasma with constant plasma intensity over varying curvatures on complex surface.

A flexibility study assessed the capability of thin printed DBD plasma sources by bending the electrode systems over various small curvatures. The study provided an analysis of the key diagnostics parameters and demonstrated reliable and uniform plasma generation at constant operating conditions for bent plasma sources. Although the flexibility is only assessed for an omni-directional flexibility, the study demonstrates the flexibility of the plasma sources and suggest their capability for various applications requiring non-thermal plasma generation over complex geometries.

6.2.4 Electrical model for complex electrode geometries

A new electrical model proposes the area segmentation for surface DBD plasma sources for complex electrode geometries.

The proposed electrical model uses a fractional segmentation to account for the dynamic behaviour of the plasma discharge volume. The surface of a DBD plasma source is split into a discharge and non-discharge area, where the dynamic behaviour of those areas is coupled to the sinusoidal power driving signal. The segmentation between discharge and non-discharge area can be estimated through semi-empirical equation for the time-variable plasma discharge propagation length, thus the discharge volume on a surface DBD plasma source. The use of a semi-empirical equation for the estimation of the discharge volume can introduce inaccuracies to the electrical model. Especially a potential frequency dependency of the discharge propagation length has been discussed and can be investigated to further increase the accuracy of the electrical model.

6.2.5 Cold radio blackout method

Thin printed DBD DBD plasma sources can be used for a new "Cold radio blackout testing" method.

A new "Cold radio blackout testing" method is proposed, which models the spatial electron density gradient over hypersonic re-entry vehicles, using a stacked assembly of printed non-thermal plasma sources. A feasibility study estimated the electron density using optical emission spectroscopy. Furthermore, radar transmissivity tests verified that sufficient EM transmissivity is provided by optimising the electrode geometry of printed DBD plasma sources. The average electron density can be controlled through the varying operating conditions and/or design parameters of the printed DBD plasma source. Although the estimation provided electron densities that comparable electron density as in the re-entry plasma sheath, a more detailed analysis of the electron density can improve the accuracy of the "Cold radio blackout testing" method.

6.2.6 Decontamination of SARS-CoV-2 on PPE

Surface DBD plasma sources generating non-thermal plasma can be used to eradicate SARS-CoV-2 on PPEs.

A new decontamination system uses printed DBD plasma sources for the treatment of SARS-CoV-2 contaminated mask samples (PPEs). The mask samples are exposed to non-thermal plasma for varying treatment time. After treatment, the mask samples underwent filtration and decontamination efficiency testing. SARS-CoV-2 has been successfully inactivated, without affecting the filtration efficiency of PPEs. It has been

identified that the plasma treatment time can play a crucial role in both the decontamination and filtration efficiency. Further, the study highlighted the influence of the distance between plasma source and mask sample, which can affect the efficiency of the method. Further treatment approaches can be assessed, such as an indirect treatment, where a flow is used to transport plasma species in the vicinity of the treatment sample. This approach can alleviate the need for close contact be between plasma source and treatment sample, however the affect on the efficiency has to be analysed.

6.2.7 Decontamination in thin and narrow channels

A new plasma yarn generating non-thermal plasma can be used to eradicate biofilms in endoscope channels and lumen.

A thin and long new plasma source, plasma yarn, is presented as a decontamination and sterilization tool for endoscope channels and lumen. Three configurations for the plasma yarn are proposed. All configurations have different limitations, a knitted plasma yarn poses a risk of surface damage on the sensitive endoscope channel due to scratching and a printed yarn has only a limited length. Further development of the printed hybrid yarn can reduce those limitations. The capability of the plasma yarn for the decontamination in endoscope channels was assessed through direct insertion of the yarn into contaminated channels. The decontamination efficiency of the plasma yarn has been successfully demonstrated against contaminated (Pseudomonas and Enterococcus) endoscope channels.

6.3 Future Work

This study showed the controllability of non-thermal plasma on printed source DBD plasma sources and demonstrated their applicability in the aerospace and biomedical field. In addition to recommended work in the previous section, further research studies are recommended to continue advancing non-thermal plasma technology and its applications.

6.3.1 Lifetime of printed plasma sources

Erosion to the electrode material and degradation to the dielectric material due to the bombardment of energy particles can affect the lifetime of DBD plasma sources. Alleviation of these effects can be achieved by using a protective coating. The lifetime of surface non-thermal plasma sources can be further improved, by using different materials during the fabrication procedure. Employing conductive inks with higher silver content

or ink materials with lower sputtering rate (stainless steel or tungsten [56]) can be investigated to study their effect on the lifetime on printed plasma sources.

6.3.2 Analytical estimation of capacitance for discharge power estimation

The proposed power law for the estimation of the discharge power is derived from a parametric study of printed plasma source. The plasma source using a hexagonal electrode pattern with a fixed linewidth of both high voltage and ground electrode. Therefore, the presented relationships accounts for the given electrode geometry, but not necessarily for varying linewidth of the printed electrode. The calculated capacitance implemented in the scaling law accounts for the fully parallel component of the powered and ground electrode pair however not for varying linewidth of the powered electrode. Coupling the power scaling law with a computed capacitance of the electrode geometries using a solver, such as COMSOL Multiphysics, can improve the accuracy of the scaling law and allow application for a wider range of geometries.

6.3.3 Dynamic discharge propagation length

In chapter four a semi-empirical estimation of the discharge propagation length has been carried out. This is implemented through the fractional segmentation of the surface DBD plasma source and has a direct affect on the assumed discharge plasma volume in the electrical model. As this can affect the accuracy of the model a more detailed prediction of the discharge volume can improve the electrical model. In the presented model, the discharge propagation length is estimated through high resolution image recordings over 1 second, thus providing the average discharge behaviour over 10000 cycles. This semi-empirical estimation of the discharge propagation length can be improved by carrying out a study to analyse the discharge propagation length on μs time scales using high speed imaging tools. High speed imaging can capture the dynamic time-resolved propagation length over one period of the sinusoidal operating voltage. This understanding can be synthesised into an empirical relation to the sinusoidal applied voltage, thus provide an accurate time-resolved discharge propagation length.

6.3.4 Electron density estimation

In chapter five the line ratio method for optical emission spectroscopy is employed to estimate the electron density of the generated non-thermal plasma. However this method relies on assumptions, such as an average electron density distribution across the plasma

source. Employing alternative methods, such as stark broadening, or Thomson scattering provides a higher accuracy, and thus can be used to achieve a more precise estimation of the electron density.

6.3.5 Analysis of reactive species

Reactive species in the generated non-thermal plasma plays a crucial role especially for its application as a decontamination method. Therefore, it is important to identify the present reactive species and their temporal behaviour, including their generation and recombination times. The employed optical emission spectroscopy method in this thesis provides a brief insight of the chemical composition of the generated plasma. The main emission spectra can be associated to the second positive system and the first negative system of nitrogen, whereas emission of atomic oxygen can currently not be detected, due to the low temporal resolution of the OES system. Using a high resolution optical method, such as laser-induced fluorescence (LIF) [193], can provide more detailed information of the reactive species.

Appendix A

Design of printed plasma sources

The following chapter contains the geometric electrode patterns of the printed plasma sources.

A.1 Electrode pattern for scalability assessment

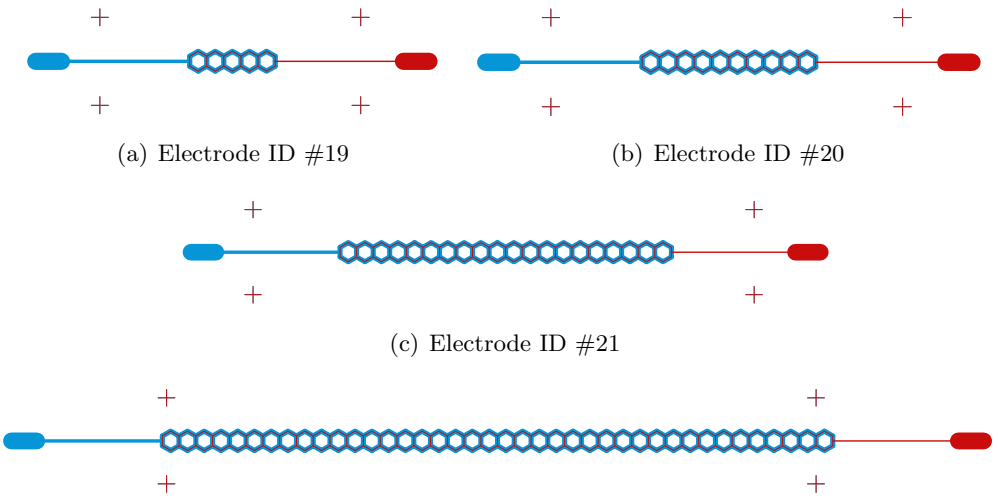

(a) Electrode ID #19

(b) Electrode ID #20

(c) Electrode ID #21

(d) Electrode ID #22

FIGURE A.1: Electrode geometries of length scalability assessment (Electrode ID #19 to #22 in section 3.2.3): (a) 10 mm; (b) 20 mm; (c) 40 mm; (d) 80 mm (Red: Ground electrode; Blue: High voltage electrode)

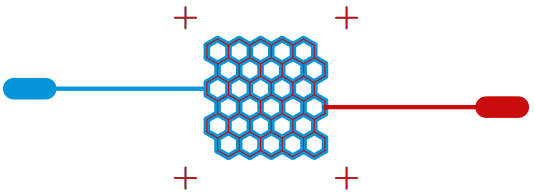

(a) Electrode ID #23

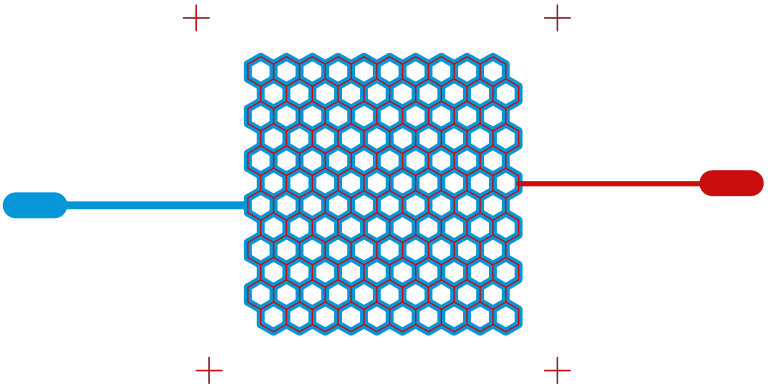

(b) Electrode ID #24

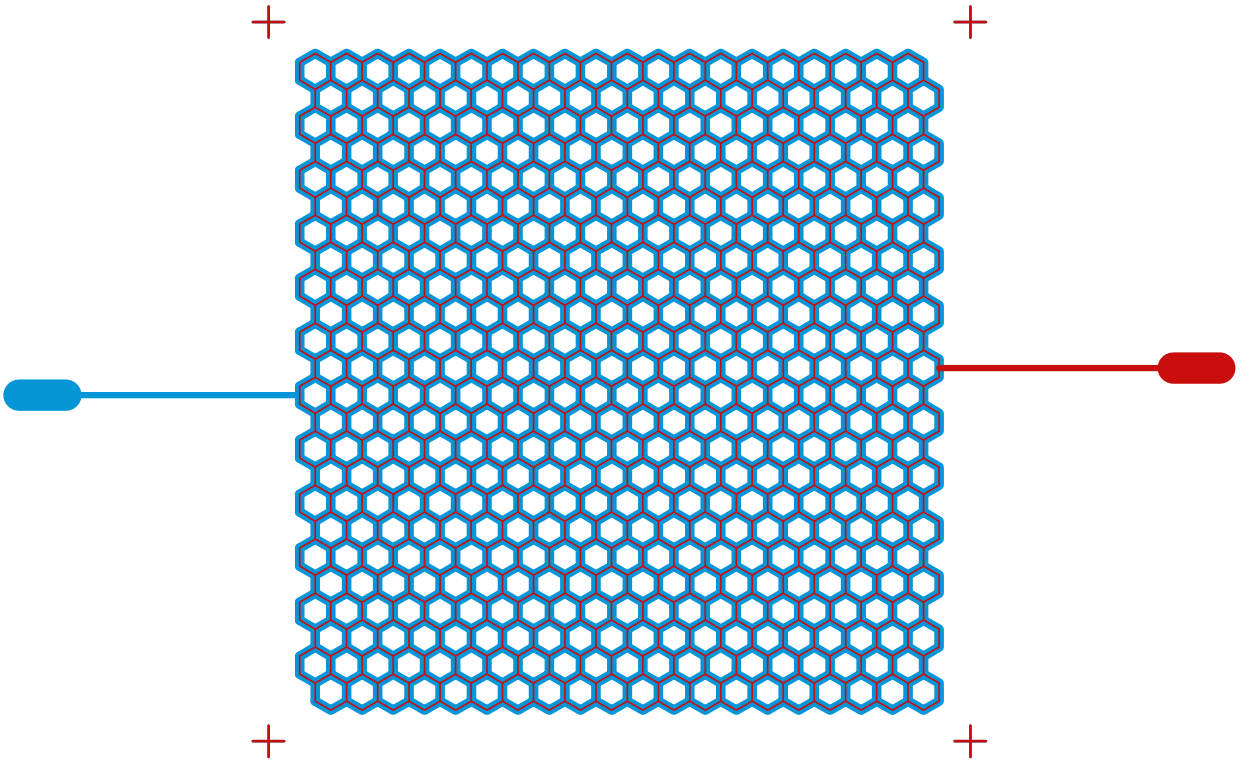

(c) Electrode ID #25

FIGURE A.2: Electrode geometries area scalability assessment (Electrode ID #23 to #25 in section 3.2.3): (a) 10 mm x 10 mm; (b) 20 mm x 20 mm; (c) 40 mm x 40 mm (Red: Ground electrode; Blue: High voltage electrode)

A.2 Electrode patterns for electrical model validation

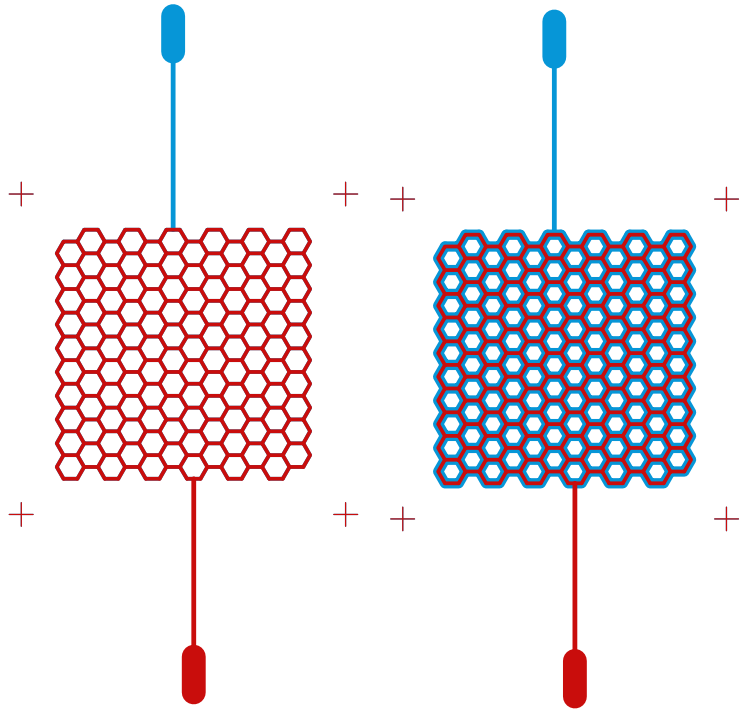

(a) Configuration #1 (b) Configuration #2

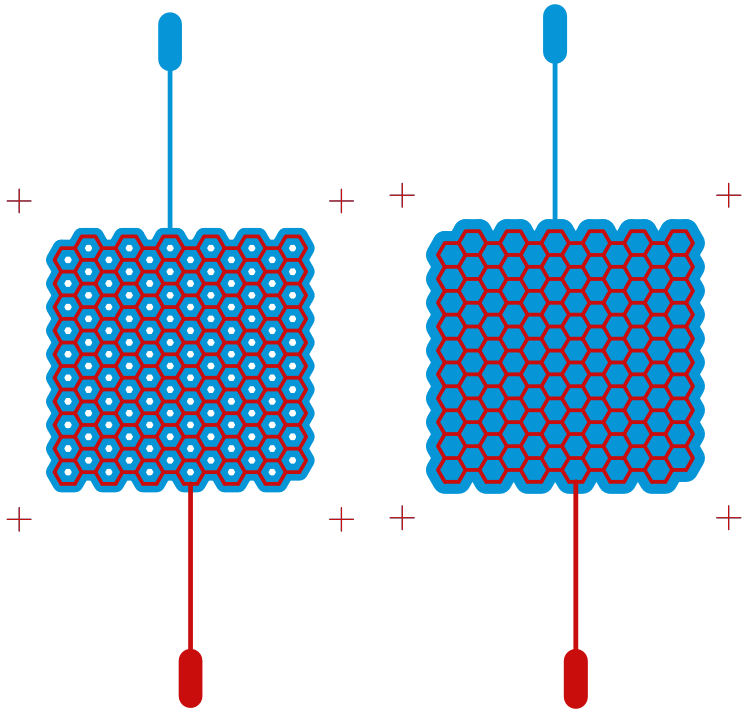

(c) Configuration #3 (d) Configuration #4

FIGURE A.3: Electrode geometries used for validation testing of electrical model in section 4.4.1: (a) Configuration #1; (b) Configuration #2; (c) Configuration #3; (c) Configuration #4 (Red: Ground electrode; Blue: High voltage electrode)

Appendix B

Printed plasma source images

The images of the printed plasma sources will be shown in the following sections. Highlighted are the electrode outlines obtained through the image processing procedure presented in section 2.2.2.1.

B.1 Printed plasma source images for operating condition assessment

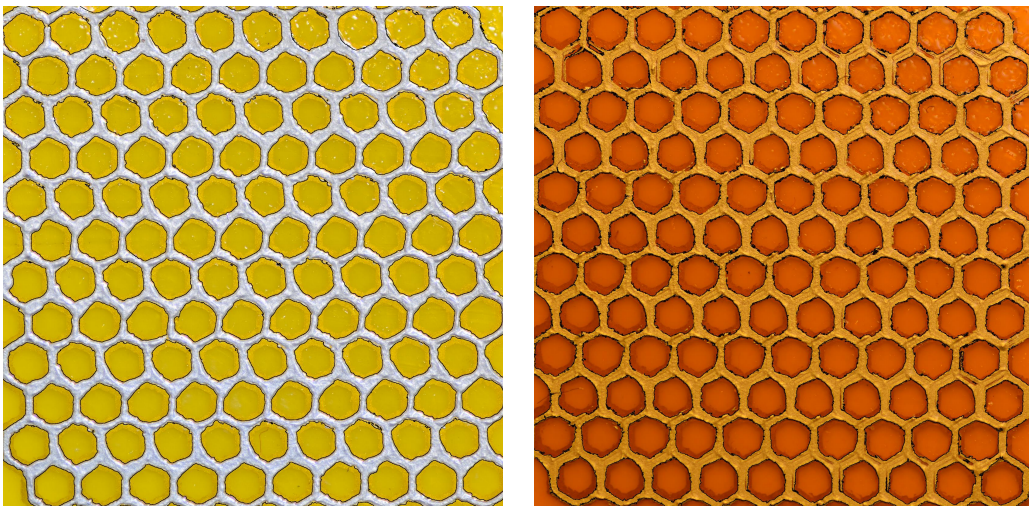

(a) 25 μm Kapton HN (ID #14)

(b) 50 μm Kapton HN (ID #15)

FIGURE B.1: Images of printed plasma sources using varying dielectric substrates (Electrode ID #14 to #18 presented in section 3.2.2): (a) 50 μm Kapton HN, (b) 50 μm Kapton HN (Highlighted is the outline of the electrode)

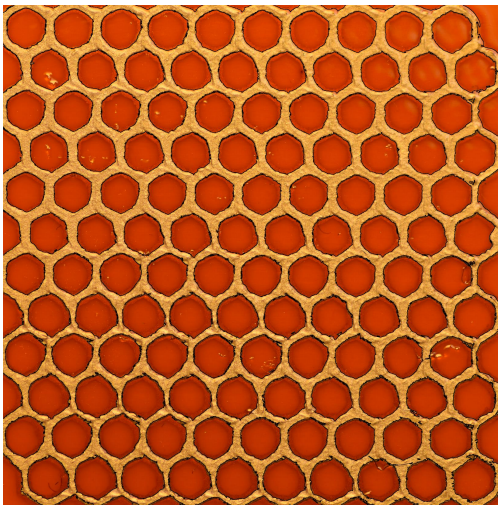

(a) 75 μm Kapton HN (ID #16)

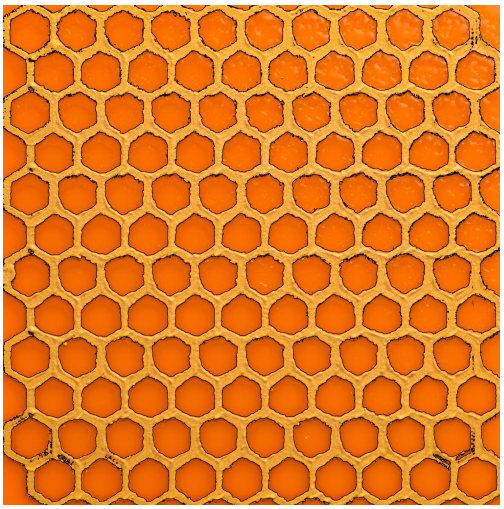

(b) 75 μm Kapton MT (ID #17)

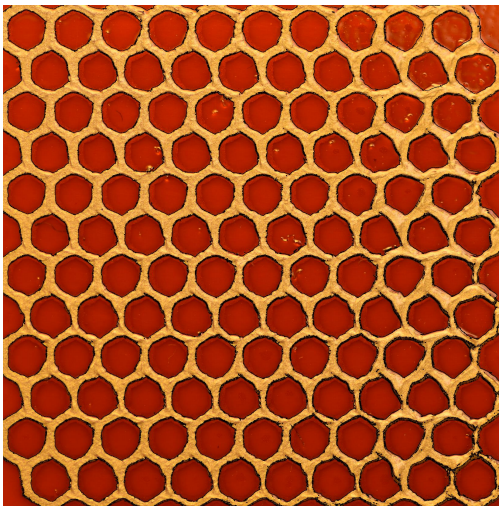

(c) 125 μmKapton HN (ID #18)

FIGURE B.2: Images of printed plasma sources using varying dielectric substrates (Electrode ID #14 to #18 presented in section 3.2.2): (a) 75 μm Kapton HN, (b) 75 μm Kapton MT, (c) 75 μm Kapton HN (Highlighted is the outline of the electrode)

B.2 Printed plasma source images for scalability assessment

(a) Electrode ID #19

(b) Electrode ID #20

(c) Electrode ID #21

(d) Electrode ID #22

FIGURE B.3: Images of printed plasma sources used for the length scalability assessment (Electrode ID #19 to #22 in section 3.2.3): (a) 10 mm; (b) 20 mm; (c) 40 mm; (d) 80 mm (Highlighted is the outline of the electrode)

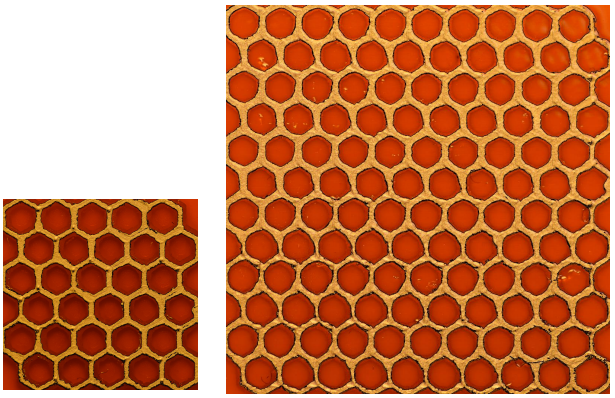

(a) Electrode ID #23

(b) Electrode ID #24

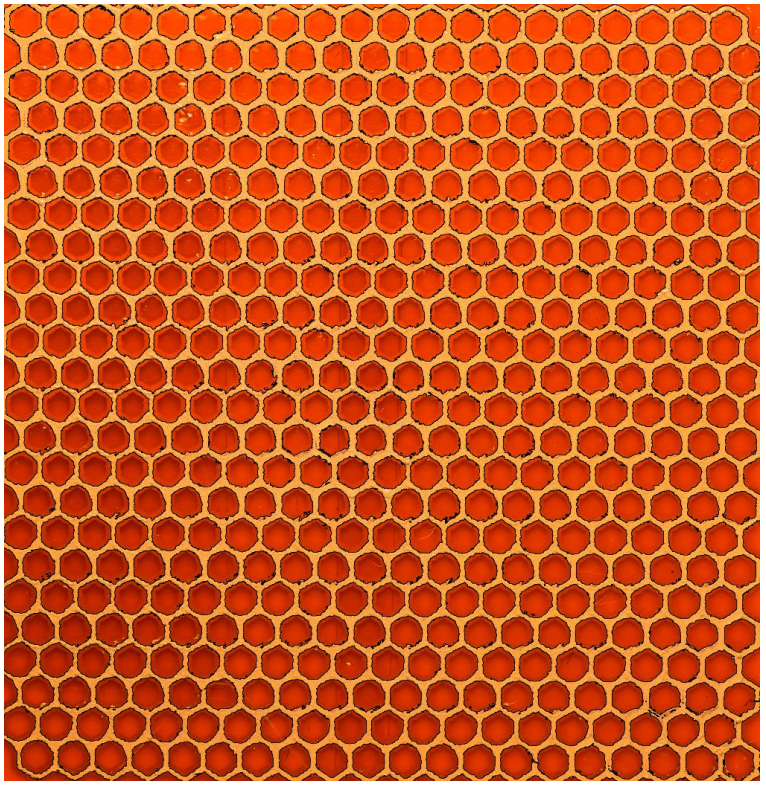

(c) Electrode ID #25

FIGURE B.4: Images of printed plasma sources used for the length scalability assessment (Electrode ID #22 to #25 presented in section 3.2.3): (a) 10 mm x 10 mm; (b) 20 mm x 20 mm; (c) 40 mm x 40 mm (Highlighted is the outline of the electrode)

Appendix C

Electrical Characterisitcs

C.1 Lissajous Graphs over varying operating conditions

The following sections provides an overview of obtained Lissajous graphs over varying operating conditions. Exemplary the Lissajous graphs obtained from operating of the printed plasma sources using using 75 μm Kapton HN dielectric material is shown (Electrode ID #16 presented in section 3.2.2).

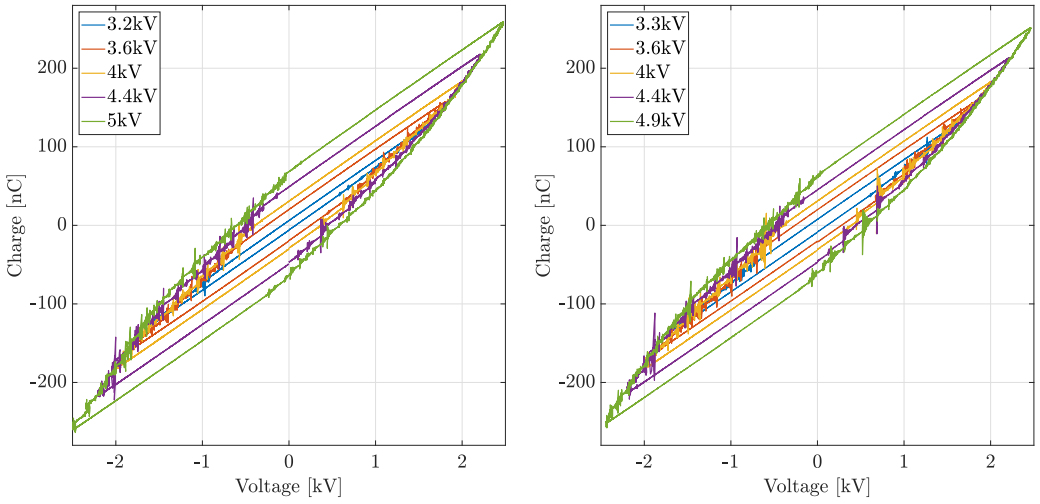

(a) Operating frequency of 6 kHz

(b) Operating frequency of 8 kHz

FIGURE C.1: Lissajous graphs for varying operating voltages of printed plasma sources using 75 μm Kapton HN dielectric substrates (Electrode ID #16 from section 3.2.2): (a) operating frequency of 6 kHz, (b) operating frequency of 8 kHz

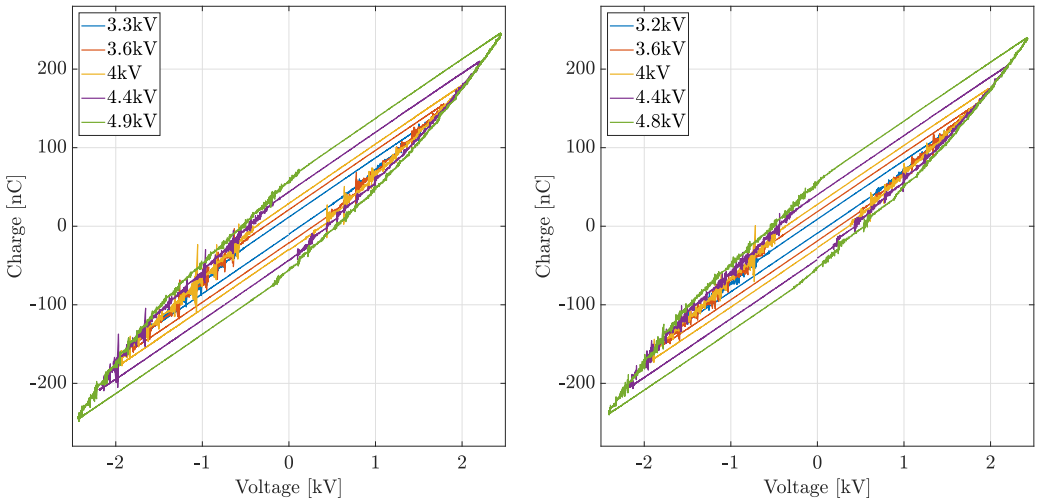

(a) Operating frequency of 10 kHz (b) Operating frequency of 12 kHz

FIGURE C.2: Lissajous graphs for varying operating voltages of printed plasma sources using 75 μm Kapton HN dielectric substrates (Electrode ID #16 from section 3.2.2): (c) operating frequency of 10 kHz, (d) operating frequency of 12 kHz

C.2 Lissajous Graphs over varying electrode configurations

The following sections provides an overview of obtained Lissajous graphs over varying electrode configurations presented in section 4.4.1 uses as the experimental validation set for the proposed electrical model. The Lissajous graphs are shown for constant operating frequency of 6 kHz over varying operating voltages

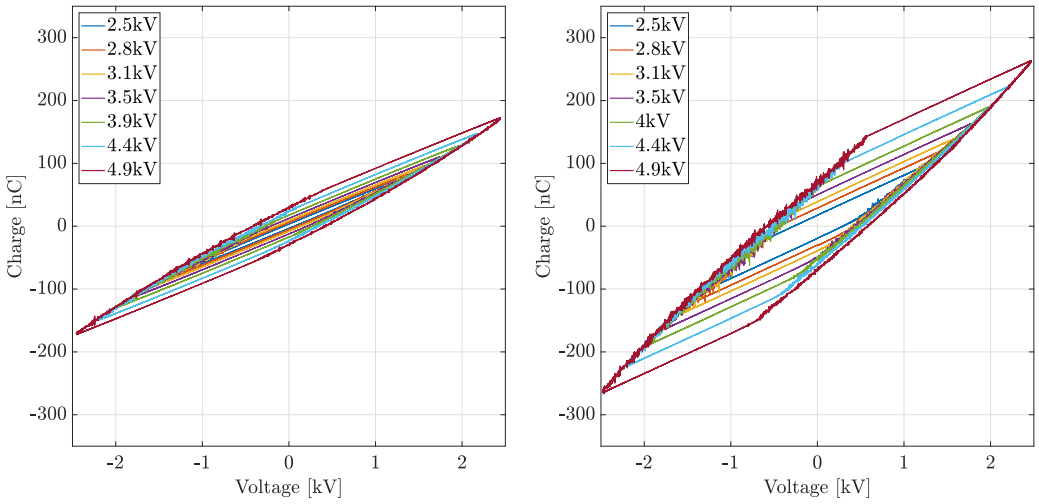

(a) Configuration #1 (b) Configuration #2

FIGURE C.3: Lissajous graphs for varying electrode configuration over varying operating voltages at constant frequency of 6 kHz (Configuration #1 and #2 from section 4.4.1): (a) Configuration #1, (b) Configuration #2

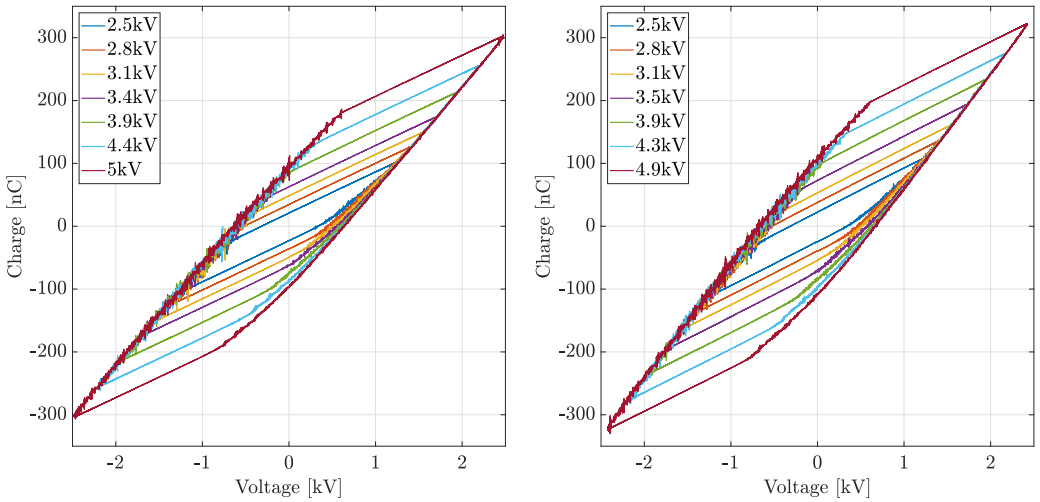

(a) Configuration #3

(b) Configuration #4

FIGURE C.4: Lissajous graphs for varying electrode configuration over varying operating voltages at constant frequency of 6 kHz (Configuration #1 and #2 from section 4.4.1): (a) Configuration #3, (b) Configuration #4

Bibliography

[1] J.-C. Wang, "Modeling Studies of Atmospheric Pressure Microplasmas: Plasma Dynamics, Surface Interaction and Applications," PhD Thesis, University of Michigan, 2014.

[2] J. R. Roth, *Industrial Plasma Engineering Volume 1: Principles*. IOP Publishing Ltd, 1995, vol. 1.

[3] D. Yan, J. H. Sherman, and M. Keidar, "Cold atmospheric plasma, a novel promising anti-cancer treatment modality," *Oncotarget*, vol. 8, no. 9, pp. 15 977–15 995, 2017.

[4] M. I. Boulos, P. Fauchais, and E. Pfender, *Thermal Plasmas - Fundamentals and Applications*. Springer Science+Business Media, LLC, 1994.

[5] C. Tendero, C. Tixier, P. Tristant, J. Desmaison, and P. Leprince, "Atmospheric pressure plasmas: A review," *Spectrochimica Acta - Part B Atomic Spectroscopy*, vol. 61, no. 1, pp. 2–30, 2006.

[6] J. Bittencourt, *Fundamentals of Plasma Physics*. Springer Science+Business Media New York, 2004.

[7] G. Kminek, C. Conley, V. Hipkin, and H. Yano, "COSPAR ' s Planetary Protection Policy," *Space Research Today*, vol. 200, pp. 12–25, 2017.

[8] B. Choudhury, S. Portugal, J. Johnson, and S. Roy, "Performance evaluation of fan and comb shaped plasma reactors for distribution of generated ozone in a confined space," in *AIAA Scitech 2020 Forum*, 2020.

[9] A. C. Schuerger, S. Trigwell, and C. I. Calle, "Use of non-thermal atmospheric plasmas to reduce the viability of Bacillus subtilis on spacecraft surfaces," *International Journal of Astrobiology*, vol. 7, no. 1, pp. 47–57, 2008.

[10] ECSS (European Cooperation for Space Standardization), "ECSS-Q-ST-70-57C: Dry heat bioburden reduction for flight hardware," 2013.

[11] ECSS (European Cooperation for Space), "ECSS-Q-ST-70-56C: Vapour phase bioburden reduction for flight hardware," 2013.

[12] S. Shimizu, S. Barczyk, P. Rettberg, T. Shimizu, T. Klaempfl, J. L. Zimmermann, T. Hoeschen, C. Linsmeier, P. Weber, G. E. Morfill, and H. M. Thomas, "Cold atmospheric plasma - A new technology for spacecraft component decontamination," *Planetary and Space Science*, vol. 90, pp. 60–71, 2014.

[13] J. D. Anderson, *Hypersonic and High-Temperature Gas Dynamics*, 2nd ed. American Institute of Aeronautics and Astronautics, Inc., 2006.

[14] W. J. Linwood Jones and A. E. Cross, "Electrostatic Probe Measurments of Plasma Surrounding Three 25 000 foot per seconds Reentry Flight Experiments," *Symposium:The Entry Plasma Sheath And Its Effects On Space Vehicle Electromagnetiac Systems*, vol. 1, no. NASA SP-25, pp. 109–136, 1970.

[15] J. L. Raper, "Project RAM Flight-Test Rocket Vehicles," *Proceeding of the NASA Conference on Communicating through plasma of atmoshperic entry and rocket exhaust*, pp. 181–189, 1964.

[16] N. D. Akey, "Overview Of The RAM Reentry Measurment Program," *Symosium: The Entry Plasma Sheath And Its Effects On Space Vehicle Electromagneitc Systems*, vol. 1, no. NASA SP-252, pp. 19–28, 1970.

[17] M. Kim, "Electromagnetic manipulation of plasma layer for re-entry blackout mitigation," PhD Thesis, University of Michigan, 2009.

[18] H. Groenig and H. Olivier, "Experimental Hypersonic Flow Research in Europe," *JSME Internationl Journal*, vol. 41, no. 2, 1998.

[19] D. Vennemann, "Hypersonic test facilities available in Western Europe for aerodynamic/aerothermal and structure/material investigations," *Philosophical Transactions of the Royal Society A: Mathematical, Physical and Engineering Sciences*, vol. 357, pp. 2227–2248, 1999.

[20] K. Xie, X. Li, and D. Liu, "Reproducing continuous radio blackout using glow discharge plasma," *Review of Scientific Instruments*, vol. 84, no. 104701, 2013.

[21] D. Liu, X. Li, K. Xie, and Z. Liu, "The propagation characteristics of electromagnetic waves through plasma in the near-field region of low-frequency loop antenna," *Physics of Plasmas*, vol. 22, no. 10, 2015.

[22] T. T. Gupta and H. Ayan, "Application of non-thermal plasma on biofilm: A review," *Applied Sciences (Switzerland)*, vol. 9, no. 17, 2019.

[23] M. Laroussi, "Low temperature plasma-based sterilization: Overview and state-of-the-art," *Plasma Processes and Polymers*, vol. 2, no. 5, pp. 391–400, 2005.

[24] M. Moreau, N. Orange, and M. G. Feuilloley, "Non-thermal plasma technologies: New tools for bio-decontamination," *Biotechnology Advances*, vol. 26, no. 6, pp. 610–617, 2008.

[25] M. G. Kong, G. Kroesen, G. Morfill, T. Nosenko, T. Shimizu, J. Van Dijk, and J. L. Zimmermann, "Plasma medicine: An introductory review," *New Journal of Physics*, vol. 11, pp. 0–35, 2009.

[26] M. Laroussi, "Low-temperature plasmas for medicine?" *IEEE Transactions on Plasma Science*, vol. 37, no. 6, pp. 714–725, 2009.

[27] Z. Kovalóvá, M. Zahoran, A. Zahoranová, and Z. Machala, "Streptococci biofilm decontamination on teeth by low-temperature air plasma of dc corona discharges," *Journal of Physics D: Applied Physics*, vol. 47, no. 22, 2014.

[28] D. Dobrynin, G. Friedman, A. Fridman, and A. Starikovskiy, "Inactivation of bacteria using dc corona discharge: role of ions and humidity," *New J Phys.*, vol. 13, no. 103033, 2011.

[29] M. Y. Alkawareek, Q. T. Algwari, G. Laverty, S. P. Gorman, W. G. Graham, D. O'Connell, and B. F. Gilmore, "Eradication of Pseudomonas aeruginosa Biofilms by Atmospheric Pressure Non-Thermal Plasma," *PLoS ONE*, vol. 7, no. 8, pp. 13–15, 2012.

[30] D. Ziuzina, S. Patil, P. J. Cullen, D. Boehm, and P. Bourke, "Dielectric barrier discharge atmospheric cold plasma for inactivation of Pseudomonas aeruginosa biofilms," *Plasma Medicine*, vol. 4, no. 1-4, pp. 137–152, 2014.

[31] S. Bekeschus, A. Schmidt, K. D. Weltmann, and T. von Woedtke, "The plasma jet kINPen A powerful tool for wound healing," *Clinical Plasma Medicine*, vol. 4, pp. 19–28, 2016.

[32] K.-D. Weltmann, K. Fricke, M. Stieber, R. Brandenburg, T. von Woedtke, U. Schnabel, and A. P. Sources, "New Nonthermal Atmospheric-Pressure Plasma Sources for Decontamination of Human Extremities," *IEEE Transactions on Plasma Science*, vol. 40, no. 11, pp. 2963–2969, 2012.

[33] B. K. H. L. Boekema, M. Vlig, D. Guijt, K. Hijnen, S. Hofmann, P. Smits, A. Sobota, E. M. van Veldhuizen, P. Bruggeman, and E. Middelkoop, "A new flexible DBD device for treating infected wounds: in vitro and ex vivo evaluation and comparison with a RF argon plasma jet," *Journal of Physics D: Applied Physics*, vol. 49, no. 4, p. 044001, feb 2016.

[34] G. S. Dijksteel, M. M. Ulrich, M. Vlig, A. Sobota, E. Middelkoop, and B. K. Boekema, "Safety and bactericidal efficacy of cold atmospheric plasma generated by a flexible surface Dielectric Barrier Discharge device against Pseudomonas aeruginosa in vitro and in vivo," *Annals of Clinical Microbiology and Antimicrobials*, vol. 19, no. 1, pp. 1–10, 2020.

[35] Y. F. Li, D. Taylor, J. L. Zimmermann, W. Bunk, R. Monetti, G. Isbary, V. Boxhammer, H. U. Schmidt, T. Shimizu, H. M. Thomas, and G. E. Morfill, "In vivo skin treatment using two portable plasma devices: Comparison of a direct and an indirect cold atmospheric plasma treatment," *Clinical Plasma Medicine*, vol. 1, no. 2, pp. 35–39, 2013.

[36] B. Boekema, M. Stoop, M. Vlig, J. V. Liempt, and A. Sobota, "Antibacterial and safety tests of a flexible cold atmospheric plasma device for the stimulation of wound healing," *Applied Microbiology and Biotechnology*, 2021.

[37] G. Isbary, W. Stolz, T. Shimizu, R. Monetti, W. Bunk, H. U. Schmidt, G. E. Morfill, T. G. Klämpfl, B. Steffes, H. M. Thomas, J. Heinlin, S. Karrer, M. Landthaler, and J. L. Zimmermann, "Cold atmospheric argon plasma treatment may accelerate wound healing in chronic wounds: Results of an open retrospective randomized controlled study in vivo," *Clinical Plasma Medicine*, vol. 1, no. 2, pp. 25–30, 2013.

[38] R. López-Callejas, R. Peña-Eguiluz, R. Valencia-Alvarado, A. Mercado-Cabrera, B. G. Rodríguez-Méndez, J. H. Serment-Guerrero, A. Cabral-Prieto, A. C. González-Garduño, N. A. Domínguez-Cadena, J. Muñoz-Infante, and M. Betancourt-Ángeles, "Alternative method for healing the diabetic foot by means of a plasma needle," *Clinical Plasma Medicine*, vol. 9, pp. 19–23, 2018.

[39] I. Molnar, J. Papp, A. Simon, and S. D. Anghel, "Deactivation of Streptococcus mutans biofilms on a tooth surface using He dielectric barrier discharge at atmospheric pressure," *Plasma Science and Technology*, vol. 15, no. 6, pp. 535–541, 2013.

[40] J. A. Pérez-Martínez, R. Peña-Eguiluz, R. López-Callejas, A. Mercado-Cabrera, R. A. Valencia, S. R. Barocio, J. S. Benítez-Read, and J. O. Pacheco-Sotelo, "An RF microplasma facility development for medical applications," *Surface and Coatings Technology*, vol. 201, pp. 5684–5687, 2007.

[41] J. Pan, K. Sun, Y. Liang, P. Sun, X. Yang, J. Wang, J. Zhang, W. Zhu, J. Fang, and K. H. Becker, "Cold plasma therapy of a tooth root canal infected with enterococcus faecalis biofilms in vitro," *Journal of Endodontics*, vol. 39, no. 1, pp. 105–110, 2013.

[42] D. B. Nelson and L. F. Muscarella, "Current issues in endoscope reprocessing and infection control during gastrointestinal endoscopy," *World Journal of Gastroenterology*, vol. 12, no. 25, pp. 3953–3964, 2006.

[43] F. Rossi, O. Kylián, H. Rauscher, M. Hasiwa, and D. Gilliland, "Low pressure plasma discharges for the sterilization and decontamination of surfaces," *New Journal of Physics*, vol. 11, pp. 0–33, 2009.

[44] A. Smith, M. Dickson, J. Aitken, and J. Bagg, "Contaminated dental instruments," *Journal of Hospital Infection*, vol. 51, no. 3, pp. 233–235, 2002.

[45] R. I. Rothstein and B. Littenberg, "Disposable, sheathed, flexible sigmoidoscopy: A prospective, multicenter, randomized trial," *Gastrointestinal Endoscopy*, vol. 41, no. 6, pp. 566–572, 1995.

[46] S. Bhatt, P. Mehta, C. Chen, C. L. Schneider, L. N. White, H. L. Chen, and M. G. Kong, "Efficacy of low-temperature plasma-activated gas disinfection against biofilm on contaminated GI endoscope channels," *Gastrointestinal Endoscopy*, vol. 89, no. 1, pp. 105–114, 2019.

[47] M. Polak, J. Winter, U. Schnabel, J. Ehlbeck, and K. D. Weltmann, "Innovative plasma generation in flexible biopsy channels for inner-tube decontamination and medical applications," *Plasma Processes and Polymers*, vol. 9, pp. 67–76, 2012.

[48] G. Fridman, A. Shereshevsky, M. M. Jost, A. D. Brooks, A. Fridman, A. Gutsol, V. Vasilets, and G. Friedman, "Floating electrode dielectric barrier discharge plasma in air promoting apoptotic behavior in Melanoma skin cancer cell lines," *Plasma Chemistry and Plasma Processing*, vol. 27, no. 2, pp. 163–176, 2007.

[49] M. Keidar, R. Walk, A. Shashurin, P. Srinivasan, A. Sandler, S. Dasgupta, R. Ravi, R. Guerrero-Preston, and B. Trink, "Cold plasma selectivity and the possibility of a paradigm shift in cancer therapy," *British Journal of Cancer*, vol. 105, no. 9, pp. 1295–1301, 2011.

[50] J. Y. Kim, Y. Wei, J. Li, P. Foy, T. Hawkins, J. Ballato, and S. O. Kim, "Single-cell-level microplasma cancer therapy," *Small*, vol. 7, no. 16, pp. 2291–2295, 2011.

[51] W. Rowe, X. Cheng, L. Ly, T. Zhuang, G. Basadonna, B. Trink, M. Keidar, and J. Canady, "The Canady Helios Cold Plasma Scalpel Significantly Decreases Viability in Malignant Solid Tumor Cells in a Dose-Dependent Manner," *Plasma*, vol. 1, no. 1, pp. 177–188, 2018.

[52] H. R. Metelmann, D. S. Nedrelow, C. Seebauer, M. Schuster, T. von Woedtke, K. D. Weltmann, S. Kindler, P. H. Metelmann, S. E. Finkelstein, D. D. Von Hoff, and F. Podmelle, "Head and neck cancer treatment and physical plasma," *Clinical Plasma Medicine*, vol. 3, no. 1, pp. 17–23, 2015.

[53] University Women's Hospital Tübingen, "Physical Cold Atmospheric Plasma for the Treatment of Cervical Intraepithelial Neoplasia (CAPCIN) (NCT03218436)," 2017. [Online]. Available: https://trialsearch.who.int/?TrialID=NCT03218436

[54] Jerome Canady Research Institute for Advanced Biological and Technological Sciences, "Canady Helios Cold Plasma Scalpel Treatment at the Surgical Margin and Macroscopic Tumor Sites (NCT04267575)," 2020. [Online]. Available: https://clinicaltrials.gov/ct2/show/NCT04267575

[55] J. R. Roth, *Industrial Plasma Engineering Volume 2: Applications To Nonthermal Plasma Processing.* IOP Publishing Ltd, 2001.

[56] M. Miclea, K. Kunze, J. Franzke, and K. Niemax, "Plasmas for lab-on-the-chip applications," *Spectrochimica Acta Part B: Atomic Spectroscopy*, vol. 57, no. 10, pp. 1585–1592, 2002.

[57] J. Winter, R. Brandenburg, and K. D. Weltmann, "Atmospheric pressure plasma jets: An overview of devices and new directions," *Plasma Sources Science and Technology*, vol. 24, no. 6, p. 64001, 2015.

[58] R. Brandenburg, "Dielectric barrier discharges: Progress on plasma sources and on the understanding of regimes and single filaments," *Plasma Sources Science and Technology*, vol. 26, no. 5, 2017.

[59] M. N. F. Zainal, N. Redzuan, M. Fadthul, and I. Misnal, "Brief Review: Cold Plasma," *Jurnal Teknologi*, vol. 10, pp. 31–39, 2013.

[60] S. Kumar, R. Singh, T. P. Singh, and B. L. Sethi, "Surface modification by electrical discharge machining: A review," *Journal of Materials Processing Technology*, vol. 209, no. 8, pp. 3675–3687, 2009.

[61] N. Misra, O. Schlueuter, and P. Cullen, *Cold Plasma in Food and Agriculture.* Elsevier, 2016.

[62] K. H. Schoenbach, R. Verhappen, T. Tessnow, F. E. Peterkin, and W. W. Byszewski, "Microhollow cathode discharges," *Journal of Vacuum Science & Technology A*, vol. 21, 2003.

[63] S. J. Park, J. Chen, C. Liu, and J. G. Eden, "Silicon microdischarge devices having inverted pyramidal cathodes: Fabrication and performance of arrays," *Applied Physics Letters*, vol. 78, no. 4, pp. 419–421, 2001.

[64] A. El-Habachi, W. Shi, M. Moselhy, R. H. Stark, and K. H. Schoenbach, "Series operation of direct current xenon chloride excimer sources," *Journal of Applied Physics*, vol. 88, no. 6, pp. 3220–3224, 2000.

[65] L. D. Biborosch, I. Petzenhauser, B.-j. Lee, K. Frank, and K. H. Schoenbach, "Excimer emission of open and closed microhollow cathode discharges in xenon," *Rom. Journ. Phys.,*, vol. 50, no. 7 - 8, pp. 711–722, 2005.

[66] D. Xiao, C. Cheng, J. Shen, Y. Lan, H. Xie, X. Shu, Y. Meng, J. Li, and P. K. Chu, "Electron density measurements of atmospheric-pressure non-thermal N2 plasma jet by Stark broadening and irradiance intensity methods," *Physics of Plasmas*, vol. 21, 2014.

[67] M. Thiyagarajan, A. Sarani, and C. Nicula, "Optical emission spectroscopic diagnostics of a non-thermal atmospheric pressure helium-oxygen plasma jet for biomedical applications," *Journal of Applied Physics*, vol. 113, no. 23, 2013.

[68] P. J. Bruggeman, F. Iza, and R. Brandenburg, "Foundations of atmospheric pressure non-equilibrium plasmas," *Plasma Sources Science and Technology*, vol. 26, no. 12, 2017.

[69] V. Nehra, A. Kumar, and H. K. Dwivedi, "Atmospheric Non-Thermal Plasma Sources," *International Journal of Engineering*, vol. 2, no. 1, pp. 53–68, 2008.

[70] K. D. Weltmann, E. Kindel, T. V. Woedtke, M. Hähnel, M. Stieber, and R. Brandenburg, "Atmospheric-pressure plasma sources : Prospective tools for plasma," *Pure and Applied Chemistry*, vol. 82, no. 6, pp. 1223–1237, 2010.

[71] N. Benard, A. Mizuno, and E. Moreau, "A large-scale multiple dielectric barrier discharge actuator based on an innovative three-electrode design," *Journal of Physics D: Applied Physics*, vol. 42, no. 23, 2009.

[72] R. C. Nelson, T. C. Corke, H. Othman, M. P. Patel, S. Vasudevan, and T. Ng, "A smart wind turbine blade using distributed plasma actuators for improved performance," in *46th AIAA Aerospace Sciences Meeting and Exhibit*, no. January, 2008.

[73] G. E. Morfill, T. Shimizu, B. Steffes, and H.-U. Schmidt, "Nosocomial infectionsa new approach towards preventive medicine using plasmas," *New Journal of Physics*, vol. 11, no. 115019, 2009.

[74] U. Kogelschatz, "Filamentary, Patterned, and Diffuse Barrier Discharge," *IEEE Transactions on Plasma Science*, vol. 30, no. 4, pp. 1400–1408, 2002.

[75] N. M. Houser, "Manufacturing of Dielectric Barrier Discharge Plasma Actuator for Degradation Resistance," MSc Thesis, University of Toronto, 2013.

[76] W. Su, B. S. Cook, Y. Fang, and M. M. Tentzeris, "Fully inkjet-printed microfluidics: A solution to low-cost rapid three-dimensional microfluidics fabrication with numerous electrical and sensing applications," *Nature Scientific Reports*, no. September, pp. 1–12, 2016.

[77] W. G. Whittow, Y. Li, R. Torah, K. Yang, S. Beeby, and J. Tudor, "Printed frequency selective surfaces on textiles," *Electronics Letters*, no. June, pp. 8–10, 2014.

[78] Y. Khan, A. E. Ostfeld, C. M. Lochner, A. Pierre, and A. C. Arias, "Monitoring of Vital Signs with Flexible and Wearable Medical Devices," *Advanced Materials*, vol. 28, no. 22, pp. 4373–4395, 2016.

[79] D. Y. Shin, S. S. Yoo, H. E. Song, H. Tak, and D. Byun, "Electrostatic-force-assisted dispensing printing to construct high-aspect-ratio of 0.79 electrodes on a textured surface with improved adhesion and contact resistivity," *Scientific Reports*, vol. 5, no. November, pp. 1–7, 2015.

[80] Novacentrix, "Metalon silver inkjet JS-B25P," 2018. [Online]. Available: https://www.novacentrix.com/

[81] W. G. Whittow, A. Chauraya, J. C. Vardaxoglou, Y. Li, R. Torah, K. Yang, S. Beeby, and J. Tudor, "Inkjet-printed microstrip patch antennas realized on textile for wearable applications," *IEEE Antennas and Wireless Propagation Letters*, vol. 13, pp. 71–74, 2014.

[82] FUJIFILM, "Dimatix Materials Printer DMP-2850," 2019. [Online]. Available: https://www.fujifilm.com/us/en/business/inkjet-solutions/inkjet-technology-integration/dmp-2850{#}

[83] K. P. Singh and S. Roy, "Impedance matching for an asymmetric dielectric barrier discharge plasma actuator," *Applied Physics Letters*, vol. 91, no. 8, 2007.

[84] Z. Chen, "Impedance Matching and Simulation of One Atmosphere Uniform Glow Discharge Plasma (OAUGDP) Reactor / Actuator Systems A Thesis Presented for The Master of Science," MSc Thesis, The University of Tennessee, 2007.

[85] T. C. Manley, "The Electric Characteristics of the Ozonator Discharge," *Transactions of The Electrochemical Society*, vol. 84, no. 1, p. 83, 1943.

[86] J. Kriegseis, B. Möller, S. Grundmann, and C. Tropea, "Capacitance and power consumption quantification of dielectric barrier discharge (DBD) plasma actuators," *Journal of Electrostatics*, vol. 69, no. 4, pp. 302–312, 2011.

[87] D. Ashpis, M. Laun, and E. Griebeler, "Progress toward Accurate Measurements of Power Consumption of DBD Plasma Actuators," in *50th Aerospace Sciences Meeting*, 2012.

[88] J. Kriegseis, S. Grundmann, and C. Tropea, "Power consumption, discharge capacitance and light emission as measures for thrust production of dielectric barrier discharge plasma actuators," *Journal of Applied Physics*, vol. 110, no. 1, 2011.

[89] S. Grundmann and C. Tropea, "Experimental damping of boundary-layer oscillations using DBD plasma actuators," *International Journal of Heat and Fluid Flow*, vol. 30, no. 3, pp. 394–402, 2009.

[90] D. M. Orlov, T. C. Corke, and M. P. Patel, "Electric circuit model for aerodynamic plasma actuator," in *44th AIAA Aerospace Sciences Meeting*, vol. 19, no. January, 2006, pp. 14 678–14 687.

[91] J. Kramida, A. and Ralchenko, Yu. and Reader and N. A. Team, "NIST Atomic Spectra Database (version 5.6.1)," *National Institute of Standards and Technology, Gaithersburg, MD.*, 2018.

[92] S. Keller, P. Rajasekaran, N. Bibinov, and P. Awakowicz, "Characterization of transient discharges under atmospheric-pressure conditions applying nitrogen photoemission and current measurements," *Journal of Physics D: Applied Physics*, vol. 45, no. 12, pp. 1–24, 2012.

[93] Z. Machala, M. Janda, K. Hensel, I. Jedlovský, L. Leštinská, V. Foltin, V. Martišovitš, and M. Morvová, "Emission spectroscopy of atmospheric pressure plasmas for bio-medical and environmental applications," *Journal of Molecular Spectroscopy*, vol. 243, pp. 194–201, 2007.

[94] R. E. Hanson, J. Kimelman, N. M. Houser, and P. Lavoie, "Effect of dielectric degradation on dielectric barrier discharge plasma actuator performance," *51st AIAA Aerospace Sciences Meeting including the New Horizons Forum and Aerospace Exposition 2013*, pp. 1–13, 2013.

[95] F. Tricot, C. Venet, D. Beneventi, D. Curtil, D. Chaussy, T. P. Vuong, J. E. Broquin, and N. Reverdy-Bruas, "Fabrication of 3D conductive circuits: Print quality evaluation of a direct ink writing process," *RSC Advances*, vol. 8, no. 46, pp. 26 036–26 046, 2018.

[96] Z. Zhang and J. Liu, "Interfacial adhesion enhancement of ink-jet printed transparent metallic grid electrodes induced by the coffee-ring effect," *Journal of Materials Chemistry C*, vol. 4, no. 19, pp. 4218–4225, 2016.

[97] U. Kogelschatz, "Dielectric-barrier Discharges : Their History, Discharge Physics, and Industrial Applications," *Plasma Chemistry and Plasma Processing*, vol. 23, no. 1, pp. 1–46, 2003.

[98] J. Kim and K. Terashima, "2.45 GHz microwave-excited atmospheric pressure air microplasmas based on microstrip technology," *Applied Physics Letters*, vol. 86, no. 19, pp. 1–3, 2005.

[99] RS Components Pro, "MSS08/011 Formex GK-17," 2020. [Online]. Available: https://uk.rs-online.com/web/p/plastic-film/7850811

[100] DuPont de Nemours Inc., "Kapton® HN general-purpose polyimide film," 2018. [Online]. Available: https://www.dupont.com/products/kapton-hn.html

[101] DuPont de Nemours Inc, "Kapton® MT," 2020. [Online]. Available: https://www.dupont.com/products/kapton-mt.html

[102] Voltera Inc., "Flex 2 Ink Cartridge," 2020. [Online]. Available: https://www.voltera.io/store/consumables/flex-2-conductive-ink

[103] Inkron, "Printable Conductive Inks," 2020. [Online]. Available: https://inkron.com/printable-conductive-inks/

[104] T. Abe, Y. Takizawa, S. Sato, and N. Kimura, "A parametric experimental study for momentum transfer by plasma actuator," in *45th AIAA Aerospace Sciences Meeting*, 2007.

[105] B. Dong, J. M. Bauchire, J. M. Pouvesle, P. Magnier, and D. Hong, "Experimental study of a DBD surface discharge for the active control of subsonic airflow," *Journal of Physics D: Applied Physics*, vol. 41, no. 15, 2008.

[106] C. L. Enloe, T. E. McLaughlin, R. D. VanDyken, K. D. Kachner, E. J. Jumper, and T. C. Corke, "Mechanisms and Responses of a Single Dielectric Barrier Plasma Actuator: Plasma Morphology," in *41st Aerospace Sciences Meeting and Exhibit*, vol. 42, no. 3, 2003.

[107] J. Pons, E. Moreau, and G. Touchard, "Asymmetric surface dielectric barrier discharge in air at atmospheric pressure: Electrical properties and induced airflow characteristics," *Journal of Physics D: Applied Physics*, vol. 38, no. 19, pp. 3635–3642, 2005.

[108] M. Forte, J. Jolibois, J. Pons, E. Moreau, G. Touchard, and M. Cazalens, "Optimization of a dielectric barrier discharge actuator by stationary and non-stationary measurements of the induced flow velocity: Application to airflow control," *Experiments in Fluids*, vol. 43, no. 6, pp. 917–928, 2007.

[109] J. W. Baughn, C. O. Porter, B. L. Peterson, T. E. McLaughlin, C. L. Enloe, G. I. Font, and C. Baird, "Momentum transfer for an aerodynamic plasma actuator with an imposed boundary layer," in *44th AIAA Aerospace Sciences Meeting*, vol. 3, no. January, 2006, pp. 2027–2041.

[110] C. O. Porter, J. W. Baughn, T. E. McLaughlin, C. L. Enloe, and G. I. Font, "Plasma actuator force measurements," *AIAA Journal*, vol. 45, no. 7, pp. 1562–1570, 2007.

[111] R. Geuns, "The Use of Dielectric Barrier Discharge Plasma Actuators for Low-Speed Flow Control," Master of Science Thesis, Delft University of Technology, 2014.

[112] C. L. Enloe, T. E. McLaughlin, R. D. VanDyken, K. D. Kachner, E. J. Jumper, and T. C. Corke, "Mechanisms and Responses of a Single Dielectric Barrier Plasma Actuator: Plasma Morphology," in *41st Aerospace Sciences Meeting and Exhibit*, vol. 42, no. 3, 2003.

[113] H. Jakob and M. Kim, "Electrical Model for Complex Surface DBD Plasma Sources," *IEEE Transactions on Plasma Science*, vol. 49, no. 10, pp. 3051–3058, 2021.

[114] T. C. Corke, C. L. Enloe, and S. P. Wilkinson, "Dielectric Barrier Discharge Plasma Actuators for Flow Control," *Annual Review of Fluid Mechanics*, vol. 42, pp. 505–529, 2010.

[115] J. Foster, B. S. Sommers, S. N. Gucker, I. M. Blankson, and G. Adamovsky, "Perspectives on the interaction of plasmas with liquid water for water purification," *IEEE Transactions on Plasma Science*, vol. 40, no. 5, pp. 1311–1323, 2012.

[116] M. Archambault-Caron, H. Gagnon, B. Nisol, K. Piyakis, and M. R. Wertheimer, "Precise energy and temperature measurements in dielectric barrier discharges at atmospheric pressure," *Plasma Sources Science and Technology*, vol. 24, no. 4, 2015.

[117] V. I. Gibalov and G. J. Pietsch, "Development of dielectric barrier discharges in gas gaps and on surfaces," *Journal of Physics D: Applied Physics*, vol. 33, no. 20, pp. 2618–2636, 2000.

[118] R. Erfani, H. Zare-Behtash, C. Hale, and K. Kontis, "Development of DBD plasma actuators: The double encapsulated electrode," *Acta Astronautica*, vol. 109, pp. 132–143, 2015.

[119] U. N. Pal, A. K. Sharma, J. S. Soni, S. Kr, H. Khatun, M. Kumar, B. L. Meena, M. S. Tyagi, B. J. Lee, M. Iberler, J. Jacoby, and K. Frank, "Electrical modelling approach for discharge analysis of a coaxial DBD tube filled with argon," *Journal of Physics D: Applied Physics*, vol. 42, no. 4, 2009.

[120] R. Valdivia-Barrientos, J. Pacheco-Sotelo, M. Pacheco-Pacheco, J. S. Benitez-Read, and R. Lopez-Callejas, "Analysis and electrical modelling of a cylindrical DBD configuration at different operating frequencies," *Plasma Sources Science and Technology Analysis*, vol. 15, no. 2, pp. 237–245, 2006.

[121] A. S. Chiper, V. Ania, C. Agheorghiesei, V. Pohoaa, M. Ania, and G. Popa, "Spectroscopic diagnostics for a DBD plasma in He/Air and He/N2 gas mixtures," *Plasma Processes and Polymers*, vol. 1, no. 1, pp. 57–62, 2004.

[122] N. Naudé, J. P. Cambronne, N. Gherardi, and F. Massines, "Electrical model and analysis of the transition from an atmospheric pressure Townsend discharge to a filamentary discharge," *Journal of Physics D: Applied Physics*, vol. 38, no. 4, pp. 530–538, 2005.

[123] A. V. Pipa, J. Koskulics, R. Brandenburg, and T. Hoder, "The simplest equivalent circuit of a pulsed dielectric barrier discharge and the determination of the gas gap charge transfer," *Review of Scientific Instruments*, vol. 83, no. 11, 2012.

[124] S. Zhou, X. Huang, and M. Liu, "Electrical model and experimental analysis of a double spiral structure surface dielectric barrier discharge," *Plasma Science and Technology*, vol. 21, no. 6, p. 65401, 2019.

[125] F. Liu, Y. Liu, Y. Lu, Z. Wang, Y. Shi, L. Ji, and J. Cheng, "Nano Energy Electrical analysis of triboelectric nanogenerator for high voltage applications exampled by DBD microplasma," *Nano Energy*, vol. 56, pp. 482–493, 2019.

[126] A. A. Flores-Fuentes, R. Peña-Eguiluz, R. López-Callejas, A. Mercado-Cabrera, R. Valencia-A, S. R. Barocio, O. G. Godoy-Cabrera, A. de la Piedad-Beneitez, J. S. Benítez-Read, and J. O. Pacheco-Sotelo, "Modelling and simulation of a DBD plasma discharge supplied by a multicell inverter," in *Proceedings of the 25th IASTED International Conference*, 2006.

[127] Z. Fang, S. Ji, J. Pan, T. Shao, and C. Zhang, "Electrical model and experimental analysis of the atmospheric-pressure homogeneous dielectric barrier discharge in he," *IEEE Transactions on Plasma Science*, vol. 40, no. 3, pp. 883–891, 2012.

[128] N. Benard, N. Zouzou, A. Claverie, J. Sotton, and E. Moreau, "Optical visualization and electrical characterization of fast-rising pulsed dielectric barrier discharge for airflow control applications," *Journal of Applied Physics*, vol. 111, no. 3, 2012.

[129] D. F. Opaits, M. N. Shneider, R. B. Miles, A. V. Likhanskii, and S. O. MacHeret, "Surface charge in dielectric barrier discharge plasma actuators," *Physics of Plasmas*, vol. 15, no. 7, 2008.

[130] A. Debien, N. Benard, L. David, and E. Moreau, "Unsteady aspect of the electrohydrodynamic force produced by surface dielectric barrier discharge actuators," *Applied Physics Letters*, vol. 100, no. 1, pp. 3–6, 2012.

[131] J. Kriegseis, S. Grundmann, and C. Tropea, "Power consumption, discharge capacitance and light emission as measures for thrust production of dielectric barrier discharge plasma actuators," *Journal of Applied Physics*, vol. 110, no. 1, 2011.

[132] J. M. Williamson, D. D. Trump, P. Bletzinger, and B. N. Ganguly, "Comparison of high-voltage ac and pulsed operation of a surface dielectric barrier discharge," *Journal of Physics D: Applied Physics*, vol. 39, no. 20, pp. 4400–4406, 2006.

[133] Y. Akishev, G. Aponin, A. Balakirev, M. Grushin, V. Karalnik, A. Petryakov, and N. Trushkin, "Spatial-temporal development of a plasma sheet in a surface dielectric barrier discharge powered by a step voltage of moderate duration," *Plasma Sources Science and Technology*, vol. 22, no. 1, 2013.

[134] D. Z. Pai, S. Stauss, and K. Terashima, "Field-emitting Townsend regime of surface dielectric barrier discharges emerging at high pressure up to supercritical conditions," *Plasma Sources Science and Technology*, vol. 24, no. 2, 2015.

[135] F. J. Peeters and M. C. Van De Sanden, "The influence of partial surface discharging on the electrical characterization of DBDs," *Plasma Sources Science and Technology*, vol. 24, no. 1, p. 15016, 2015.

[136] A. V. Pipa, R. Hink, R. Foest, and R. Brandenburg, "Dependence of dissipated power on applied voltage for surface barrier discharge from simplest equivalent circuit," *Plasma Sources Science and Technology*, pp. 0–6, 2020.

[137] V. R. Soloviev, "Analytical estimation of the thrust generated by a surface dielectric barrier discharge," *Journal of Physics D: Applied Physics*, vol. 45, no. 2, 2012.

[138] X. Chen, Y. Zhu, Y. Wu, J. Hao, X. Ma, and P. Lu, "Numerical investigations of nanosecond surface streamers at elevated pressure," *Plasma Sources Science and Technology*, pp. 0–12, 2021.

[139] M. V. Sokolova, V. V. Voevodin, J. I. Malakhov, N. L. Aleksandrov, E. M. Anokhin, and V. R. Soloviev, "Barrier properties influence on the surface dielectric barrier discharge driven by single voltage pulses of different duration," *Journal of Physics D: Applied Physics*, vol. 52, no. 32, 2019.

[140] V. I. Gibalov and G. J. Pietsch, "Dynamics of dielectric barrier discharges in different arrangements," *Plasma Sources Science and Technology*, vol. 21, no. 2, 2012.

[141] S. Goekce, "Plasma Diagnostics and Modelling of Nanosecond Pulsed Surface Dielectric Barrier Discharge Actuators," PhD Thesis, École Polytechnique Fédérale de Lausanne, 2014.

[142] Y. Zhu, S. Shcherbanev, B. Baron, and S. Starikovskaia, "Nanosecond surface dielectric barrier discharge in atmospheric pressure air: I. measurements and 2D modeling of morphology, propagation and hydrodynamic perturbations," *Plasma Sources Science and Technology*, vol. 26, no. 12, 2017.

[143] Y. Zhu and Y. Wu, "The secondary ionization wave and characteristic map of surface discharge plasma in a wide time scale," *New Journal of Physics*, vol. 22, no. 10, 2020.

[144] Plasma-Tech, "Surface Dielectric Barrier DischargeDesigner," 2020. [Online]. Available: www.plasma-tech.net/sdbdesigner/

[145] V. R. Soloviev, I. V. Selivonin, and I. A. Moralev, "Breakdown voltage for surface dielectric barrier discharge ignition in atmospheric air," *Physics of Plasmas*, vol. 24, no. 10, 2017.

[146] F. J. Peeters, R. F. Rumphorst, and M. C. Van De Sanden, "Dielectric barrier discharges revisited: The case for mobile surface charge," *Plasma Sources Science and Technology*, vol. 25, no. 3, pp. 0–6, 2016.

[147] E. D. Gillman, J. E. Foster, and I. M. Blankson, "Review of Leading Approaches for Mitigating Hypersonic Vehicle Communications Blackout and a Method of

Ceramic Particulate Injection Via Cathode Spot Arcs for Blackout Mitigation," *NASA Glenn Research Center*, vol. NASA/TM20, p. 25, 2010.

[148] M. Keidar, M. Kim, and I. Boyd, "Electromagnetic Reduction of Plasma Density During Atmospheric Reentry and Hypersonic Flights," *Journal of Spacecraft and Rockets*, vol. 45, no. 3, pp. 445–453, 2008.

[149] H. Jakob and M. Kim, "Feasibility study on the use of non-thermal plasma for a cold radio blackout experiment," in *AIAA Scitech 2020 Forum*, 2020, pp. 1–14.

[150] M. Qian, C. Ren, D. Wang, J. Zhang, and G. Wei, "Stark broadening measurement of the electron density in an atmospheric pressure argon plasma jet with double-power electrodes," *Journal of Applied Physics*, vol. 107, no. 6, 2010.

[151] S. Y. Moon, W. Choe, H. S. Uhm, Y. S. Hwang, and J. J. Choi, "Characteristics of an atmospheric microwave-induced plasma generated in ambient air by an argon discharge excited in an open-ended dielectric discharge tube," *Physics of Plasmas*, vol. 9, no. 9, p. 4045, 2002.

[152] J. Torres, J. Jonkers, M. J. Van de Sande, J. J. Van der Mullen, A. Gamero, and A. Sola, "An easy way to determine simultaneously the electron density and temperature in high-pressure plasmas by using Stark broadening," *Journal of Physics D: Applied Physics*, vol. 36, no. 13, 2003.

[153] N. Balcon, A. Aanesland, and R. Boswell, "Pulsed RF discharges, glow and filamentary mode at atmospheric pressure in argon," *Plasma Sources Science and Technology*, vol. 16, no. 2, pp. 217–225, 2007.

[154] G. J. M. Hagelaar and L. C. Pitchford, "Solving the Boltzmann equation to obtain electron transport coefficients and rate coefficients for fluid models," *Plasma Sources Science and Technology*, vol. 14, no. 4, pp. 722–733, 2005.

[155] A. Phelps and L. Pitchford, "Anisotropic scattering of electrons by N2 and its effect on electron transport," *Physical Review A*, vol. 31, no. 5, pp. 2932 – 2949, 1985.

[156] D. H. Crandall, W. E. Kauppila, R. A. Phaneuf, P. O. Taylor, and G. H. Dunn, "Absolute cross sections for electron-impact excitation of N2+," *Physical Review A*, vol. 9, no. 6, pp. 2545–2551, 1974.

[157] P. Rajasekaran, N. Bibinov, and P. Awakowicz, "Quantitative characterization of a dielectric barrier discharge in air applying non-calibrated spectrometer, current measurement and numerical simulation," *Journal of Measurement Science and Technology*, vol. 23, no. 8, 2012.

[158] S. V. Pancheshnyi, S. M. Starikovskaia, and A. Y. Starikovskii, "Collisional deactivation of N 2 (C3 Pi u , v = 0 , 1 , 2 , 3) states by N2 , O2 , H2 and H2O molecules," *Chemical Physics*, vol. 262, pp. 349 – 357, 2000.

[159] G. Dilecce, P. F. Ambrico, and S. D. Benedictis, "On the collision quenching of N2 and O2 and its influence on the measurement of E/N by intensity ratio of nitrogen spectral bands," *Journal of Physics D: Applied Physics*, vol. 43, no. 19, p. 195201, 2010.

[160] A. J. Ball, T. Blancquaert, O. Bayle, L. V. Lorenzoni, and A. F. C. Haldemann, "The ExoMars Schiaparelli Entry, Descent and Landing Demonstrator Module (EDM) System Design," *Space Science Reviews*, 2022.

[161] M. Kim, J. Lawson, R. Hervé, H. Jakob, B. Ganapathisubramani, and C. W. Keevil, "Development of a rapid plasma decontamination system for decontamination and reuse of filtering facepiece respirators," *AIP Advances*, vol. 11, no. 10, p. 105311, 2021.

[162] J. C. BAILAR, O. S. BURKE, L. M. BROSSEAU, H. J. COHEN, E. J. GALLAGHER, K. F. GENSHEIMER, A. L. HACK, S. JAYARAMAN, F. E. KARASZ, A. Y. LIU, A. MCGEER, and C. M. T. OSTERHOLM, *Reusability of facemasks during an influenza pandemic: Facing the flu*, 2006.

[163] World Health Organization, "Advice on the use of masks in the context of COVID-19," Tech. Rep. April, 2020.

[164] H. Kumar, A. Azad, A. Gupta, J. Sharma, H. Bherwani, N. K. Labhsetwar, and R. Kumar, "COVID-19 Creating another problem? Sustainable solution for PPE disposal through LCA approach," *Environment, Development and Sustainability*, vol. 23, no. 6, pp. 9418–9432, 2021.

[165] K. O'Hearn, S. Gertsman, M. Sampson, R. Webster, A. Tsampalieros, R. Ng, J. Gibson, A. T. Lobos, N. Acharya, A. Agarwal, S. Boggs, G. Chamberlain, E. Staykov, L. Sikora, and J. D. McNally, "Decontaminating N95 and SN95 masks with ultraviolet germicidal irradiation does not impair mask efficacy and safety," *Journal of Hospital Infection*, vol. 106, no. 1, pp. 163–175, 2020.

[166] L. F. Ludwig-Begall, C. Wielick, L. Dams, H. Nauwynck, P. F. Demeuldre, A. Napp, J. Laperre, E. Haubruge, and E. Thiry, "The use of germicidal ultraviolet light, vaporized hydrogen peroxide and dry heat to decontaminate face masks and filtering respirators contaminated with a SARS-CoV-2 surrogate virus," *Journal of Hospital Infection*, vol. 106, no. 3, pp. 577–584, 2020.

[167] L. Anderegg, C. Meisenhelder, C. O. Ngooi, L. Liao, W. Xiao, S. Chu, Y. Cui, and J. M. Doyle, "A scalable method of applying heat and humidity for decontamination of n95 respirators during the covid-19 crisis," *PLoS ONE*, vol. 15, no. 7 July, pp. 1–9, 2020.

[168] D. J. Viscusi, M. S. Bergman, B. C. Eimer, and R. E. Shaffer, "Evaluation of five decontamination methods for filtering facepiece respirators," *Annals of Occupational Hygiene*, vol. 53, no. 8, pp. 815–827, 2009.

[169] D. J. Viscusi, W. P. King, and R. E. Shaffer, "Effect of decontamination on the filtration efficiency of two filtering facepiece respirator models," *International Society for Respiratory Protection*, vol. 24, pp. 93–107, 2007.

[170] A. Lacombe, B. A. Niemira, J. B. Gurtler, J. Sites, G. Boyd, D. H. Kingsley, X. Li, and H. Chen, "Nonthermal inactivation of norovirus surrogates on blueberries using atmospheric cold plasma," *Food Microbiology*, vol. 63, pp. 1–5, 2017.

[171] T. Xia, A. Kleinheksel, E. M. Lee, Z. Qiao, K. R. Wigginton, and H. L. Clack, "Inactivation of airborne viruses using a packed bed non-thermal plasma reactor," *Journal of Physics D: Applied Physics*, vol. 52, no. 25, 2019.

[172] British Standard Institution, "Respiratory Protective Devices: Filtering Half Masks to Protect Against Particles. Requirements, Testing, Marking (BS EN 149)," 2009.

[173] H. Jakob and M. K. Kim, "Generation of non-thermal plasmas over large and complex surfaces," *Plasma Research Express*, vol. 2, no. 3, p. 35010, 2020.

[174] M. Kim, R. Hervé, H. Jakob, and C. W. Keevil, "A novel plasma source for treating biofilm on narrow endoscope channel lumens," in *8th International Conference on Plasma Medicine*, 2021.

[175] R. Hervé and C. W. Keevil, "Current limitations about the cleaning of luminal endoscopes," *Journal of Hospital Infection*, vol. 83, no. 1, pp. 22–29, 2013.

[176] M. Liedlgruber and A. Uhl, "A Summary of Research Targeted at Computer-Aided Decision Support in Endoscopy of the Gastrointestinal Tract," Tech. Rep. April, 2011.

[177] M. B. Kimmery, D. A. Burnett, D. L. Carr-Locke, A. J. DiMarino, D. M. Jensen, R. Katon, B. V. MacFadyen, M. W. Scobey, T. N. Stein, and S. M. Steinberg, "Transmission Of Infection By Gastrointestinal Endoscopy," *Gastrointestinal Endoscopy*, vol. 39, no. 6, pp. 885–888, 1993.

[178] A. Srinivasan, "Epidemiology and prevention of infections related to endoscopy," *Current Infectious Disease Reports*, vol. 5, no. 6, pp. 467–472, 2003.

[179] S. Wang, Z. Y. Chen, X. H. Wang, D. Li, A. J. Yang, D. X. Liu, M. Z. Rong, H. L. Chen, and M. G. Kong, "Propagation characteristics of atmospheric-pressure He+O2 plasmas inside a simulated endoscope channel," *Journal of Applied Physics*, vol. 118, no. 20, 2015.

[180] H. Eto, Y. Ono, A. Ogino, and M. Nagatsu, "Low-Temperature Internal Sterilization of Medical Plastic Tubes Using a Linear Dielectric Barrier Discharge," *Plasma Processes and Polymers*, vol. 5, pp. 269–274, 2008.

[181] Public Health England, "Mandatory Health Care Associated Infection Surveillance," Tech. Rep. 1, 2019.

[182] Y. C. Hong, S. C. Cho, J. H. Kim, and H. S. Uhm, "A long plasma column in a flexible tube at atmospheric pressure," *Physics of Plasmas*, vol. 14, no. 7, 2007.

[183] A. M. Pointu, A. Ricard, E. Odic, and M. Ganciu, "Nitrogen atmospheric pressure post discharges for surface biological decontamination inside small diameter tubes," *Plasma Processes and Polymers*, vol. 5, no. 6, pp. 559–568, 2008.

[184] S. N. Siadati, F. Sohbatzadeh, and A. Valinataj Omran, "DC superimposed AC high voltage: A new strategy for transferring stable He atmospheric pressure cold plasma bullets through long dielectric tubes," *Physics of Plasmas*, vol. 24, no. 6, 2017.

[185] E. Robert, E. Barbosa, S. Dozias, M. Vandamme, C. Cachoncinlle, R. Viladrosa, and J. M. Pouvesle, "Experimental study of a compact nanosecond plasma gun," *Plasma Processes and Polymers*, vol. 6, no. 12, pp. 795–802, 2009.

[186] C. P. Hancock, "Microwave Plasma Sterilisation System and Application therefor," 2014.

[187] J. Winter, T. M. Nishime, R. Bansemer, M. Balazinski, K. Wende, and K. D. Weltmann, "Enhanced atmospheric pressure plasma jet setup for endoscopic applications," *Journal of Physics D: Applied Physics*, vol. 52, no. 2, 2019.

[188] J. Winter, T. M. Nishime, S. Glitsch, H. Lühder, and K. D. Weltmann, "On the development of a deployable cold plasma endoscope," *Contributions to Plasma Physics*, vol. 58, no. 5, pp. 404–414, 2018.

[189] C. P. Hancock, "Dual-functioning plasma and non-ionising microwave coagulating electrosurgical instrument and electrosurgical apparatur incorporating the same," 2016.

[190] J. Pollak, M. Moisan, D. Kéroack, J. Séguin, and J. Barbeau, "Plasma sterilisation within long and narrow bore dielectric tubes contaminated with stacked bacterial spores," *Plasma Processes and Polymers*, vol. 5, no. 1, pp. 14–25, 2008.

[191] T. Sato, O. Furuya, K. Ikeda, and T. Nakatani, "Generation and transportation mechanisms of chemically active species by dielectric barrier discharge in a tube for catheter sterilization," *Plasma Processes and Polymers*, vol. 5, no. 6, pp. 606–614, 2008.

[192] H. Eto, Y. Ono, A. Ogino, and M. Nagatsu, "Sterilization of Tubular Medical Instruments Using Wire-type Dielectric Barrier Discharge," *Journal of Plasma Fusion*, vol. 8, pp. 568–572, 2009.

[193] R. Ono, "Optical diagnostics of reactive species in atmospheric-pressure nonthermal plasma," *Journal of Physics D: Applied Physics*, vol. 49, no. 8, 2016.